

**Analyses of Structure and Functional  
Dynamics of Penicillin-binding Proteins  
in *Staphylococci***

**Dissertation**

**Submitted to the Faculty of Mathematics, Informatics and Natural  
Sciences of the University of Hamburg, Department of Chemistry, for the  
acquisition of the Doctorate of Natural Sciences (Dr. rer. nat.)**

**by**

**Martin Schwinzer**

**Hamburg, 2024**



## **Reviewers:**

1st Reviewer: **Prof. Dr. Dr. Christian Betzel**, University of Hamburg; Germany, Institute for Biochemistry and Molecular Biology, Department of Chemistry

2nd Reviewer: **Prof. Dr. Holger Rohde**, University Medical Center Hamburg-Eppendorf; Germany, Institute for Medical Microbiology, Virology and Hygiene

## **Committee Members:**

1st Member: **Prof. Dr. Dr. Christian Betzel**, University of Hamburg; Germany, Institute for Biochemistry and Molecular Biology, Department of Chemistry

2nd Member: **Dr. Thomas Hackl**, University of Hamburg; Germany, Department of Chemistry, Scientific Services, NMR Spectroscopy

3rd Member: **Prof. Dr. Hartmut Schlüter**, University Medical Center Hamburg-Eppendorf, Germany, Institute of Clinical Chemistry and Laboratory Medicine Diagnostic Center

**Disputation: 08.03.2024**

**Druckfreigabe: 24.03.2024**





This work was carried out from August 2019 to January 2024 in the research group of Prof. Dr. Dr. Ch. Betzel at the Laboratory for Structural Biology of Infection and Inflammation at the Institute for Biochemistry and Molecular Biology of the Department of Chemistry at the University of Hamburg.



## I: Publications

1. Schwinzer, M et al. (2023). Structure and Dynamics of the Penicillin-Binding Protein 3 from *Staphylococcus Epidermidis* native and in Complex with Cefotaxime and Vaborbactam. International Journal of Applied Biology and Pharmaceutical Technology 14.

The author has made contributions to the publications listed below:

2. Günther, S. et al. (2021). X-ray screening identifies active site and allosteric inhibitors of SARS-CoV-2 main protease. Science 372, 642-646.

3. Srinivasan, V et al. (2022). Antiviral activity of natural phenolic compounds in complex at an allosteric site of SARS-CoV-2 papain-like protease. Commun. Biol. 5, 805.



## II: Table of Contents

I: Publications .....	8
II: Table of Contents.....	9
III: Abbreviations .....	11
IV: Units.....	12
Zusammenfassung .....	13
Abstract.....	15
Introduction.....	17
Antibiotics and the Rise of Antimicrobial Resistance .....	17
Mode of Action of Antibiotics and Mechanism of Antimicrobial Resistance .....	22
Gram positive <i>Staphylococci</i> .....	27
Structure of the Bacterial Cell Wall in gram-positive Cells.....	28
<i>Staphylococcus aureus</i> .....	30
<i>Staphylococcus epidermidis</i> .....	33
Biofilm Formation.....	36
Penicillin-binding Proteins .....	38
Biochemical Reaction of Transpeptidases .....	42
Mechanism of $\beta$ -Lactam Antibiotics and Resistance in PBPs .....	43
Penicillin-binding Protein 2a.....	45
Penicillin-binding Protein 3.....	46
Aim of this Thesis .....	48
Material and Methods.....	49
Materials .....	49
Chemicals.....	49
Media, Buffers and Solutions.....	49
Size Marker.....	50
Kits.....	50
Equipment .....	50
Consumables.....	52
Software.....	52
Bacterial Strains .....	53
Methods.....	56

Molecular Biological Methods.....	56
Biochemical Methods .....	64
Spectroscopic Methods .....	73
Biophysical Methods.....	76
Bioinformatical Methods .....	83
<b>Results and Discussion .....</b>	<b>87</b>
Part One: Penicillin-binding Protein 3 from <i>Staphylococcus epidermidis</i> .....	88
Recombinant Expression and Purification.....	88
Protein Characterization .....	90
Crystallization.....	94
Interpretation of the Model.....	106
Analysis of the Flexibility of SePBP3 .....	116
Part One: Conclusion and Outlook .....	125
Part Two: Penicillin-binding Protein 2a from <i>Staphylococcus epidermidis</i> and <i>aureus</i> .....	126
Recombinant Expression and Purification.....	126
Protein Characterization .....	130
Crystallization.....	132
Analysis of the Influence of the allosteric Domain on the active Site of PBP2a .....	138
Part Two: Conclusion and Outlook .....	151
References.....	152
<b>SUPPLEMENTARY INFORMATION.....</b>	<b>166</b>
SUPPLEMENTARY FIGURES .....	167
CHEMICALS AND HAZARDOUS SUBSTANCES .....	171
LIST OF FIGURES .....	177
LIST OF TABLES .....	181
ACKNOWLEDGMENTS.....	182
EIDESSTATTLICHE ERKLÄRUNG .....	183

### III: Abbreviations

<b>AA</b>	Amino Acid
<b>AMPs</b>	Antimicrobial Peptides
<b>AMR</b>	Antimicrobial Resistance
<b>Ala</b>	Alanine or Alanyl
<b>CD</b>	Circular Dichroism Spectroscopy
<b>DHF</b>	Dihydrofolate
<b>DLS</b>	Dynamic Light Scattering
<b>DNA</b>	Deoxyribonucleic Acid
<b>EPS</b>	Extracellular Polymeric Substances
<b>EU</b>	European Union
<b>GRE</b>	Glycopeptide-resistant <i>Enterococci</i>
<b>HIV</b>	Human Immunodeficiency Viruses
<b>HMW</b>	High-molecular Weight
<b>ITC</b>	Isothermal Titration Calorimetry
<b>KanR</b>	Kanamycin-resistance-gene Cassette
<b>LB</b>	Lysogeny Broth
<b>LMW</b>	Low-molecular Weight
<b>MCS</b>	Multiple Cloning Site
<b>MD</b>	Molecular Dynamics
<b>MGT</b>	Monofunctional Glycosyltransferases
<b>MME</b>	MonoMethyl Ether
<b>MRSA</b>	Methicillin-resistant <i>Staphylococcus aureus</i>
<b>MRSE</b>	Methicillin-resistant <i>Staphylococcus epidermidis</i>
<b>MecA</b>	Methicillin resistance-conferring Alternative
<b>Ni-NTA</b>	Nickel-nitrilotriacetic Acid
<b>PABA</b>	p-Aminobenzoic Acid
<b>PBPs</b>	Penicillin-binding Proteins
<b>PEG</b>	Polyethylene Glycol
<b>QALYs</b>	Quality-adjusted Life Years
<b>RNA</b>	Ribonucleic Acid
<b>SCCmec</b>	Staphylococcal Cassette Chromosome mec
<b>SDS</b>	Sodium Dodecyl Sulfate
<b>SDS-PAGE</b>	SDS-Polyacrylamide Gel Electrophoresis
<b>SEC</b>	Size Exclusion Chromatography
<b>SEM</b>	Scanning Electron Microscopy
<b>SMART</b>	Simple Modular Architecture Research Tool
<b>SOC</b>	Super Optimal Broth with Catabolite Repression
<b>ST2</b>	Sequence Type 2
<b>TB</b>	Terrific Broth
<b>TEV</b>	Tobacco Etch Virus Nuclear-inclusion-a Endopeptidase
<b>THF</b>	Tetrahydrofolate
<b>USA</b>	United States of America

<b>VRSA</b>	Vancomycin-resistant <i>Staphylococcus aureus</i>
<b>WHO</b>	World Health Organization
<b>o.n.</b>	Over Night
<b>sub-MIC</b>	Sub-minimal Inhibitory Concentration
<b>tm</b>	Melting Temperature
<b>vanA</b>	Vancomycin A

## IV: Units

<b>Symbol</b>	<b>Meaning</b>
°C	Degree Celsius
Å	Angstrom
AU	Absorption Units
Da	Dalton
g	Gram
h	Hour
K	Kelvin
L	Liter
m	Meter
M	Molar (mol/l)
min	Minute
s	Second
V	Volt

## Zusammenfassung

Die Bewältigung der Herausforderungen, die durch multiresistente Bakterieninfektionen, insbesondere durch *Staphylococcus epidermidis* und *Staphylococcus aureus*, entstehen, ist von zentraler Bedeutung in der modernen medizinischen Forschung. Diese Dissertation konzentriert sich auf die Untersuchung der Penicillin-Bindenden Proteine (PBPs), speziell auf *SePBP3*, als wesentliche Ziele für die Entwicklung neuer antibakterieller Medikamente. Ein Kernpunkt dieser Studie ist die Kokristallisation von *SePBP3* mit den Antibiotika Cefotaxim und Vaborbactam. Cefotaxim, ein weit verbreitetes Cephalosporin der dritten Generation, bekannt für seine Wirksamkeit gegen ein breites Spektrum von Gram-positiven und Gram-negativen Bakterien, wird häufig zur Behandlung schwerer Infektionen eingesetzt, oft in Kombination mit Beta-Lactamase-Inhibitoren wie Vaborbactam, um seine antibakterielle Reichweite und Wirksamkeit zu erhöhen. Die beobachtete hohe Affinität zwischen *SePBP3* und diesen Antibiotika deutet auf die potenzielle Rolle von *SePBP3* als einen möglichen Decoy-Rezeptor hin, was eine innovative Strategie zur Bekämpfung bakterieller Resistenz darstellen könnte. Darüber hinaus unternimmt diese Forschung eine detaillierte Analyse der dynamischen Strukturzustände von *SePBP3*, wobei mittels Kleinwinkel-Röntgenstreuung (SAXS) und Molekulardynamik (MD) Simulationen offene und geschlossene Konformationen identifiziert wurden, die für Interaktionen mit noch unbekanntem molekularen Einheiten entscheidend sein könnten. Die Untersuchung der Interaktionsdynamik von *SePBP3* mit Cefotaxim und Vaborbactam trägt wesentlich zum Verständnis bakterieller Resistenzmechanismen bei und ebnet den Weg für innovative Ansätze in der antibakteriellen Therapieentwicklung.

Weiterhin erweitert diese Arbeit unser Verständnis von PBP2a aus *Staphylococcus aureus* und aus *Staphylococcus epidermidis*. Die Studie umfasst umfassende *in-silico* Analysen von PBP2a, einschließlich molekularer Docking- und MD-Simulationen mit natürlichen Verbindungen aus der Karachi-Bibliothek. Diese Analysen decken komplexe Interaktionen auf, insbesondere die Bindungseffizienz bestimmter Quercetinderivate und die Einführung einer neuen Klasse von chemischen Verbindungen für PBP2a, den Triterpenen. Die Bindung der Triterpene an der allosterischen Stelle von PBP2a bewirkt

eine signifikante Konformationsänderung, welche den aktiven Bereich des Hohlraums öffnet. Diese Transformation ist gekennzeichnet durch eine Verschiebung des Proteindeckels, die eine Verschiebung der Helixstruktur ermöglicht, wodurch das aktive Serin für Antibiotikainteraktion zugänglich wird. Die Aufklärung der Triterpenbindung an der allosterischen Stelle durch Docking- und MD-Simulationen erweitert nicht nur das Verständnis der molekularen Dynamik von PBP2a, sondern eröffnet auch neue Wege für die Entwicklung von Therapeutika gegen antibiotikaresistente *Staphylococcus aureus*. Im Rahmen dieser Studie wurde ein neues Expressions- und Reinigungsprotokoll für PBP2a entwickelt und im Vergleich zum bestehenden Protokoll evaluiert. Dieses innovative Protokoll ermöglicht eine effiziente Produktion von löslichem Protein, welches für Kristallisationsstudien geeignet ist. Ein signifikanter Vorteil dieses Verfahrens besteht darin, dass es die Prozesszeit für die Gewinnung von PBP2a verkürzt. Im Gegensatz zum etablierten Protokoll treten keine Einschlusskörper auf, wodurch zeitaufwendige Schritte wie das Entfalten und erneute Falten des Proteins überflüssig werden.

Diese Dissertation präsentiert somit eine umfassende Untersuchung der PBPs im Kontext von Antibiotikaresistenzen und bietet neue Struktur- und Funktion-bezogene Erkenntnisse und potenzielle Strategien für die Entwicklung wirksamer Behandlungen gegen resistente Stämme von *Staphylococcus*.

## Abstract

Addressing the challenge posed by multi-resistant bacterial infections, particularly those caused by *Staphylococcus epidermidis* and *Staphylococcus aureus*, is paramount in modern medical research. This dissertation delves into the study of Penicillin-binding Proteins (PBPs), with a specific focus on *SePBP3*, as essential targets for novel antibacterial drug development. Central to this study is the structure-analysis of *SePBP3* in complex with the antibiotics cefotaxime and vaborbactam. Cefotaxime, a widely utilized third-generation cephalosporin, known for its efficacy against a broad spectrum of Gram-positive and Gram-negative bacteria. It is often employed in treating severe infections, typically in conjunction with beta-lactamase inhibitors like vaborbactam to augment its antibacterial range and potency. The observed high-affinity interaction between *SePBP3* and these antibiotics suggests the potential role of *SePBP3* as a decoy receptor, offering a novel strategy to counteract bacterial resistance. Additionally, in terms of my research activities, I performed an in-depth analysis of the dynamic structural states of *SePBP3*, employing Small Angle X-ray Scattering (SAXS) measurements and molecular dynamics (MD) simulations to identify its open and closed conformations, pivotal for interactions with yet-unknown molecular entities. Investigating *SePBP3*'S interaction with cefotaxime and vaborbactam substantially contributes to the understanding of bacterial resistance mechanisms, thus providing data to develop innovative antibacterial therapy approaches.

Further, this thesis expands the knowledge of PBP2a from *Staphylococcus aureus* and *Staphylococcus epidermidis*. The study encompasses extensive *in silico* analysis of PBP2a, integrating molecular docking and MD simulations with natural compounds sourced from the Karachi library. These analyses uncover complex interactions, notably demonstrating the binding efficacy of specific quercetin derivatives and introducing a new class of compounds for PBP2a, triterpenes. The triterpenes' binding at the allosteric site of PBP2a induces a significant conformational change, opening the active site cavity. This transformation is characterized by a displacement of the protein's lid, which facilitates a shift in the helix structure, making the active serine site accessible for

antibiotic interaction. The analysis of triterpene binding at the allosteric site through both docking and MD simulations not only enhances our understanding of PBP2a's molecular dynamics but also opens up new avenues for developing therapeutic agents against antibiotic-resistant *Staphylococcus aureus*. Additionally, in terms of this study, a novel expression and purification protocol for PBP2a was developed. This advanced protocol facilitates the efficient production of soluble protein suitable for crystallization studies. A significant advantage of this method is the reduction in process time for PBP2a harvesting. Contrary to the established protocol, the occurrence of inclusion bodies is notably absent, thereby eliminating the need for time-consuming protein unfolding and refolding steps.

This dissertation thus presents a comprehensive exploration of PBPs in the context of antibiotic resistance, offering novel insights and potential strategies for developing effective treatments against resistant strains of *Staphylococcus*.



## Introduction

### **Antibiotics and the Rise of Antimicrobial Resistance**

Antimicrobial resistance (AMR) poses a profound global health threat, amplifying morbidity and mortality rates. The World Health Organization (WHO) reports that 4.9 million fatalities have been linked to AMR (WorldHealthOrganization, 2023). Additionally, a study from the European Union (EU) suggests that the death toll from AMR might approach that of cancer-related deaths in 2050 (O'Neill, 2016). Despite AMR challenges humanity in the modern world, resistance to antibiotics is an ancient phenomenon, with some estimations tracing the origin of natural antibiotics to over 40 million years ago, with resistance going alongside (D'Costa et al., 2011; Miner et al., 2021). Bacteria from Arctic permafrost, over 5,000 years old, demonstrate resistance not only to archaic antibiotics such as beta-lactams, aminoglycoside and tetracyclines but also to contemporary semi-synthetic compounds like amikacin (Perron et al., 2015).

Today's reasons for the increasing number of AMR microbes are plenty. The most common reasons are still the misuse or overuse of antibiotics. For instance, in agriculture, antibiotics are crucial for animal health and food security. However, globally, many are used not for infected individuals, but for infection prevention or growth promotion to compensate poor farming practice (O'Neill, 2016). A significant portion of these antibiotics, vital for humans, are used in animals. For example, in livestock, the application of antibiotics deemed critical for human health constitutes over 80% of the total consumption (Van Boeckel et al., 2017). In 2017, China increased its antibiotic use for veterinary purposes, accounting for 45% of global consumption, making it the top consumer worldwide (Tiseo et al., 2020). Beyond agriculture, there's a widespread issue of misuse or excessive prescription in outpatient medical environments by physicians. A study by Shapiro et al. revealed that approximately 70% of individuals in the United States of America with respiratory complaints were prescribed antibiotics prophylactically, without any corresponding supporting tests (Shapiro et al., 2014). In low- and middle-income countries, particularly Vietnam and Bangladesh, antibiotics are readily available at unregulated outlets. Often, essential antibiotics are easily obtained

from standard pharmacies for minor ailments. This easy access risks misuse due to limited understanding of antibiotics and unawareness of AMR (Do et al., 2021).

Since Sir Alexander Fleming's discovery of penicillin in 1927, various antibiotics have been introduced to the public. Regrettably, drug-resistant strains often surfaced shortly after an antibiotic was marketed, and in some cases, even before its release. The first known antimicrobial drug employed against a bacterial infection was Arsphenamine, also known as Salvarsan, used to combat syphilis, specifically targeting *Treponema pallidum*. Since this drug was synthesized by Paul Ehrlich and Sahachirō Hata, and not derived from or emulating microbial compounds, it does not qualify as an antibiotic in the traditional sense. But even it was completely synthesized and had no natural origin, resistance emerged 14 years later in 1924 (Greither; Jones, 1911; Riethmiller, 2005). For the synthesized drug sulfonamide, which inhibits the folate synthesis, a resistant strain was identified as early as 1942, merely seven years post its introduction (Gelmo, 1908; Raju, 1999). The first drug classified as antibiotic was the Penicillin G rediscovered by Sir Alexander Fleming in 1928. Upon examining a petri dish containing a *Staphylococcus* strain, he noted contamination with a fungus identified as *Penicillium rubens*. In the immediate vicinity of this fungal presence, the bacterial colonies were annihilated. He hypothesized that the mold was producing an antimicrobial substance. This compound, once isolated, was subsequently termed penicillin (Bigger et al., 1927; Fleming, 1929). In 1942, the inaugural patient treatment with penicillin was carried out using a formulation produced by Merck & Co, which led to the mass production for the World War II (Grossman, 2008). Remarkably, resistance to penicillin had already been observed prior to its market introduction, with the first resistant strain (*Staphylococcus aureus*) identified in 1940. Abraham and Chain were able to ascertain that the degradation was mediated by an enzyme, initially termed Penicillinase, which was later renamed  $\beta$ -Lactamase (Abraham and Chain, 1940).

The introduction of penicillin marked the inception of what is often referred to as the "Golden Age" of antibiotic research. This epoch is delineated by the fast identification of novel antimicrobial agents, resulting in significant implications for the advancement of

public health. Streptomycin, introduced to tackle tuberculosis, saw resistance within two years of its 1946 debut (Schatz A Fau - Bugie et al., 1944). Chloramphenicol, developed to treat typhoid in 1949, encountered a resistant strain by 1950 (Rebstock et al., 1949). Erythromycin, launched in 1952, targeted gram-positive bacterial infections, notably those penicillin resistant. However, resistance to erythromycin surfaced by 1955 (Washington and Wilson, 1985). Tetracycline, introduced concurrently with Erythromycin in 1952, observed resistance by 1959 (Finlay Ac Fau - Hobby, 1950). Methicillin was introduced in 1960, designed to combat penicillin resistance (Rutenburg et al., 1960). Vancomycin came into marked 1958 and could sustain without a corresponding resistant-strain until 1987 (McCormick et al., 1955). The "Golden Age" culminated in 1962, as the presence of methicillin-resistant *Staphylococcus aureus* (MRSA) was observed. As per the WHO's recent data, MRSA continues to be the second most common AMR infection (WorldHealthOrganization, 2023).

Subsequent years are frequently termed the "Me-Too era" in antibiotic research. This period saw a limited discovery of novel antibiotic classes; instead, the primary focus was on mimicking pre-existing antibiotic classes and their mechanisms of inhibition (Aronson and Green, 2020). Some scientists categorize the period from 2000 to the present as the "post-antibiotic era." This characterization arises from the observation that the emergence of antibiotic-resistant bacterial strains has overwhelmingly outpaced the introduction of new antibiotic classes (Alanis, 2005).

Figure 1 chronologically delineates the introduction of antibiotics across distinct eras and their associated emergence of AMR bacterial strains. This representation underscores the imperative of investment in drug discovery, a sentiment echoed by both the EU and the WHO in their respective AMR action plans (O'Neill, 2016; WorldHealthOrganization, 2023). Following is an exhaustive enumeration of antibiotic classes and subclasses.

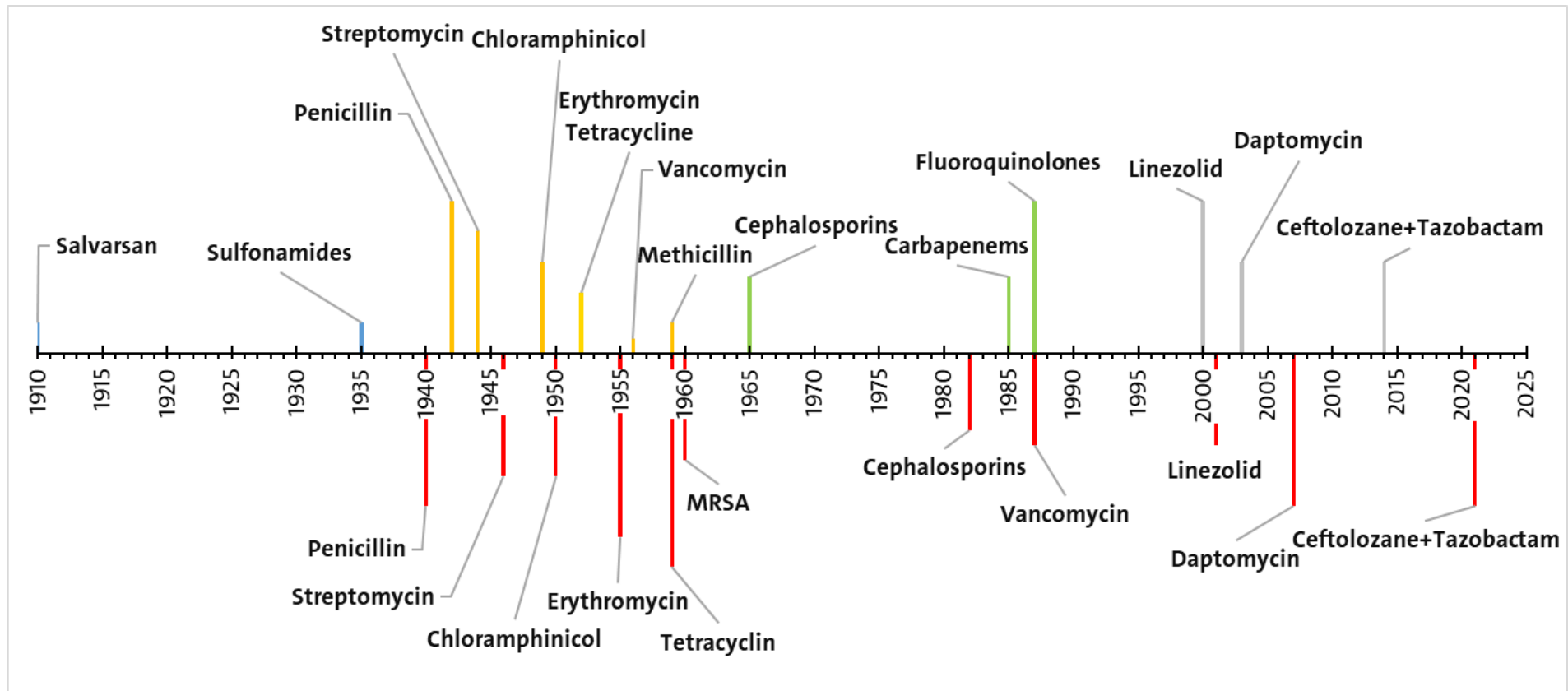


**Figure 1: Chronological Presentation of selected Antibiotics and their corresponding Emergence of antibiotic-resistant Bacterial Strains.** The timeline is demarcated with color codes: blue signifies the inception phase with the earliest drugs; yellow denotes the "Golden Age" of antibiotic discovery; green represents the "Me-Too era" characterized by modifications of established antibiotic classes; and grey marks the "post-antibiotic era." Instances where resistance emerged post the introduction of antibiotics into clinical practice are highlighted in red (O'Neill, 2016; WorldHealthOrganization, 2023).

**Table 1: Historical Introduction of selected antibiotics: A chronological Overview (Hutchings et al., 2019)**

<b>Antibiotic Class</b>	<b>Example</b>	<b>Year</b>	<b>Notes</b>
<b>Penicillins</b>	<b>Benzylpenicillin (Penicillin G)</b>	<b>1942</b>	<b>Heralded a new era of antibacterial treatment</b>
	<b>Phenoxymethylpenicillin (Penicillin V)</b>	<b>1948</b>	
	<b>Methicillin</b>	<b>1959</b>	<b>Led to the identification of MRSA</b>
	<b>Nafcillin</b>	<b>1960</b>	
	<b>Ampicillin</b>	<b>1961</b>	
	<b>Dicloxacillin</b>	<b>1962</b>	
	<b>Amoxicillin</b>	<b>1972</b>	
	<b>Piperacillin</b>	<b>1978</b>	
<b>Cephalosporins</b>	<b>First Generation (e.g., Cephalexin, Cefazolin)</b>	<b>Late 1960s</b>	<b>Active against Gram-positive bacteria</b>
	<b>Second Generation (e.g., Cefaclor, Cefuroxime)</b>	<b>1970s</b>	<b>Extended Gram-negative activity</b>
	<b>Third Generation (e.g., Ceftriaxone, Ceftazidime)</b>	<b>1980s</b>	<b>Enhanced Gram-negative spectrum</b>
	<b>Fourth Generation (e.g., Cefepime)</b>	<b>1990s</b>	<b>Broad-spectrum with activity against both Gram-positive and Gram-negative organisms</b>
<b>Carbapenems</b>	<b>Imipenem</b>	<b>1985</b>	<b>Known for its broad antibacterial spectrum</b>
	<b>Meropenem</b>	<b>1996</b>	
	<b>Ertapenem</b>	<b>2001</b>	
<b>Aminoglycosides</b>	<b>Streptomycin</b>	<b>1943</b>	<b>The inaugural effective treatment for tuberculosis</b>
	<b>Neomycin</b>	<b>1949</b>	
	<b>Kanamycin</b>	<b>1957</b>	
	<b>Gentamicin</b>	<b>1963</b>	
	<b>Tobramycin</b>	<b>1975</b>	
	<b>Amikacin</b>	<b>1976</b>	
<b>Tetracyclines</b>	<b>Tetracycline</b>	<b>1948</b>	<b>Characterized by its broad-spectrum activity</b>
	<b>Doxycycline</b>	<b>1967</b>	
	<b>Minocycline</b>	<b>1972</b>	

<b>Macrolides</b>	<b>Erythromycin</b>	<b>1952</b>	<b>A potent alternative for patients with penicillin allergies</b>
	<b>Azithromycin</b>	<b>1988</b>	
	<b>Clarithromycin</b>	<b>1991</b>	
<b>Fluoroquinolones</b>	<b>Ciprofloxacin</b>	<b>1987</b>	<b>Renowned for its Gram-negative activity</b>
	<b>Levofloxacin</b>	<b>1996</b>	
	<b>Moxifloxacin</b>	<b>1999</b>	
<b>Sulfonamides and Related Compounds</b>	<b>Sulfanilamide</b>	<b>1936</b>	<b>A precursor in the sulfonamide class</b>
	<b>Sulfamethoxazole (often paired with trimethoprim)</b>	<b>1961</b>	
<b>Glycopeptides</b>	<b>Vancomycin</b>	<b>1958</b>	<b>Instrumental in treating resistant Gram-positive infections</b>
	<b>Teicoplanin</b>	<b>1980s</b>	
<b>Miscellaneous</b>	<b>Chloramphenicol</b>	<b>1947</b>	
	<b>Clindamycin</b>	<b>1967</b>	
	<b>Linezolid</b>	<b>2000</b>	
	<b>Daptomycin</b>	<b>2003</b>	
	<b>Rifampin (Rifampicin)</b>	<b>1968</b>	
	<b>Metronidazole</b>	<b>1960</b>	
	<b>Trimethoprim (commonly co-formulated with sulfamethoxazole)</b>	<b>1962</b>	
	<b>Relebactam</b>	<b>2019</b>	<b>Approved in a fixed combination with Imipenem and Cilastatin.</b>

### **Mode of Action of Antibiotics and Mechanism of Antimicrobial Resistance**

Antibiotics can be broadly categorized based on their mechanistic action. There are bacteriostatic agents that inhibit bacterial growth and bactericidal agents that directly cause bacterial cell death. These agents predominantly target vital bacterial cell components, including folate synthesis, the integrity and formation of the cell membrane and cell wall, deoxyribonucleic acid (DNA) or ribonucleic acid (RNA) metabolism, and protein synthesis (Figure 2) (Kohanski et al., 2010). For instance,

aminoglycosides, such as gentamicin and kanamycin, exhibit dual mechanisms of action. Owing to their positive charge, they can interact with the negatively charged bacterial membrane, leading to pore accumulation. Additionally, they can bind to the 30S ribosomal subunit of the 16S RNA, resulting in translation errors (Davis BD, 1986 ).  $\beta$ -lactam antibiotics covalently bind to the active serine site of Penicillin-binding proteins (PBPs), thereby inhibiting bacterial cell wall synthesis. Their efficacy stems from their structural mimicry of the peptide stem of peptidoglycan (Lima et al., 2020). Glycopeptides, such as vancomycin, complex with the l-lysine-d-alanyl-l-alanine peptide terminus of peptidoglycan, obstructing cell wall assembly (Lima et al., 2020). Several antibiotics, including lincosamides, oxazolidinones, macrolides, streptogramins, tetracyclines, and phenicols, act by inhibiting ribosomal translation. Their mode of action entails binding to specific regions of ribosomal subunits or ribosomal RNAs (Swaney Steve et al., 1998; Jerala, 2007; S. Schwarz et al., 2016; Spížek and Řezanka, 2017; Markley and Wencewicz, 2018). Lipopeptides induce cell membrane depolarization by insertion, disrupting ATP production and ultimately causing cell death (Jerala, 2007). Pyrimidines and sulfonamides specifically target folate synthesis pathways, while quinolones inhibit DNA replication by targeting enzymes such as DNA gyrase and topoisomerase IV (Sköld, 2000; Correia et al., 2017; Wróbel et al., 2020).

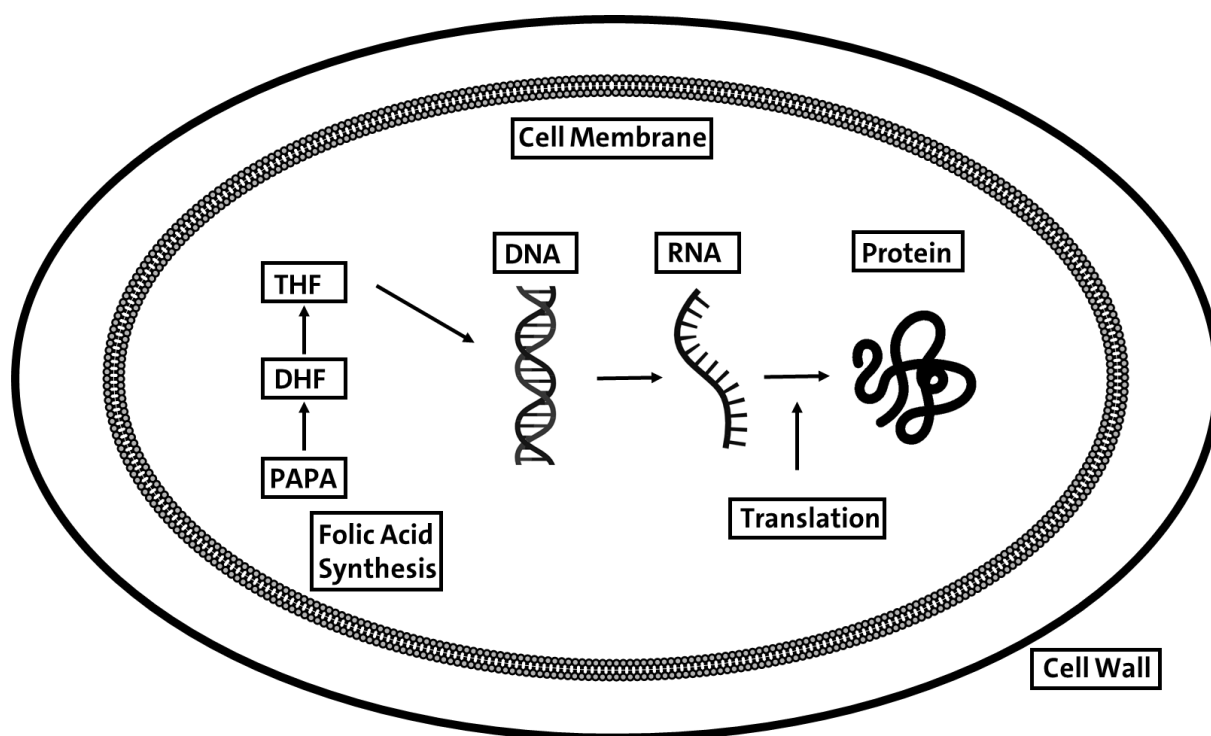


**Figure 2: A schematic Elucidation of Antibiotic Targets within Bacteria.** The illustration delineates the bacterial cell membrane and wall, emphasizing primary antibiotic interaction sites. These sites include nucleic acid dynamics (DNA & RNA), translational processes, protein synthesis pathways, cellular membrane and wall, as well as pathways in folic acid biosynthesis, notably involving p-aminobenzoic acid (PABA), dihydrofolate (DHF), and tetrahydrofolate (THF) (Kohanski et al., 2010).

Bacteria have developed numerous strategies to counteract antibiotic effects (Figure 3). A well-studied strategy is the reduction of membrane permeability. This is particularly crucial for gram-negative bacteria, which possess a double membrane, inherently diminishing the efficacy of certain antibiotics primarily effective against gram-positive bacteria (Draper, 1998; Mishra et al., 2012). Another one is impeding the influx of antibiotics by downregulating influx porins or mutate specific loops to alter specificity or charge (Pratt et al., 1996; Lou et al., 2011; Wong et al., 2019). Prevent antibiotics to enter the cell is one way of resistance, the other one is pumping them actively out of the cell. These efflux pumps are huge complexes that span both the cell membrane and the cell wall. Especially, macrolides, pyrimidine analogues, or tetracyclines can be actively extruded from the bacterial cell via efflux pumps (Roberts, 2008; Markley and Wencewicz, 2018; Wróbel et al., 2020). When an antibiotic penetrates the cytosol and cannot be effluxed, the bacterial cell evolves multiple mechanisms to counteract its inhibitory effects. One primary mechanism is a target mutation. This can manifest in



decreased binding affinity due to amino acid substitutions that influence the stability of the antibiotic-target complex. Alternatively, mutations might cause conformational changes in the target, rendering it less susceptible to antibiotic binding (Sköld, 2000; Floss and Yu, 2005; S. Schwarz et al., 2016; Correia et al., 2017). Such target mutations are pervasive among many antibiotics, emphasizing their significance. This has prompted the development of the Mutation-induced drug resistance DataBase (MdrDB) dedicated solely to protein structures associated with mutations (Z. Yang et al., 2023). Another mechanism is target-modifications. Many antibiotic resistance types correlate with modifications, such as ribonucleic acid (RNA) methylation in ribosomes. This is particularly notable in the case of resistances against aminoglycosides, lincosamides, macrolides, and oxazolidinones (Poehlsgaard and Douthwaite, 2005; Long et al., 2006; Roberts, 2008; Wachino et al., 2020; Stefan Schwarz et al., 2021). Bacteria might also resort to target overproduction, necessitating a significant increase in antibiotic concentration for efficacy (Thom and Prescott, 1997). Alternatively, bacterial cells can express new proteins possessing analogous enzymatic functions as the original target but are unaffected or less effected by the antibiotic. This phenomenon is evident in certain  $\beta$ -lactam antibiotics (Lim and Strynadka, 2002). Drug modification serves as another resistance avenue. A classic example is the modification obscuring the binding site of glycopeptides like vancomycin, preventing the antibiotic from reaching its target (Stogios and Savchenko, 2020). Perhaps one of the most recognized mechanisms is the synthesis of enzymes specialized in degrading the antibiotic. For instance,  $\beta$ -lactamases can hydrolyze the  $\beta$ -lactam ring present in numerous  $\beta$ -lactam antibiotics (Ridley and Phillips, 1965). A comprehensive overview of various antibiotic classes, their modes of action, and corresponding resistance mechanisms is presented in table 2.

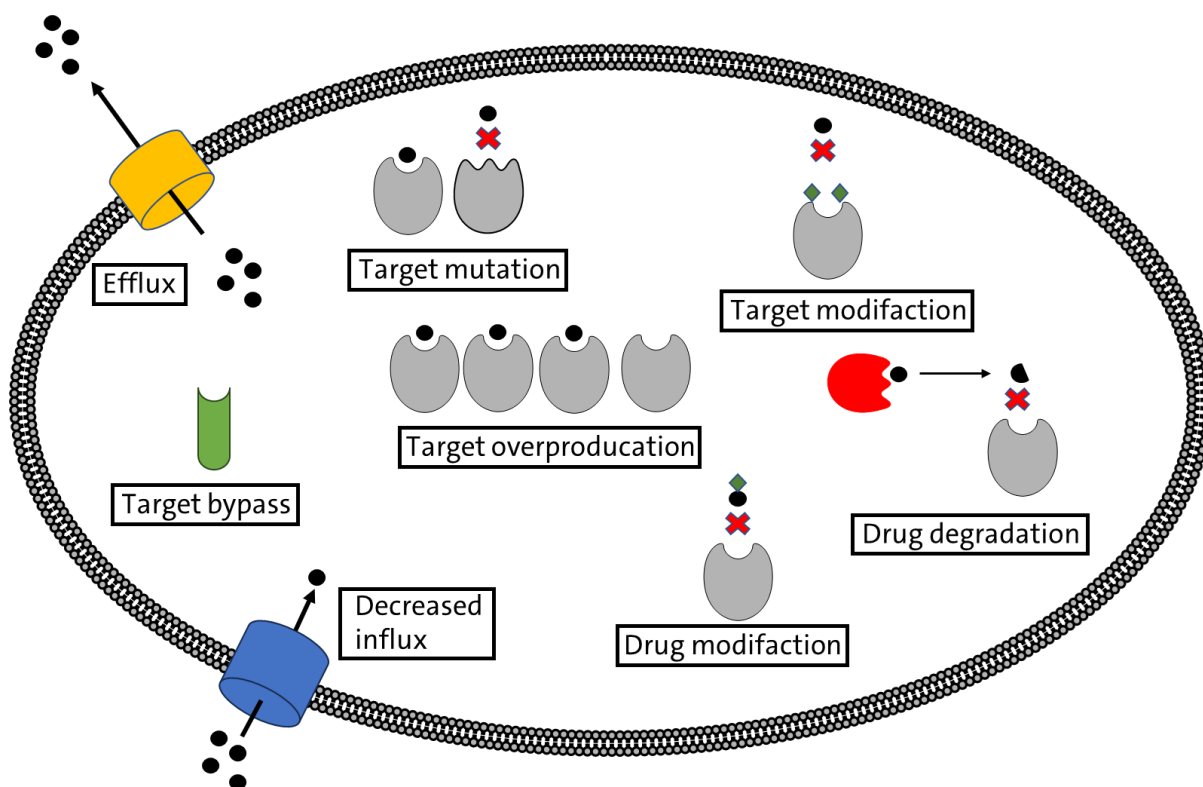


**Figure 3: A schematic Representation of Antibiotic Resistance Mechanisms.** The cartoon depicts the bacterial cell membrane, highlighting both efflux and influx pumps. Within the cytosol, mechanisms such as target mutations, modifications, bypass, and overproduction are illustrated. Additionally, drug degradation and modification processes are also shown (Wilson, 2014).

**Table 2: A detailed overview of selected antibiotic classes, emphasizing their mode of action and associated resistance mechanisms.**

	Action	Resistance
<b>Aminoglycosides</b>	Interact with ribosomal subunits to interrupt protein synthesis (Davis BD, 1986 ).	Enzymatic modification and RNA mutations (Wachino et al., 2020).
<b>β-lactams</b>	Block cell wall synthesis by inhibiting penicillin-binding proteins (Lima et al., 2020).	Production of beta-lactamases, PBPs modification and cell wall modifications (Lim and Strynadka, 2002; Zapun et al., 2008; ur Rahman et al., 2018).
<b>Cationic peptides</b>	Bind to lipid A, making outer membrane permeable (Andrade et al., 2020).	Lipid alterations (Y.-Y. Liu et al., 2016).
<b>Glycopeptides</b>	Block cell wall synthesis by binding to D-alanyl-D-alanine in the peptide chains (Zeng et al.).	Changes in cell membrane permeability and peptide alterations (Zeng et al.).

<b>Lincosamides</b>	Halt protein synthesis by targeting rRNA (Spížek and Řezanka, 2017).	RNA modifications and protein inactivation (Long et al., 2006).
<b>Lipopeptides</b>	Integrate into membranes, disrupting cell functionality (Jerala, 2007).	Cell membrane modifications (Mishra et al., 2012).
<b>Macrolides</b>	Stop protein synthesis by interacting with rRNA (Vázquez-Laslop and Mankin, 2018).	RNA modifications and efflux processes (Poehlsgaard and Douthwaite, 2005).
<b>Oxazolidinones</b>	Restrict protein synthesis by binding to rRNA (Swaney Steve et al., 1998).	RNA modifications (Stefan Schwarz et al., 2021).
<b>Phenolics</b>	Inhibit protein synthesis by targeting ribosomal units (S. Schwarz et al., 2016).	Ribosomal alterations and enzymatic inactivation (S. Schwarz et al., 2016).
<b>Pyrimidines</b>	Affect metabolism and protein synthesis by targeting enzyme activity (Wróbel et al., 2020).	Enzymatic alterations and efflux processes (Wróbel et al., 2020).
<b>Quinolones and fluoroquinolones</b>	Halt DNA synthesis by affecting enzymes (Correia et al., 2017).	Genetic mutations and protein alterations (Correia et al., 2017).
<b>Rifamycins</b>	Stop RNA synthesis by targeting RNA polymerase (Floss and Yu, 2005).	Enzymatic modification (Floss and Yu, 2005).
<b>Streptogramins</b>	Restrict protein synthesis by binding to rRNA (Beyer and Pepper, 1998).	RNA modifications and enzymatic processes (S. Schwarz et al., 2016).
<b>Sulfonamides</b>	Inhibit folic acid synthesis by affecting enzymes (Sköld, 2000).	Enzymatic alterations (Sköld, 2000).
<b>Tetracyclines</b>	Prevent protein synthesis by interacting with ribosomal units (Markley and Wencewicz, 2018).	Efflux mechanisms and enzymatic modifications (Markley and Wencewicz, 2018).

### **Gram positive *Staphylococci***

Bacteria can be classified based on their response to gram staining, a differential staining technique. The stain's retention depends on the structure of the bacterial cell wall, predominantly composed of peptidoglycans. Gram-positive bacteria possess a thick peptidoglycan layer, enabling them to retain the crystal violet dye even after the ethanol washing step in the staining protocol. In contrast, gram-negative bacteria have an

additional outer membrane enveloping their cell wall. Given their comparatively thinner peptidoglycan layer, the crystal violet dye is easily washed away during the ethanol wash, resulting in a negative stain (Coico, 2006).

### Structure of the Bacterial Cell Wall in gram-positive Cells

In gram-positive cells, the cell wall is situated externally to the cell membrane, with the intervening space referred to as the periplasmic space. The cell wall is primarily composed of two sugar molecules: N-Acetylglucosamine and N-Acetylmuramic acid. In addition to these sugar molecules, the cell wall also incorporates an oligopeptide that contains two d-alanine residues (Figure 4) (Pasquina-Lemonche et al., 2020).

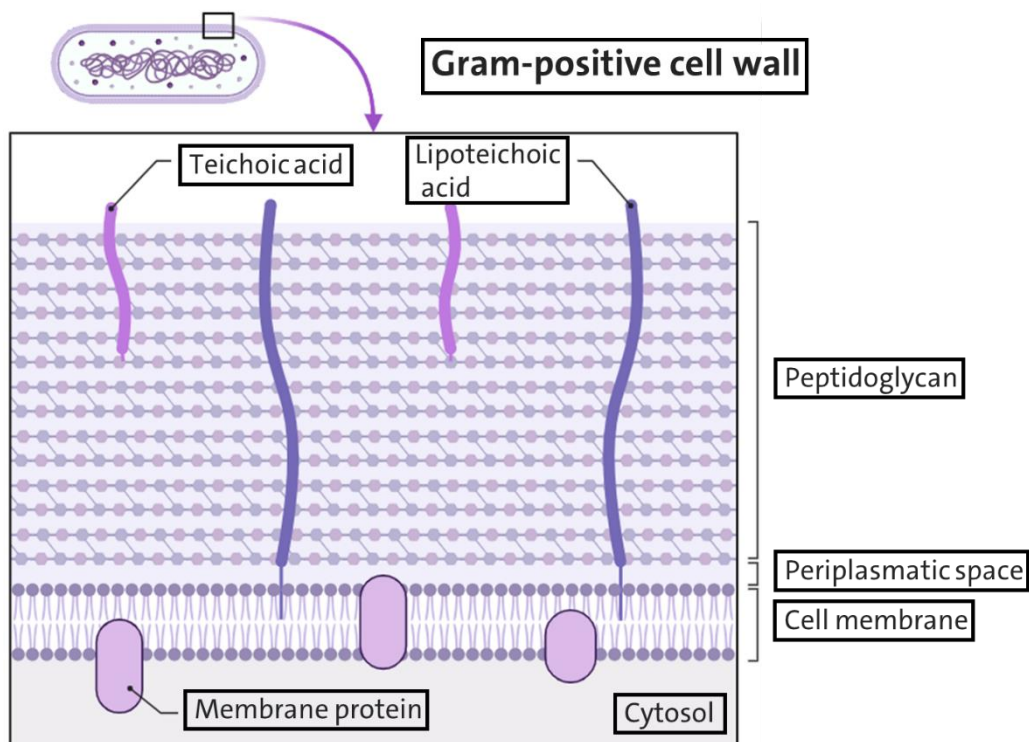


**Figure 4: Schematic Representation of the gram-positive Bacterial Cell Wall.** The thick layer of peptidoglycan is depicted with embedded key components including teichoic acid and lipoteichoic acid. The hexagonal patterns symbolize the sugar molecules, N-Acetylglucosamine and N-Acetylmuramic acid, integral to the peptidoglycan matrix, while the connecting lines signify the oligopeptide chains. This layered structure is external to the cell membrane, separated by the periplasmic space (Pasquina-Lemonche et al., 2020). Created with BioRender.com.

This differentiation is not solely for distinguishing bacterial cells from a biological classification perspective; it also holds clinical significance due to the differential infections and responses of these bacteria to various antibiotic treatments.

Gram-negative bacteria are equipped with an additional outer membrane that selectively permits substances to enter the cell, thereby limiting the access of certain antibiotics. This structural attribute fundamentally enhances their defense against antibacterial agents (Mühlberg et al., 2020). Additionally, these bacteria possess efflux pumps—mechanisms that actively transport antibiotics out of the cell, further augmenting their inherent resistance to antibiotic treatment (Colclough et al., 2020). In contrast, gram-positive bacteria lack this outer membrane and have less complex efflux systems, rendering them generally more susceptible to antibiotics. However, antibiotics such as cephalosporins and carbapenems are designed to penetrate the outer membrane of gram-negative bacteria, making them effective options for targeting these organisms. On the other hand, the efficacy of these antibiotics against gram-positive bacteria is often compromised due to the presence of specific  $\beta$ -lactamases (Tang et al., 2014). Understanding the resistance mechanisms of gram-positive bacteria is critical given their role in causing a wide array of infections. For instance, *Staphylococcus aureus* epitomizes a dichotomous microorganism, harmoniously coexisting as an asymptomatic commensal within the nasal mucosa of approximately 30% of individuals, while concurrently standing as the principal gram-positive pathogen responsible for skin and soft tissue infections. This facultative pathogen exhibits a noteworthy propensity for transitioning from a quiescent colonizer to an invasive agent, precipitating conditions ranging from superficial skin abscesses to severe necrotizing fasciitis (Tong et al., 2015). In the United States of America (USA), pneumonia constitutes the main cause of hospital admissions and mortality among adults, with the gram-positive bacterium *Streptococcus pneumoniae* being one of the top three etiological agents, alongside viral pathogens. This encapsulated organism is a significant contributor to community-acquired pneumonia, with its pervasive presence and virulence solidifying its position as a critical public health concern (Jain et al., 2015). Not only infections but foodborne illnesses frequently implicate gram-positive bacteria such as *Bacillus cereus* and *Staphylococcus aureus*, which are capable of secreting enterotoxins. These toxins, once ingested, can provoke gastrointestinal symptoms characteristic of food poisoning. The enterotoxins produced by these bacteria exhibit resistance to proteolytic degradation and can withstand the

acidic environment of the stomach, thereby retaining their capacity to cause illness even when the bacteria that produced them are no longer viable (Argudín et al., 2010).

This study is focused on proteins of gram-positive bacteria, specifically *Staphylococcus aureus* and *Staphylococcus epidermidis*. Consequently, the subsequent chapters will delve into detailed discussions regarding these two bacterial species.

### ***Staphylococcus aureus***

*Staphylococcus aureus* is a gram-positive bacterium with a distinctive spherical morphology known as cocci. This species is consistently catalase-positive, a trait shared among the *Staphylococcus* genus. However, it is particularly characterized by its production of coagulase, an enzyme that uniquely qualifies it within its genus for its role in converting fibrinogen to fibrin, thus promoting the formation of clots (Ahmad-Mansour et al., 2021). Sir Alexander Ogston, a Scottish surgeon, first identified this bacterium in 1880, observing its characteristic grape-like clustering. The identification was complemented by the observations of the golden-yellow pigmentation it presented in culture, a feature that inspired the species epithet *aureus*, meaning golden (Ogston, 1882). It was Friedrich Julius Rosenbach, a German physician, who in 1884, discerned this species from other members of the *Staphylococcus* genus and formally named it *Staphylococcus aureus* (Rosenbach, 1884).

Nowadays, *Staphylococcus aureus* is estimated to colonize the nasal mucosa of 20-40% of the human population as a component of the commensal microbiota, residing asymptotically. Predominantly harbored within the nasal passages, it typically exists in a quiescent state, not eliciting any apparent detrimental effects (Wertheim et al., 2005; Becker et al., 2017). However, the disruption of mucosal barriers—whether through surgical interventions, trauma, or underlying disease processes—can facilitate the transition of *Staphylococcus aureus* from a benign colonizer to an opportunistic pathogen. Upon breaching these defenses, it has the potential to invade the bloodstream and establish severe systemic infections (Lowy, 1998). It is responsible for a multitude of infections, including bacteremia, infective endocarditis, various skin and soft tissue infections such as impetigo, folliculitis, furuncles, carbuncles, cellulitis, and scalded skin

syndrome, as well as osteomyelitis, septic arthritis, infections associated with prosthetic devices, pulmonary conditions like pneumonia and empyema, gastroenteritis, meningitis, toxic shock syndrome, and urinary tract infections (Tong et al., 2015).

Humans constitute the primary reservoir for *Staphylococcus aureus*, yet there is substantial evidence indicating the bacterium's capacity for host-switching, successfully colonizing various animal species. Livestock such as cows, pigs, sheep, and goats play a significant role in maintaining and propagating these bacterial populations (Zhou et al., 2018; Haag et al., 2019). Furthermore, a diverse array of other animals, including birds, rodents, rabbits, hedgehogs, and domestic pets like dogs and cats, have also been implicated in harboring *Staphylococcus aureus* (Haag et al., 2019; Matuszewska et al., 2020; Park and Ronholm, 2021). Particularly noteworthy is the context of intensive livestock farming, where mass breeding practices of cows, pigs, or chickens not only provide a reservoir for the bacterium but also potentiate the risk of engendering new multi-drug resistant variants of *Staphylococcus aureus*. The dense conditions and frequent antibiotic use in these settings create an environment conducive to the emergence and selection of resistant strains, posing a heightened challenge to public health (Casey et al., 2013; Van Boeckel et al., 2017).

### **Resistant mechanism of *Staphylococcus aureus***

*Staphylococcus aureus* first exhibited resistance not to methicillin, but to penicillin. This resistance is facilitated by the expression of the *bla<sub>Z</sub>* gene, which codes for a  $\beta$ -lactamase enzyme (Abraham and Chain, 1940; Olsen et al., 2006), 1940. The  $\beta$ -lactamase mediates resistance through the hydrolytic degradation of the  $\beta$ -lactam core of penicillin antibiotics. It achieves this by cleaving the  $\beta$ -lactam ring, a crucial structural component of these antibiotics, rendering them incapable of effectively binding to their target PBPs on the bacterial cell wall. Without proper binding to PBPs, penicillin antibiotics are unable to exert their bactericidal effect, which normally involves inhibiting the synthesis of the bacterial cell wall and thus leading to cell lysis (Abraham and Chain, 1940; Olsen et al., 2006). Methicillin, a semi-synthetic  $\beta$ -lactam antibiotic, was developed in response to the emergence of penicillin-resistant *Staphylococcus aureus*, mediated by  $\beta$ -lactamase enzymes. Intriguingly, genetic analyses indicate that the first strains of MRSA were

identified even before methicillin was clinically introduced. This suggests that the selective pressure exerted by widespread penicillin use may have been a critical factor in the evolution of MRSA (Harkins et al., 2017). The resistance to methicillin in *Staphylococcus aureus* is facilitated by the *mecA* gene, which is disseminated through the horizontal gene transfer of a mobile genetic element known as the staphylococcal cassette chromosome *mec* (SCC*mec*). The *mecA* gene is responsible for the production of penicillin-binding protein 2a (PBP2a), an enzyme critical for catalyzing the cross-linking of peptidoglycan layers within the bacterial cell wall. PBP2a is characterized by its reduced binding affinity for  $\beta$ -lactam antibiotics, a property that confers resistance to this broad group of antibiotics. While  $\beta$ -lactam antibiotics typically inhibit the activity of standard PBPs, PBP2a compensating for the inactivated PBPs and ensuring the continuation of cell wall synthesis necessary for bacterial survival and growth (Lim and Strynadka, 2002). The economic burden of MRSA infections extends significantly beyond the clinical setting. In German hospitals alone, the direct costs incurred due to MRSA are estimated to be formidable, ranging from approximately 354.29 million to as high as 1.55 billion euros. This financial strain is further compounded when considering the broader economic implications, specifically the productivity losses which are estimated to be at least 92.77 million euros, resulting from the extended duration of illness among patients (Becker et al., 2017). From a health economics perspective, the impact of MRSA infections on patient well-being is measurable in terms of quality-adjusted life years (QALYs), with an estimated deficit of 0.292 QALYs per infected individual (Claus et al., 2014; Becker et al., 2017). The advent of MRSA has been a watershed in the context of antimicrobial resistance, delineating the end of the golden era of antibiotic discovery. In the wake of MRSA's proliferation, strains exhibiting resistance to vancomycin, designated as VRSA (Vancomycin-resistant *Staphylococcus aureus*), have also been identified, predominantly through the acquisition of the vancomycin A (*vanA*) resistance gene cluster and its associated operon, via horizontal gene transfer from *Enterococcus* species such as *Enterococcus faecium* or *Enterococcus faecalis*. This leads to the production of an altered cell wall with an increased thickness of the peptidoglycan layer. This structural modification impedes the diffusion of vancomycin, thereby obstructing its ability to



reach its target sites within the bacterial cell wall and diminishing its bactericidal efficacy (Chang et al., 2003; McGuinness et al., 2017; Stogios and Savchenko, 2020). Efflux pumps serve as another mechanism for developing resistance, not just to antibiotics but also to antiseptics. Some efflux pumps are encoded by genes located on plasmids, which are mobile genetic elements that can be transferred between bacteria. This attribute can lead to the phenomenon of multidrug resistance, as efflux pumps can reduce the intracellular concentration of antibiotics to a sub-minimal inhibitory concentration (sub-MIC) (Costa et al., 2013). *Staphylococcus aureus* can transition from a free-floating, planktonic state to a sessile biofilm community. This adaptive behavior serves natural purposes, including community survival and resource sharing. Concurrently, the dense extracellular matrix of the biofilm acts as a defensive barrier, impeding the penetration of many antibiotics. When residing within this biofilm, it exhibits multidrug-resistant characteristics, making infections caused by these biofilms particularly challenging to treat (Parastan et al., 2020).

### ***Staphylococcus epidermidis***

In 1884, the bacteriologist Friedrich Julius Rosenbach made the initial discovery of what we now know as *Staphylococcus epidermidis*. He initially referred to this bacterium as "*Staphylococcus albus*" based on its distinctive characteristic of forming white colonies. This nomenclature was chosen in contrast to *Staphylococcus aureus*, which typically forms colonies with a yellow-golden hue (Rosenbach, 1884).

*Staphylococcus epidermidis* is a gram-positive bacterium that has a spherical (cocci) morphology. It shares the characteristic of being catalase-positive with other staphylococci bacteria. However, it differs from *Staphylococcus aureus* in that it is coagulase-negative, meaning it does not produce the coagulase enzyme. *Staphylococcus epidermidis* can be distinguished from another coagulase-negative species, *Staphylococcus saprophyticus*, by its sensitivity to the antibiotic novobiocin. This sensitivity to novobiocin is a diagnostic feature that helps to differentiate between these two similar bacteria (Schleifer and Kloos, 1975; Kloos, 1980).

*Staphylococcus epidermidis* is a bacterium that is widely distributed on the human skin (System, 2004). Despite the challenging conditions presented by the human skin, including its relatively low pH value, elevated salt concentration, low level of nutrition, and occasional anaerobic environments, *Staphylococcus epidermidis* stands out as the most prevalent bacterium inhabiting our skin. This microorganism is probiotic, as it plays a crucial role in maintaining skin health by forming a protective barrier and producing antimicrobial peptides that help fend off invasive bacteria and pathogens (Q. Liu et al., 2020).

*Staphylococcus epidermidis* itself possesses a relatively limited repertoire of virulence factors. However, it functions as a reservoir for mobile genetic elements (20% of the whole genome is mobile) carrying genes responsible for antibiotic resistance (Conlan et al., 2012). These mobile elements play a pivotal role in disseminating resistance traits, contributing to the overall resistance profile of this bacterium and, consequently, impacting its clinical significance. As an example, the SCCmec, which is responsible for providing methicillin resistance, can be horizontally transferred from Methicillin-resistant *Staphylococcus epidermidis* (MRSE) to *Staphylococcus aureus*. This transfer process enables the conversion of *Staphylococcus aureus* into MRSA (Fišarová et al., 2021). Furthermore, it has been identified in domesticated animals, including human pets. In a manner consistent with other Staphylococci, even those of potential pathogenicity, *Staphylococcus epidermidis* has been detected in livestock. Notably, it ranks as the most frequently isolated bacterium in cases of bovine mastitis, a common udder infection in cattle (Pizauro et al., 2021). This situation is further complicated by the detection of drug-resistant *Staphylococcus epidermidis* strains in cow's milk (Piessens et al., 2012).

*Staphylococcus epidermidis* is often termed an 'accidental pathogen' by the scientific community, a designation arising from the genomic similarity between the commensal strains residing on human skin and those implicated in clinical infections. Traits that traditionally facilitate benign colonization, such as biofilm formation, are leveraged as virulence mechanisms in pathogenic contexts. Biofilms provide a mechanical barrier

against antimicrobial peptides (AMPs) and contribute to resistance against other invasive microbial strains. The bacterium's secretion of proteases represents a biochemical defense against all kinds of secretions from invasive bacteria, while the expression of matrix adhesion molecules aids in establishing infection sites. These characteristics underscore the bacterium's adaptive duality in both symbiotic and pathogenic interactions with the host (Otto, 2009). A study has shown that a single multidrug-resistant *Staphylococcus epidermidis* lineage, classified as sequence type 2 (ST2), accounts for roughly 74% of clinical isolates on a global scale. The ST2 lineage is characterized by its nosocomial origin, exhibiting a pronounced propensity for robust biofilm formation and an enhanced invasive capacity when compared to other *Staphylococcus epidermidis* strains (Thomas et al., 2007; Lee et al., 2018). Furthermore, additional research has posited that approximately 70% of nosocomial *Staphylococcus epidermidis* strains exhibit resistance to methicillin, thereby classified as MRSE (Krediet et al., 2004).

#### **Device-associated infections of *Staphylococcus epidermidis***

Device-associated infections represent a critical concern within medical facilities, predominantly attributed to the capability of *Staphylococcus epidermidis* to generate tenacious biofilms on the surfaces of medical devices. This biofilm formation, as seen in infected intravenous catheters examined through Scanning Electron Microscopy (SEM), is often accompanied by an amorphous substance that seems to protect the bacterial colonies from host defenses and antibiotics (G. Peters et al., 1981). Further studies also using SEM have documented the stages of coagulase-negative staphylococci colonization on catheters, demonstrating that these microorganisms can adhere to and proliferate on catheter surfaces, eventually leading to the production of a slimy material that encapsulates the bacterial colonies. Such biofilms complicate the treatment and increase the risk of persistent infections (Georg Peters et al., 1982). The clinical isolates of *Staphylococcus epidermidis* obtained from implantable medical devices were characterized for biofilm-forming abilities. A significant proportion exhibited the *mecA* gene and the IS256 element, both associated with antibiotic resistance and biofilm formation. This suggests that a variety of determinants, beyond those previously

characterized, are involved in biofilm development on medical devices, posing a considerable threat to patient safety and necessitating more sophisticated strategies for prevention and treatment (Petrelli et al., 2006). In an orthopedic hospital, a 15-year surveillance of primary hip and knee replacements revealed that coagulase-negative *staphylococci* were the leading cause of deep infections post-surgery. These infections were detected early and treated effectively, indicating the critical role of early intervention and the benefits of specialized surgical environments in mitigating the risks of device-associated infections (Phillips et al., 2006). Sepsis and the corresponding septic shock are serious complications with high mortality rates, often associated with catheter-related infections. The mortality rate for septic shock can reach 20 to 30%. Infections like prosthetic valve endocarditis or native valve endocarditis can result in severe complications, including septic emboli, mycotic aneurysm, perivalvular abscess, and heart failure (Dong et al., 2018; Fišarová et al., 2021).

*Staphylococcus epidermidis* establishes itself as an opportunistic pathogen, inciting disease predominantly in the presence of specific predisposing factors. These factors range from intrinsic patient conditions, such as prematurity and hereditary immunodeficiencies, to acquired clinical states including human immunodeficiency viruses (HIV) infection, immunosuppression subsequent to hematopoietic stem cell or solid organ transplantation, and chemotherapy-induced neutropenia (Goldmann and Pier, 1993; Rupp and Archer, 1994).

### **Biofilm Formation**

Bacteria, like *Staphylococcus aureus* and *Staphylococcus epidermidis* possess the capability to initiate biofilm formation, a process integral to their survival and pathogenicity, facilitating both communal existence on host tissues and the development of antibiotic resistance (J. William Costerton et al., 1995). Consequently, this chapter delves into the mechanistic underpinnings and implications of biofilm genesis in these bacteria (Figure 5).

The formation starts with a part which is called reversible phase (Landini et al., 2010). Cells are approaching the surface, which can be artificial or biological until they can

adhere to them. From there the maturation starts with an attachment and the formation of the matrix. Which is made of roughly 10% bacteria and 90% self-produced extracellular polymers (EPS). These EPS consist of an assortment of molecules such as polysaccharides, proteins, nucleic acids, and lipids that create a sticky three-dimensional framework. This framework effectively traps the bacteria, leading to a dense community that encourages cell-to-cell interactions. The network is designed to allow nutrients to flow in and waste to flow out through specialized channels. Even components from dead cells, like DNA, are kept and repurposed within the biofilm (Flemming and Wingender, 2010). Additionally, the EPS serves as a shield, guarding the bacteria against external threats including antibiotics and host immune defenses (Høiby et al., 2010). The process of dispersion, involving the detachment of clusters of cells and their surrounding matrix, facilitates the spread of bacteria, initiating a new cycle of colonization and biofilm formation. This critical phase not only perpetuates the biofilm life cycle but also contributes to the dissemination of bacteria across new environments and surfaces. A biofilm typically comprises a diverse consortium of bacterial strains rather than a monoculture. It functions as a hub for the horizontal transfer of mobile genetic elements. Specifically, as outlined previously, *Staphylococcus epidermidis* frequently acts as a genetic reservoir harboring an array of resistance genes. These genes can be transferred to other, more pathogenic bacteria such as *Staphylococcus aureus*, potentially augmenting their virulence and resistance profiles. This gene transfer mechanism within biofilms underscores their role in the evolution and dissemination of antimicrobial resistance, posing a significant challenge in both clinical and environmental settings (Fišarová et al., 2021).

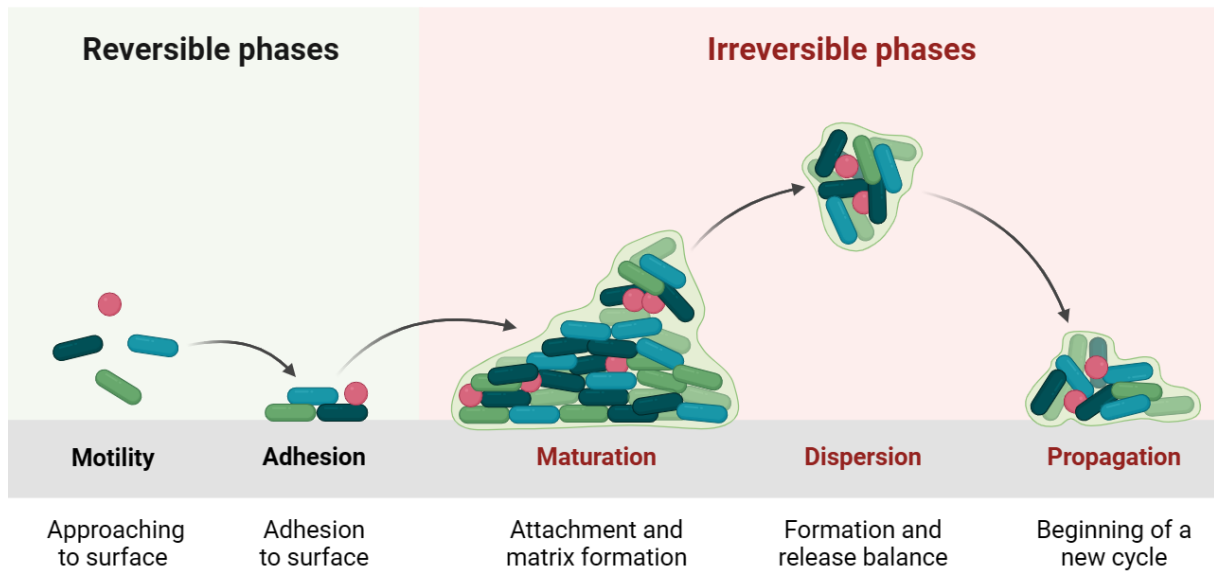


**Figure 5: biofilm formation cycle.** The cycle is partitioned into two principal stages: the reversible and the irreversible phase. In the initial reversible phase, cells transiently approach and adhere to the substrate. The subsequent irreversible phase encompasses the maturation of the biofilm, the dispersion of individual cells from the established biofilm, and the propagation phase, which denotes the inception of a new cycle (Crouzet et al., 2014). Created with BioRender.com.

Biofilms represent a significant concern for public health because they account for approximately 60-80% of bacterial infections in humans (J. W. Costerton et al., 1999; Lewis, 2001). The protective matrix contributes to the persistence of infections, especially in healthcare settings where biofilms can form on medical devices and surfaces, leading to chronic infections that resist typical treatment methods (Petrelli et al., 2006).

### Penicillin-binding Proteins

PBPs are a group of enzymes known as penicilloyl-serine transferases that play a critical role in the biosynthesis of bacterial cell walls. These enzymes catalyze the cross-linking of the bacterial cell wall peptidoglycan, a key process for maintaining cell wall integrity (Sauvage et al., 2008).

They are categorized into three principal classes based on structural and functional characteristics. Each class is further differentiated into specific types, delineated by their distinct roles in bacterial cell division and cell wall synthesis and maintenance. The numbering of PBPs is historically based on their migration in Sodium Dodecyl Sulfate-Polyacrylamide Gel Electrophoresis (SDS-PAGE). This method can lead to confusion, as PBPs from different bacteria may be assigned the same number despite not belonging to the same class or type. For instance, PBP2 from *Escherichia coli* is similar to PBP3 from

*Staphylococcus aureus*, whereas PBP2 from *Staphylococcus aureus* shows similarities to PBP1b from *Escherichia coli*. Table 3 offers an exhaustive catalog of select PBPs, systematically organized by their respective class, type, bacterial species, and nomenclature (Rodriguez-Tebar and Vazquez, 1984).

**Table 3: Comprehensive Catalog of selected PBP Classes (Sauvage et al., 2008).**

Class	Type	Bacteria	Penicillin-binding protein
HMW Class A	A1	<i>Escherichia coli</i> K12	PBP1a; PBP1b
		<i>Neisseria gonorrhoeae</i> FA 1090	PBP1
	A2	<i>Escherichia coli</i> K12	PBP1c
	A3	<i>Escherichia coli</i> K12	ponA
	A4	<i>Escherichia coli</i> K12	ponB
	A5	<i>Escherichia coli</i> K12	pbpC
	A6	<i>Neisseria gonorrhoeae</i> FA 1090	ponA
HMW Class B	B1	<i>Staphylococcus aureus</i> MRSA252	PBP3
		<i>Enterococcus faecalis</i> V583	PBP3
		<i>Streptococcus pneumoniae</i> R6	PBP2
	B2	<i>Staphylococcus aureus</i> MRSA252	pbpA
		<i>Enterococcus faecalis</i> V583	pbpC
		<i>Streptococcus pneumoniae</i> R6	pbpA
	B3	<i>Staphylococcus aureus</i> MRSA252	ftsI
		<i>Enterococcus faecalis</i> V583	spoVD
		<i>Streptococcus pneumoniae</i> R6	pbp3
	B4	<i>Enterococcus faecalis</i> V583	pbpA
	B5	<i>Enterococcus faecalis</i> V583	pbpB
	B6	<i>Streptococcus pneumoniae</i> R6	pbp3
LMW Class C	Typ-4	<i>Staphylococcus aureus</i> MRSA252	PBP4
		<i>Escherichia coli</i> K12	PBP4
		<i>Streptococcus pneumoniae</i> R6	PBP4

	Typ-5	<i>Staphylococcus aureus</i> MRSA252	PBP5
		<i>Enterococcus faecalis</i> V583	dacA; dacC; dacB
		<i>Actinomyces</i>	Various genes (e.g. dacB1, dacB2)
	Typ-7	<i>Staphylococcus aureus</i> MRSA252	pbpG
		<i>Enterococcus faecalis</i> V583	pbpG

PBPs can be taxonomically classified based on molecular weight into high-molecular weight (HMW) and low-molecular weight (LMW) categories. HMW PBPs are characterized by their multi-domain structures. These PBPs play a pivotal role in the polymerization of peptidoglycan, a key component in bacterial cell wall synthesis, as they are instrumental in the incorporation of newly synthesized peptidoglycan into the existing cell wall matrix. These enzymes can be further stratified into Class A and Class B (Goffin and Ghuysen, 2002).

HMW Class A PBPs are characterized as multi-functional enzymes. They facilitate the crosslinking of peptidoglycan sugar moieties through their N-terminal glycosyltransferase domains. Additionally, they catalyze the crosslinking of the peptide-stems within the peptidoglycan structure via their C-terminal transpeptidase domains. HMW class A PBPs are not always essential. Monofunctional glycosyltransferases (MGT) can compensate for the loss of HMW Class A PBPs but for some bacteria, like in *Escherichia coli*, this compensation is not possible (Goffin and Ghuysen, 2002; Sauvage et al., 2008).

HMW Class B PBPs are distinctively characterized by the presence of a transpeptidase domain and a N-terminal pedestal domain. The pedestal domain is theorized to facilitate interactions with auxiliary proteins, playing a crucial role in the protein's functional dynamics. Notably, this pedestal domain occupies the same position as the glycosyltransferase domain found in HMW Class A PBPs. This structural distinction underlines a significant difference in the functional architecture between these two classes of PBPs. Since this class of PBPs contains only a transpeptidase domain, collaboration with MGTs is essential for the full crosslinking of peptidoglycans, involving both sugar residues and peptide stems (Goffin and Ghuysen, 2002; Sauvage et al., 2008).



In both gram-positive and gram-negative bacteria, the transpeptidation domains are characterized by highly conserved motifs (Figure 6). Motif 1, denoted as [S]XX[K], incorporates a catalytic and indispensable serine residue, succeeded by two variable amino acids and culminating in a lysine residue. This motif is oriented towards the catalytic cavity and anchored on a  $\alpha$ -helix. The second motif, [S/Y]X[N/C], is situated on a loop interlinking two  $\alpha$ -helices, while motif 3, defined as [K/H][T/S]GT, is located on a  $\beta$ -sheet. Both motifs 2 and 3 straddle motif 1 (Goffin and Ghuysen, 2002; Sauvage et al., 2008).

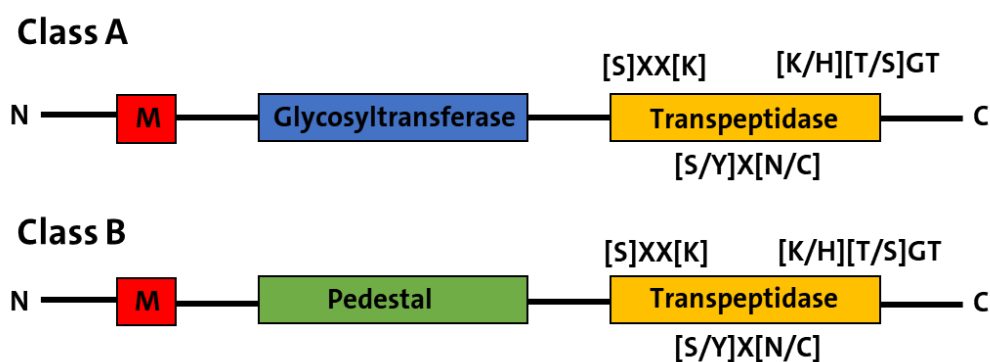


**Figure 6: A simplified schematic Figure of Class A and B PBPs.** Both classes feature a membrane anchor (colored red) and a transpeptidase domain (yellow), including the conserved sequence motifs indicated above and below the transpeptidase domain. The key distinction lies in the presence of a glycosyltransferase domain (blue) in Class A PBPs, and a pedestal domain (green) in Class B PBPs (Sauvage et al., 2008).

Low-molecular-weight (LMW) Class C Penicillin-binding Proteins (PBPs) are characterized by the absence of the N-terminal glycosyltransferase and pedestal domains that are typically present in high-molecular-weight (HMW) PBPs. Their primary function centers on the maintenance and degradation of the bacterial cell wall, primarily acting as DD-carboxypeptidases. These LMW Class C PBPs are further classified into types 4,5 and 7, with each type being named after notable representative PBPs, such as PBP4 from *Escherichia coli*. The distinctions among these types are primarily based on structural variations, such as the absence of a membrane anchor, and on the low sequence homology observed between them (Kishida et al., 2006; Potluri et al., 2010).

## Biochemical Reaction of Transpeptidases

The synthesis of cross-links between the peptidyl components of adjacent glycan chains occurs via a biphasic reaction. Initially, a base attacks the OH group of the active serine, leading to the activation of the serine. It is hypothesized that this base is a conserved lysine, part of motif 1. The activated catalytic serine can then hydrolyze the D-alanyl-D-alanine linkage within a nascent peptide substrate. This hydrolysis coincides with the departure of the terminal D-alanine, resulting in an acylated enzyme intermediate. Subsequently, this acylated intermediate is resolved, leading to the formation of a new peptide bond. Prior to this resolution, another base, also hypothesized to be a lysine from the conserved motif 3, activates the peptidoglycan end of the incorporated peptidoglycan. This bond forms between the carbonyl portion of the D-alanyl segment and the amine group of an alternative peptide substrate (Figure 7) (Goffin and Ghuysen, 2002).

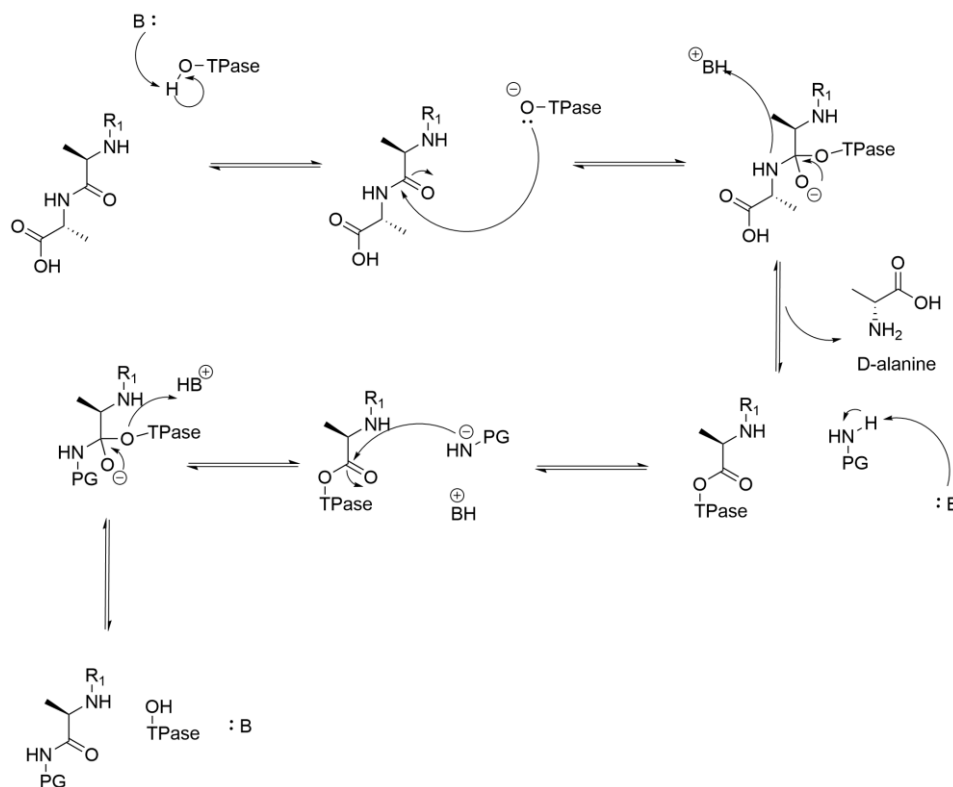


**Figure 7: Biochemical Reaction Mechanism of Transpeptidases.** The process initiates with an activated catalytic serine residue, which hydrolyzes and facilitates the release of the terminal D-alanine from a peptidoglycan precursor. This action results in the formation of an acyl-enzyme intermediate. Subsequently, this acylated intermediate undergoes dissolution, leading to the creation of a new peptide bond. This bond forms between the nascent intermediate and an existing strand of the peptidoglycan, thus integrating into the bacterial cell wall Figure by Omarg10/ CC BY (Goffin and Ghuysen, 2002).

### Mechanism of $\beta$ -Lactam Antibiotics and Resistance in PBPs

The Tipper-Strominger hypothesis underscores a critical structural similarity between  $\beta$ -lactam antibiotics and the D-Ala-D-Ala moiety of peptidoglycans. This hypothesis posits that the  $\beta$ -lactam ring, a structural component of antibiotics such as penicillin, not only mimics the D-Ala-D-Ala dipeptide of peptidoglycans in its physical structure but also replicates the spatial distribution of three electrostatically negative sites (Figure 8) (Tipper and Strominger, 1965). These sites are typically recognized and cross-linked by PBPs during cell wall synthesis. Consequently,  $\beta$ -lactam antibiotics are able to bind irreversibly to the active site serine within the transpeptidase domain. This irreversible binding leads to the inactivation of PBPs, thereby inhibiting the cross-linking process essential for the structural integrity of the peptidoglycan layer. The resultant weakening of the bacterial cell wall eventually causes cell lysis and, ultimately, bacterial death (Yocum et al., 1980).

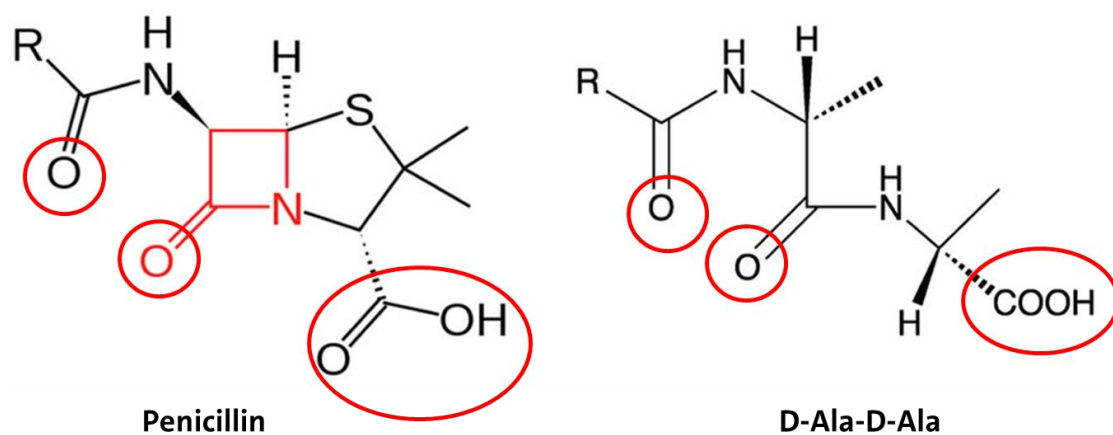


**Figure 8: Structural Similarity of Penicillin and D-ala-D-ala Peptide backbone of the Peptidoglycan.** The  $\beta$ -lactam ring is highlight in red. the regions of negative electrostatic potential are indicated by red circles (Tipper and Strominger, 1965; Yocum et al., 1980).

The resistance of bacterial cells to  $\beta$ -lactam antibiotics is predominantly mediated through the expression of  $\beta$ -lactamases. These enzymes specifically target and hydrolyze the  $\beta$ -lactam ring, thereby preventing their binding to PBPs and averting the subsequent inhibition of cell wall synthesis. However, not all bacterial cells, such as certain *streptococci* or *enterococci*, harbor genes that encode  $\beta$ -lactamases (Bush and Bradford,

2020). In such cases, bacteria may deploy alternative resistance mechanisms involving modifications to PBPs themselves. The most well-known and extensively studied mechanism of resistance against  $\beta$ -lactam antibiotics involves the expression of the *mecA* gene. This gene encodes for PBP2a, a low-affinity Class B PBP. PBP2a's unique structure plays a crucial role in its resistance to  $\beta$ -lactam antibiotics. Notably, the active serine residue, essential for the binding and activity of PBPs, is positioned behind a  $\beta$ -sheet in PBP2a. This structural arrangement effectively shields the hydroxyl group of the serine residue, rendering it less accessible to inhibitors such as  $\beta$ -lactam antibiotics (Lim and Strynadka, 2002; Acebron et al., 2015). Consequently, this shielding mechanism allows PBP2a to maintain its enzymatic activity in the presence of these antibiotics, leading to continued cell wall synthesis and antibiotic resistance. The activation of the enzymatic activity necessitates an allosteric activation. This activation triggers a conformational change, disrupting the helical structure that houses the active serine residue. As a result of this structural alteration, the serine residue shifts upwards, becoming more accessible for interaction with the peptidoglycan substrate. The activation mechanism of the allosteric domain, which is about 60 Å away from the active site, remains a complex and unresolved aspect (Acebron et al., 2015). Three additional resistance mechanisms in *Staphylococcus aureus* have been identified. Clinical isolates have shown mutations in *SaPBP1* and *SaPBP2*, resulting in reduced affinity, though the precise mechanisms are not fully understood (Tomasz et al., 1989). Intriguingly, some resistant strains exhibit overproduction of *SaPBP4*, a LMW PBP. This overproduction of *SaPBP4* leads to more robust crosslinking of the bacterial cell wall, indicating that *SaPBP4* may function as a secondary transpeptidase, despite its usual role as a carboxypeptidase (Henze and Berger-Bächi, 1996). In cells lacking *SaPBP3*, there is an observed increase in the MIC compared to cells with *SaPBP3*. Given that *SaPBP3* is not essential under normal conditions, it is hypothesized that it may act as a decoy receptor, affecting antibiotic susceptibility (Pinho et al., 2000). In many *enterococci* bacteria, a low-affinity PBP exists that can compensate for the activity of other inhibited PBPs, leaving the cell wall network unaffected. Mutants of this PBP, commonly PBP5, arise spontaneously at a high rate, and this protein is often found to be overproduced. A loss

of this protein consistently results in heightened susceptibility to antibiotics in the bacteria (Fontana et al., 1985; Fontana et al., 1994; Sifaoui et al., 2001). Sequencing studies have disclosed that mosaic genes encode for PBP2b, PBP2x, and PBP1a in the majority of resistant clinical strains from *Streptococcus pneumoniae* (Dowson et al., 1989; Laible et al., 1991; Martin et al., 1992). The origins of these sequence blocks in mosaic pbp genes are largely elusive, although there are notable exceptions for pbp2x. In the case of pbp2x, fragments of sequences from susceptible *Streptococcus mitis* and *Streptococcus oralis* have been identified in numerous pbp2x alleles of resistant pneumococci (Sibold et al., 1994; Chi et al., 2007). In PBP2 from *Neisseria gonorrhoeae* a connecting loop close to the active serine is mutated and therefore more flexible but also a mutation with a reduced flexibility in the same loop region can increase the resistance, like in PBP2b from *Streptococcus pneumonia* (Contreras-Martel et al., 2009; Fenton et al., 2021). Predominantly, resistance mechanisms in PBPs involve reduced affinity towards specific  $\beta$ -lactam antibiotics. Additionally, overproduction of PBPs is another recognized strategy. The concept of expressing decoy receptors as a resistance mechanism is also being explored (Yoshida et al., 2012).

### **Penicillin-binding Protein 2a**

The Penicillin-binding protein 2a (PBP2a) has played a pivotal role in altering the landscape of antibiotic research, particularly marking the end of the so-called "Golden Era" of antibiotics (Rutenburg et al., 1960). Initially identified in *Staphylococcus aureus*, PBP2a imparts a distinctive resistance to methicillin, thereby characterizing the strain as Methicillin-resistant *Staphylococcus aureus* (MRSA). MRSA remains pertinent in contemporary healthcare, especially in nosocomial infections where it is the second most frequently reported bacterium after *Escherichia coli*, accounting for about 20% of cases (WorldHealthOrganization, 2023). The PBP2a protein is encoded by the *MecA* gene, which is a part of a 21- to 60-kb SCCmec, a mobile genetic element. This element's mobility facilitates the spread of the gene through horizontal gene transfer, a process particularly enhanced in biofilms (Høiby et al., 2010). This mechanism significantly contributes to the dissemination and persistence of MRSA in clinical settings. Two prevailing theories have been proposed to elucidate the evolutionary emergence of

MRSA strains. The first, known as the single clone hypothesis, is grounded in the early analysis of restriction fragment length polymorphisms of MRSA isolates from global sources, utilizing probes for *mecA* and Tn554. This hypothesis posits that *mecA* was integrated into the *Staphylococcus aureus* gene pool once, leading to the emergence of a singular MRSA clone that has subsequently proliferated globally. The alternative hypothesis, informed by the detection of *mecA* across various *Staphylococcus aureus* multilocus enzyme electrophoresis types, suggests that MRSA strains have evolved multiple times through the horizontal transfer of *mecA* into genetically diverse methicillin-susceptible *Staphylococcus aureus* (MSSA) progenitor strains (Enright et al., 2002). PBP2a is recognized for its low affinity towards most  $\beta$ -lactam antibiotics. In comparison to other PBPs, PBP2a demonstrates a notably more restricted active site. The active serine residue in PBP2a is obstructed by a  $\beta$ -sheet structure, and the presence of a flexible loop proximal to the active serine further contributes to its categorization as a low-affinity PBP (Lim and Strynadka, 2002).

### **Penicillin-binding Protein 3**

In *Staphylococcus aureus*, the Penicillin-binding protein 3 (PBP3) is encoded by the *pbpC* gene. The sequencing of this gene has elucidated a protein structure comprising 691 amino acids, consistent with the attributes of a class B HMW PBP. This protein structure incorporates all canonical motifs, notably the transpeptidase-conserved motifs SXXK, SXN, and KTGT (Pinho et al., 2000; Yoshida et al., 2012). Targeted insertional inactivation of the *pbpC* gene, followed by reintroduction of the intact gene into a laboratory-generated mutant deficient in *SaPBP3*, substantiated the role of *pbpC* in encoding staphylococcal PBP3. Disruption of *pbpC* did not manifest in discernible changes in the muropeptide composition of the cell wall peptidoglycan, nor did it significantly affect the bacterial growth rates. However, a minor yet significant reduction in autolytic activity was noted. Furthermore, the cultivation of *pbpC*-inactivated bacteria in the presence of a sub-minimum inhibitory concentration (sub-MIC) of methicillin yielded cells with aberrant sizes and morphologies, as well as misaligned septa (Pinho et al., 2000).

In *Staphylococcus epidermidis*, there is a notable homology in PBP3, though its precise functional role remains to be fully elucidated. In specific clinical isolates of *Staphylococcus epidermidis*, characterized by marginal resistance to methicillin and the absence of the *mecA* gene, a reduced binding affinity of PBP3 towards methicillin has been detected (Petinaki et al., 2001). The identification of a clinical *Staphylococcus epidermidis* strain exhibiting altered affinity of *Se*PBP3 to methicillin underscores the potential involvement of other PBPs, beyond PBP2a, in mediating the expression of methicillin resistance.

### **Aim of this Thesis**

The objective of this study was to conduct a detailed analysis of selected PBPs in *Staphylococcus epidermidis* and *Staphylococcus aureus*, focusing on antimicrobial resistance mechanisms. This investigation targets two specific PBPs: PBP3 from *Staphylococcus epidermidis* and PBP2a from *Staphylococcus epidermidis* and *Staphylococcus aureus*.

SePBP3, a structurally and functionally uncharacterized PBP from *Staphylococcus epidermidis*, presents a novel research avenue. A key focus is the structural comparison with Class B PBPs, particularly examining the active sites where resistance mechanisms are often localized. PBP3's involvement in multi-drug resistant strains *Staphylococcus epidermidis*, notably those lacking the *MecA* gene, necessitates an in-depth analysis of its structure, dynamics, and function.

PBP2a, well-recognized for its role in multidrug resistance in both *Staphylococcus epidermidis* and *Staphylococcus aureus*, features a unique allosteric center among PBPs. The study addresses the challenges in its expression and purification, given the propensity of *Escherichia coli* to sequester the protein in inclusion bodies, underscoring the need for an optimized protocol for future structural and biochemical analyses. Furthermore, the dynamics of the active site, particularly the mechanism of activation via displacement of the active serine, remains elusive. A comprehensive molecular dynamics (MD) simulation study is proposed to uncover potential new inhibitory mechanisms.

This thesis aims to expand the understanding of PBP-mediated resistance in *Staphylococci*, providing insights critical for future therapeutic strategies.



## Material and Methods

### Materials

#### Chemicals

All chemicals utilized in this study were sourced in analytical grade from reputable suppliers including Thermo Scientific, Sigma-Aldrich, Serva, Merck, Fluka, and Applichem.

#### Media, Buffers and Solutions

Unless specified otherwise, the various media, solutions, and buffers were prepared using distilled water. The pH value was adjusted with hydrochloric acid or sodium hydroxide as needed.

**Table 4: Media and Composition.**

Medium	pH-value	Components	Concentration
<b>SOC (Super Optimal Broth + glucose)</b>	~7.2	Tryptone	2% (w/v)
		Yeast extract	0.5% (w/v)
		NaCl	10 mM
		KCl	2.5 mM
		MgCl <sub>2</sub>	10 mM
		MgSO <sub>4</sub>	10 mM
Glucose	20 mM		
<b>LB (Lysogeny broth)</b>	~7.0	NaCl	5.0 g/l
		Tryptone	10 g/l
		Yeast extract	5.0 g/l
<b>TB (Terrific broth)</b>	~7.2	Tryptone	12 g/l
		Yeast extract	24 g/l
		K <sub>2</sub> HPO <sub>4</sub>	12.5 g/l
		KH <sub>2</sub> PO <sub>4</sub>	2.3 g/l
<b>2 x YT (Yeast / Tryptone)</b>	~6.8	Tryptone	16 g/l
		Yeast Extract	10 g/l
		NaCl	5 g/l

**Table 5: Buffers and Composition.**

<b>Buffer</b>	<b>pH-value</b>	<b>Components</b>	<b>Concentration</b>
<b>Lysis buffer / Equilibration buffer</b>	<i>SePBP3</i> = 8.0 <i>SePBP2a</i> = 7.4	NaH <sub>2</sub> PO <sub>4</sub> · 2 H <sub>2</sub> O NaCl Glycerol <b>Imidazol</b>	50 mM 300 mM 2 % <b>10 mM</b>
<b>Wash buffer</b>		NaH <sub>2</sub> PO <sub>4</sub> · 2 H <sub>2</sub> O NaCl Glycerol <b>Imidazol</b>	50 mM 300 mM 2 % <b>20 mM</b>
<b>Elution buffer</b>		NaH <sub>2</sub> PO <sub>4</sub> · 2 H <sub>2</sub> O NaCl Glycerol <b>Imidazol</b>	50 mM 300 mM 2 % <b>250 mM</b>
<b>SEC buffer (size exclusion buffer)</b>		Tris-HCl NaCl	20 mM 100 mM

### **Size Marker**

For SDS-PAGE, the Unstained Protein Molecular Weight Marker from Fermentas was used as the size marker.

### **Kits**

For the isolation of plasmids, the peqGold Plasmid Miniprep Kit I was utilized. A specialized kit provided by PEQLAB Biotechnologie, known for its efficacy in plasmid purification.

### **Equipment**

Following Equipment was used during this study (Table 6).

**Table 6: Overview of Equipment.**

<b>Equipment</b>	<b>Equipment Type</b>	<b>Manufacturer</b>
<b>CD-Spectrometer</b>	J-815 CD	Jasco
<b>DLS-Instruments</b>	SpectroLight 600	Xtal Concepts GmbH
	SpectroSize 300	Xtal Concepts GmbH
<b>Fast protein liquid chromatography</b>	ÄKTApurifier System	GE Healthcare, USA
<b>Gel Electrophoresis Chamber</b>	SE 260 Mighty Small II	Hoefer
<b>Gel Electrophoresis Power Supply</b>	EV231	PEQLAB Biotechnology
<b>In-House Detector</b>	Mar345S	MarRESEARCH
<b>In-House Radiation Source</b>	IpSCU	Incoatec
<b>Incubation Shaker</b>	Innova 44	New Brunswick Scientific
	KS 3000 i control	IKA
<b>Incubator</b>	BD 56	Binder
<b>Crystallization Robot</b>	Honeybee 961	Genomic Solutions
	Oryx4	Douglas Instruments
<b>Magnetic Stirrer</b>	VMS-A	VWR International
<b>Microscopes</b>	SZX12	Olympus
	CLSM	Zeiss
<b>NanoDrop Spectrometer</b>	ND-1000	PEQLAB Biotechnology
	ND-2000	PEQLAB Biotechnology
<b>pH Meter</b>	SevenEasy	Mettler-Toledo
<b>Photometer</b>	GeneQuant™ 1300	GE Healthcare, USA
<b>Roller Shaker</b>	RS-TR05	Phoenix Instruments
<b>Shaker</b>	GFL-3014	GFL
<b>Thermomixer</b>	Comfort	Eppendorf
<b>Ultrasonic Device</b>	Soniprep 150	MSE
<b>Scales</b>	TE3102S	Sartorius

	CP2245-OCE	Sartorius
<b>Centrifuge</b>	Multifuge X1R	Heraeus
	5415 R	Eppendorf
	5418 R	Eppendorf
	Minispin Plus	Eppendorf

### Consumables

Following consumables were used during this study (Table 7).

**Table 7: Overview of Consumables.**

<b>Description</b>	<b>Manufacturer</b>
<b>Reaction Vessels</b>	Sarstedt
<b>Falcon Tubes</b>	Sarstedt
<b>Pipette Tips</b>	Sarstedt
<b>Serological Pipettes</b>	Fisher Scientific
<b>Amicon Ultra 4, Ultra 15, Ultra 0.5, MWCO 3 kDa, 50 kDa</b>	Merck Millipore
<b>Dialysis Tubing Membrane</b>	Roth
<b>Ni-NTA Agarose Matrix</b>	Qiagen
<b>Syringes 1 ml, 5 ml, 10 ml, 20 ml</b>	VWR
<b>Syringe Filter Tip 0.22 µm</b>	VWR

### Software

Following software were used during this study (Table 8).

**Table 8: Overview of Software.**

<b>Software</b>	<b>Application</b>	<b>Reference</b>
<b>BioXTAS RAW</b>	Analysis and Illustration of SAXS Data	J. B. Hopkins et al. 2017
<b>CCP4i</b>	Refinement	Winn, Ballard et al. 2011
<b>ClustalΩ</b>	Sequence Alignment	Madeira, Park et al. 2019
<b>CrystFEL</b>	Processing of Serial Data	White, Kirian et al. 2012

<b>Desmond</b>	MD Simulation	Bowers et al. 2006
<b>Expasy</b>	Calculation of Molecular Weight	Gasteiger et al. 2005
<b>Gussi</b>	ITC Illustration	Brautigam 2015
<b>MolProbity</b>	Evaluation of Protein Structures	Williams et al. 2018
<b>NITPIC</b>	ITC Peak Shape Analysis	Keller et al 2012
<b>Phenix</b>	Molecular Replacement and Refinement	Liebschner et al. 2019
<b>ScÅtter</b>	Analysis and Illustration of SAXS Data	S. Förster et al. 1998
<b>Schrödinger's Maestro Suite</b>	Docking and MD Simulation	Madhavi et al. 2013
<b>SEDPHAT</b>	ITC Analysis of Molecular Interaction	Zhao et al. 2015
<b>XDS</b>	Processing	Kabsch et al. 2010

## Bacterial Strains

### ***Escherichia coli* DH5α**

DH5α competent cells (Invitrogen), a highly efficient and chemically competent strain of *Escherichia coli*, are optimally designed for a plasmid amplification. Equipped with the  $\phi 80\text{dlacZ}\Delta\text{M15}$  marker, these cells facilitate  $\alpha$ -complementation of the  $\beta$ -Galactosidase gene from pUC or analogous vectors, thus enabling effective blue-white colony screening on Blue-Gal or X-Gal containing bacterial agar plates. The presence of RecA1 and endA1 mutations in the DH5α cells significantly improves the stability of genetic insertions and the quality of the resultant plasmid DNA. Transformation efficiency surpassing  $1 \times 10^9$  transformants per microgram of pUC19 DNA and therefore, these cells are particularly well-suited for both routine cloning tasks and high-throughput operations. The included genetic markers facilitate efficient blue-white colony screening.

Genotype: F–  $\phi 80\text{lacZ}\Delta\text{M15}\Delta(\text{lacZYA-argF})\text{U169 recA1 endA1 hsdR17 (rK– mK+) phoA supE44 } \lambda\text{- thi–1 gyrA96 relA1}$ .

### ***Escherichia coli* TOP10 (DE3)**

The TOP10 chemically competent *Escherichia coli* cells (Invitrogen), characterized by a transformation efficiency of  $1 \times 10^9$  transformants per microgram of plasmid DNA, are

ideally suited for highly efficient cloning and plasmid propagation tasks. These cells are adept at the stable replication of high-copy number plasmids and are consistent with the competent cells included in various standard cloning kits. The TOP10 *Escherichia coli* cells feature the *hsdR* gene for efficient transformation of unmethylated DNA from PCR, and the *mcrA* gene for transforming methylated genomic DNA. They include the LacZ $\Delta$ M15 marker for easy blue-white screening of recombinant clones. The EndA1 mutation enhances DNA purity and processing by preventing nonspecific digestion by Endonuclease I, while the *recA1* mutation minimizes nonspecific recombination in the cloned DNA.

Genotype: F-mcrA  $\Delta$ (*mrr*-*hsdRMS*-*mcrBC*)  $\Phi$ 80LacZ $\Delta$ M15  $\Delta$  LacX74 *recA1* *araD139*  $\Delta$ (*araleu*)7697 *galU galK rpsL* (StrR) *endA1 nupG*.

### ***Escherichia coli* BL21 (DE3)**

BL21(DE3) (Invitrogen) competent cells are specifically engineered for the efficient expression of non-toxic, heterologous genes. These cells incorporate the Lambda DE3 prophage, which harbors the T7 RNA polymerase gene regulated by a *lacUV5* promoter, facilitating IPTG-mediated activation of T7 RNA polymerase. As part of the *Escherichia coli* B lineage, the BL21(DE3) strain is devoid of *lon* protease and outer membrane protease *OmpT*, significantly reducing the proteolytic degradation of heterologously expressed proteins. Characterized by a high transformation efficiency, exceeding  $1 \times 10^7$  transformants/ $\mu$ g pUC19 DNA, these cells are tailored for enhanced recombinant protein production and incorporate genetic markers that limit RNA and protein degradation.

Genotype: F- *ompT hsdSB* (*rB*-, *mB*-) *gal dcm* (DE3).

### ***Escherichia coli* BL21 (DE3) Star**

BL21 Star (DE3) (Invitrogen) chemically competent *Escherichia coli* cells are specifically designed for efficacious expression of non-toxic recombinant proteins, utilizing low-copy T7 promoter-based systems. Exhibiting a high transformation efficiency of  $1 \times 10^8$  transformants per microgram of plasmid DNA, these cells are characterized by a genotype that bolsters mRNA stability and protein output. They are optimized for compatibility with low-copy number T7 promoter-based plasmids. The presence of DE3

lysogen in these cells, which includes the T7 RNA polymerase gene controlled by the lacUV5 promoter, necessitates IPTG for induction. The RNaseE gene mutation (*rne131*) in these cells diminishes the activity of endogenous ribonucleases and mRNA degradation, thereby amplifying mRNA transcript stability and protein production. The absence of Lon protease and OmpT protease further enhances the expression by reducing the degradation of heterologous proteins.

Genotype: F-ompT hsdSB (rB-, mB-) gald.

### **Vector**

The pET-28b(+) vector was employed in this study for its efficacy in recombinant protein synthesis within *Escherichia coli* host cells. Central to its selection is the incorporation of a T7 promoter, which is specifically recognized by T7 RNA polymerase. This interaction facilitates a high level of transcriptional activity, crucial for enhanced protein yield. Incorporated within the vector is a lac operon, providing an inducible control mechanism for gene expression. This feature allows for the precise regulation of the gene of interest, a critical factor in experimental reproducibility. The vector's architecture includes a multiple cloning site (MCS), enabling the straightforward integration of target genetic sequences. Furthermore, the presence of a polyhistidine (His-tag) sequence adjacent to the MCS facilitates the affinity-based purification of the recombinant protein, utilizing nickel-nitrilotriacetic acid (Ni-NTA) chromatography. This His-tag purification method is pivotal for achieving a high purity of the expressed protein. Another feature of the pET-28b(+) vector is its antibiotic resistance gene, conferring resistance to kanamycin. This aspect is instrumental in ensuring the stable maintenance and selection of the vector within the bacterial culture (Figure 8).

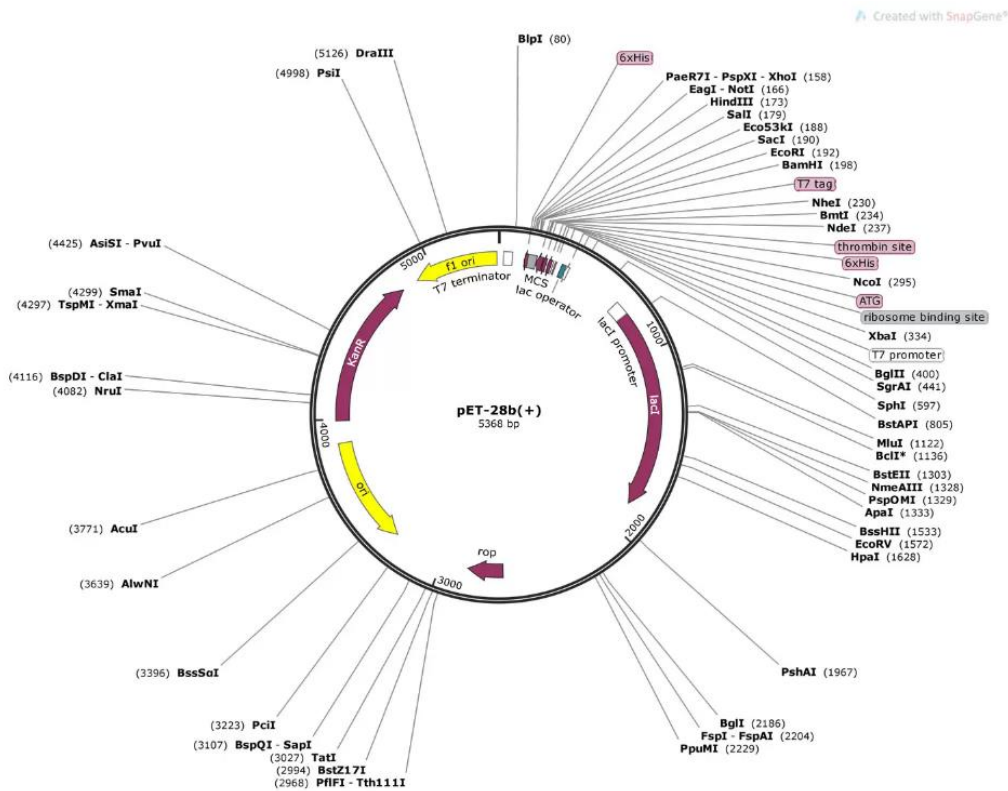


**Figure 8: Vector map of pEt-28b(+)** created with SnapGene®. Vector contains a kanamycin-resistance-gene cassette (KanR).  $\Delta 47\text{SePBP3}$  was cloned into the multiple cloning site (MCS) between NcoI and NdeI as 5' restriction site and 3' restriction sites.

## Methods

### Molecular Biological Methods

#### Plasmid-DNA Construct

##### SePBP3

The Sequence of SePBP3 from RP62A (GenBank ID: CP000029.1 and Uniprot ID: Q5HNZ7) was analysed by using SignalP - 5.0 (webserver: <https://services.healthtech.dtu.dk/services/SignalP-5.0/>) and SMART (Simple Modular Architecture Research Tool / webserver: <https://smart.embl.de/>) to identify the signal peptide and the transmembrane region (Figure 9 and Table 6). The results enabled to design the truncated protein  $\Delta 47\text{SePBP3}$  for protein overexpression in cytosol fraction of the *Escherichia coli* host system. The gene was subsequently modified by replacing the signal peptide and membrane anchor with a 6 x histidine tag and a TEV protease (Tobacco Etch Virus nuclear-inclusion-a endopeptidase) - cleavage site at the N-terminal (Table 9). The nucleotide sequence was codon optimized for *Escherichia coli* t-RNAs. NcoI and NdeI were



selected for 5' restriction site and 3' restriction site. pET-28b(+) was chosen as the vector system as it contains a kanamycin resistance (Figure 8). An ampicillin resistance needed to be ruled out since PBPs are able to bind  $\beta$ -lactam antibiotics. Ampicillin could block the active site of SePBP3 and would hinder an interaction study with potential inhibitors. The company BioCat GmbH (Heidelberg, Germany) produced the whole construct.

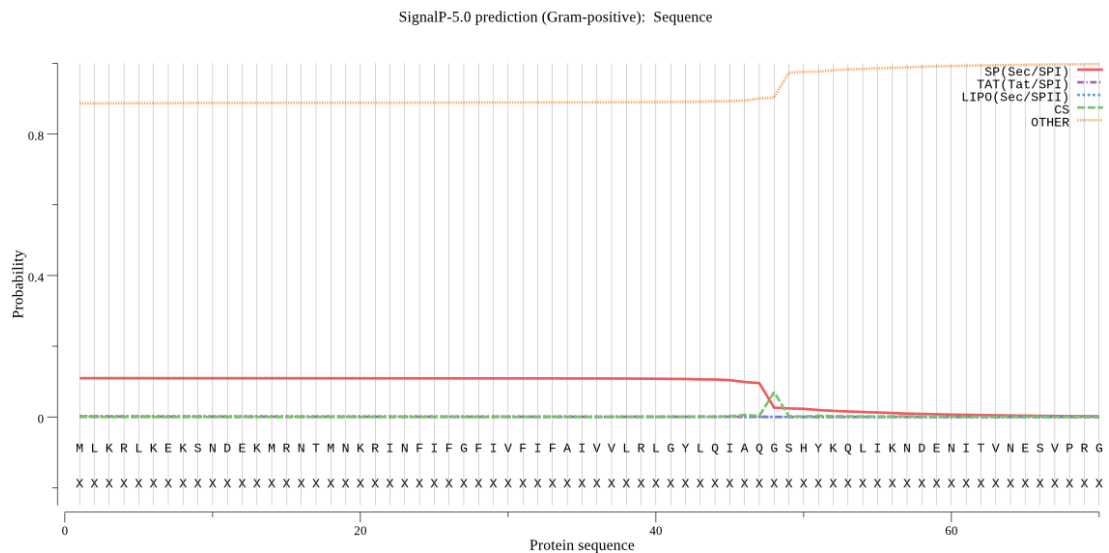


**Figure 9: Output of SignalP - 5.0 signal peptide prediction.** SignalP - 5.0 suggests to truncate SePBP3 at AA residue number 47.

**Table 9: Confidently predicted Domains, Repeats, Motifs and Features made by SMART.**

Name	Start [aa]	End [aa]	E value
transmembrane region	21	43	N/A
Pfam:PBP_dimer	64	306	1.8e-43
Pfam:Transpeptidase	350	666	5.8e-61
low complexity	678	686	N/A

**Table 10. Original Nucleotide Sequences of SePBP3 from RP62A. (PMID: 15774886)**

> Original nucleotide sequence of SePBP3 from RP62A (PMID: 15774886)

```
ATCTTCTTCTCTTCGTTATTAGATTGAGAGTCATCTTTTTATTATCCTTATCTTTAAAATAGTAGTTGATTA
CGTCTCTACCTAAATCTCCACCATTTAACCAAGGTGGTGAACAGGTTGATTTGTATAGACAATTGAAAA
AGATAATTTAGGATCATCGACGGGTGCATAACCGATATATGTTGAGTTAACTCTAGGTTCTCCGCTCTTGAA
AACTTCAGCAGTTCCTGTTTTACCAGCTGAAGGTACTACAGTATTTCTAAACTAGCATAACCTGTACCT
TGCTTTTCATTGAAAGCCATTTGAAGCCTTCTTGAAGTCTTTAATTTTCGTCATTTGAGTTATTTACCTTAT
TTAAACATTACCCTTAATTTACGTTTTAATGGACCAGTTTCATCTTTATTAGTAGATTCATAAATAGACAA
TCCAATATGTGGTTGAATTCTATAGCCATCATTAGCAATAGTTGATACGTATTGGGACAACTGAAGTGGTG
```

TATATGTGTCGTATTGTCCAATAGCTAAGTCTAAATAGTTACCAGGATTATTAGTTAAGGGTTCTATTTGGC  
 CTGGCGTTTCGTTCCGGTAAGTCAATACCTGTTTTTAAGCCAAGACCTACTTGATTTAACCCTTTACGCAAT  
 TTACGACCAGCATCTGCTATATTATTAGGTAATGACATACCTGAAGTATAGGGGTCACCTGCTAATTTAAG  
 TGCGGTTTTAAACATGTATACGTTTGATGAATGCATAAGTGCTTGTATTATCATCGATAGATACATGACCATT  
 TTTATTAATAAGAACGCTTAGTTAAACCACCTTGGAAATTTAATGGCTCATCTACCATAGTTTCTCCAAC  
 ATTAATAGCTTTATTTGGTATCCAGCTAATAATGTTCTCCTTTTACTGAAGAACCTACTGTGTATTGAGC  
 TGTAAGTTGCCGATATCATAATCTTTGAGTTTACCTTGCTTATCAATTTGCTTTCCTGCAATAGCGAGAAT  
 GTCTCCATTTTTAGGATTTTGACAACCATTAACGCATTGTCCATATCCTTAGCACCTTGACTACGTAATTT  
 AGAAATTTGTTTTCTAATAAAGATTCTACTTTTTCTGTAAATCAATATCTATAGTTAATTGTAAATCATGA  
 CCTTTGAGCCAGGATTAAGTACTTCTGAACTTATTACTCTTCCAGATTTATCAGTTGTATATTTCAATTTGTT  
 TCTTCGTGCCTTAAGAACATCTTCGTATTGATATTCAAGATAAGATTTACCGACCCGATCATTTCGTGAAT  
 AACTTTTGATAAATATTGTTTCAGTTAATTCTTTAGGTATACCTTCAGTCGAAGTCGACACATCTCCAATA  
 TGCCTCTTAAAGTATCACCGTATGGGTATTTTCTATCCCAATCCATTGTAGTATTTACACCAGGTAATTTAGA  
 AAGCTGTTGTGATACGGCTGCATATCTTTCTCGTTACGTCTTCATTTTTAATTGTTTGAGGATCTAGAGT  
 TGACCCAGCGTTCATTTCCCGATAAATTGCTAAAACCTGCAAATCTTTTTAGTTAACTGTTTTAATTGTTT  
 TTTTCTATTTTATCTCTAAGTTGGGTATCAAATTGGTCTTGTGAAATACTGCCATCCTCTAACATTAATTGT  
 TCTTTTCTCATTAACTTTTTAGCAGATGACGGATACATTGAATCCAAAATCCTTTTTATCTCTCTCAGTAA  
 TTTTATCTGTATCCATTTAATTAATCTGTCAGTTTCTTAGCAGTATTTAACATTTCTTTTGATGTTTTA  
 CGGTTTCTAGTGATGTAATAGACATCTTTGAAGCATTATCAACTAGTACTTTGCCATTTCTATCTAGTATTC  
 GGCCTCTTGGTACTGATTCATTAACAGTTATGTTTTCATCGTTTTTGATTAATTGTTTGAATGAGATCCTTG  
 TGCTATTTGTAATAACCTAATCTCAATACGACTATAGCAAAGATAAATACTATAAATCCAAATATGAAATT  
 GATTCTTTTATCATGGTGTTCATTTTTTCATCATTGATTTTTCTTTAATCTTTTTAGCAA

**Table 11: Modified and *Escherichia coli* -Codon optimized Nucleotide Sequence of SePBP3.**

Truncated SePBP3 gene was without the signal peptide and the membrane anchor. Attached to N-terminal sequence are the 6 x Histidine tag (depicted in yellow), the TEV protease cleavage side (depicted in green) and the linker sequences (depicted in red). Start codon is depicted in rose. Highly conserved motifs are depicted in teal.

**>modified and *Escherichia coli* -Codon optimized nucleotide sequence of SePBP3**

ATGGGTAGCAGTCATCATCATCACCATAGCAGTGGCGAAAATCTGATTTTCAGAGTGGTAGCCATTA  
 TAAACAGCTGATTAAGAATGATGAGAACATTACCGTGAATGAAAGTGTGCCGCGCGGTGCTATTCTGGA  
 TCGCAATGGTAAAGTTCTGGTGGATAATGCCAGTAAAATGAGTATTACCTATACCCGCAATCGTAAAACC  
 AGTCAGAAAGAAATGCTGAATACCGCAAAAAGCTGACCGATCTGATTAAGATGGATACCGATAAAATT  
 ACCGAACGCGATAAAAAAGATTTCTGGATTGAGATGTACCCGAGTAGTGCAAAAAGTTAATGCGCAAA  
 GAACAGCTGATGCTGGAAGATGGCAGCATTAGTCAGGATCAGTTTGATACCCAGCTGCGTGATAAAATT  
 GGCAAAAACAGCTGAAACAGCTGACCAAAAAGATCTGCAGGTTCTGGCAATCTATCGCGAAATGAA  
 TGCAGGTAGCACCTGGATCCGACAGACCATTAAGAATGAAGATGTTAGCGAAAAGAGTATGCAGCAG  
 TGAGCCAGCAGCTGAGCAAAGTCCCGGTGTAATACCACAATGGATTGGGATCGCAAATATCCGTATG  
 GTGACACCTGCGCGGTATTTTTGGCGATGTGAGCACCAGCACCGAAGGTATTCCGAAAGAAGTACC  
 GAACAGTATCTGAGTAAAGGCTATAGTCGTAATGATCGCGTGGTAAAAGCTATCTGGAATATCAGTATG  
 AAGATGTTCTGAAAGGCACCAAAAACAGATGAAATATACCACCGATAAGAGTGGCCGTGTTATTAGCA  
 GTGAAGTTCTGAATCCGGGTAGCCGTGGTCATGATCTGCAGCTGACCATTGATATTGATCTGCAGAAAAA  
 AGTGAAAGTCTGCTGAAAAACAGATTAGTAAACTGCGCAGCCAGGGCGCAAAAGATATGGATAAT  
 GCACTGATGGTGGTTTCAAGTCCGAAAATGGTGACATTCTGGCAATTGCAGGCAAAACAGATTGATAAA  
 CAGGGTAAACTGAAAGATTACGATATTGGCAATTTACCCGCACAGTATACCGTGGGACAGTAGCGTTAAA  
 GGCGCACCTGCTGGCAGGTTATCAGAATAAGGCAATTAATGTTGGTGAACAATGTTGATGAACC

GCTGAAATTCAGGGTGGTCTGACCAAACGCAGTTATTTAATAAGAATGGTCACGTTAGCATCGATGAT  
 AAACAGGCACTGATGCATAGTAGCAATGTGTATATGTTAAGACCCGCCCTGAAACTGGCAGGTGACCCG  
 TATACCAGTGGTATGAGCCTGCCGAATAATATTGCAGATGCAGGTCGTAAACTGCGTAAAGGTCTGAATC  
 AGGTGGGCCTGGGTCTGAAAACCGGTATTGATCTGCCGAATGAAACCCCGGGTCAGATTGAACCGCTG  
 ACCAATAATCCGGGCAATTATCTGGATCTGGCCATTGGTCAGTATGATACCTATACCCCGCTGCAGCTGAG  
 CCAGTATGTTAGTACCATTGCAAATGATGGCTATCGCATTAGCCGCATATTGGCCTGAGTATCTATGAAA  
 GCACCAATAAGGATGAAACCGGCCCGCTGAAACGCAAATAAAGGGTAATGTTCTGAATAAGGTGAAT  
 AATAGCAACGATGAAATCAAAGAAGTGCAGGAAGGTTTTAAAATGGCCTTTAATGAAAAGCAGGGTAC  
 CGGCTATGCCAGCTTTCGTAATACCGTGGTGGCAGTGCAGGCAAACCCGGCACCCGAGAAGTGTTC  
 AGGATGGCGAACCGCGCGTGAATAGTACCTATATTGGTTATGCACCGGTGGATGATCCGAAACTGAGCT  
 TTAGTATTGTGTATACCAATCAGCCGGTCCCGCCCGTGGCTGAATGGTGGTGACCTGGGTGCTGATG  
 TTATTAATTATTATTTCAAGGACAAGGACAACAAGAAAGATGATAGTCAGAGTAATAACGAAGAAAAAG  
 AAGATTAACATATG

**Table 12. Original Protein Sequence of SePBP3 from RP62A.** Original sequences from RP62A are shown as protein sequence. Signal peptide is highlighted in turquoise. Start codon(methionine) is depicted in rose. Highly conserved motifs are depicted in teal.

> **Original protein sequence of SePBP3 from RP62A (PMID: 15774886)**

MLKRLKEKSNDEKMRNTMNKRINFIFGFVIFAIIVLRLGYLQIAQ GSHYKQLIKNDENITVNESVPRGRIL  
 DRNGKVLVDNASKMSITYTRNRKTSQKEMLNTAKKLDLIKMDTDKITERDKKDFWIQMYPSSAKKLMR  
 KEQLMLEDGSISQDQFDTQLRDKIGKKQLKQLTKKDLQVLAIYREMNAGSTLDPQTIKNEVDSEKEYAAVS  
 QQLSKLPGVNTTMDWDRKYPYGDTLRGIFGDVSTSTEGIPKELTEQYLSKGYSRNDRVKGKSYLEYQYEDVL  
 KGTKKQMKYTTDKSGRVISSEVLNPGSRGHDLQLTIDIDLQKKVESLLEKQISKLR SQGAKDMDNALMVV  
 QNPKNKDILAIAGKQIDKQGLKDYDIGNFTAQYTVG SSVKGGTLLAGYQNKAINVGETMVDEPLKFQ  
 GLTKRSYFNKNGHVSIDDKQALMH SSNVVMFKTALKLAGDPYTSGM SLPNNIADAGRKLRLKGLNQVGL  
 GLKTGIDLNETPGQIEPLTNNPGNYLDAIGQYDITYPLQLSQYVSTIANDGYRIQPHIGLSIYESTNKDET  
 GPLKRIKIGNVNLKNVNSNDEIKEVQEGFKMAFNEKQGTGYASFRNTVVPSAG KTGTAEVFQDGEPRVN  
 STYIGYAPVDDPKLSFSIVYTNQPVPPWLNGGDLGRDVINYFYKDKDNKKDSSQSNNEEKD

**Table 13. Protein Sequences of SePBP3 from RP62A.** Truncated SePBP3 gene was modified without the signal peptide and the membrane anchor. Attached to N-terminal sequence are the 6 x Histidine tag (depicted in yellow), the TEV protease cleavage side (depicted in green) and the linker sequences (depicted in red). Start codon(methionine) is depicted in rose. Highly conserved motifs are depicted in teal.

> **modified and Escherichia coli -Codon optimized protein sequence of SePBP3**

MGSSHHHHHSSGENLYFQS GSHYKQLIKNDENITVNESVPRGRILDRNGKVLVDNASKMSITYTRNRK  
 TSQKEMLNTAKKLDLIKMDTDKITERDKKDFWIQMYPSSAKKLMRKEQLMLEDGSISQDQFDTQLRDKI  
 GKKQLKQLTKKDLQVLAIYREMNAGSTLDPQTIKNEVDSEKEYAAVSQQLSKLPGVNTTMDWDRKYPY  
 DTLRGIFGDVSTSTEGIPKELTEQYLSKGYSRNDRVKGKSYLEYQYEDVLKGTKKQMKYTTDKSGRVI  
 SSEVLNPGSRGHDLQLTIDIDLQKKVESLLEKQISKLR SQGAKDMDNALMVVQNPKNKDILAIAGKQID  
 KQGLKDYDIGNFTAQYTVG SSVKGGTLLAGYQNKAINVGETMVDEPLKFQGGTLTKRSYFNKNGHVS  
 IDDKQALMH SSNVVMFKTALKLAGDPYTSGM SLPNNIADAGRKLRLKGLNQVGLGLKTGIDLNETPGQ  
 IEPLTNNPGNYLDAIGQYDITYPLQLSQYVSTIANDGYRIQPHIGLSIYESTNKDETGPLKRIKIGNV  
 NLKNVNSNDEIKEVQEGFKMAFNEKQGTGYASFRNTVVPSAG KTGTAEVFQDGEPRVNSTYIGYAPV  
 DDPKLSFSIVYTNQPVPPWLNGGDLGRDVINYFYKDKDNKKDSSQSNNEEKD



**Table 14: Confidently predicted Domains, Repeats, Motifs and Features made by SMART.**

Name	Start [aa]	End [aa]	E value
transmembrane region	7	24	N/A
Pfam:MecA_N	25	140	6.9e-29
Pfam:PBP_dimer	146	313	7e-32
Pfam:Transpeptidase	345	658	5.1e-73

**Table 15. Original Nucleotide Sequences of MecA from RP62A (PMID: 15774886)**

**> Original nucleotide sequence of MecA from RP62A (PMID: 15774886)**

ATGACTGAACGTCGGATAAAAATATATAATAGTTTAGGCGTTAAAGATATAAACATTCAGGATCGTAAAAT  
 AAAAAAAGTATCTAAAAATAAAAAACGAGTAGATGCTCAATATAAAATTTAAAACAACTACGGTAACATT  
 GATCGCAACGTTCAATTTAATTTTGTAAAGAAGATGGTATGTGGAAGTTAGATTGGGATCATAGCGTCA  
 TTATCCAGGAATGCAGAAAGACCAAAGCATAACATATTGAAAATTTAAAATCAGAACGTGGTAAAATTTT  
 AGACCGAAACAATGTGGAATTGGCCAATACAGGAACAGCATATGAGATAGGCATCGTTCCAAAGAATGT  
 ATCTAAAAAAGATTATAAAGCAATCGCTAAAGAATAAGTATTTCTGAAGACTATATCAAACAACAAATG  
 GATCAAAAAGTGGGTACAAGATGATACCTTCGTTCCACTTAAACCCTTAAAAAATGGATGAATATTTAA  
 GTGATTTGCAAAAAAATTTTCATCTTACAATAATGAAACAGAAAGTCGTAACATCCTCTAGAAAAAGC  
 GACTTCACATCTATTAGGTTATGTTGGTCCCATTAACCTGAAGAATTAACAACAAAAGAATATAAAGGC  
 TATAAAGATGATGCAGTTATTGGTAAAAAGGGACTCGAAAAACTTTACGATAAAAAAGCTCCAACATGAA  
 GATGGCTATCGTGCACAATCGTTGACGATAATAGCAATACAATCGCACATACATTAATAGAGAAAAAGA  
 AAAAAGATGGCAAAGATATTCAACTAATGATGCTAAAGTTCAAAGAGTATTATAACAACATGAA  
 AAATGATTATGGCTCAGGTAAGTCTATCCACCCTCAAACAGGTGAATTATTAGCACTTGTAAGCACACCTT  
 CATATGACGTCTATCCATTTATGTATGGCATGAGTAACGAAGAATATAATAAATTAACCGAAGATAAAAA  
 GAACCTCTGCTCAACAAGTTCCAGATTACAACCTCACCAGGTTCAACTCAAAAAATATTAACAGCAATGA  
 TTGGGTTAAATAACAAAACATTAGACGATAAAACAAGTTATAAAATCGATGGTAAAGGTTGGCAAAAAG  
 ATAAATCTTGGGGTGGTTACAACGTTACAAGATATGAAGTGGTAAATGGTAATATCGACTTAAAACAAGC  
 AATAGAATCATCAGATAACATTTTCTTTGCTAGAGTAGCACTCGAATTAGGCAGTAAGAAATTTGAAAA  
 GGCATGAAAAAAGTAGGTGTTGGTGAAGATATACCAAGTGAATATCCATTTATAATGCTCAAATTTCAA  
 CAAAAATTTAGATAATGAAATATTATTAGCTGATTCAGGTTACGGACAAGGTGAAATACTGATTAACCCA  
 GTACAGATCCTTTCAATCTATAGCGCATTAGAAAATAATGGCAATATTAACGCACCTCACTTATTAAGA  
 CACGAAAAACAAAGTTTGAAGAAAAATATTATTCCAAAGAAAAATATCAATCTATTAAGTATGATGGTATG  
 CAACAAGTCGTAATAAAACACATAAAGAAGATATTATAGATCTTATGCAAACCTAATTGGCAAATCCG  
 GTACTGCAGAACTCAAATGAAACAAGGAGAACTGGCAGACAAATTGGGTGGTTTATATCATATGATA  
 AAGATAATCCAACATGATGATGGCTATTAATGTTAAAGATGTACAAGATAAAGGAATGGCTAGCTACAA  
 TGCCAAAATCTCAGGTAAAGTATGATGAGCTATATGAGAACGGTAATAAAAAATACGATATAGATGAA  
 TAA

**Table 16: Modified and *Escherichia coli* -Codon optimized Nucleotide Sequence of MecA.** Truncated MecA gene was without the signal peptide and the membrane anchor. Attached to N-terminal sequence are the 6 x Histidine tag (depicted in yellow), the TEV protease cleavage side (depicted in green) and the linker sequences (depicted in red). Start codon is depicted in rose. Highly conserved motifs are depicted in teal.

>modified and *Escherichia coli* -Codon optimized nucleotide sequence of MecA

ATGGGTAGCAGTCATCATCATCACCATAGCAGTGGCGAAAATCTGATTTTCAGAGTGCAAGCAAAG  
ATAAAGAAATTAATAACACCATCGACGCCATTGAAGATAAAAATTTAAGCAGGTGTACAAGGATAGCA  
GTTATATTAGTAAAAGCGATAACGGTGAAGTTGAAATGACCGAACGCCGATTAAGATCTATAATAGCCT  
GGCGTGAAAGATATTAATATTCAGGATCGTAAGATCAAGAAGGTGAGCAAAAATAAGAAACGTGTTG  
ATGCACAGTATAAAATTAAGACCAATTACGGCAATATCGATCGTAATGTTTCAGTTAATTTTCGTGAAAGAA  
GACGGTATGTGGAACTGGATTGGGATCATAGTGTATTATTCCGGGCATGCAGAAAGATCAGAGCATT  
CATATTGAAAATCTGAAAAGCGAACGTGGTAAAATCTGGATCGTAATAATGTTGAACTGGCAAATACCG  
GCACCGCATACGAAATTGGCATTGTTCCGAAAATGTGAGTAAAAAAGACTATAAGGCCATTGCCAAAG  
AACTGAGTATTAGTGAAGATTATATCAAGCAGCAGATGGATCAGAATTGGGTGCAGGATGATACCTTTGT  
GCCGCTGAAAACCGTGAAAAGATGGATGAATATCTGAGTGATTTTCGAAAAAAGTTTCATCTGACCAC  
CAATGAAACCGAAAGCCGTAATTATCCGCTGGGCAAAGCCACCAGCCATCTGCTGGGTTATGTTGGCCC  
GATTAATAGCGAAGAAGTGAACAGAAAGAATATAAAGGTTACAAGAACGATGCCGTTATTGGTAAAA  
AAGGTCTGAAAAACTGTATGATAAGAACTGCAGCATGAAGATGGTTATCGCGTTACCATTGTGGATG  
ATAATAGCAATACCATTGCCCATACCTGATTGAAAAGAAAAAGAAAGATGGTAAAGACATCCAGCTGA  
CCATTGATGCCAAAGTGCAGAAAAGCATCTATAATAATATGAAGAACGACTACGGCAGTGGTACCGCCA  
TTCATCCGCAGACCGGCGAACTGCTGGCCCTGGTTAGCACCCCGAGCTATGATGTGTATCCGTTTATGTA  
TGGTATGAGCAATGAAGAATACAATAAGCTGACCGAAGATAAAAAAGAACCGCTGCTGAATAAGTTTCA  
GATTACCACCAGCCCGGCGAGTACCCAGAAAATTCTGACCGCAATGATTGGCCTGAATAATAAGACCCT  
GGATGATAAAACCAGTTATAAAATTGACGGTAAAGGTTGGCAGAAAGATAAAAGTTGGGGCGGTTATA  
ATGTGACCCGCTATGAAGTTGTGAATGGTAATATTGATCTGAAACAGGCCATTGAAAGCAGTGATAATAT  
TTTCTTTGCCGTTGCACTGGAAGTGGGAGTAAAAAATTTGAAAAGGCATGAAAAGCTGGGGCG  
TGGGCGAAGATATTCCGAGCGATTATCCGTTTATAATGCCAGATTAGCAATAAGAACCTGGATAATGA  
AATCCTGCTGGCAGATAGTGGCTATGGCCAGGGCGAAATCTGATTAATCCGTTTCAGATTCTGAGCATC  
TATAGCGCACTGGAAAATAATGGTAATATCAATGCCCGCATCTGCTGAAAGATACCAAAAATAAGGTGT  
GGAAAAGAATATCATCAGTAAAGAAAACATCAACCTGCTGACCGATGGTATGCAGCAGGTTGTGAATA  
AGACCCATAAAGAAGATATCTATCGCAGCTATGCCAATCTGATTGGCAAAAGTGGTACCGCGGAACTGA  
AAATGAAACAGGGTGAACCGGCCGTCAGATTGGCTGGTTTATTAGCTATGATAAAGATAATCCGAACA  
TGATGATGGCCATTAATGTGAAAGATGTTTCAGGATAAAGGTATGGCCAGCTATAATGCAAAAATTAGTGG  
CAAAGTTTACGATGAACTGTATGAAAATGGCAATAAGAAATACGATATCGATGAATAA

**Table 17. Original Protein Sequence of SePBP2a from RP62A.** Original sequences from RP62A are shown as protein sequence. Signal peptide is highlighted in turquoise. Start codon (methionine) is depicted in rose. Highly conserved motifs are depicted in teal.

> Original protein sequence of SePBP2a from RP62A (PMID: 15774886)

MILIVVVVGFYIYFASKDKEINNTIDAIEDKNFKQVYKDSYISKSDNGEVEMTERPIKIYNSLGVKDINI  
QDRKIKKVSKNKKRVDAQYKIKTNYGNIDRNVQFNFKEDGMWKLWDHSHVPIPGMQKDQSIHIEN  
LKSERGKILDRNNVELANTGTAYEIGIVPKNVSKDYKAIKELISEDYIKQQMDQNWVQDDTFVPLK  
TVKKMDEYLSDFAKKFHLLTNETESRNYPLGKATSHLLGYVGPINSEELKQKEYKGYKNDAVIGKKGLEK  
LYDKKLQHEDGYRVTIVDDNSNTIAHTLIEKKKKDGKDIQLTIDAKVQKSIYNNMKNDYGSGTAIHPQT

GELLALVSTPSYDVYPFMYGMSNEEYNKLTEDKKEPLLNFQITTPSGSTQKILTAMIGLNNKTLDDKTSY  
 KIDGKGWQKDKSWGGINVTRYEVVNGNIDLKQAIESSDNIFARVALELGSKKFEKGMKGLGVGEDIP  
 SDYPFYNAQISNKNLDNEILLADSGYGQGEILINPVQILSIYSALENNGNINAPHLLKDTKNKVWKKNIIS  
 KENINLLTDGMQQVVKTHKEDIYRSYANLIGKSGT AELKMKQGETGRQIGWFISYDKDNPMMMA  
 INVKDVQDKGMASYNKISGKVYDELYENGNKKYDIDE

**Table 18. Protein Sequences of SePBP2a from RP62A.** Truncated PBP3 gene was modified without the signal peptide and the membrane anchor. Attached to N-terminal sequence are the 6 x Histidine tag (depicted in yellow), the TEV protease cleavage side (depicted in green) and the linker sequences (depicted in red). Start codon(methionine) is depicted in rose. Highly conserved motifs are depicted in teal.

**>modified and *Escherichia coli* -Codon optimized protein sequence of SePBP2a**

MGSSHHHHHHSSGENLYFQASAKDKEINNTIDAIEDKNFKQVYKDSYISKSDNGEVEMTERPIKIYN  
 SLGVKDINIQRKIKKVSKNKKRVDAQYKIKTNYGNIDRNVQFNFKEDGMWKLWDHVSIIIPGMQ  
 KDQSIHIENLKSERGKILDRNNVELANTGTAYEIGIVPKNVSKKDYKAIKELISEDYIKQQMDQNWV  
 QDDTFVPLKTVKKMDEYLSDFAKKFHLTTNETESRNYPLGKATSHLLGYVGPINSEELKQKEYKGYKND  
 AVIGKKGLEKLYDKKLQHEDGYRVTIVDDNSNTIAHTLIEKKKDKGKDIQLTIDAKVQKSIYNNMKNDY  
 GSGTAIHPQTGELLALVSTPSYDVYPFMYGMSNEEYNKLTEDKKEPLLNFQITTPSGSTQKILTAMIGLN  
 NKTLLDDKTSYKIDGKGWQKDKSWGGINVTRYEVVNGNIDLKQAIESSDNIFARVALELGSKKFEKGMKGLGVGEDIP  
 SDYPFYNAQISNKNLDNEILLADSGYGQGEILINPVQILSIYSALENNGNINAPHLLKDT  
 KNKVWKKNIISKENINLLTDGMQQVVKTHKEDIYRSYANLIGKSGT AELKMKQGETGRQIGWFISYD  
 KDNPNMMMAINVKDVQDKGMASYNKISGKVYDELYENGNKKYDIDE

**Preparation of Competent Cells**

The preparation of chemical competent cells were necessary for the transformation of the SePBP3-pET-28b(+) construct. DH5α / TOP10 competent *Escherichia coli* cells were used for plasmid amplification and BL21 DE3 / BL21 Star competent *Escherichia coli* cells were used for protein expression. The desired bacterial cell line plated on a LB-ager plate and incubated over night at 37 °C. The following day 250 ml of SOC medium was inoculated and incubated at 18 °C and 180 rpm. Cells grew until an OD<sub>600</sub> = 0.6 was reached and subsequently incubated on ice for 10 minutes. After the incubation on ice cells were pelleted at 4000 rpm for 10 minutes at 4 °C. Supernatant was discarded and cell pellet was washed with ice cold 100 mM CaCl<sub>2</sub> solution four times and subsequently resuspended in 1 mL of ice cold 100 mM and subsequently resuspended in CaCl<sub>2</sub> solution containing 10% glycerol. Cells were aliquoted and flash frozen in liquid nitrogen to be stored at -80 °C.

## Transformation

Transformation was conducted according to *New England Biolab® GmbH* most efficient protocol. 50 µl of cells were thawed on ice and afterwards incubated with the plasmid construct (chapter Plasmid-DNA construct). 50 ng of the  $\Delta 47SePBP3$  - pET-28b(+) plasmid was added as soon as the last trace of ice disappeared. It was important to avoid rough mixing or vortexing but applying gentle stirring with the pipette tip. The sample was incubated on ice for 30 °C. Subsequently, cells were treated with a heat shock at 42 °C. BL21 (DE3) and BL21 (DE3) Star cells were shocked for 20 seconds but DH5 $\alpha$  and TOP10 cells were shocked for 30 seconds. Immediately after the heat shock, cells incubated on ice for 2 minutes. Afterwards, 500 µl of SOC medium was added and cells recovered at 37 °C and 350 rpm for 60 minutes. Reducing the recovery time, using LB medium and incubating without shaking would reduce the transformation efficiency. After the recovery time, agar plates (1% w/v agar in LB media and 50 µg/ml of kanamycin) were inoculated with the freshly transformed cells and incubated at 37 °C over night.

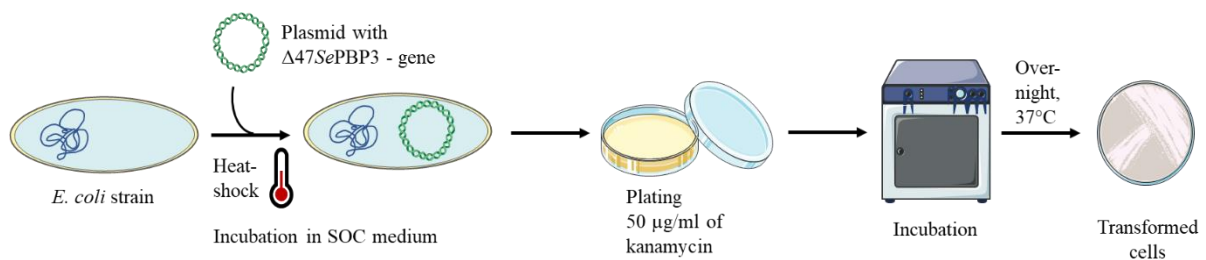


**Figure 11: A schematic Figure of a Transformation.** Created with BioRender.com.

## Biochemical Methods

### Glycerol Stock Production

A glycerol stock is transformed *Escherichia coli* cells which are mixed with the cryo-protector glycerol to be prepared for further expression cultures. Freshly picked colonies were transferred into cultural tubes together with 5 ml LB medium and 50 µg/ml kanamycin. Culture grew at 37 °C and 180 rpm until an  $OD_{600} = 0.6$  and fastest growing culture was used for expression tests. For the production of glycerol stocks 2 ml of culture was mixed with 2 ml of 100 % glycerol. Aliquots of 50 µl were flash frozen in liquid nitrogen to be stored at -80 °C.



### **Plasmid Isolation / Mini Prep**

Plasmid amplification and isolation is a useful method to enhance the amount of plasmid you have. A DH5 $\alpha$ -transformant was used for the replication and amplification of the SePBP3-pET-28b(+) construct and SePBP2a-pET-28b(+) construct. One glycerol aliquot was added to 5 ml LB medium and 50  $\mu$ g/ml kanamycin and culture was grown for 12-16 hours. Cells were pelleted by centrifugation at 6.000 x g for 30 seconds. The supernatant was discarded and pellet was resuspended in 200  $\mu$ l of the RNase solution until no clumps are visible. Cells were disrupted by adding 250  $\mu$ l of alkaline lysis buffer and inverting the tube five times until the solution become clear. 350  $\mu$ l of the neutralization buffer reduced to pH-value to 7. Cell debris and chromosomal DNA was pelleted and supernatant, containing the plasmid DNA, was loaded onto the GeneJET spin column by centrifugation at 6.000 x g for 1 minute. Flowthrough was discarded and column was washed twice with 500  $\mu$ l of ethanol containing washing buffer. Plasmid-DNA was eluted by adding 50  $\mu$ l of water and centrifugation at 6.000 x g for 1 minute. DNA concentration was measured with Thermo Scientific™ NanoDrop™. Plasmid solution was stored at -20 °C.

### **Gene Expression**

Gene expression tests of  $\Delta$ 47SePBP3 and  $\Delta$ 15SePBP2a in BL21 (DE) and BL21 (DE) Star cells were conducted to observe the most efficient expression time, medium and temperature (Table 19). One aliquot of the glycerol stock of each transformant was used to produce an overnight culture consisting of each 200 ml of LB medium and 50  $\mu$ g/ml kanamycin. The overnight culture grew 14 hours at 37 °C and 180 rpm. The expression culture for each transformant consisted of 1 L of medium, 50  $\mu$ g/ml kanamycin and 5% inoculant (overnight culture). Cells grew at 37 °C and 180 rpm until an OD<sub>600</sub> = 0.6 was reached. Gene expression was induced with 1 mM of IPTG and temperature was reduced to 20 °C and 30 °C for each transformant. Samples of the expression culture was taken and centrifuged at 4000 x g at room temperature after 3, 4, 5 and 14 hours. Cell pellet of all samples was stored at -20°C for an SDS-PAGE analysis. An analysis of the gene expression of all conditions showed the best expression with LB medium in BL21 (DE) at 30°C for 3 hours with 1 mM IPTG.

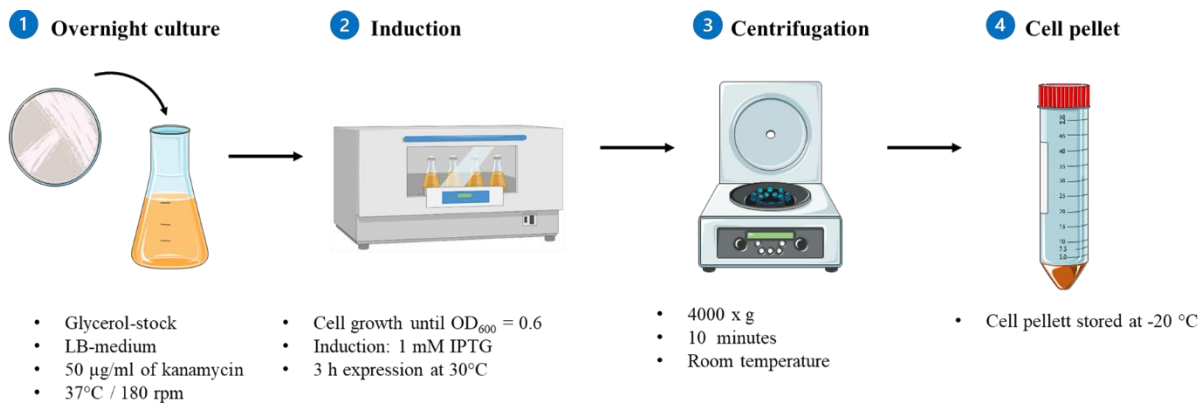


**Figure 12: A schematic Figure of the final Gene Expression Protocol.** Created with BioRender.com.

**Table 19: Gene Expression Tests.**

Strain	Medium	Temperature [°C]	Duration [hrs]
BL21 (DE)	LB medium	20 °C	3 hrs
		30 °C	4 hrs
	TB medium	20 °C	5 hrs
		30 °C	14 hrs
	YT medium	20 °C	
		30 °C	
BL21 (DE) Star	LB medium	20 °C	
		30 °C	
	TB medium	20 °C	
		30 °C	
	YT medium	20 °C	
		30 °C	

### Cell Lysis and Ni-NTA Affinity Chromatography

Cell pellets from gene expression were thawed on ice and resuspended with lysis buffer until no agglutination were visible. Subsequently, cells were disrupted by sonification by the following protocol: 30 % amplitude, 15 minutes total time, 5 seconds pulse and 10 pause. The sonification process was performed on ice to avoid a denaturing

temperature. The protein containing lysate was separated from the cell debris by centrifugation at 15.000 x g, 4 °C and 30 minutes.

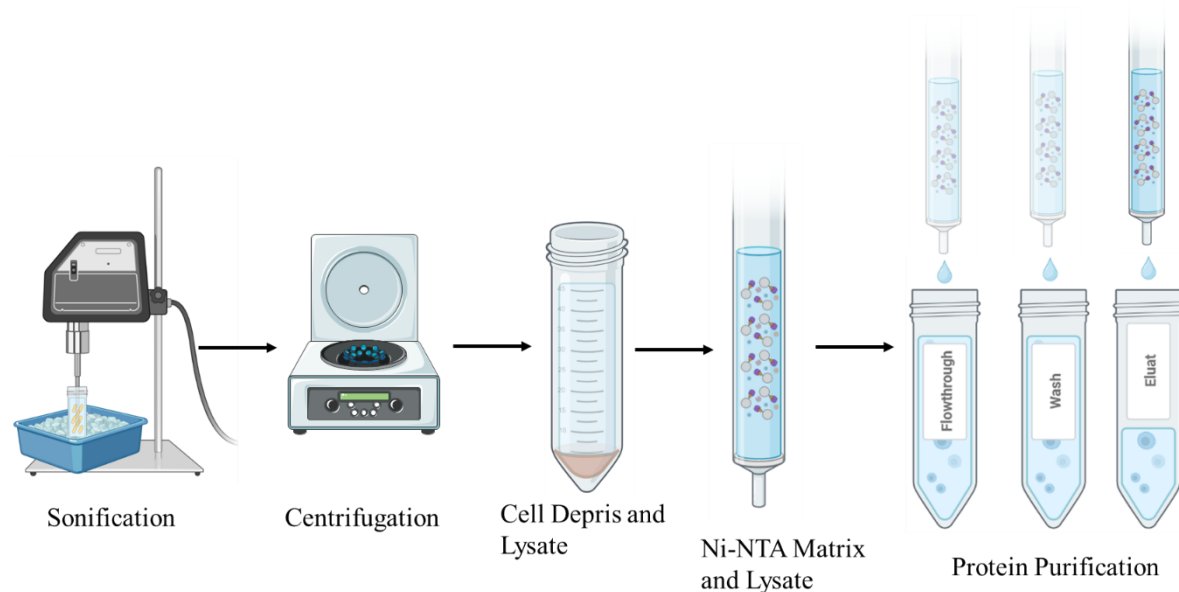


**Figure 13: A schematic Figure of the Principle of a Ni-NTA Affinity Chromatography.** Created with BioRender.com.

Following steps were applied for the Ni-NTA affinity chromatography:

1. Column was stored on 20 % Ethanol and needed to be washed with 5 column volumes of ddH<sub>2</sub>O.
2. Column was equilibrated with 5 column volumes of the lysis buffer / equilibration buffer.
3. Cell lysate containing the soluble protein fraction was loaded onto the column and mixed with the matrix.
4. The Ni-NTA matrix – cell lysate mixture was incubated for 1 hour at 4 °C.
5. Unbound protein went through the column and were defined as flow through fraction.
6. Unspecific bound *Escherichia coli* protein was washed from the column with 5 column volumes of the washing buffer.
7. His-tagged protein was eluted from the column with 1 column volume of the elution buffer.

All buffers are listed in table 5. and the schema of the workflow of the principle of a Ni-NTA affinity chromatography are shown in figure 13. A scheme of the His-tagged protein in complex with the Ni-NTA matrix is shown in figure 14.

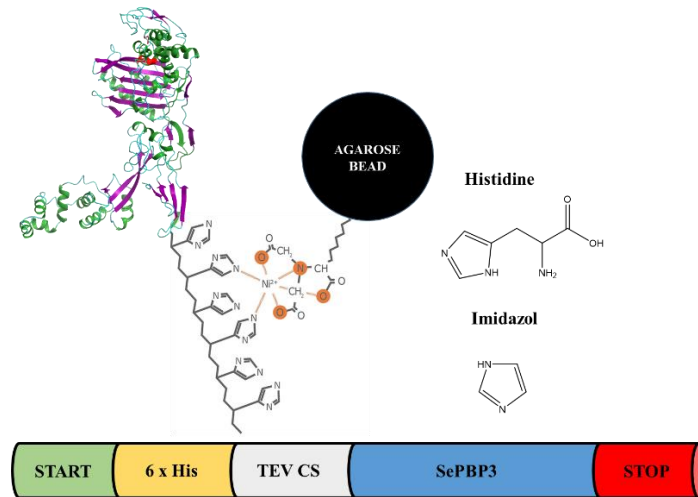


**Figure 14: A schematic Figure of the 6 x His-tagged Protein binding to a Ni-NTA Matrix.**

### Dialysis

The buffer was exchanged via dialysis to prepare the next purification step. The freshly purified protein solution was transferred into a dialysis bag which contains pores with the size of 3.5 kDa resulting in an exchange of buffer components without an exchange of the protein (Figure 15). The protein solution was about 5 ml and the tank solution with the preferred protein buffer contained 5 Liter hence the dilution factor of imidazole was 1:1000. The tank solution contained the buffer for the next purification step: the size exclusion chromatography (Table 5).

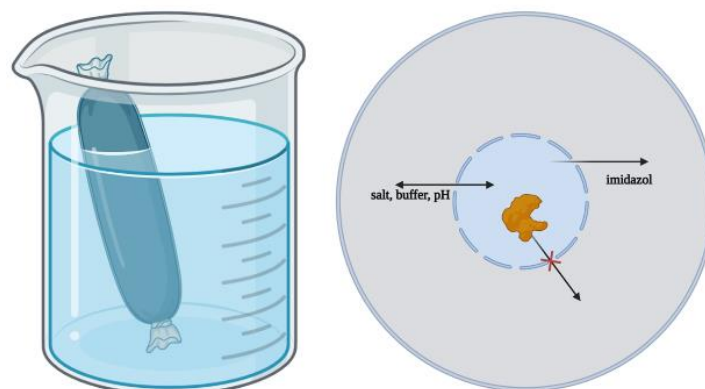


**Figure 15: A schematic Figure of the Dialysis.** Created with BioRender.com.

### **Size Exclusion Chromatography**

A polishing step is often necessary to get a monodisperse protein solution for the crystallization part. The Äkta purifier / or the Äkta start was used to run a size exclusion chromatography (SEC). Hiload 16/60 Superdex 75 SEC column or a Hiload 16/600 Superdex 200 SEC column was utilized. Following steps were applied for the SEC:

1. Column and pumps were stored on 20 % Ethanol and needed to be washed. The pumps were washed with 10 ml and the columns with 2 column volumes of ddH<sub>2</sub>O.
2. Column and pumps were equilibrated with 2 column volumes of the SEC buffer and 10 ml of the SEC buffer for the pumps.
3. Freshly dialyzed protein solution was loaded into a 5 ml loop which was assembled at the Äkta system.
4. The 5 ml loop was emptied with 5.5 ml of the SEC buffer and the loop content was loaded directly onto the column.
5. The protein solution was separated by size with a flowrate of 1 ml / min and a maximal pressure of 0.5 MPa. The purification was performed with 1.5 column volumes and the first 30 % of the column volume was discarded. Protein was detected at 280 nm wavelength and the fraction size was defined as 2 ml per fraction.
6. Protein fractions with the corresponding peak were collected.
7. Pumps and column were washed with ddH<sub>2</sub>O and stored at 20 % ethanol.

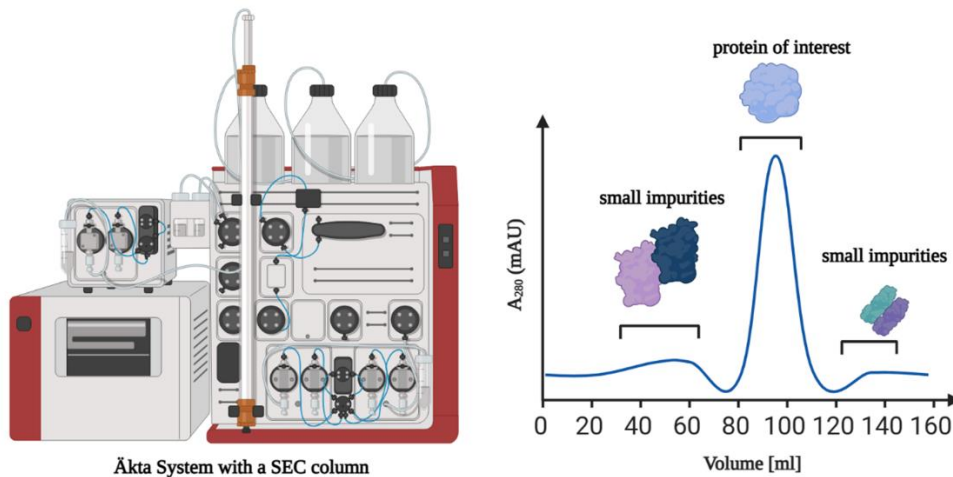


**Figure 16: A schematic Figure of the Principle of a Size Exclusion Chromatography used as a polishing Step.** Created with BioRender.com.

### **Sodium Dodecyl Sulfate–Polyacrylamide Gel Electrophoresis (SDS – PAGE)**

An SDS – PAGE is a biochemical method, which separates proteins according to their size. Therefore, all proteins need to be denatured with 2-mercaptoethanol or dithiothreitol, sodium dodecyl sulfate (SDS) and by cooking at 96 °C for 5 minutes. The reducing agents open disulfide bridges and the SDS are necessary for an equally distributed negative charge around the peptide chains. Proteins are now able to wander through a gel at a speed according to their logarithmic size. The gel itself is casted with an acrylamide concentration fitting to the protein size of interest. A high percentage of acrylamide separates smaller proteins more precise and lower percentages are suitable for bigger proteins of interests. The stacking gel has a very low concentration of acrylamide and a pH value of 6.8. The proteins are stacked at the same height because they run between chloride ions and glycine. The separation gel has a higher pH value (8.8) and is higher concentrated. The proteins can run separately and be distinguished after a coomassie blue staining. Coomassie Brilliant Blue R-250 is a negatively charged molecule and can bind to cationic and hydrophobic side chains of proteins. The minimal amount of proteins for a detection with Coomassie Brilliant Blue R-250 is in a range of 100 – 50 ng (Brunelle and Green, 2014). The method was overall performed according to Laemmli (Laemmli, 1970) with differences shown in table 20. The protein solution was cooked with the sample buffer and centrifuged at 16.000 x g for 10 minutes. Afterwards the vertical

gel electrophoresis was used with a 1 x running buffer applying 120 V and 25 mA current for the stacking gel and 180 V and 25 mA current for the separation gel. The gel was transferred into a box with a coomassie staining solution and incubated for 30 minutes. The overnight destaining process with acidic acid revealed all protein bands.

**Table 20: Composition of the Stacking Gel, the Separation Gel and the running Buffer.**

Stacking gel (4%)	Separation gel (12 %)	Running buffer (10 x)
9.2 ml H <sub>2</sub> O	10.2 ml H <sub>2</sub> O	30.3 g Tris base
2 ml 30 % acrylamide	12 ml 30 % acrylamide	144 g glycine
3.8 ml stacking gel buffer (0.5 M Tris-HCl, pH = 6.8)	7.5 ml stacking gel buffer (1.5 M Tris-HCl, pH = 8.8)	10 g SDS
150 µl 10% SDS	300 µl 10% SDS	Ad 1000 ml
15 µl TEMED	15 µl TEMED	
75 µl 10% APS	150 µl 10% APS	

**Table 21: Composition of the Sample Buffer, Coomassie staining Solution and the destaining Solution.**

Sample buffer	Coomassie Staining solution	Destaining solution
3.55 ml H <sub>2</sub> O	250 ml isopropanol	200 ml of 100% acidic acid
1.25 ml stacking gel buffer (0.5 M Tris-HCl, pH = 6.8)	100 ml acetic acid	ad 1000 ml H <sub>2</sub> O
2.5 ml glycerol	1 g Coomassie Brilliant Blue R-250	
2 ml 10% SDS	ad 1000 ml H <sub>2</sub> O	
0.2 ml 0.5 % (w/v) bromophenol blue		

### Isothermal Titration Calorimetry

Isothermal Titration Calorimetry (ITC) is a sophisticated analytical technique used to study biomolecular interactions. It measures the heat change associated with molecular interactions, providing direct insights into the thermodynamics of binding processes, including enthalpy ( $\Delta H$ ), entropy ( $\Delta S$ ), and binding constants ( $K_{Da}$ ). At the core of ITC is the principle that molecular binding is always accompanied by heat absorption or release. ITC quantifies this heat, allowing for the calculation of thermodynamic parameters. A typical ITC experiment involves the gradual titration of a ligand into a solution containing a macromolecule of interest, with a sensitive calorimeter detecting

heat changes (Figure 17) (Bastos et al., 2023). Our ITC experiments were conducted using Malvern PEAQ-ITC. The instrument consists of two cells: a sample cell, where the macromolecule was placed, and a reference cell. The ligand was incrementally injected into the sample cell, and the instrument recorded the differential heat between the sample and reference cells. Proteins and ligands were prepared in a buffer solution identical to that of the experimental setup to avoid heat effects due to dilution or buffer mismatch. The concentrations of protein and ligand were optimized to obtain significant measurable heat changes. The protein utilized for isothermal titration calorimetry (ITC) experiments was prepared following previously detailed protocols and was subsequently concentrated to a final concentration of 40  $\mu\text{M}$ . The ligand was concentrated to a final concentration of 400  $\mu\text{M}$ . The protein solution was loaded into the sample cell, while the ligand was placed in the syringe. This was succeeded by 13 systematic injections, each dispensing a volume of 3  $\mu\text{l}$  over 6 seconds, with a 150-second interlude between injections to guarantee equilibration and full heat dissipation. A consistent stirring speed of 750 rpm was maintained throughout the procedure to facilitate rapid mixing and even heat distribution. The heat changes from each injection were integrated to obtain a binding isotherm. The data accrued from these experiments were processed utilizing NITPIC (version: 1.2.7) (Keller et al., 2012). Further thermodynamic analysis and data fitting were executed with SEDPHAT (version 15.2b) (H. Zhao et al., 2015), and data representation was accomplished via the Gussi software package (version: 1.3.0) (Brautigam, 2015). Each interaction between the protein and a unique ligand was assayed individually to ensure distinct binding profiles.

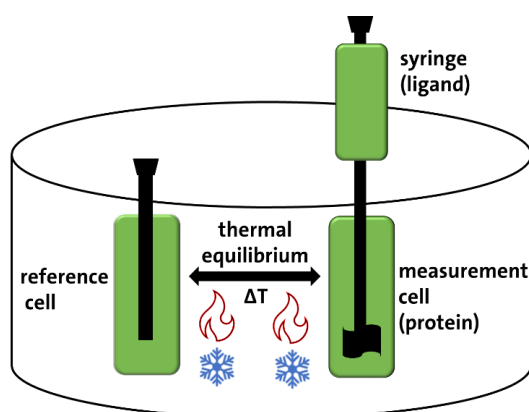


**Figure 17: A schematic Figure of the Principle of an Isothermal Titration Calorimetry Setup.**



## **Spectroscopic Methods**

### **Determination of the protein concentration**

The concentration of the purified protein solution was determined via photometric measurements with the nano drop spectrophotometer. This device measures the absorbance of light due to the amount of tyrosine and tryptophan within a specific volume. The molar absorption coefficient according to the Beer–Lambert law is unique for each specific protein (Beer, 1852). The online tool “ProtParam” ([www.expasy.org](http://www.expasy.org)) was used to calculate the theoretical molar absorption coefficient. The protein concentration can be calculated with the absorbance by applying the methods of Gill and von Hippel (Gill and von Hippel, 1989).

### **Circular dichroism spectroscopy (CD spectroscopy)**

In a bioanalytical CD spectroscopic measurement, circular polarised light is utilized to analyse the chirality of macromolecules, like proteins, through the optical activity. The principle of a secondary structure analysis lies in the differentiated absorption of left-handed and right-handed circularly light. Proteins are composed of amino acids that exhibit characteristic electronic transitions in the ultraviolet (UV) and visible regions of the electromagnetic spectrum. When circularly polarized light passes through a protein sample, the absorption of the light can differ depending on the protein's secondary structure elements, such as alpha-helices, beta-sheets, and random coils. Alpha-helices exhibit a strong positive peak around 190-200 nm and a negative peak around 208-222 nm. Beta-sheets display a negative peak around 218-222 nm and a positive peak around 195-200 nm. Random coils, which lack a defined secondary structure, typically exhibit prominent negative peak around 195-200 nm. They contribute to the overall background signal. The intensity and shape of the peaks in the CD spectrum provide information about the relative proportions of different secondary structure elements within the protein. By comparing the experimental CD spectrum with reference spectra of proteins with known secondary structures, one can estimate the composition and relative abundance of alpha-helices, beta-sheets, and random coils in the protein of interest.  $\pi$ -electrons in conjugated systems can absorb photons of specific energies corresponding to the energy gap between the occupied and unoccupied molecular orbitals. The absorption of light in the  $\pi$ -to- $\pi^*$  transition range can be detectable around 190 nm. A  $n$ -

to- $\pi^*$  transition, also known as a non-bonding to  $\pi^*$  transition, involves the movement of an electron from a non-bonding orbital (n) to an empty  $\pi^*$  antibonding orbital. Similar to the  $\pi$ -to- $\pi^*$  transition, the n-to- $\pi^*$  transition results in the absorption of light at specific wavelengths (210-220 nm) (Greenfield, 2004).

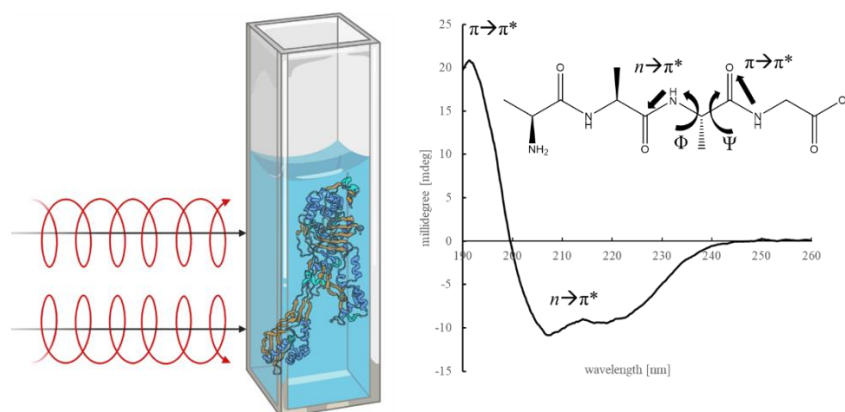


**Figure 18: A schematic Figure of the Principle of a CD Spectroscopic Analysis of the Secondary Structure.** Created with BioRender.com.

$$\Delta A = A_L - A_R \text{ (Formula 1)}$$

Formula 1: Delta absorbance  $\Delta A$  is the sum of the absorbance of left-handed and right-handed circularly light.

$$\Delta A = (\epsilon_L - \epsilon_R)cl \text{ (Formula 2)}$$

Formula 2: Delta absorbance  $\Delta A$  is the sum of the molar extinction coefficient of left-handed and right-handed circularly light. C is the concentration of the protein and l is the length of the cuvette.

$$[\theta]_\lambda = f_\alpha[\theta]_\alpha + f_\beta[\theta]_\beta + f_t[\theta]_t + f_u[\theta]_u \text{ (Formula 3)}$$

Formula 3: A CD spectroscopic analysis of the secondary structure is the sum of all fractions from the ellipticity from alpha helices, beta sheets, turns and unfolded part.  $\theta_{\lambda i}$  is the ellipticity of each wavelength ( $\lambda$ ) and secondary part of the protein (i), whereas  $f_i$  are the secondary structure fractions (Beychok, 1966).

In this study only purified protein was used to measure CD spectroscopy. The concentration was between 0.05 and 0.2 mg/ml and the wavelength was set from 260 to 190 nm. Protein sample was measured 15 times, all spectra were merged, buffer sample was measured 5 times, and all spectra were merged. The final protein spectra were the result of merged protein sample minus merged buffer sample. For melting curve analysis, the protein solution was between 0.05 and 0.2 mg/ml and the wavelength was set from 260 to 190 nm. The temperature was set from 20 °C to 90 °C with 10°C jumps in between. Each temperature contained 3 measurements.

### **Dynamic Light Scattering**

Dynamic Light Scattering (DLS) is an effective and accessible method for measuring the hydrodynamic radius and related parameters of macromolecules and nanoparticles in solution, without the need for chromatographic separation. It is crucial for assessing protein size, purity, and the presence of aggregates in a range of samples up to 2500 nm. Importantly, it determines the dispersity of samples, essential for protein crystallization, as monodisperse samples are often required for forming high-quality crystals. This non-destructive technique, requiring minimal sample preparation, is highly valuable in biochemistry and nanotechnology research (Ross-Murphy, 1977).

The Boltzmann constant, often associated with Einstein in the context of Brownian motion, is a fundamental element in describing this phenomenon. It establishes a direct relationship between the temperature of a system and the kinetic energy of its particles. In the theory of Brownian motion, developed by Albert Einstein, it is postulated that the average kinetic energy of a particle is directly proportional to the absolute temperature of the system. Here, the Boltzmann constant serves as the proportionality factor. This principle is crucial in linking the macroscopic observables, like temperature, to microscopic particle behavior, thereby bridging thermodynamics and statistical mechanics.

The Stokes-Einstein equation is given by:

$$D = \frac{kBT}{6\pi\eta r} \text{ (Formula 4)}$$

Where:

- $D$  is the diffusion coefficient of the particle.
- $k_B$  is the Boltzmann constant ( $1.380649 \times 10^{-23} \frac{\text{J}}{\text{K}}$ ).
- $T$  is the absolute temperature of the fluid.
- $\eta$  is the viscosity of the fluid.
- $r$  is the hydrodynamic radius of the particle.

In DLS, the diffusion coefficient  $D$  is determined from the autocorrelation function of the fluctuating light scattering intensity, which is a result of the Brownian motion of particles. Once  $D$  is known, the Stokes-Einstein equation can be used to calculate the size of the particles (through the hydrodynamic radius  $r$ ), assuming the temperature  $T$  and viscosity  $\eta$  of the fluid are known. This is a fundamental principle in DLS for sizing particles, such as proteins or nanoparticles, in solution (Stetefeld et al., 2016).

In this study, the purification of SePBP3 and SaPBP2a was assessed by examining their solution dispersity, ensuring sample homogeneity for advanced analyses. Protein concentrations and buffer conditions were standardized to levels suitable for Small-Angle X-ray Scattering (SAXS), Isothermal Titration Calorimetry (ITC) or crystallization experiments.

## **Biophysical Methods**

### **Small-angle X-ray Scattering (SAXS)**

SAXS (Small-Angle X-ray Scattering) is a versatile technique employed in various fields such as material sciences, physics, and notably in structural biology. It provides insights into protein behavior, dynamics, and flexibility in solution. Compared to X-ray crystallography, SAXS has a lower resolution limit, typically around 10-20 Å. Protein analyses can be performed using SEC-SAXS (size exclusion chromatography small-angle X-ray scattering) or in-batch measurements. In this process, a monodisperse protein solution is irradiated with X-rays at a small angle. For our experiments, the Petra III U29 undulator served as the X-ray source, and the Eiger 4M detector was used for detection. Data was collected at the Beamline P12; DESY (Blanchet et al., 2015).

The resulting diffraction data are plotted as a function of the scattering vector, defined as:

$$q = \frac{2\pi}{\lambda} \sin(\theta) \text{ (Formula 5)}$$

- This formula defines the scattering vector  $q$ .
- $\lambda$  is the wavelength of the incident X-ray beam.
- $\theta$  is the scattering angle.

The scattering vector  $q$  is a fundamental parameter in SAXS, relating the angle at which X-rays are scattered to the scale of structural features being probed in the sample (D. I. Svergun and Koch, 2003).

One of the primary analyses in SAXS involves the Guinier equation, which is used to determine the radius of gyration ( $R_g$ ) and is given by:

$$I(q) = I(0) \times \exp - \frac{R_g^2 q^2}{3} \text{ (Formula 6)}$$

- This equation is used to calculate the radius of gyration ( $R_g$ ).
- $I(q)$  is the intensity of the X-rays scattered at the vector  $q$ .
- $I(0)$  is the forward scattering intensity, representing the intensity at zero angle.

The radius of gyration ( $R_g$ ) reflects the mass distribution of the particle around its center of mass. It provides an idea of the size of the scattering particle. This equation is applicable in the low- $q$  region of the scattering data, providing insights into the overall dimensions of the protein (D. I. Svergun and Koch, 2003).

Another crucial aspect of SAXS data analysis is the calculation of the pair distance distribution function,  $P(r)$ , which offers a real-space view of the protein's shape (D. I. Svergun and Koch, 2003). This function is determined by the indirect Fourier transform of the scattering data:

$$P(r) = \frac{1}{2\pi^2} \int q^2 I(q) \sin(qr) dq \text{ (Formula 7)}$$

- **P(r):** This is the Pair Distance Distribution Function, giving a real-space profile of the particle's structure. It indicates how often each internal distance ( $r$ ) occurs within the particle.
- **q:** The scattering vector, related to the X-ray scattering angle, gives information about the spatial properties of the particle.
- **I(q):** The intensity of X-rays scattered at the scattering vector  $q$ , measured in the experiment.
- **r:** A distance within the particle.  $P(r)$  maps the frequency of these distances.
- **Integral ( $\int \dots dq$ ):** A mathematical summing up over all  $q$  values, converting SAXS data from  $q$ -space to real-space, which provides an intuitive view of the particle's internal structure.

For this study, the protein was expressed and purified as described previously and subsequently dialyzed overnight in 20 mM Tris-HCl, 100 mM NaCl, 3% glycerol, pH 8.0. SAXS measurements were performed at 293.15 K using the in-batch measurement method, starting with a serial dilution from 5 mg/ml down to 1 mg/ml. The dialyzation buffer was used to dilute the protein solution. Data were processed and illustrated using BioXTAS RAW, ScÅtter and ATSAS GNOM (D. Svergun, 1992; Schneidman-Duhovny et al., 2013; Hopkins et al., 2017).

### **Application of the Porod-Debye Law in Small-Angle Scattering Techniques**

The Porod-Debye law is a fundamental concept in the analysis of small-angle X-ray scattering (SAXS) data, especially when investigating the structural properties of proteins. In essence, this law relates the intensity of scattered X-rays to the scattering vector ( $q$ ) for homogeneous particles. According to the Porod-Debye law, at high scattering angles, the intensity of scattered X-rays ( $I(q)$ ) should decrease proportionally to the fourth power of the scattering vector ( $q^{-4}$ ). This relationship is indicative of a smooth surface of the scattering particles. In the context of proteins, this law becomes particularly relevant when assessing protein flexibility. Proteins, being dynamic structures, often exhibit varying degrees of flexibility and disorder. The Porod-Debye law

serves as a benchmark in SAXS analyses; deviations from the  $q^{-4}$  trend can indicate the presence of structural heterogeneity or flexibility within the protein. For instance, a protein with a rigid, well-defined structure would adhere more closely to the Porod-Debye behavior, while deviations might suggest regions of disorder or significant flexibility (Rambo and Tainer, 2011).

### Biological Macromolecular X-ray Crystallography

X-ray crystallography remains a predominant method in structural biology, contributing significantly to the Protein Data Bank (PDB). It accounts for over 180,000 structures, representing the majority of entries in the PDB. Over the past five years, it has added approximately 10,000 entries annually on average. This exceeds the combined number of entries generated by 3D electron microscopy (about 3,000 entries) and NMR spectroscopy (around 300 entries) during the same period. This underscores the ongoing importance and efficacy of X-ray crystallography in the exploration and elucidation of protein structures. The fundamental principle of X-ray crystallography is anchored in the Bragg's Law of X-ray diffraction (Figure 19), a phenomenon observed when X-ray beams interact with the periodic lattice of a crystalline sample. As X-rays strike the crystal, they are scattered by the electrons within the atoms (W. H. Bragg and Bragg, 1913).

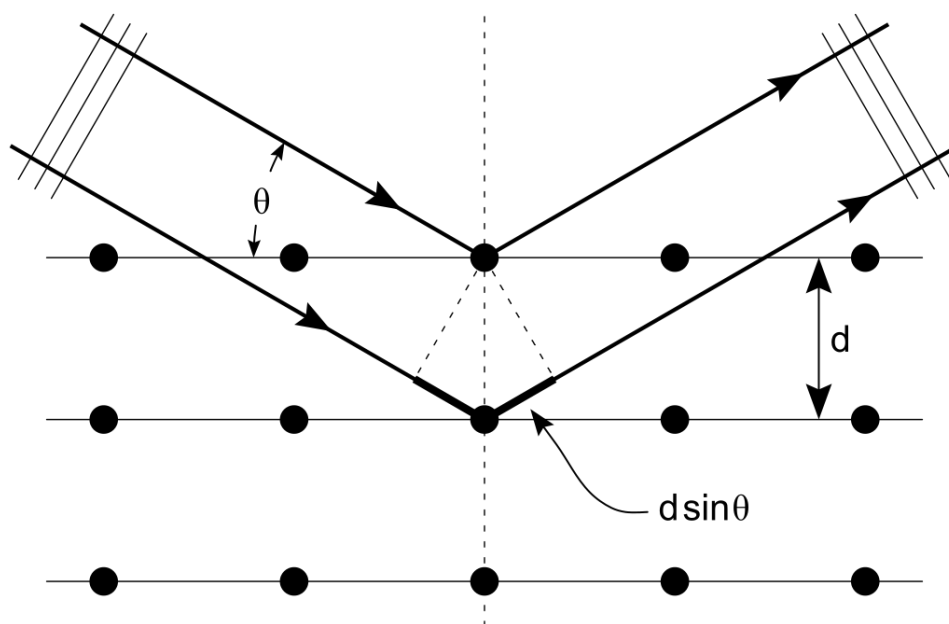


Figure 19: A schematic Figure of the Principle of a Bragg Diffraction. Figure by Hadmack/ CC BY.

These scattered waves interfere constructively or destructively, leading to a diffraction pattern only when they meet Bragg's condition, expressed as (W. H. Bragg and Bragg, 1913):

$$n\lambda = 2d \sin \theta \text{ (Formula 8)}$$

Where:

- $n$  is an integer (the order of the reflection)
- $\lambda$  is the wavelength of the incident X-ray beam
- $d$  is the distance between crystal planes
- $\theta$  is the angle of incidence

From the diffraction pattern, the electron density can be determined using the Fourier transform, which translates the diffraction data into electron density maps (Aubert and Lecomte, 2007). The relationship is governed by the formula:

$$\rho(\mathbf{r}) = \frac{1}{V} \sum_{\mathbf{h}} F(\mathbf{h}) e^{-2\pi i \mathbf{h} \cdot \mathbf{r}} \text{ (Formula 9)}$$

Where:

- $\rho(\mathbf{r})$  is the electron density at position  $\mathbf{r}$
- $V$  is the volume of the unit cell
- $F(\mathbf{h})$  is the structure factor
- $\mathbf{h}$  represents the Miller indices of the crystal plane
- $e^{-2\pi i \mathbf{h} \cdot \mathbf{r}}$  is the phase factor and contains the phase information

The formula for the structure factor,  $F(\mathbf{h})$ , in X-ray crystallography is essential for converting the observed diffraction pattern into an electron density map of the crystal. The structure factor is a complex number whose magnitude reflects the amplitude of the diffracted wave and whose phase relates to the position of the atoms within the crystal lattice (L. Bragg, 1968). The formula is given as:

$$F(hkl) = \sum_j f_j e^{2\pi i (hx_j + ky_j + lz_j)} \text{ (Formula 10)}$$

Where:



- $F(hkl)$  is the structure factor for the Miller indices  $h$ ,  $k$ , and  $l$
- The summation  $\sum_j$  is over all atoms  $j$  in the unit cell
- $f_j$  is the atomic form factor for the  $j^{\text{th}}$  atom, representing the scattering power of the atom
- $h, k, l$  are the Miller indices corresponding to the planes contributing to the diffraction
- $x_j, y_j, z_j$  are the fractional coordinates of the  $j^{\text{th}}$  atom within the unit cell

This formula is fundamental in the process of determining the atomic structure from X-ray crystallography data, as it mathematically relates the observed diffraction pattern to the arrangement of atoms within the crystal. By analyzing these electron density maps, the positions of the atoms within the crystal can be deduced, allowing for the elucidation of the molecular structure (L. Bragg, 1968).

### Phase Diagram

Protein crystallization, a pivotal yet challenging process in structural biology, is frequently facilitated through the vapor diffusion method. This technique entails the formation of a droplet by amalgamating a protein solution with a precipitating agent, subsequently positioned adjacent to or atop a precipitant-filled reservoir (Benvenuti and Mangani, 2007). Owing to the disparity in precipitant concentrations between the droplet and the reservoir, an osmotic gradient is established, prompting water molecules to migrate from the droplet into the reservoir. This osmotic shift results in an incremental elevation of protein and precipitant concentrations within the droplet (Figure 20). In this evolving microenvironment, the system traverses through a saturation threshold, setting the stage for potential crystallization. However, the initiation of crystallization is contingent upon surpassing an activation energy barrier. This critical juncture is not attained in the metastable zone but is realized in the labile zone, also termed the nucleation zone. It is within this domain that spontaneous nucleation of diminutive crystal nuclei occurs. After nucleation, the crystal formation

engenders a reduction in protein concentration in the droplet, thereby reverting it to a metastable state where additional crystal growth is feasible. Conversely, excessive supersaturation within the droplet may lead to the undesirable precipitation of the protein (Asherie, 2004).

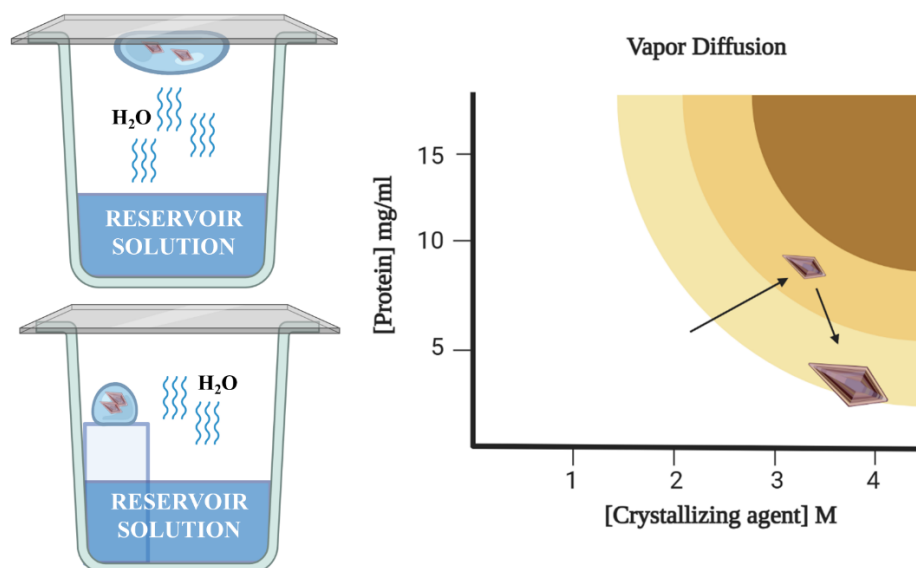


**Figure 20: A schematic Figure of the Principle of a Hanging Drop and Sitting Drop as Examples of Vapour Diffusion Crystallization Approach and of the Phase Diagram.** Created with BioRender.com.

### Crystallization Condition of *SePBP3*

For crystallization experiments a monodisperse solution of *SePBP3* at a concentration of 20 mg/ml was prepared; Dynamic light scattering was applied prior to crystallization experiments to analyze the dispersity in solution. X-ray suitable crystals were obtained by the hanging drop vapor diffusion technique at 20 °C. 1 µl of the protein solution was mixed with an equal volume of crystallization agent solution composed of 2.2 M AmSO<sub>4</sub> at pH value of 8. This combination was set against a 1 ml reservoir liquor with identical composition. Crystals were observed within 3 days. Prior to data collection, these crystals were cryo-protected using a solution of 2.2 M AmSO<sub>4</sub>, 12% glycerol, and pH value of 8. For co-crystallization experiments, the aforementioned protocol was followed with a slight modification: 0.1 µl of an inhibitor solution (100 mM concentration, solubilized in 5% DMSO) was added to the drop containing the protein solution.

### **Crystallization Condition of SePBP2a**

For the crystallization experiments, a monodisperse solution of SaPBP2a at a concentration of 20 mg/ml was prepared; dynamic light scattering was used prior to the crystallization experiments to analyze the dispersity in solution. X-ray suitable crystals were obtained using the hanging drop vapor diffusion method at 20 °C. 1 µl of the protein solution was mixed with an equal volume of a crystallization agent solution. This solution consisted of 10%, 20%, or 30% (v/v) PEG 550 MME, 0.8 mM, 0.9 mM, or 1 mM NaCl, 0.1 M HEPES at pH 6, 7, or 8, and 16 mM CdCl<sub>2</sub>. This combination was set against a 1 ml reservoir with an identical composition. Crystals were observed within 2 days. Prior to data collection, these crystals were cryo-protected using a solution of the respective PEG 550 MME concentration, the corresponding NaCl concentration, 12% glycerol, and the respective pH value.

### **Diffraction Data Collection and Structure Determination of SePBP3 and SePBP2a**

X-ray diffraction data were collected applying synchrotron radiation collected at 100 K at the beam line P13 (PETRA III, DESY) (Cianci et al., 2017) and P11 (PETRA III, DESY) (Meents et al., 2013). The data were subsequently processed with the XDS program package (Kabsch, 2010). The phase problem was solved by molecular replacement, using SaPBP3 from *Staphylococcus aureus* (PDBID: 3VSK) for SePBP3 and SaPBP2a from *Staphylococcus aureus* (PDBID: 1VQQ) for SePBP2a and using the Phaser-MR's one-component interface program embedded within the Phenix software suite (version 1.19.2-4158) (McCoy et al., 2007; Liebschner et al., 2019). The structure refinement was performed with the Phenix.refine tool (Afonine et al., 2012), while the structure modelling was performed with WinCoot 0.9.8.7.1 (Emsley et al., 2010).

## **Bioinformatical Methods**

### **Molecular Docking**

Molecular docking is a computational technique in structural biology, critically employed to predict the optimal orientation of molecules binding together to form stable complexes. Its significance is particularly pronounced in drug discovery, where it is used to ascertain the binding affinity and orientation of small molecule ligands towards

protein or nucleic acid targets. This process is fundamental in identifying potential therapeutic agents and understanding their interaction mechanisms at a molecular level. The essence of molecular docking lies in simulating the molecular recognition process, involving two primary entities: the target (commonly a protein or nucleic acid) and the ligand (typically a drug or a small bioactive molecule). Docking algorithms are tasked with predicting the ligand's most favorable binding mode to the target, a process that involves assessing various ligand orientations and conformations (Madhavi Sastry et al., 2013). These algorithms rigorously evaluate factors such as the geometric and electrostatic properties of the target's docking site, the ligand's conformational dynamics, and the role of solvent molecules. Central to molecular docking studies is the concept of the docking score. This score is a quantified representation, derived from scoring functions, designed to approximate the strength and stability of the ligand-target interaction (Friesner et al., 2006). These functions integrate various interaction energies, including van der Waals forces, hydrogen bonds, electrostatic interactions, and solvation parameters. Formally, the docking score (*DS*) can be represented as:

$$DS = f(VDW, HB, EI, DSolv) \text{ (Formula 11)}$$

Where:

- ***VDW*** represents van der Waals forces
- ***HB*** stands for hydrogen bonding interactions
- ***EI*** represents electrostatic interactions
- ***DSolv*** stands for desolvation effects.

In drug discovery, the docking score is pivotal; it not only predicts the binding affinity but also guides the ranking of various ligands in terms of their potential efficacy. A lower docking score is indicative of a higher binding affinity, implying a more stable and potentially effective ligand-target complex. This aspect of molecular docking is invaluable during the initial phases of drug design, allowing researchers to screen and prioritize compounds for further development (Friesner et al., 2006).

A key initial step in the molecular docking process is the preparation of the protein (target) (Madhavi Sastry et al., 2013). This involves refining the protein structure, which may include removing crystal water molecules, adding missing atoms or residues, and optimizing the structure for docking. Subsequently, a 'grid' around the active site of the protein is defined. This grid represents the area where the docking algorithm will search for potential ligand binding sites, accounting for the spatial and electronic properties essential for ligand-protein interactions. Concurrently, the ligands undergo a preparation process. This includes optimizing their structure, defining torsional degrees of freedom, and computing possible conformations. This preparation ensures that the ligands are in a suitable form for the docking simulations, allowing for a realistic and effective exploration of binding modes (Madhavi Sastry et al., 2013). For this study, the crystal structure of *Sa*PBP2a was used as targets and the natural compounds of the Karatschi library were used as ligands.

### **Molecular Dynamics Simulation**

Molecular Dynamics (MD) simulation is a powerful computational technique used to study the behavior of biomolecules in a simulated environment over time. It allows for the observation of atomic-level interactions and dynamics under various conditions, providing insights into the structural, thermodynamic, and kinetic properties of biological systems. The crystallographic structure of *Se*PBP3 and *Sa*PBP2a (PDBID:1VQQ) served as the starting point for our molecular dynamic simulation studies. The simulation process can be divided into several key steps: The protein structures underwent extensive preparation using the protein preparation workflow in Schrodinger's Maestro suite (Sastry et al., 2013). Initially, missing hydrogen atoms were added systematically to achieve chemical completeness. The hydrogen-bonding network was then refined using PROPKA, optimizing hydrogen bond assignments based on predicted pKa values and the protein's local environment (Bochevarov et al., 2016). A restrained minimization step followed, employing the OPLS4 force field to stabilize the structure, with crystallographic waters being removed (C. Lu et al., 2021). For the MD simulation, we used a solvated system using the TIP4P water model (Abascal and Vega, 2005). This step involved enclosing the protein in an orthorhombic periodic boundary

box, ensuring a minimum distance of 20 Å between the protein and the box edges to prevent direct interaction with its periodic images. Additionally, to emulate physiological conditions, a 150 mM NaCl salt concentration and a pH value of 7.4 were introduced, replicating the ionic environment typically found in biological systems. The simulations were conducted using the NPT ensemble, which maintains constant particle number (N), pressure (P at 1.01325 bar), and temperature (T at 310.15 K). This ensemble choice is critical as it reflects the physiological conditions under which most biological processes occur. The OPLS4 force field was employed, providing a sophisticated and accurate representation of molecular interactions and energetics. The MD simulations were executed over a 100 ns trajectory for *Se*PBP3 and 20 ns for *Sa*PBP2a (included bound ligands), with configurations saved every 20 ps (Bowers et al., 2006).

## Results and Discussion

This section is structured into two distinct parts.

### **Part One: Penicillin-binding Protein 3 from *Staphylococcus epidermidis***

The first segment delves into SePBP3. It encompasses a comprehensive discussion of the X-ray structural analysis of SePBP3, juxtaposed with its homologues. Additionally, the dynamics of the SePBP3 are scrutinized, with a particular focus on the rigidity observed in the transpeptidase domain. In contrast, the pedestal domains exhibit notable flexibility, a point that is explored in depth to understand its implications in the protein's overall function.

### **Part Two: PBP2a from *Staphylococcus epidermidis* and *aureus***

The second portion of this chapter shifts focus to PBP2a, from *Staphylococcus epidermidis* and *Staphylococcus aureus*. Here, the problem of expression and purification of SaPBP2a is discussed with an alternative expression protocol and subsequent crystallization. Additionally, the allosteric center of PBP2a from *Staphylococcus aureus* is brought into the light. This discussion centers on how the binding of natural compounds at the allosteric center can have an impact on the dynamic of the active site.

## Part One: Penicillin-binding Protein 3 from *Staphylococcus epidermidis*

### Recombinant Expression and Purification

The expression of SePBP3 was conducted as detailed in the 'Methods' chapter. The expression protocol was optimized through preliminary test expressions of SePBP3 using various *Escherichia coli* strains, at temperatures of 20 °C and 30 °C, and over different expression durations. Figure 21 showcases the most favorable results, obtained using *Escherichia coli* BL21 DE3 cells. The expression of the protein was found to be consistently successful across various durations and temperatures, indicating the process's flexibility. Nevertheless, the established protocol for expression was defined as a 3-hour incubation at 30 °C, following induction at an optical density  $OD_{600} = 0.6$  and with 1 mM IPTG.

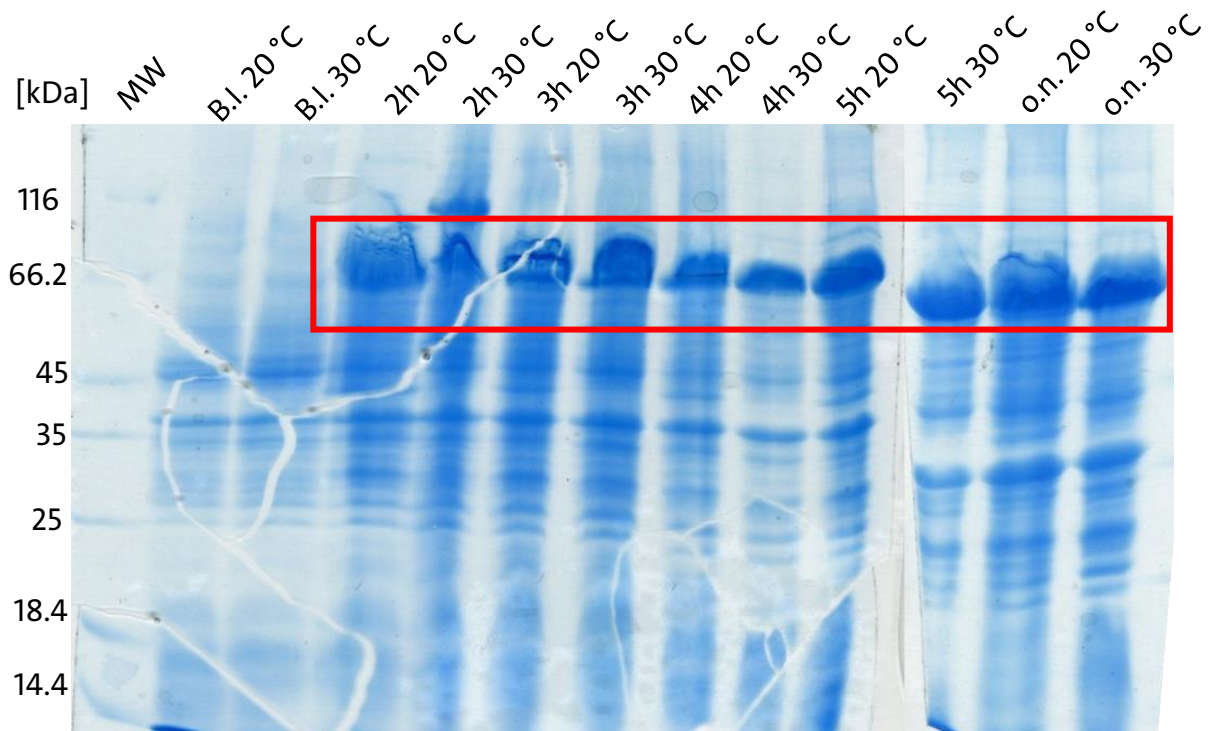


**Figure 21: SDS-PAGE Analysis of the Test Expression at 20 °C and 30 °C of SePBP3 in BL21 DE3 cells at a 12% Polyacrylamide Gel.** MW: Unstained Protein Molecular Weight; B.I.: before induction with 1mM IPTG; 2h: two hours of expression; 3h: three hours of expression; 4h: four hours of expression; 5h: five hours of expression; o.n.: overnight expression. Overexpressed SePBP3 is highlighted within red rectangle and fits approximately with the calculated size of 74.8 kDa.

Figure 22 presents the results of an SDS-PAGE analysis conducted post-purification of SePBP3. The absence of protein in the cell debris fraction post-sonication serves as an



initial indication of the protein's solubility. The primary purification step for *SePBP3* involved Ni-NTA affinity chromatography, which segregates unbound proteins in the flow-through fraction, nonspecifically bound proteins in the wash fraction, and the target protein in the elution fraction. As depicted in Figure 22, the majority of *SePBP3* was not present in the cell debris fraction, suggesting that the sonication protocol outlined in the 'Methods' chapter effectively disrupted the cells and released the protein into the lysis buffer. The presence of protein in the cell debris fraction could be attributed to incomplete cell disruption. The detection of protein in both the flow-through and wash fractions may indicate a saturation of the Ni-NTA matrix with *SePBP3*. The elution fraction prominently features a protein band at the expected molecular weight of 74.8 kDa.

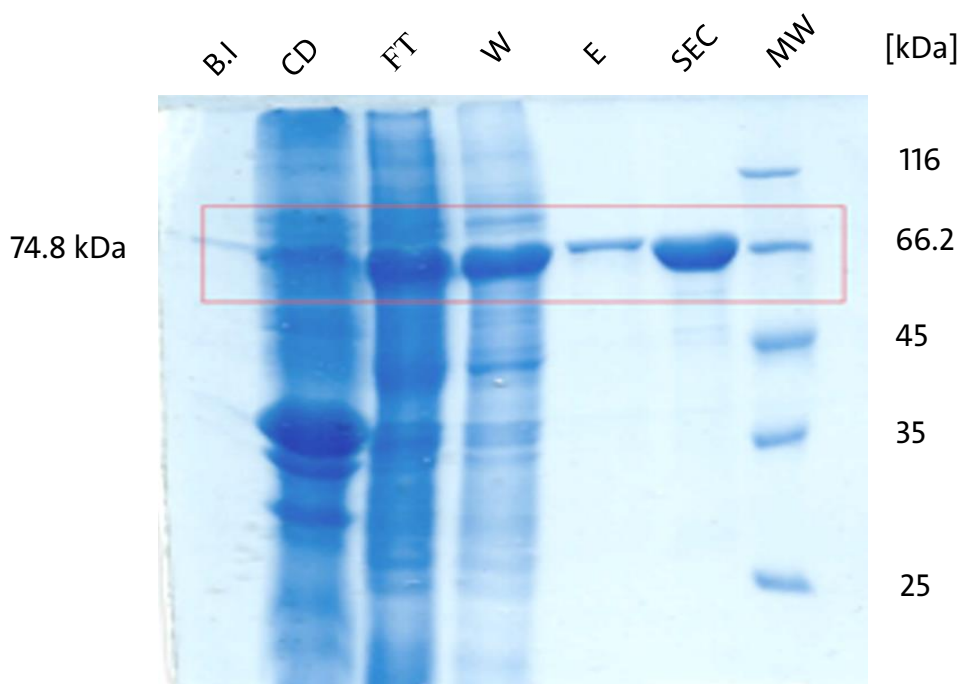


**Figure 22: SDS-PAGE Analysis of the Expression and Purification of *SePBP3* at a 12% Polyacrylamid Gel.** MW: unstained protein molecular weight; CD: cell debris after sonification and centrifugation; FT: flow-through of unbound protein; W: removal of unspecific bound protein with 20 mM imidazole; E: elution of *SePBP3* with 250 mM imidazole; SEC: size-exclusion chromatography. FT, W and E refers to Ni-NTA affinity chromatography purification. Overexpressed *SePBP3* is highlighted within red rectangle and fits approximately with the calculated size of 74.8 kDa.

The second stage of the purification process was implemented as a polishing step to diminish minor impurities. To achieve this, the protein sample was subjected to SEC, as depicted in Figure 23 (labeled 'SEC fraction'). Following the chromatography, only the fractions corresponding to the targeted protein peak, shown in figure 23, were collected.

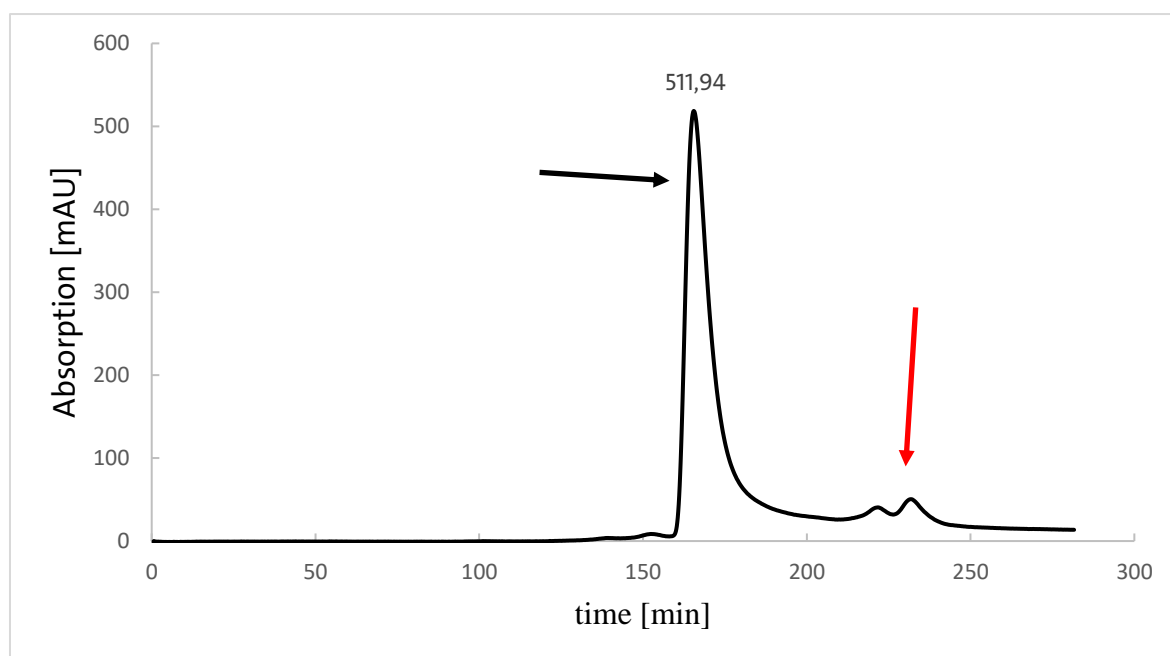


**Figure 23: Size Exclusion Chromatogram (SEC) of SePBP3 after Ni-NTA Affinity Chromatography Purification.** SEC was used after Ni-NTA affinity chromatography purification as a polishing step. SePBP3 SEC profile (black arrow) exhibits a distinct peak between 150 and 200 minutes (flow rate at 1 ml/min). Small impurities (red arrow) were not collected.

### Protein Characterization

DLS was conducted to observe the dispersity of the purified and concentrated SePBP3 protein solution. Figure 24 exhibits the hydrodynamic radius ( $5.17 \pm 0.6$  nm) of a monodisperse protein solution with a concentration of 18 mg/ml. The calculated molecular weight of the hydrodynamic radius with 143.2 kDa is a factor 2 higher than the calculated molecular weight of the protein sequence with 74.8 kDa. However, the formation of a SePBP3 dimer can be discounted. The improbability of a SePBP3 dimer is attributed to the calculated hydrodynamic radius, which includes additionally the water shell surrounding a protein. The calculation of the radius is being specifically optimized for spherical particles. This factor significantly reduces the likelihood of a SePBP3 dimer formation.

A dimerization of the homologue from *Staphylococcus aureus* could also be excluded (Yoshida et al., 2012). Therefore, the protein is defined as a monomer.

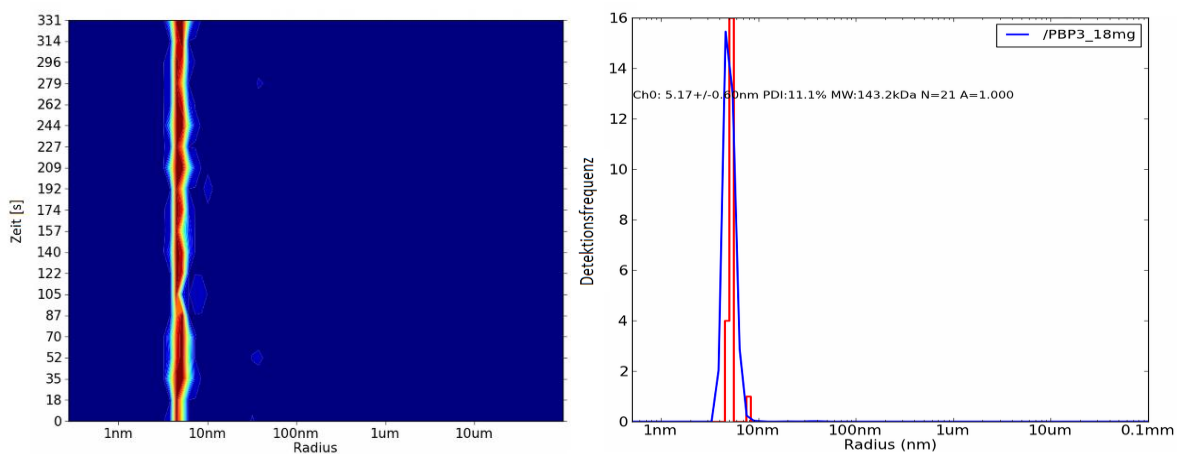


**Figure 24: Dynamic Light Scattering Dispersity Profile of SePBP3 after SEC Purification.** Monodispersity of purified protein solution (18 mg/ml) was confirmed by DLS measurements. Left: heat map of radius distribution. Right: hydrodynamic radii against frequency of detection confirmed a monomer in solution. Calculation of the molecular weight (143.2 kDa) is optimized for spherical particles and therefore not correlating with the actual molecular weight of the L-shaped PBP3 (74.8 kDa).

The secondary structure of the SePBP3 protein in a monodisperse solution was analyzed using CD spectroscopy in the wavelength range of 190 to 260 nm. The CD spectrum of SePBP3 was recorded 15 times, with all individual spectra being subsequently merged to enhance accuracy. To establish a baseline, the buffer solution was measured five times; these measurements were also merged to form a consolidated background signal. The final spectrum of the protein was obtained by subtracting this buffer spectrum from the merged SePBP3 spectrum. Figure 25 illustrates the relationship between millidegree and wavelength in the protein's spectrum. The presence of a high percentage of folded protein is indicated by the spectral features, revealing a composite of  $\alpha$ -helices,  $\beta$ -sheets, and disordered regions.

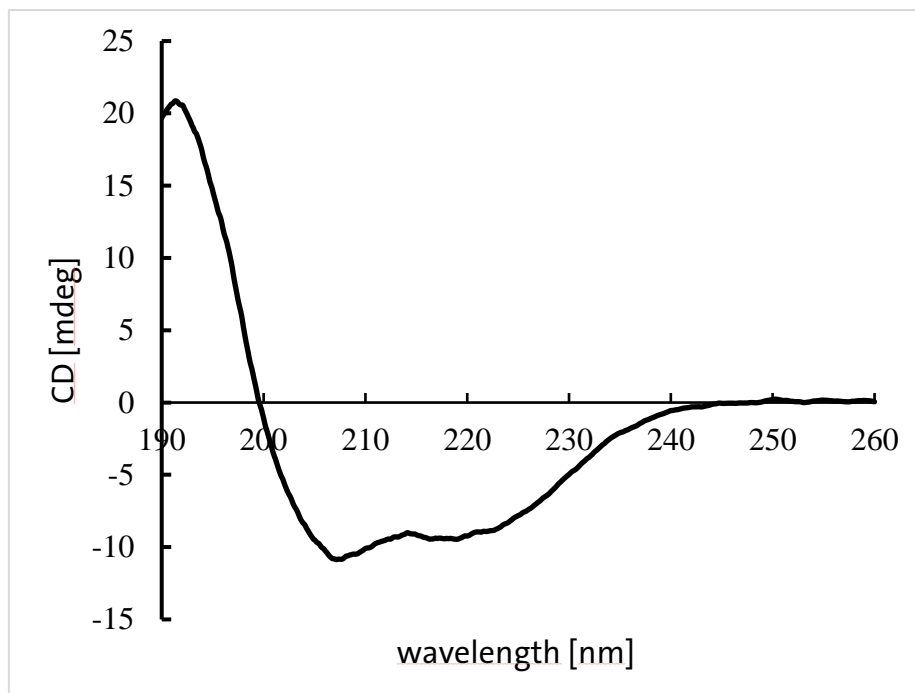


**Figure 25: Circular Dichroism Plot of SePBP3 after SEC Purification.** Secondary structure analysis of SePBP3 revealed  $\alpha$ -helices and  $\beta$ -sheets and confirmed a folded protein. Measurement was conducted with a protein concentration of 0.1 mg/ml.

The estimation of the secondary structure by Yang et al. indicates 41.8%  $\alpha$ -helices, 26.1%  $\beta$ -sheets and 32.1% random parts with an RMS value of 10.33 (Figure 26) (J. T. Yang et al., 1986).

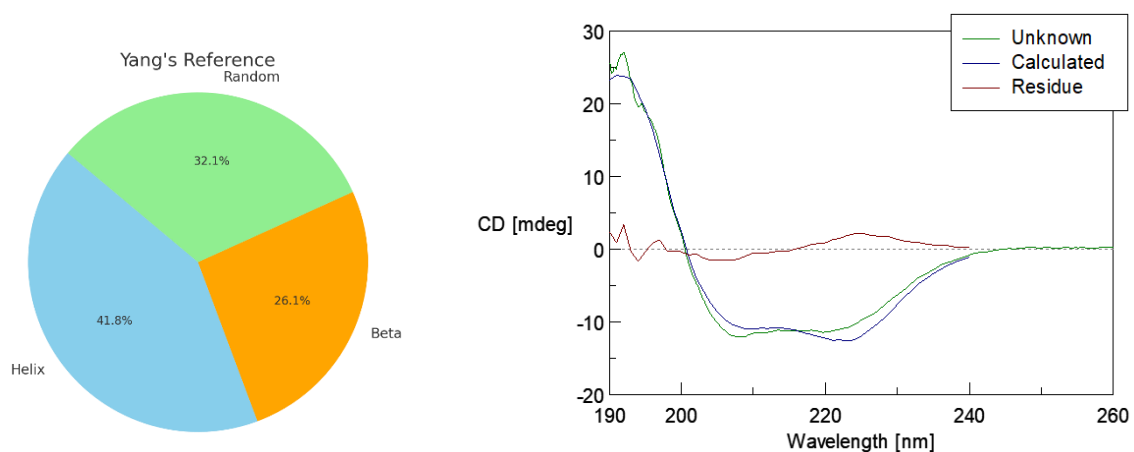


**Figure 26: Secondary Structure Estimation and Reference Plot according to Yang et al. (J. T. Yang et al., 1986).**

The estimation of the secondary structure by Reeds et al. indicates 69.5%  $\alpha$ -helices, 3.5%  $\beta$ -sheets and 11.4% turns with an RMS value of 5.2 (Figure 27) (Reed and Reed, 1997).

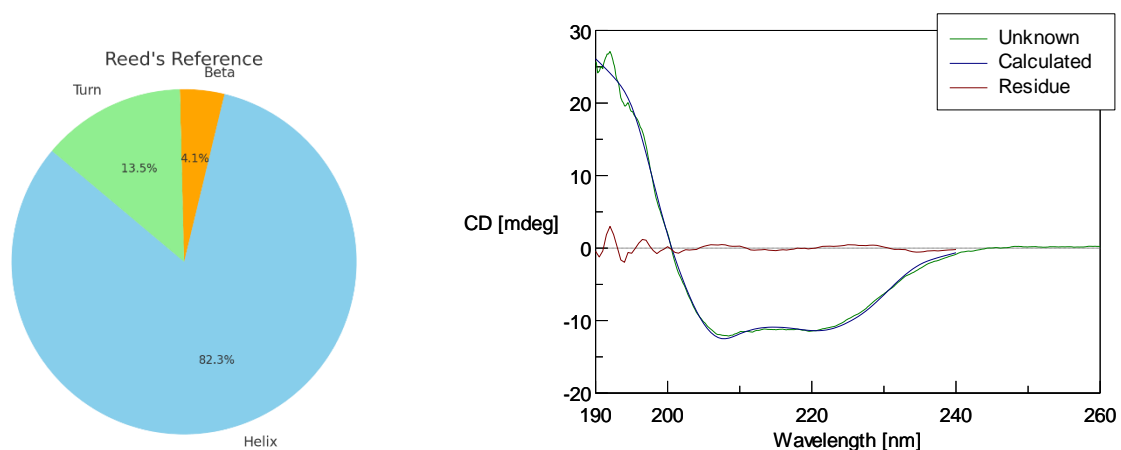


**Figure 27: Secondary Structure Estimation and Reference Plot according to Reed et al. (Reed and Reed, 1997).**

The current estimations do not accurately reflect the actual percentages of secondary structural elements, as there is a substantial deviation in Yang's prediction. Reed's prediction exhibits a lower deviation, yet a higher amplitude resolution would be advantageous for a more precise estimation. Consequently, CD measurements are primarily employed to confirm the folding of the purified protein, which was utilized in subsequent experiments.

The stability of the folding of the protein, eluted in the crystallization buffer (comprising 20 mM Tris-HCl, 100 mM NaCl, pH 8), was analyzed through the generation of melting curves using CD spectroscopy. A temperature rise above 30 °C a gradual decrease in the ellipticity at 230 nm and 190 nm was observed, indicating a loss of  $\alpha$ -helical content. This transition suggests the onset of protein denaturation. The melting temperature ( $T_m$ ), which was 40°C, where 50% of the protein is unfolded, was identified by analyzing the inflection point of the melting curve (Figure 28). This temperature provides a crucial insight into the thermal stability of the protein investigated. The protein stays stable within the range of 20 to 30 °C which is the temperature preferred for the crystallization, SAXS measurements and ITC measurements.

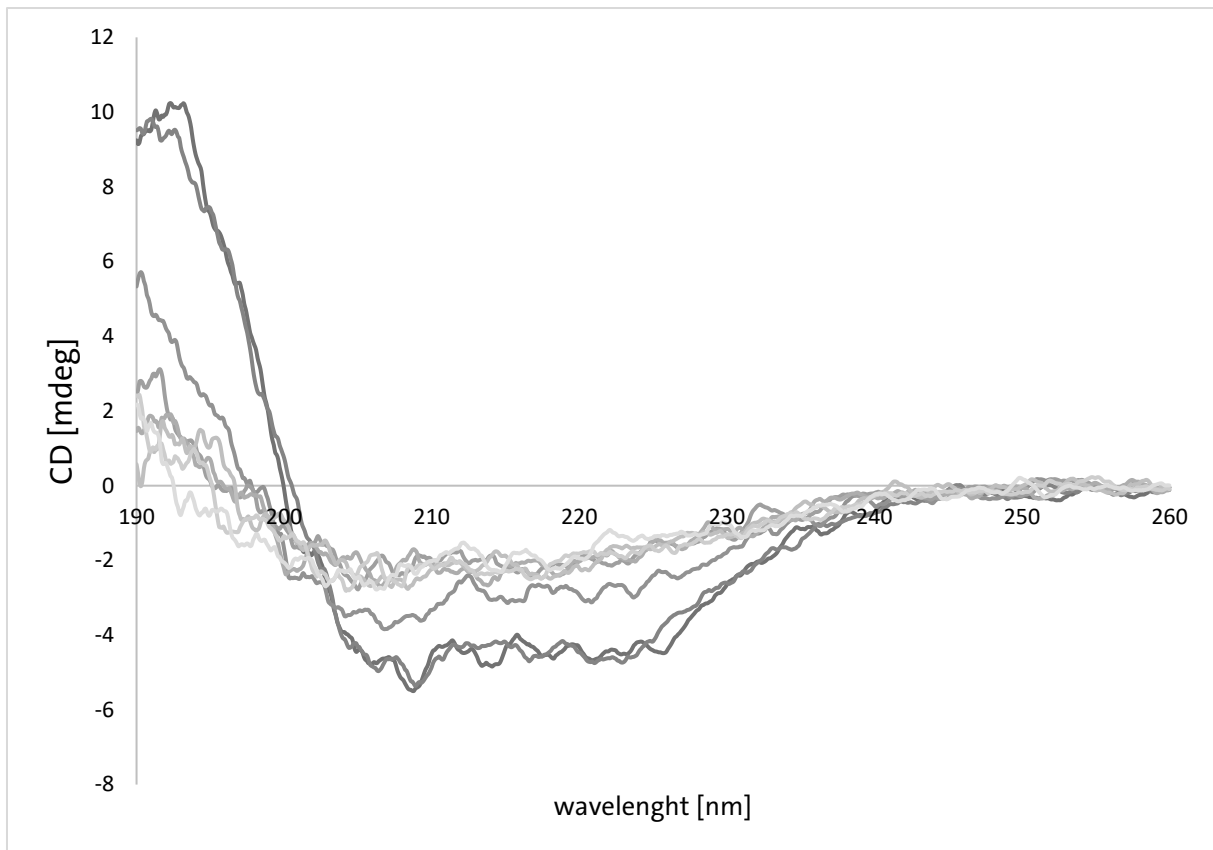


**Figure 28: Melting Curves of SePBP3 as measured via Circular Dichroism (CD) Spectroscopy.** The measurements were conducted in the same buffer that was utilized for the crystallization of SePBP3. Each measurement was performed over a temperature interval of 10°C, commencing at 20°C. In the graphical representation, darker curves correspond to lower temperatures, while lighter curves represent higher temperatures.

### Crystallization

Crystallization trials of the protein were conducted under various conditions. The initial screening was carried out using the 'Honeybee 961' crystallization robot. One of the prevalent methods for protein crystallization is the vapor diffusion method (Benvenuti and Mangani, 2007). This technique relies on the difference in crystallization agent concentration between the reservoir solution and the crystallization drop. Water molecules diffuse from the drop to the reservoir, resulting in a gradual increase in the concentration of both the protein solution and the crystallization agent. Upon reaching the labile zone, also known as the supersaturation zone, the energy barrier required for crystal nucleation is surmounted, leading to the formation of nucleation sites. Following this, a reduction in protein concentration occurs, transitioning the system back to the metastable zone where crystal growth takes place (Asherie, 2004).

For the screening, different predefined conditions were tested. The only crystallization condition which provided crystals was 2M ammonium sulfate ( $\text{AmSO}_4$ ).  $\text{AmSO}_4$  is a widely used crystallization agent in protein crystallography. It is favored for its ability to facilitate the production of large amounts of microcrystals, which are essential for serial crystallography experiments. Its role as a precipitant primarily involves modulating the solubility of the protein (Stohrer et al., 2021).

The effectiveness of  $\text{AmSO}_4$ , along with other agents like polyethylene glycol (PEG), has been acknowledged in the field, with these agents contributing to numerous successful crystallization efforts. However, it is essential to note that the process of finding the right crystallization agent can be challenging, as it's difficult to predict in advance which agent will yield the best results for crystal formation (McPherson and Gavira, 2014).

In addition to its role in producing microcrystals,  $\text{AmSO}_4$  is also utilized in advanced methods of protein crystallization. These methods aim to increase the success rate of crystallization projects by producing larger and higher-quality single crystals. It is the most widely used precipitant of the salt type, highlighting its significance in the field of structural biology (Moreno, 2017).

SePBP3 was observed to crystallize within two days at a concentration of 20 mg/ml, displaying a tetragonal-trapezoidal morphology. The sizes of the crystals varied significantly, ranging from 1.7 mm to a few micrometers. Consistent crystal dimensions could not be achieved across all wells; some exhibited microcrystals with approximate dimensions of 10  $\mu\text{m}$ , while others contained a single crystal within the millimeter size range. As previously mentioned, such variability is characteristic of proteins crystallizing under  $\text{AmSO}_4$  conditions. The crystallization was primarily conducted at a temperature of 20 °C; however, similar results in terms of morphology and size were also observed when crystals were grown at 4 °C over the same two-day period. Figure 29 represents crystals obtained at 20 °C and at 4 °C.

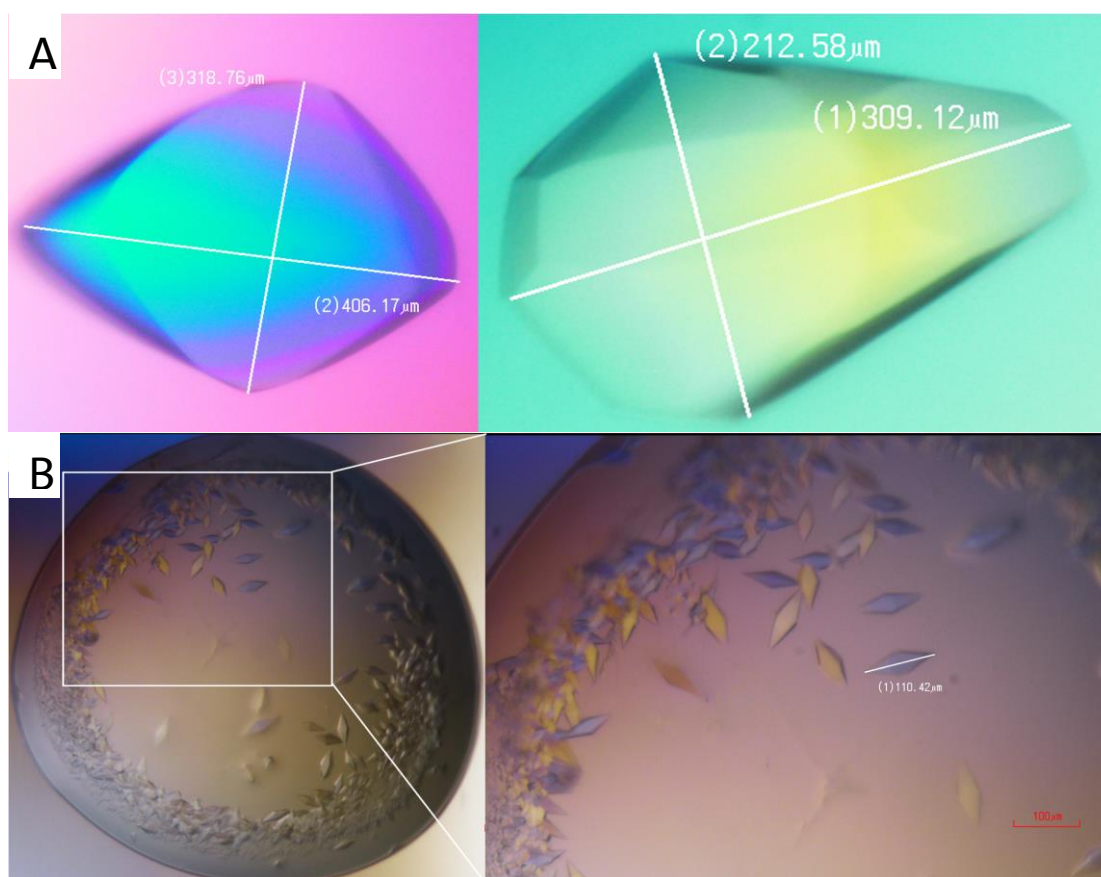


**Figure 29: Apo-Crystals in two different Morphologies.** A: The crystals are showing a tetragonal-trapezoidal morphology with a size of approximate 0.4 mm. The left side: crystals obtained at 4 °C. The right side: crystals obtained at 20 °C. B: Smaller crystals with a size of 0.1 mm exhibiting a tetragonal-pyramidal morphology. Tetragonal systems are known to have three axis of equal symmetry (x,y,z) and all angles at 90° ( $\alpha=\beta=\gamma$ ), two sides of equal length ( $a=b$ ) and one shorter or longer side (c).

In this study, part of the investigation focused on *SePBP3* as a potential drug target, which included conducting co-crystallization experiments. The initial approach to obtain a protein-ligand complex involved soaking, but this method was only effective for water-soluble ligands, which bound after one hour of soaking. However, most of the tested ligands were soluble only in DMSO, rendering them unsuitable for soaking experiments. Consequently, co-crystallization was employed. The ligand was dissolved in DMSO at a concentration of 100  $\mu\text{M}$ , and 1% of this solution was added to the crystal drop. This resulted in ligand precipitation, but crystals still formed within or adjacent to the precipitate. This approach altered the crystallization dynamics, extending the crystallization time to one month from the original two days. Additionally, a significant number of the resulting crystals displayed cracks. Despite these changes, the



morphology and size of the crystals remained consistent with previous observations. Figure 30 displays co-crystals obtained with vaborbactam and cefotaxime.

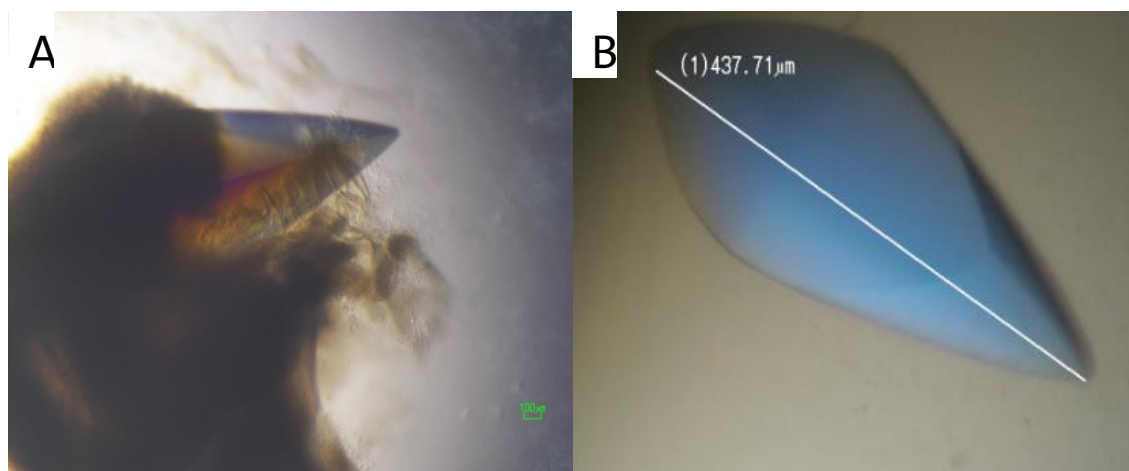


**Figure 30: Co-Crystals with Vaborbactam and Cefotaxime.** A: Vaborbactam is low soluble in water and therefore precipitated inside the crystal drop. SePBP3 crystal grew inside the precipitated vaborbactam and obtained ligand molecules over time (1 month). B: Cefotaxime co-crystal exhibit a tetragonal-trapezoidal morphology. Growth time and size did not distinguish compared to apo-crystals.

As SePBP3 also crystallized in the form of microcrystals using vapor diffusion methods, an in-batch crystallization approach was adopted. For the in-batch crystallization process diffusion is not a factor. Therefore, it's crucial to select crystallization conditions that ensure the initial crystallization mixture is already situated within the labile zone. This strategic positioning at the outset is vital for the success of the crystallization. (Wey and Karpinski, 2002). This was aimed at achieving microcrystals with homogeneous dimensions, which is crucial for performing serial crystallography. To facilitate this, macrocrystals were crushed to generate a seed stock of varying concentrations. After several refinement steps, the seed stock comprised a solution with nanometer-sized crystals. Introducing this seed into the protein solution and crystallization agent bypasses the nucleation phase. This process enables the growth of numerous nanocrystals into microcrystals, ensuring an even distribution of proteins among the crystals (Bergfors, 2003). Serial X-ray diffraction experiments were initially attempted, but the accumulation of  $\text{AmSO}_4$  led to clogging of the instrument's nozzle, rendering data collection unfeasible. As a result, this study is exclusively focused on conventional X-ray diffraction techniques.

### **Data Collection of the Macromolecular Crystals**

Radiolytic degradation poses a significant impediment to the acquisition of X-ray crystallographic data, with free radicals acting as agents of secondary damage within the protein crystal matrix (Teng and Moffat, 2000). Such molecular lesions include the cleavage of disulfide bonds, the decarboxylation of glutamic and aspartic acid residues, and the depletion of hydroxyl groups from tyrosine side chains. These alterations can modulate unit cell dimensions, increase of B-factor values and decrease diffraction efficacy, culminating in the reduction of high-resolution structural information. Mitigatory strategies for the abatement of radiolytic damage have been implemented, wherein macromolecular crystals are harvested by a capton loop (Figure 31), immersed in a cryoprotectant solution, and subsequently vitrified in liquid nitrogen. This cryoprotectant medium replace the solvent within the crystal lattice, averting its crystallization upon freezing, which might otherwise compromise the integrity of the crystal or engender supplementary diffraction phenomena. Such spurious diffraction can occlude the intrinsic diffraction pattern of the crystal, thereby rendering segments of the data intractable. Data acquisition was performed at the beamlines P13 at PETRA III, DESY (Cianci et al., 2017). During this process, the crystal underwent systematic rotation to facilitate the recording of diffraction data across all angular orientations, at 100 K. Figure 32 illustrates that the resolution remained relatively constant throughout the rotation of the crystal. However, the quantity of diffractive spots and the intensity of these spots fluctuated in accordance with the crystal's volume. Notably, one facet of the crystal exhibits a pronounced flatness, which resulted in a discernible decrement in intensity at each 180° interval of rotation. The raw data were processed applying the software XDS algorithm (Kabsch, 2010), followed by precision refinement of the coordinates utilizing the PhenixRefine program (P. D. Adams et al., 2010) within the Phenix computational suite (Liebschner et al., 2019).

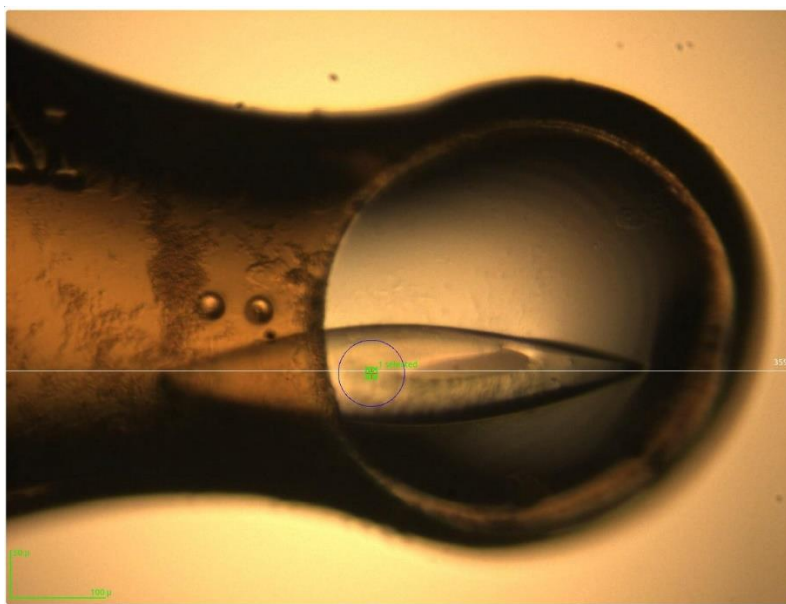


**Figure 31: One SePBP3 Crystal inside a Micro-loop.**

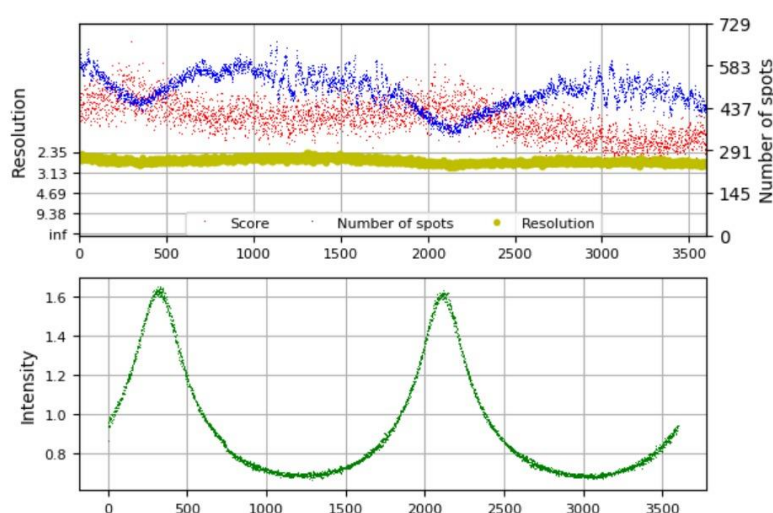


**Figure 32: Resolution, Number of Spots and Intensity of the Crystal during the Measurement.**

### **Assessment of Data Quality in X-ray Crystallography**

The assessment of crystallographic data quality is a critical step in the validation of structural models obtained by X-ray crystallography. The analysis focused on three datasets: *SePBP3*, *SePBP3* complexed with Cefotaxime and *SePBP3* complexed with Vaborbactam. For the *SePBP3* dataset, the data completeness of 99.7% was exceptional, with a Wilson B-factor of 56.24 Å<sup>2</sup> indicating a favorable crystal environment. The resolution ranged from 80.69 to 2.5 Å, with a significant amount of data ( $I/\sigma I = 3.1$ ) in the high-resolution shell, demonstrating a strong signal in comparison to the noise level. The redundancy-independent R-factor ( $R_{meas}$ ) was remarkably low at 0.014, and the

correlation coefficient ( $CC_{1/2}$ ) of 0.999 indicated excellent agreement between symmetry-related intensities. The *SePBP3*-Cefotaxime complex showed a slightly increased Wilson B-factor of 90.32 Å<sup>2</sup>, which could be indicative of increased molecular motion within the crystal lattice. Nevertheless, the completeness of the data remained high at 99.9%, with an  $R_{\text{meas}}$  of 0.026, suggesting a slightly higher level of data inconsistency which could be associated with the binding of the ligand. The resolution for this dataset was notably higher, spanning from 49.24 to 2.51 Å. The dataset for *SePBP3* complexed with Vaborbactam displayed the lowest Wilson B-factor of 36.29 Å<sup>2</sup>, suggesting the best crystal packing among the three datasets. Completeness was high at 98.1%, albeit slightly lower than the other datasets, but still indicative of a comprehensive data collection. The resolution was like that of the *SePBP3* dataset, and the  $I/\sigma$  value was the highest at 4.8, reflecting a very high-quality dataset with clear signal distinction from noise. Across all datasets, the high  $CC_{1/2}$  values confirmed the internal consistency of the data. Collectively, these metrics attest to the good to high quality of the crystallographic data, which is foundational for accurate structural interpretation (Kleywegt, 2000; Wlodawer et al., 2008; Chen et al., 2010; Gore et al., 2012; Paul D. Adams et al., 2016; Wlodawer, 2017).

**Table 22: Data Collection and Refinement of *SePBP3*, *SePBP3*– Cefotaxime and *SePBP3*-Vaborbactam.**

Data Collection	<i>SePBP3</i>	<i>SePBP3</i> - Cefotaxime	<i>SePBP3</i> - Vaborbactam
X-ray source	P13, Petra III, DESY	P13, Petra III, DESY	P13, Petra III, DESY
Detector	EIGER 16M	EIGER 16M	EIGER 16M
Space group	P4 <sub>1</sub> 2 <sub>1</sub> 2	P4 <sub>1</sub> 2 <sub>1</sub> 2	P4 <sub>1</sub> 2 <sub>1</sub> 2
Cell dimensions a=b, c (Å)	83.67, 305.16	83.21, 305.28	83.15, 306.14
Wavelength (Å)	0.97625	1.033	0.82655
Resolution (Å)	80.69- 2.5 (5.88- 2.5)	49.24 – 2.51 (2.512- 2.51)	80.24 – 2.3 (2.37- 2.3)

Total reflections	71280 (7833)	70884 (7997)	89288 (8349)
Total unique reflections	46353 (2318)	38258 (11304)	48019 (3160)
Wilson B-factor ( $\text{\AA}^2$ )	56.24	90.32	36.29
Rmeas	0.014 (0.464)	0.026 (0.227)	0.030 (0.283)
CC1/2	0.999 (0.996)	0.999 (0.956)	0.9642 (0.872)
I/ $\sigma$ I	16.8 (3.1)	20.5 (3.0)	25.2 (4.8)
Completeness	99.7 (95.2)	0.999 (0.950)	98.1 (99.3)
<b>Refinement</b>			
Reflection used	35596	36231	63242
Rwork	0.22	0.23	0.20
Rfree	0.26	0.25	0.23
<b>No. atoms</b>			
Protein	4870	4944	4870
Ligand/ion	-	26	20
Water	60	5	338
<b>Average B-factor (<math>\text{\AA}^2</math>)</b>			
Protein	71.73	110.21	50.9
Ligand/ion	-	81.05	35.97
Water	66.32	119.58	46.34
<b>R.m.s. deviations</b>			
Bond lengths ( $\text{\AA}$ )	0.0082	0.018	0.0079
Bond angles ( $^\circ$ )	1.04	1.641	0.995
<b>Ramachandran</b>			
favored (%)	93.02	84.34	94.29
allowed (%)	5.55	12.34	3.62
outliers (%)	1.43	3.32	2.09
PDBID	8C5B	8C5W	8C5O

### Assessment of the Crystal Parameters

The crystal, characterized by the space group  $P4_12_12$  with a fourfold axis. The probability assessment for the number of molecules per asymmetric unit (Nmol) yielded a high likelihood for a monomeric presence (Nmol=1) with a probability of 0.84, indicating one molecule within the asymmetric unit. (Figure 33). The metric parameters of the unit cell with axis lengths of  $a = b = 83.67 \text{ \AA}$  and  $c = 305.16 \text{ \AA}$  refer to a crystalline lattice that accommodates a total of approximately eight of these protein molecules (Figures 33 - 35).

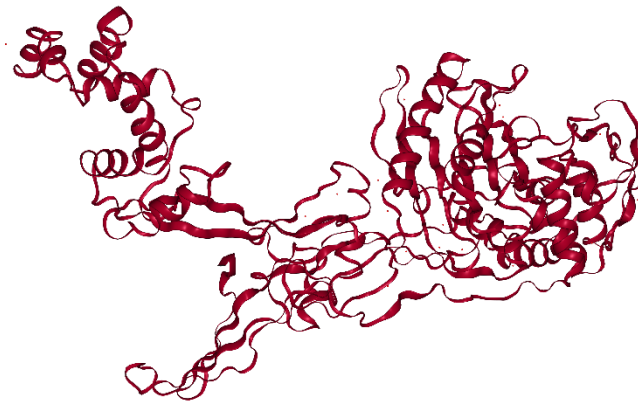


Figure 33: One Protein is in one Asymmetric Unit.

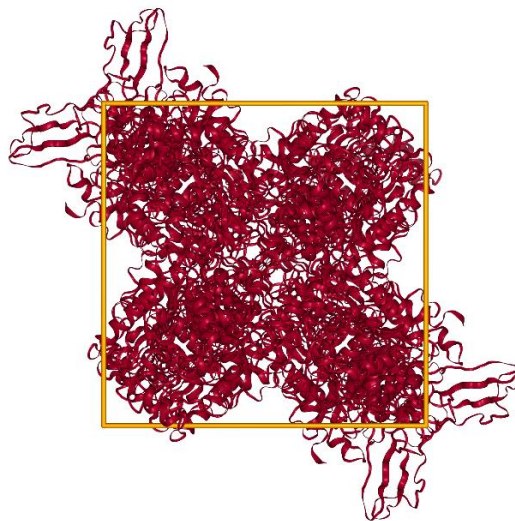
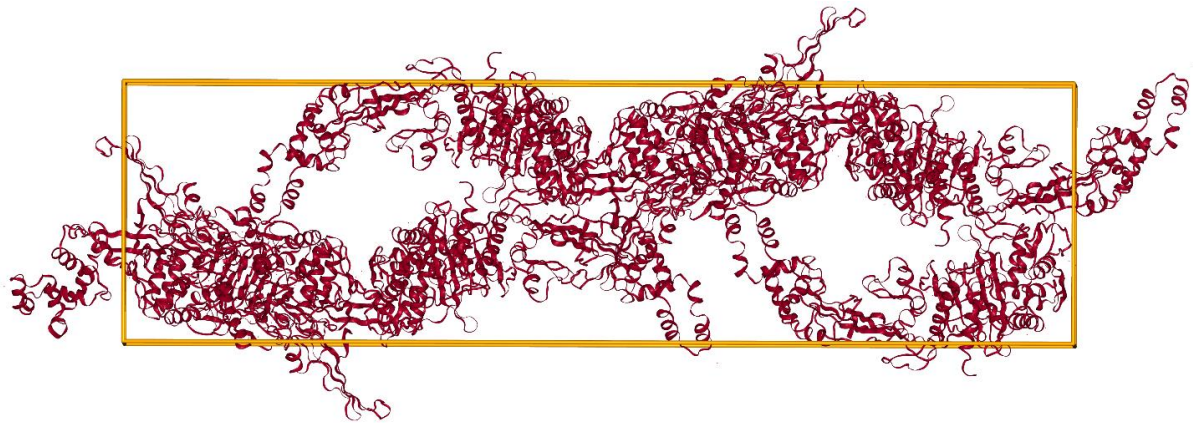
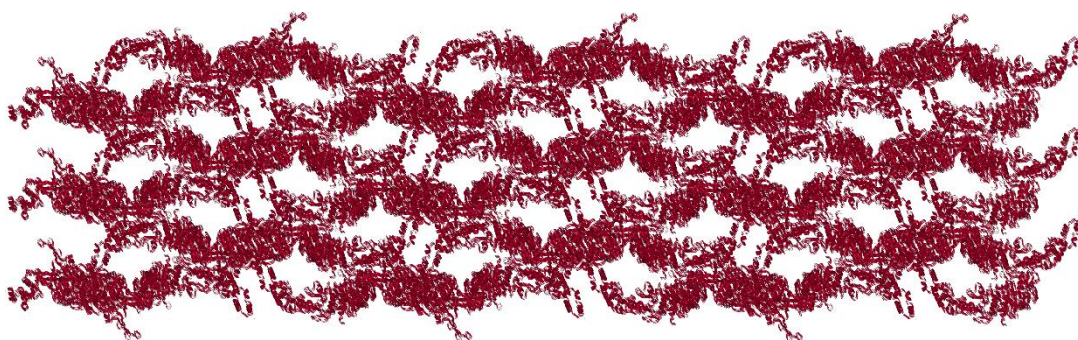


Figure 34: The Symmetry  $P4_12_12$  has a fourfold Symmetry Axis.



**Figure 35: Approximate eight Proteins are fitting inside one Unit Cell.**

In the structural elucidation of the protein crystal, the application of the Matthews coefficient ( $V_M$ ) has provided significant insights into the molecular packing within the crystal lattice (Matthews, 1968). The calculated  $V_M$  of  $3.51 \text{ \AA}^3/\text{Da}$ , derived from the estimated molecular weight of 73480 Da for 668 residues and the crystal cell volume of  $2110016.8 \text{ \AA}^3$ , suggests a solvent content of approximately 65%. This value falls within the anticipated range for protein crystals, which typically exhibits solvent contents between 40% and 70% (Kantardjieff and Rupp, 2003). Consequently, the physicochemical parameters extrapolated from the Matthews coefficient report are highly suggestive of a crystal with favorable characteristics for X-ray crystallographic studies including soaking or co-crystallization experiments (Figures 36 and 37).



**Figure 36: A Super Cell of the Protein Crystal with extended Solvent Channels.**

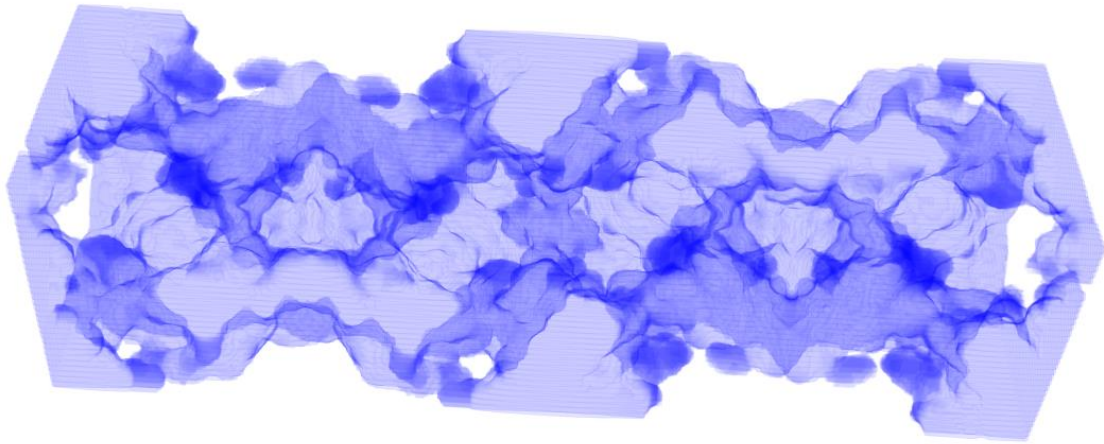


**Figure 37: The Solvent Content within a Unit Cell of the SeBPB3 Crystal (Pletzer-Zelgert et al., 2023).**

The examination of the active site yielded the following metrics: volumetric and morphological descriptors indicate a volume of approximate  $282 \text{ \AA}^3$  and a surface area of  $560 \text{ \AA}^2$ , with a depth of  $14 \text{ \AA}$  (Volkamer et al., 2010; Volkamer et al., 2012; Graef et al., 2023) (Figure 38). The capaciousness and profundity of this active site render it amenable to accommodating conventional  $\beta$ -lactam antibiotics as well as antibiotics within the same size range, providing sufficient spatial allowance for efficacious molecular interaction within the catalytic site.



**Figure 38: Volume (green) of the active Site of SeBPB3 (red).** The Volume and the Depth of the Active Site is sufficient for conventional Antibiotics, like  $\beta$ -lactam Antibiotics to fit inside.

In Figure 39, we observe a tight clustering of diffraction spots, a phenomenon attributable to the elongated axis of the unit cell, extending beyond  $300 \text{ \AA}$ . This



considerable axial length engenders a reduction in the angular separation between adjacent spots, resulting in a diffraction pattern where the spots are close to each another. The proximity of the diffraction spots is a direct reflection of the substantial dimensions of the crystal's lattice parameters, particularly the extended c-axis, which compresses the reciprocal space. Such a compact arrangement in the reciprocal lattice can pose challenges for the resolution of individual spots, especially during integration of the diffraction data. When the lattice parameter of the unit cell is markedly lengthened, its corresponding reciprocal dimension is consequentially condensed.

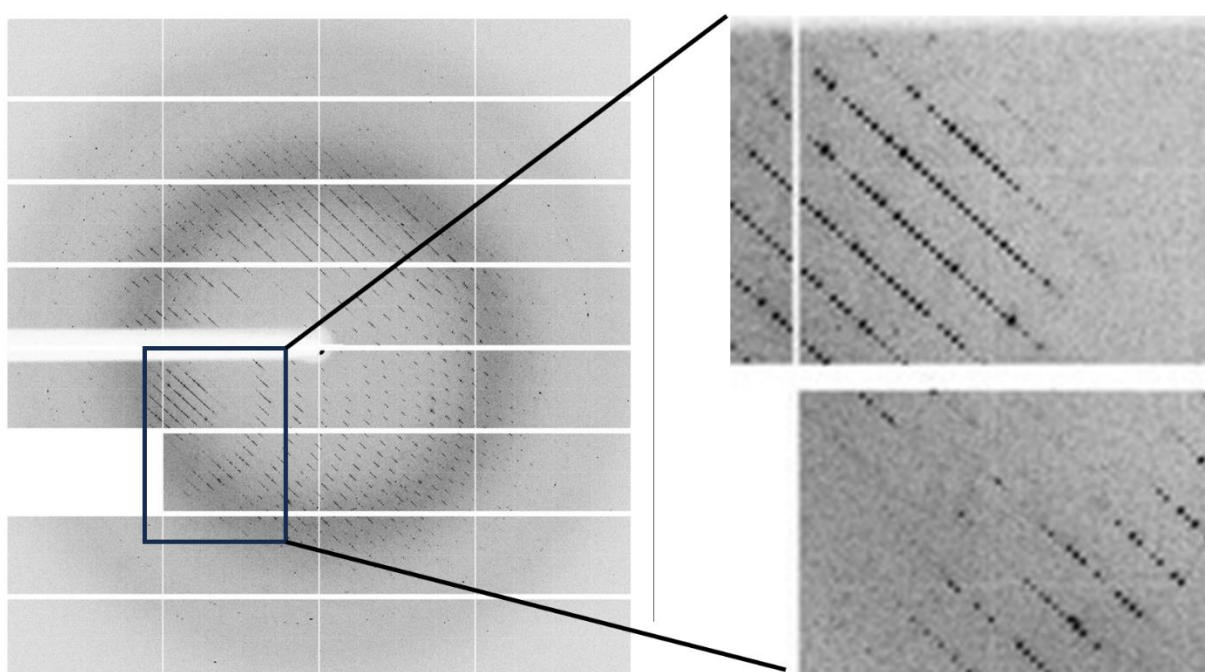


**Figure 39: Diffraction Pattern of SeBPB3 with a magnified Area to highlight the Closeness of Spots.**

## Interpretation of the Model

### Secondary Structure Elements

The secondary structure analysis of the protein, based on crystallographic data, reveals a composition of 32.2% alpha-helical content, 21.7% beta strands, and 46.1% other structural elements such as turns (Figure 40) (Laskowski, 2022). These proportions diverge significantly from estimations by Yang et al. and Reeds et al.. This discrepancy underscores the limitations of CD structural analysis, particularly when algorithms are not optimized for the obtained maximal curve resolution. The existence of multiple reference databases alone indicates that CD measurements should be utilized as evidence of folding patterns rather than definitive structural determinations. As observed in this instance, the CD-derived estimations should be considered with caution, considering the intrinsic limitations and potential for variance when not tailored to the specific spectral analysis required.

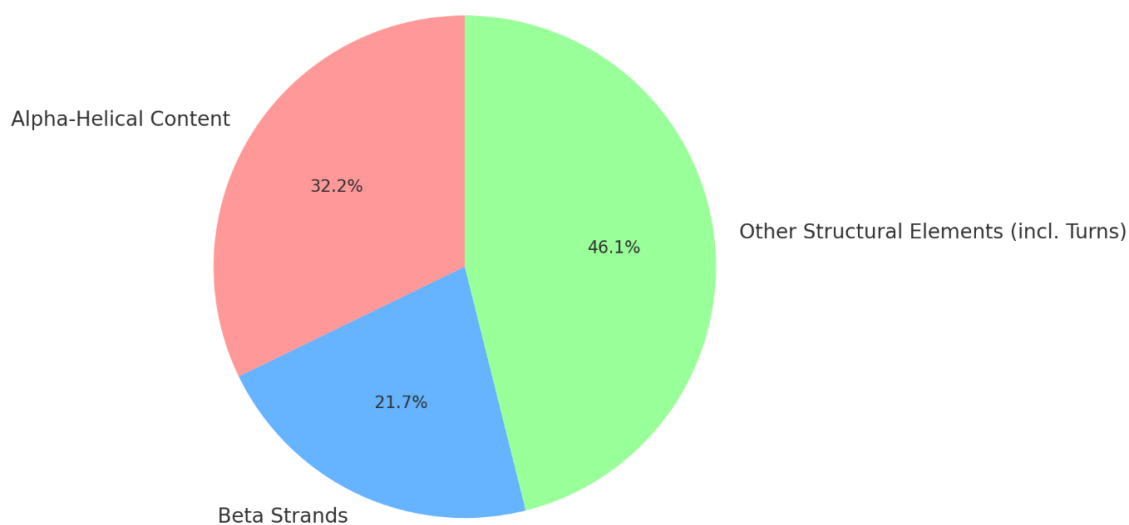


**Figure 40: Secondary Structure Elements according to the X-ray Structure of SePBP3 (Laskowski, 2022).**

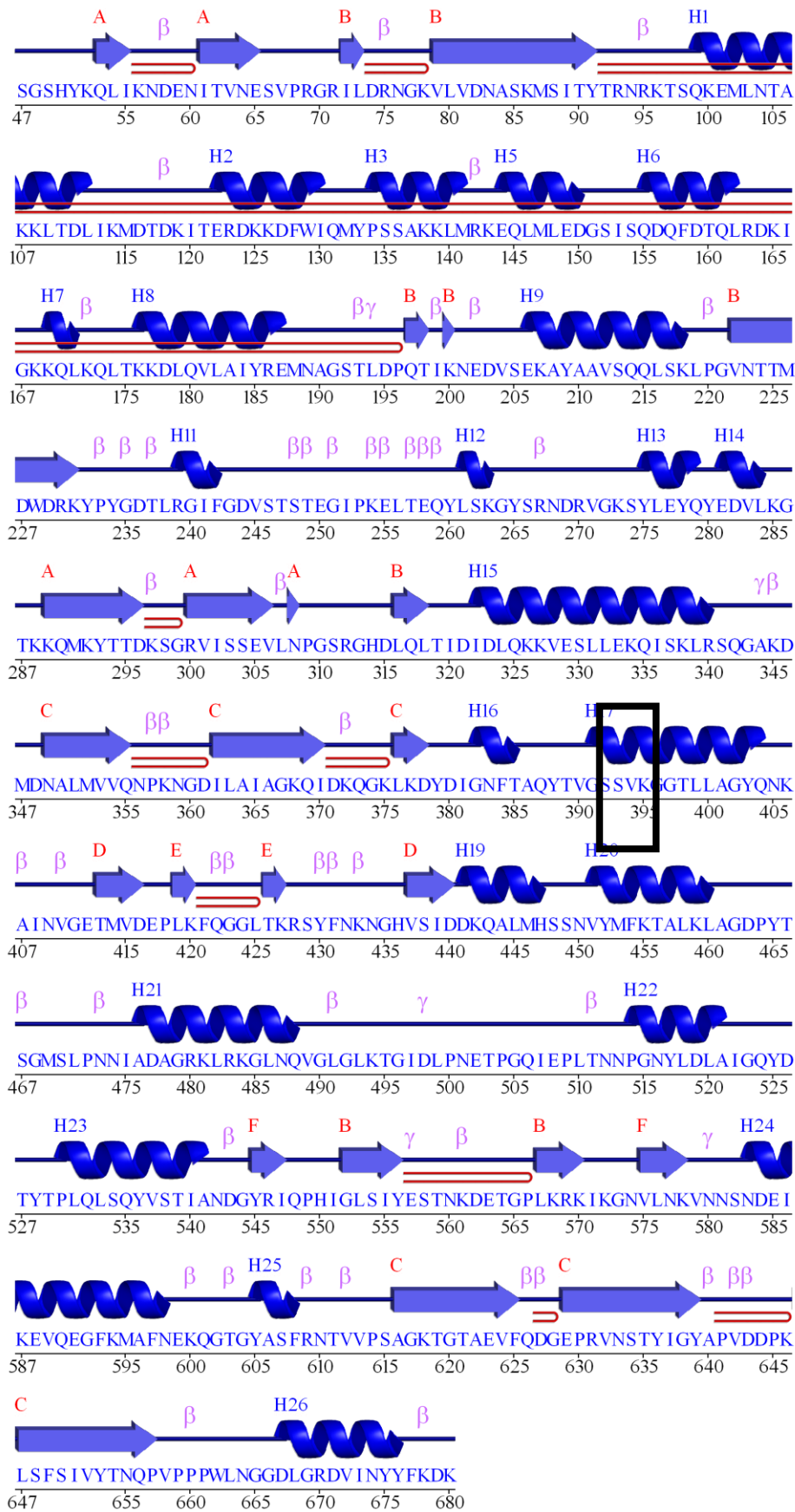


**Figure 41. Secondary Structure Elements together with the Sequence of SePBP3. Active serine (SSVK) is highlighted within the box. The secondary structure elements were extracted from the PDB file by PDBSum (Laskowski, 2022).**

## X-Ray Structure

*Se*PBP3 manifests structural similarities with the canonical domains identified in class B PBPs, paralleling previous characterizations by Sauvage (Sauvage et al., 2008). Its architecture is segmented into two distinct domains: the transpeptidase and the pedestal, the latter comprising three sub-domains: the N-terminal anchor, the head sub-domain, and the intervening linker domain. A two-dimensional topology diagram delineates these domains, with an emphasis on the linkers between domains (Figure 42). The transpeptidase domain is comprised of a distinctive fold, including ten  $\beta$ -sheets and twelve  $\alpha$ -helices, forming a structure corresponding to the DD-alanine transpeptidase /transpeptidase-like fold, with a core scaffold constructed from a series of  $\beta$ -sheets. Encircling  $\alpha$ -helices fortify this central  $\beta$ -structure. The domain encompasses three highly conserved sequence motifs essential for catalytic activity: the active-site serine at helix 13's terminus, the SSN motif amidst  $\alpha$ -helices 14 and 15, and the KTGT motif within  $\beta$ -sheet 21. The serine's reactivity is hypothesized to be enhanced by a lysine residue, enabling it to initiate a nucleophilic assault on the peptidoglycan's peptide stem. The linker domain contains three  $\beta$ -sheets and  $\alpha$ -helices, where Goffin and Ghuysen have identified a unique motif to class B Penicillin-binding proteins that presumably contributes to structural stabilization via a triad of spatially configured amino acids (Goffin and Ghuysen, 2002). The N-terminal domain is typically tethered to the membrane anchor and organized into four antiparallel  $\beta$ -sheets, known as the sugar tong domain (Finn et al., 2016; S. Lu et al., 2020). Contrary to expectations of disorder, this domain in *Se*PBP3 is characterized by a relative low electron density, suggesting an intrinsic flexibility. Dimerization at this domain, noted within the crystal lattice by Yoshida et al., hints at a potential role in oligomerization, although such dimeric interaction is not observed in solution (Yoshida et al., 2012). In the crystal lattice *Se*PBP3 does not form intermolecular contacts at this domain, nor are such contacts observed in a solubilized state.

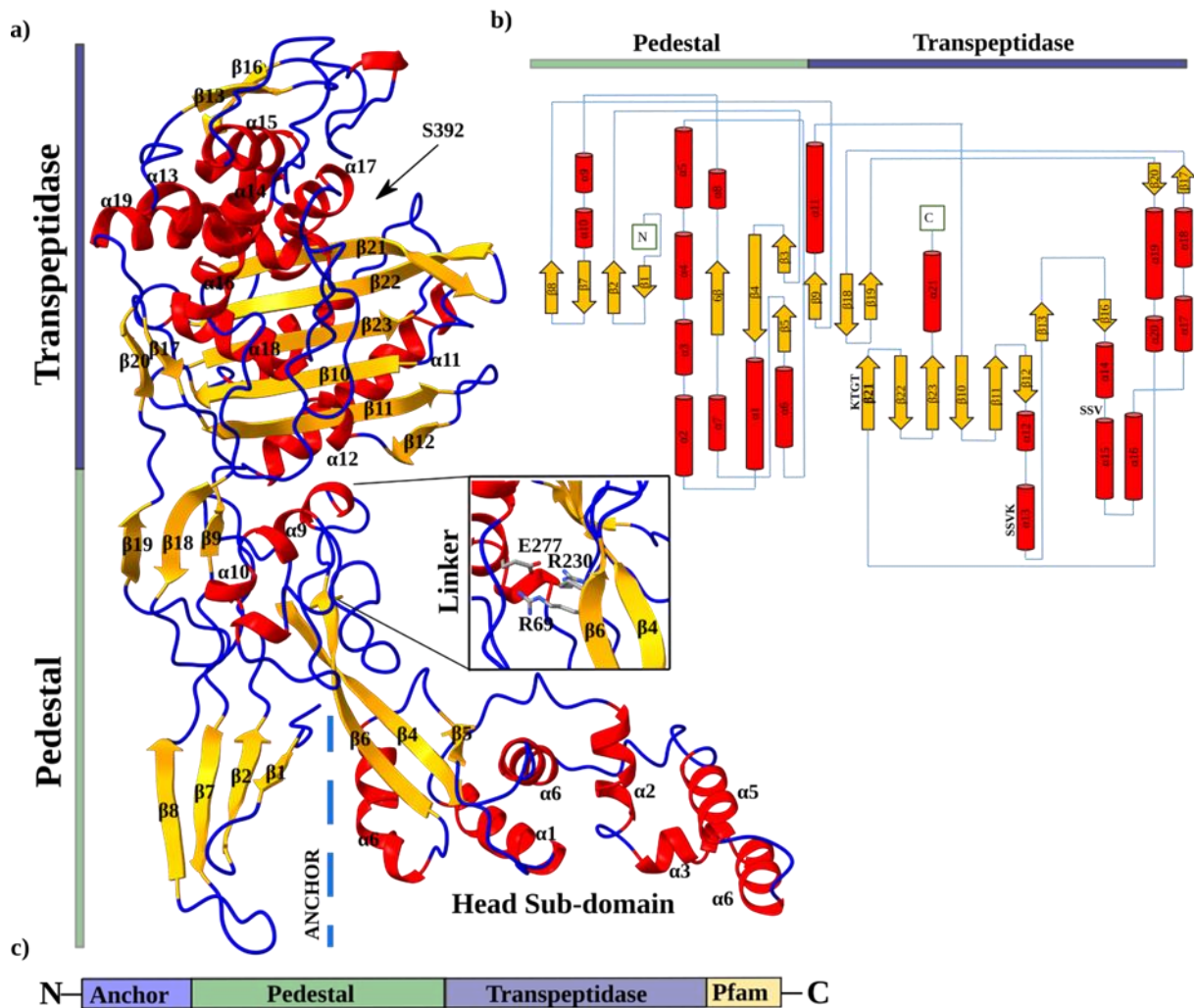


**Figure 42. Cartoon and Topology Plot of *SePBP3*.** a) The secondary structure is indicated in different colours. Loops are depicted in blue, sheets in yellow and helices in red. The membrane anchor is indicated by dashed lines. The linker domain is highlighted as it contains a 3D motif. b) The topology plot is depicted in the same colour scheme and highlights the interdomain connections. c) A simplified cartoon of *SePBP3* including the position of the membrane anchor.

### Comparative Structural and Sequence Analysis of Penicillin-binding Proteins

The transpeptidase domain of *SePBP3*, homologous to other PBPs, displays a highly conserved structural backbone. This structural conservation spans across both high molecular weight (HMW) and low molecular weight (LMW) PBPs, as well as  $\beta$ -lactamases (Figure 43). A detailed structural conservation analysis of the transpeptidase domain in *SePBP3* reveals a pronounced pattern of evolutionary preservation, especially in its core region, as illustrated in figure 44. This domain is characterized by a higher conservation score, indicating the presence of structural and functional motifs that have been maintained across different species. This conservation suggests a pivotal role for these

motifs in the enzyme's catalytic activity. Contrastingly, the pedestal domains demonstrate considerable structural diversity, making them non-comparable across different proteins. This diversity is clearly highlighted in figure 44, where the pedestal domains of various class B PBPs show notable differences in their positioning and amino acid sequence length.

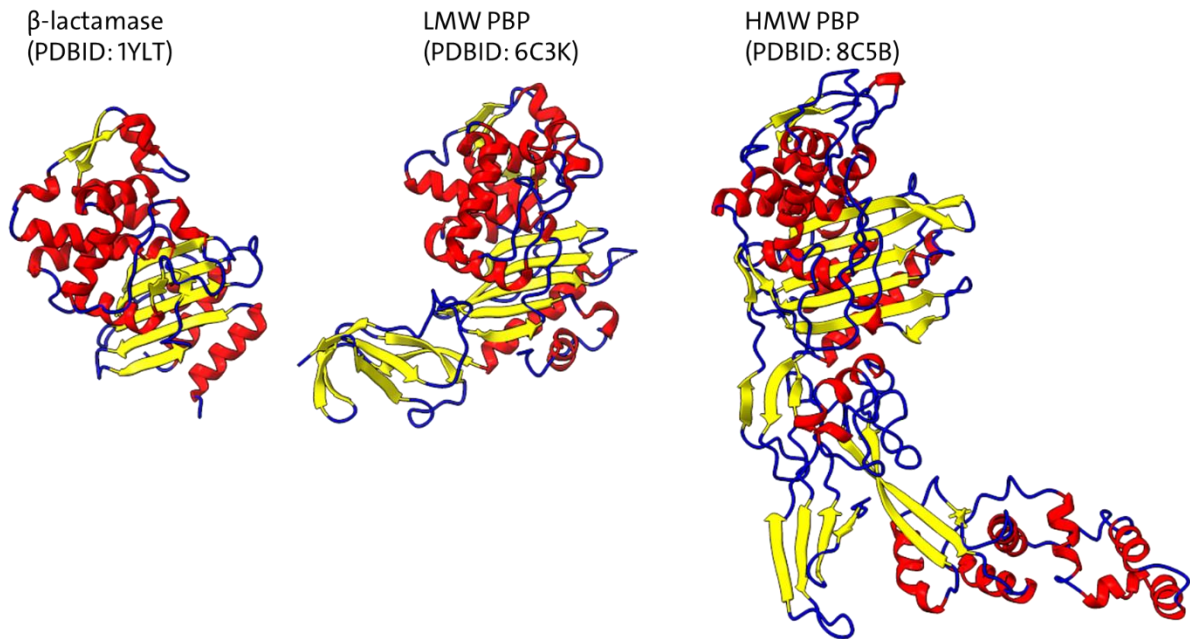


**Figure 43: Conserved of 3D-Structure in the Transpeptidase Domain.** This figure demonstrates the structural resemblance of the transpeptidase domain across different proteins. The  $\beta$ -lactamase CTX-14 from *Escherichia coli* (PDBID: 1YLT) showcases a structural similarity to a typical transpeptidase domain. Additionally, the low molecular weight (LMW) PBP 4 from *Staphylococcus aureus* (PDBID: 6C3K), a carboxypeptidase, exhibits structural homology to the high molecular weight (HMW) PBP3 (PDBID: 8C5B) from *Staphylococcus epidermidis*, particularly in its transpeptidase domain.

The domain superposition and the calculated Root Mean Square Deviation (RMSD) values, considering both the entire protein and exclusively the transpeptidase domain, highlights this diversity. For *Se*PBP3 compared to *Sa*PBP3, a significant C $\alpha$  RMSD value of 7.6 Å is observed for the entire protein structure, which is reduced to 0.35 Å when only the transpeptidase domain is considered. Similarly, the comparison between *Se*PBP3 and *Pa*PBP3 yields RMSD values of 3.6 Å for the full protein and 1.5 Å for the transpeptidase domain. The analysis involving *Se*PBP3 and *Sp*PBP2B reveals RMSD values of 6.8 Å for the complete protein structure and 0.8 Å for the transpeptidase domain alone. These

structural variations are mirrored in the sequence homology among *Se*PBP3 and its counterparts, including *Sa*PBP3, *Pa*PBP3, and *Sp*PBP2B. *Se*PBP3 shares an 85% homology with *Sa*PBP3, but only 22% with *Pa*PBP3 and 35% with *Sp*PBP2B. These percentages correlate well with the observed RMSD values for the entire protein structures. A sequence alignment, presented in figure 45 underscores these variations, highlighting the low-affinity residues as well as the highly conserved motifs among these proteins. This alignment not only demonstrates the shared core structure in the transpeptidase domain but also the significant divergence in the pedestal domains, offering insights into the evolutionary adaptations and functional diversities among these PBPs.

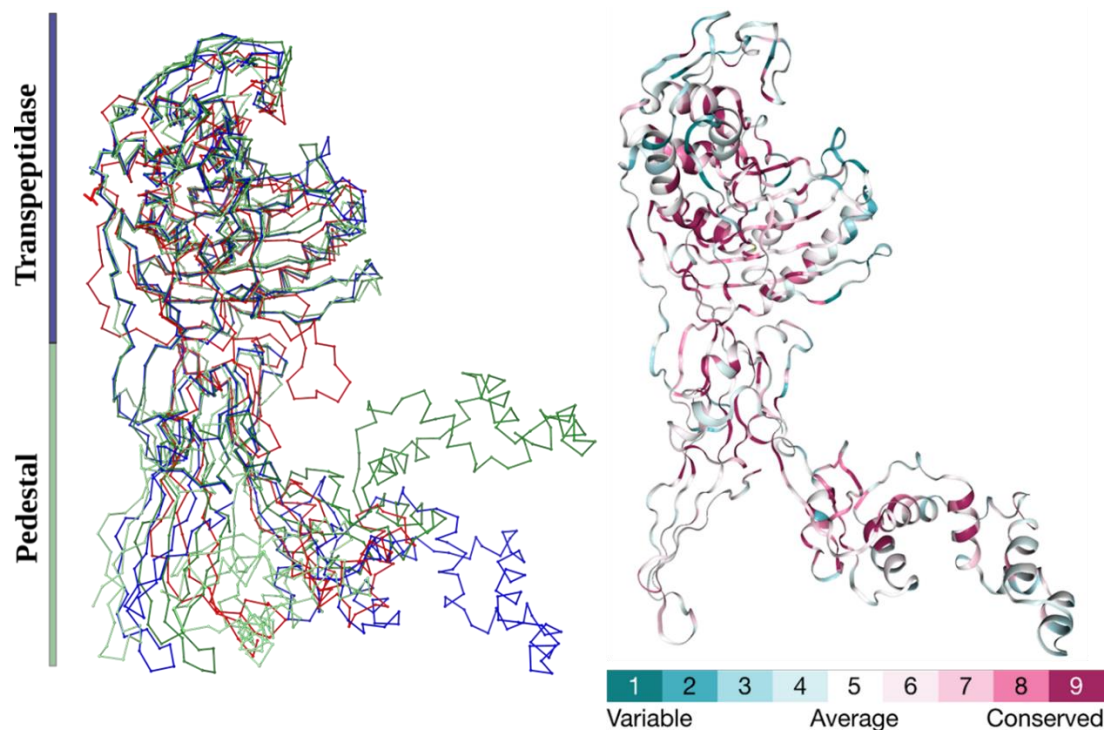


**Figure 44: Comparative C-alpha Backbone Analysis of Penicillin-binding Protein Structures: Conserved Transpeptidase and Linker Domains with structural varied N-terminal Anchor and Head Sub-domains.** Superimposed crystal structures of penicillin-binding proteins from *Staphylococcus epidermidis* (*Se*PBP3; blue), *Staphylococcus aureus* (*Sa*PBP3/ PDBID: 3vsk, dark-green), *Pseudomonas aeruginosa* (*Pa*PBP3/ PDBID: 7auh, green), and *Streptococcus pneumoniae* (*Sp*PBP2B/ PDBID: 2wad, red). The analysis of conservation clearly underscores the transpeptidase core as a region of significant evolutionary conservation.

SePBP3

SePBP3  
SaPBP2a  
SaPBP3  
SpPBP2B  
PaPBP3

SePBP3

SePBP3  
SaPBP2a  
SaPBP3  
SpPBP2B  
PaPBP3

SePBP3

SePBP3  
SaPBP2a  
SaPBP3  
SpPBP2B  
PaPBP3

SePBP3

SePBP3  
SaPBP2a  
SaPBP3  
SpPBP2B  
PaPBP3

SePBP3

SePBP3  
SaPBP2a  
SaPBP3  
SpPBP2B  
PaPBP3

SePBP3

SePBP3  
SaPBP2a  
SaPBP3  
SpPBP2B  
PaPBP3

SePBP3

SePBP3  
SaPBP2a  
SaPBP3  
SpPBP2B  
PaPBP3

SePBP3

SePBP3  
SaPBP2a  
SaPBP3  
SpPBP2B  
PaPBP3

SePBP3

SePBP3  
SaPBP2a  
SaPBP3  
SpPBP2B  
PaPBP3

SePBP3

SePBP3  
SaPBP2a  
SaPBP3  
SpPBP2B  
PaPBP3

SePBP3

SePBP3  
SaPBP2a  
SaPBP3  
SpPBP2B  
PaPBP3

SePBP3

SePBP3  
SaPBP2a  
SaPBP3  
SpPBP2B  
PaPBP3



**Figure 45: Sequence Alignment of SePBP3 from *Staphylococcus epidermidis*, SaPBP2a and SaPBP3 from *Staphylococcus aureus*, SpPBP2B from *Streptococcus pneumoniae* and PaPBP3 from *Pseudomonas aeruginosa* including Secondary Structure Elements of SePBP3.** Identical amino acids are highlighted in red. Secondary structure elements of SePBP3 are placed on top of the sequences. Figure was created applying ESPript 3.0 (Robert and Gouet, 2014).

### **X-ray Co-crystallography and Isothermal Titration Calorimetry Analysis**

The structural evaluation of SePBP3, when complexed with  $\beta$ -lactam and boron-based antibiotics, was conducted through co-crystallization assays, revealing a pronounced openness of its active site. Antibiotics were introduced at a concentration of 100 mM in a 5% DMSO solution, leading to an elongated crystallization period extending from 3 days to a span of 3-4 weeks. Remarkably, the resultant crystalline structures maintained the cell constants and crystal symmetry of the native SePBP3 form. The SePBP3-cefotaxime complex diffracted to 2.51 Å resolution, and the SePBP3-vaborbactam complex to 2.3 Å. Notably, the electron density map for cefotaxime disclosed an unexpected open-ring conformation, indicative of an enzymatic reaction occurring during the crystallization process. These findings highlight that the active site of SePBP3 is not merely passive but actively partakes in the transformation of the substrate during the crystallization phase. In the structural analysis, the active site of SePBP3 presented a unique conformation. Ligand binding did not elicit the expected conformational changes, typically facilitated by the inherent flexibility of distinct loops and sheets within the PBPs active sites (Contreras-Martel et al., 2009; Fenton et al., 2021). This divergence from other PBPs, where active site binding correlates with substantial structural flexibility, is particularly noteworthy in SePBP3's case. The protein's interconnection region, despite being compact, is well delineated, with the  $\beta$ 21 sheet exhibiting an extended conformation that bends away from the active serine residue, contrasting sharply with the configurations observed in other PBP structures, where this particular  $\beta$ -sheet shields the active serine (Lim and Strynadka, 2002). This distinctive structural feature of SePBP3, where the  $\beta$ 21 sheet is positioned further from the active serine compared to similar proteins, provides a rationale for the observed structural phenomena during antibiotic binding. The relative positioning of this sheet is in contrast

to the protective orientation seen in *Sa*PBP2a and implies a more accessible and potentially reactive active site in *Se*PBP3 (Figure 46).

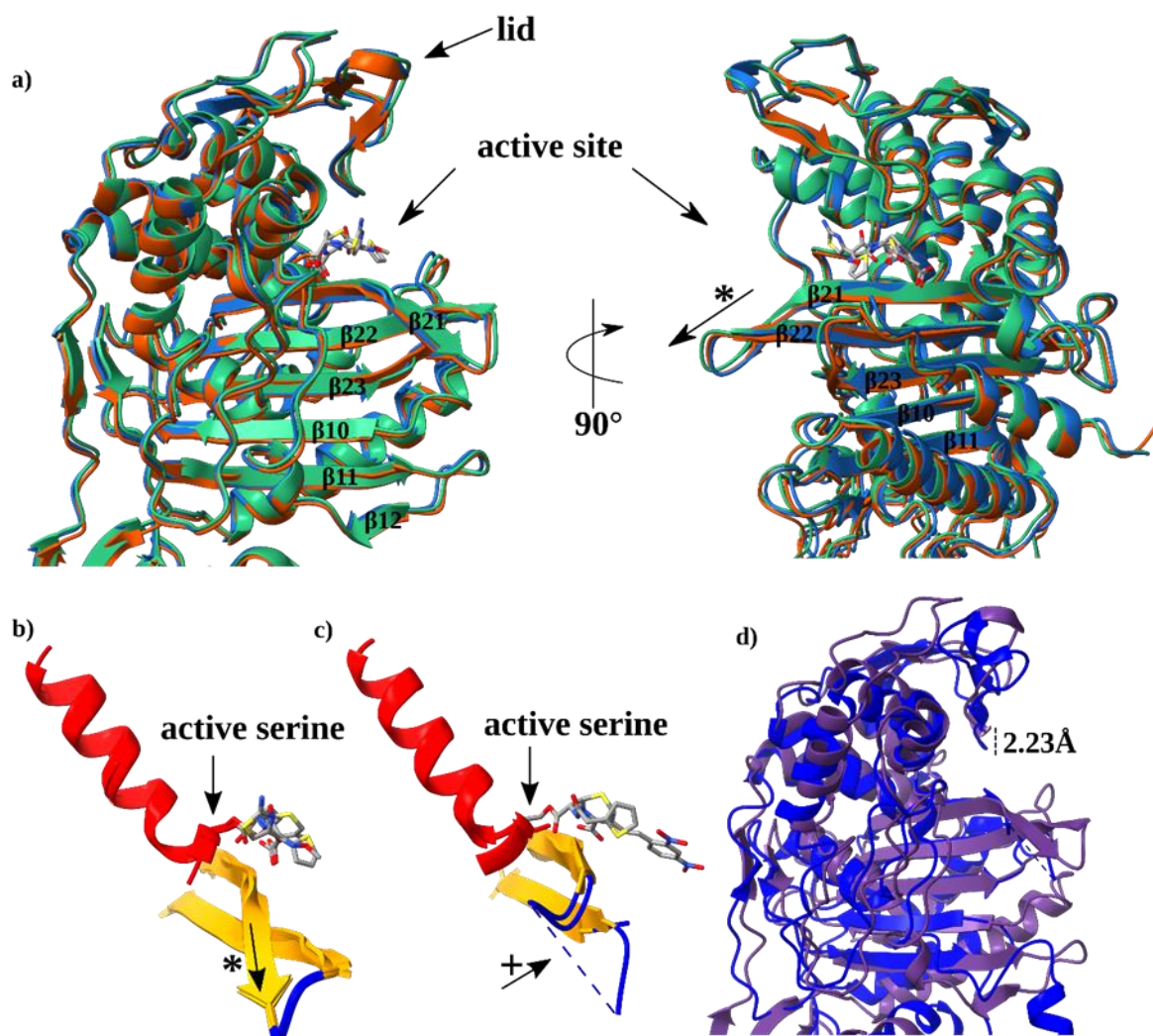


**Figure 46. Comparative Structural Analysis of *Se*PBP3 and *Sa*PBP2a.** a) Superposition of *Se*PBP3 in its apo form (blue) and when complexed with cefotaxime (orange) and vaborbactam (green). A structural superimposition of b) *Se*PBP3 in apo form and in complex with cefotaxime and vaborbactam and c) *Sa*PBP2a in apo form and in complex with penicillin G. d) A superimposition of the transpeptidase domains between *Se*PBP3 (blue) and *Sa*PBP2a (violet) reveals an open lid, exhibiting a deviation of 2.23 Å, highlighting the open cavity of *Se*PBP3. The asterisk (\*) symbol highlights the bending of  $\beta$ -sheet 21 and the plus (+) symbol the flexible loop region.

The interactions of vaborbactam and cefotaxime were further analyzed by examining the role of conserved motifs within the *Se*PBP3 structure. A covalent interaction at the catalytic serine residue at position 329 (motif 1/SSNK) was identified, which concurrently establishes hydrogen bonds with serine 446 (motif 2/SSN) and is further stabilized by interactions with two threonine residues at positions 619 and 621 (motif 3/KTGT), as depicted in figure 47.

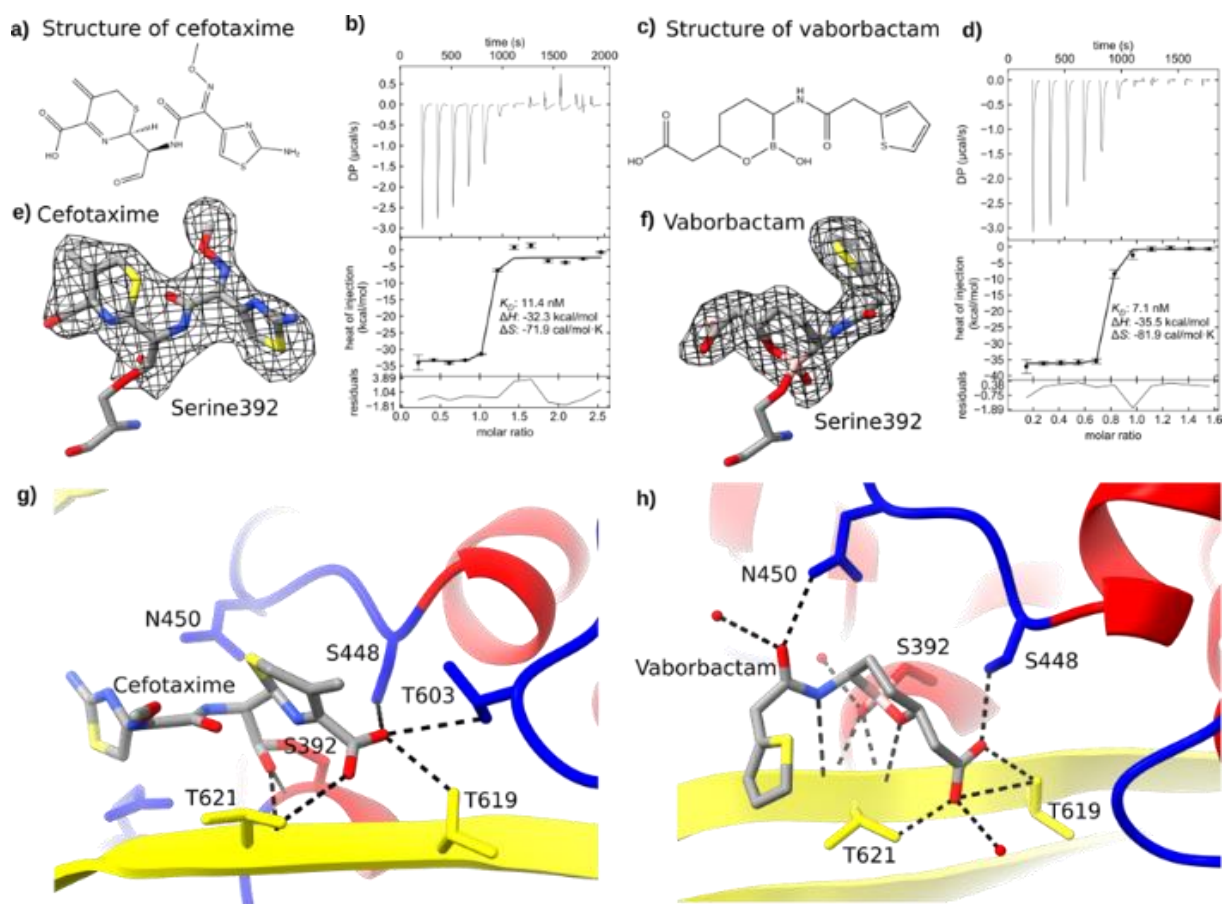


**Figure 47: Binding Characterization of Cefotaxime and Vaborbactam with *SePBP3*.** Panel (a) illustrates the open-form structure of cefotaxime, catalyzed by *SePBP3* during co-crystallization, while panel (c) depicts the structure of vaborbactam, which is not catalyzed. Both ligands bind with high affinity: (b) cefotaxime with a  $K_D$ -value of 11.4 nM and (d) vaborbactam with a  $K_D$ -value of 7.1 nM. The ligands are embedded into the electron density at sigma levels of e) 2.0 for cefotaxime and f) 1.0 for vaborbactam in the omit map, respectively. Dashed lines represent the hydrogen bonds for (g) cefotaxime and for (h) vaborbactam.

In exploring the hypothesized role of *SePBP3* decoy receptor within the cellular milieu, investigations extended to quantifying the binding affinities of distinct ligands to this enzyme. Elucidating the putative role of *SaPBP3* as a decoy receptor led to the gauge of the affinity of both ligands to it. Former publications reveal that *SaPBP3* plays a vital role in cell survival and the missing activity of *SaPBP3* applying sub-MIC levels induces an alteration in cellular morphology (Pinho et al., 2000). It was observed with considerable interest that *SePBP3* manifested a high binding affinity for both cefotaxime—a third-generation cephalosporin—and vaborbactam, a novel non-suicidal  $\beta$ -lactamase inhibitor. The binding kinetics are characterized by an approximate dissociation constant ( $K_D$ ) of around 10 nM. This sharply contrasts with the affinity observed in other PBPs for

standard  $\beta$ -lactam antibiotics, which exhibit  $K_D$  values as high as 10 mM, indicating a thousand-fold weaker affinity. (W. P. Lu et al., 1999). The comparable affinities observed for vaborbactam and cefotaxime with *SePBP3* underscore the potential of *SePBP3* as a decoy receptor, not only for  $\beta$ -lactam antibiotics but also for newer antibiotic classes. Given that the active site remains perpetually open and lacks flexibility in the active site region, antibiotics similar in size to  $\beta$ -lactams can easily access it. The similarity in the binding mechanisms of vaborbactam and cefotaxime further accounts for their analogous affinities. Discussions are ongoing about the flexibility of  $\beta$ -sheets and the loops that connect these regions. In the case of *NgPBP2* (PDBID: 6XQV) from *Neisseria gonorrhoeae* and certain mutants of *SpPBP2B* (PDBID: 2WAD) from *Streptococcus pneumoniae*, these connecting loops exhibit flexibility, as evidenced by the lack of traceable electron density. This contrasts with drug-sensitive strains, where these regions show distinct electron density (Contreras-Martel et al., 2009; Fenton et al., 2021). In *SePBP3*, the interconnecting region, although shorter, is well-defined. The notable distinction here is the elongation of the  $\beta_{21}$  sheet, which deviates from the active site Serine 392.

### **Analysis of the Flexibility of *SePBP3***

The dynamic nature of PBPs has captured scientific interest, particularly in the context of identifying their interactive partners. The synergistic relationship between shape, elongation, division, and sporulation (SEDS) proteins with class B PBPs is suggested to be integral to the peptidoglycan crosslinking process. During this intricate process, the membrane anchor and N-terminal anchor domain of PBPs engage with proteins like RodA, a known glycosyltransferase. The interface formed between the head sub-domain and the N-terminal anchor domain is hypothesized to be pivotal for the binding of proteins in association with RodA, including MreC (Sjodt et al., 2020). Additional complexities arise with PBPs such as the low-affinity PBP2a, which features a distinctive allosteric site situated amid the pedestal domains, implicated in the mechanism of  $\beta$ -lactam antibiotic resistance (Lim and Strynadka, 2002). The precise function of the head sub-domain (HSD) in class B PBPs remains a subject of ongoing investigation. Beyond its putative role in protein-protein interactions, the HSD is thought to act as a

spatial obstacle that precludes the transpeptidase region from nearing the cell membrane too closely (Macheboeuf et al., 2006). Observations of variable conformations in the pedestal region, as those seen for *EfPBP5* from *Enterococcus faecium*, have been reported, illustrating the structural versatility inherent to these proteins (Moon et al., 2018). In the structural comparison of *SePBP3* and *SaPBP3* (Yoshida et al., 2012), both proteins exhibited analogous arrangements in their head sub-domains, consisting of an assembly of seven  $\alpha$ -helices and three  $\beta$ -sheets. Although these domains align closely, the introduction of bends in  $\beta$ -sheets 4 and 6 culminates in a discernible displacement of the entire domain. A rotational shift of approximately  $30^\circ$  was noted in the HSD, alongside a variation of approximately  $30 \text{ \AA}$  in the spatial separation between the two forms. Moreover, a  $10 \text{ \AA}$  increase in the distance from the apex of the HSD to the N-terminal anchor domain was observed for *SePBP3* and *SaPBP3*. While no closed conformations were detected in this analysis, two distinct structural states were identified: an extended state and a compressed state (Figure 48). Compellingly, computational predictions by AlphaFold suggest with high confidence a closed conformation at the interface area for both proteins (ENTRYID: *SePBP3*: Q5HNZ7; *SaPBP3*: A0A389VKU4). The pedestal region, not just the HSD, demonstrates flexibility, as inferred from the ambiguous electron density associated with the N-terminal anchor domain. In contrast, *SaPBP3* exhibits a more defined electron density, which might be attributed to crystal contacts constraining movement at this domain. For the N-terminal anchor domains of PBPs low electron density is observed, particularly in instances where crystal packing does not inhibit domain mobility, such as in *EfPBP4* from *Enterococcus faecalis*.

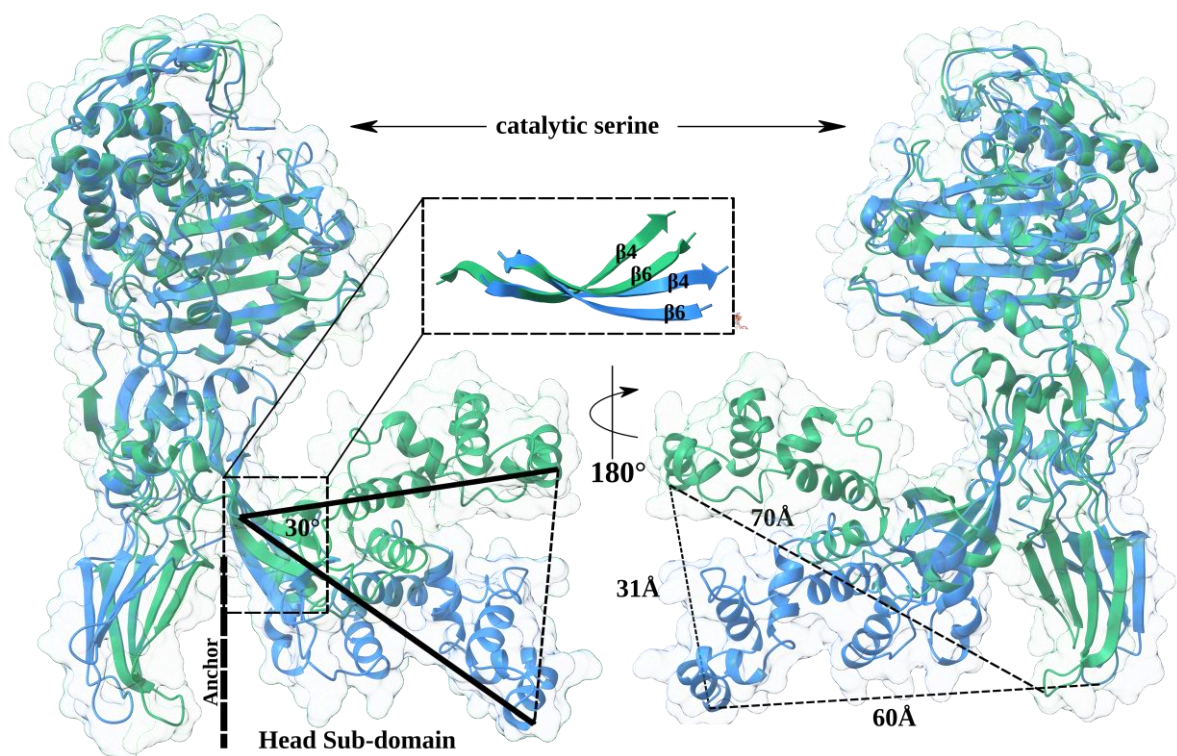


**Figure 48. Superimposed Structures of Penicillin-binding Protein 3 (PBP3) from *Staphylococcus epidermidis* (SePBP3; blue) and *Staphylococcus aureus* (SaPBP3, green).** The head sub-domain (HSD) exhibits two distinct states, an extended and a compressed conformation towards the N-terminal anchor domain. SaPBP3, with a separation of 70 Å, shows a greater distance than that observed for SePBP3, with 60 Å. The distance between the two ends of the head subdomain is 31 Å and the angle between them is approximate 30°. The origin of the curved conformation is located in  $\beta$ -sheets 4 and 6. No well-interpretable electron density was found in the N-terminal anchor domain of SePBP3, suggesting relative high mobility of this region.

### Flexibility in Solution: SAXS Studies

Small-Angle X-ray Scattering (SAXS) experiments were performed to further investigate the conformational flexibility of SePBP3 in solution. Analysis using a dimensionless Kratky plot revealed a non-globular folding pattern for SePBP3. This was evidenced by the displacement of the characteristic peak for globular proteins towards higher  $qR_g$  values, surpassing the threshold of 1.73, as shown in figure 49c. This shift aligns with the structural characteristics typical of class B PBPs. Moreover, the SAXS data suggest an elongated conformation of SePBP3, as indicated by the protracted tail in the distance distribution function curve  $[P(r)]$ . This observation complicates the determination of the maximum particle dimension ( $D_{max}$ ), as illustrated in figure 49d. Consequently, it becomes challenging to accurately validate the dynamic shifts of the head sub-domain (HSD) across various conformational states, as also summarized in table 23.

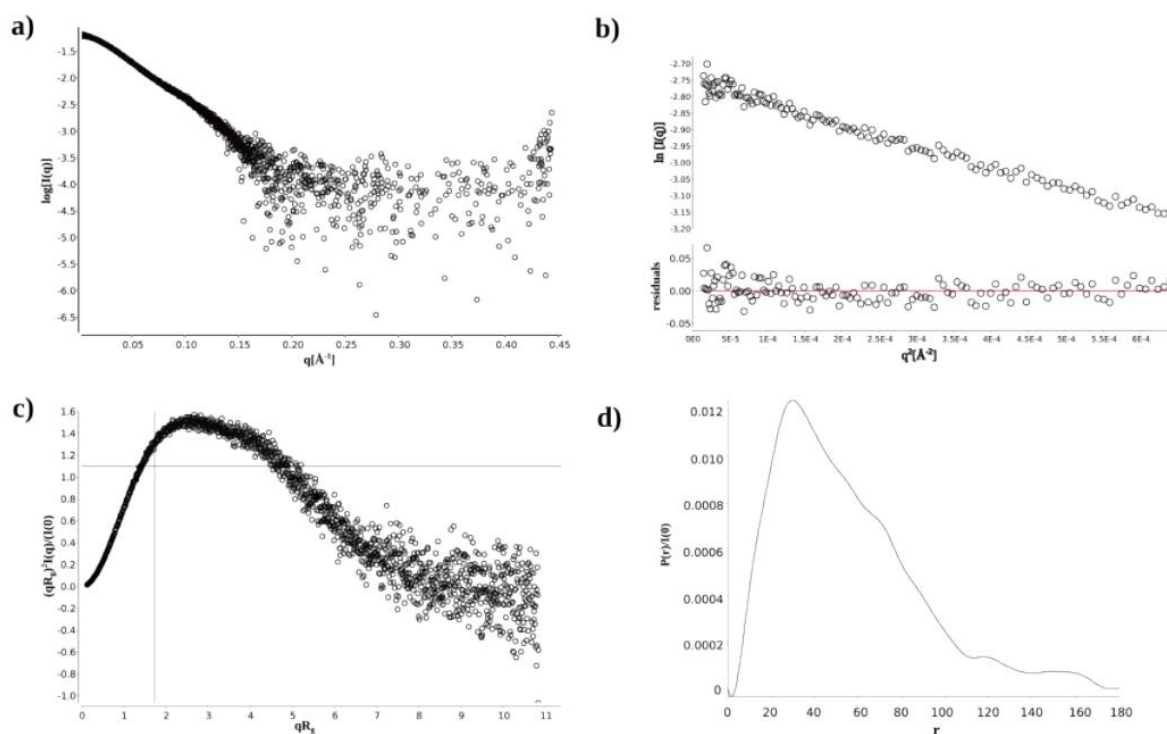


**Figure 49: SAXS Data Summary for SePBP3.** Scattering profile in a log-line scale (a). Guinier fit (top) and fit residuals (bottom) (b). Dimensionless Kratky plot. Dashed line shows where a globular system would peak (c).  $P(r)$  function normalized by  $I(0)$  (d).

To further analyze the protein's compactness and flexibility, the Porod-Debye law was applied. According to this principle, the scattering intensity of a compact particle should decay following a  $q^{-4}$  trend, and a plot of  $q^4 I(q)$  versus  $q^4$  for such particles typically reaches a plateau, indicative of a uniform electron density contrast between the particle and the solvent, as depicted in figure 50b. In contrast, proteins exhibiting considerable flexibility, such as SePBP3, show a scattering intensity declining slower than  $q^{-4}$ , failing to achieve a plateau in the Porod-Debye plot. Instead, these proteins display a plateau in the Kratky-Debye plot ( $q^2 I(q)$  versus  $q^2$ ), as observed in the SAXS data analysis of SePBP3, presented in Figure 50c. This data corroborates and substantiates the flexibility of this protein.

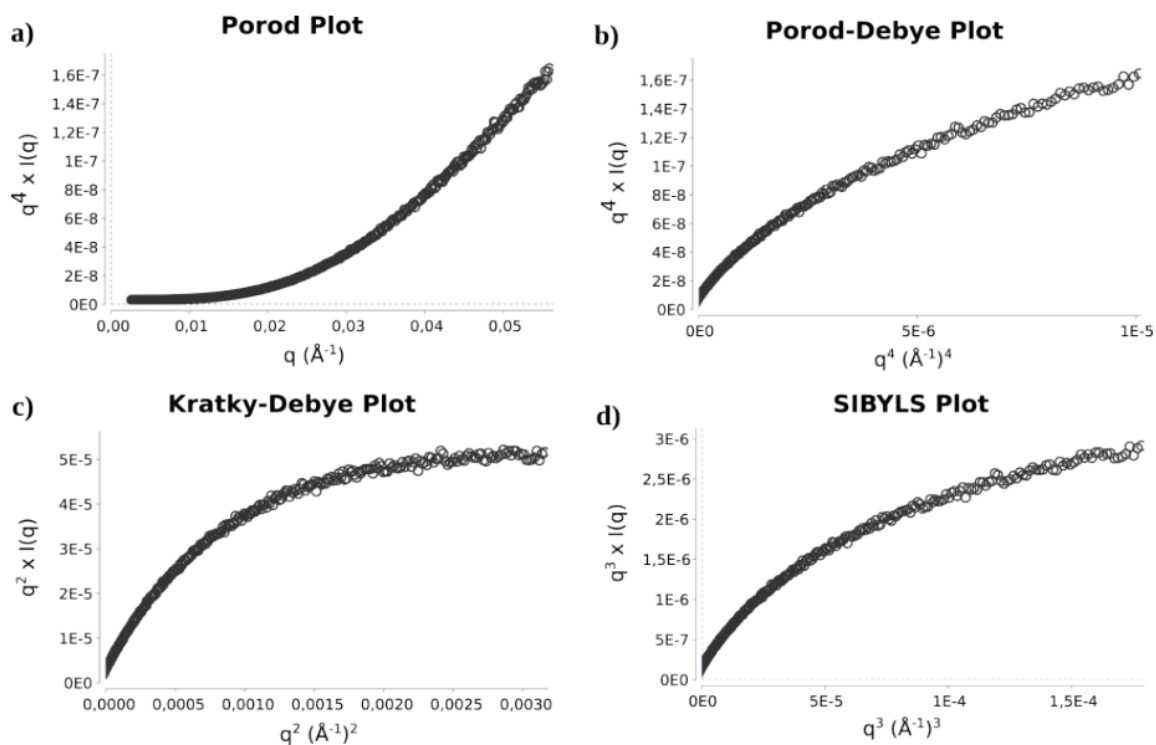


**Figure 50: Exploiting of the Porod Power-Law Relation to Analyse the SePBP3 Conformation.** Experimental SAXS data transformed as Porod plot ( $q^4 I(q)$  vs.  $q$ ) (a), Porod-Debye plot ( $q^4 I(q)$  vs.  $q^4$ ) (b), Kratky-Debye plot ( $q^2 I(q)$  vs.  $q^2$ ) (c) and SIBYLS plot ( $q^3 I(q)$  vs.  $q^3$ ) (d).

**Table 23. Guinier Analysis and P(r) Function Analysis of SAXS Measurements.**

Guinier analysis		P(r) function analysis	
<b>R<sub>g</sub> (Å)</b>	$4.34 \pm 0.02$	$4.91 \pm 0.23$	<b>R<sub>g</sub> (Å)</b>
<b>I(0) (arb.)</b>	$0.06 \pm 1.47e^{-4}$	$0.06 \pm 4.37e^{-4}$	<b>I(0) (arb.)</b>
<b>q-range (1/Å)</b>	0.0319-0.2555	0.0319-2.038	<b>q-range (1/Å)</b>
<b>qR<sub>g</sub> range</b>	0.139-1.109	unclear	<b>D<sub>max</sub> (Å)</b>
<b>R<sup>2</sup></b>	0.982	1.102	<b>χ<sup>2</sup></b>

### Flexibility in Silico: MD Simulations

Molecular dynamics (MD) simulation is a computational method that models the behavior of atoms and molecules over time. By applying Newtonian mechanics, MD simulation calculates the motion of each atom according to the forces acting upon it, which are determined by the interactions with other atoms and the potential energy surface of the system. This technique allows for the exploration of the temporal



evolution of a molecular system of atomic resolution, providing insights into the dynamic nature of molecules such as proteins. The conformational dynamics of *SePBP3* as analyzed with enhanced granularity through a 100 ns MD simulation, utilizing the computational capabilities of Schrodinger's Maestro suite (Sastry et al., 2013). The simulation process entails the computation of atomic trajectories by iteratively solving the equations of motion for the atoms within *SePBP3*, thereby offering a temporal window into the protein's structural fluctuations. The alignment of the alpha carbons (C $\alpha$ ) of *SePBP3* across all simulated frames, as illustrated in figure 51, revealed consistent structural motifs across various PBPs. The transpeptidase core was characterized by an impressive stability, mirroring the robustness of the adjoining linker region. Conversely, the N-terminal anchor domain exhibited limited shifts, attributed to its location within a permissive crystal packing field that allows for such movements. This may elucidate the weaker electron density observed in this region of *SePBP3*. Within the crystal lattice, the head sub-domain's mobility is restricted due to proximity with adjacent protein molecules. Nonetheless, an extended simulation duration of 100 ns uncovered a significant angular reorientation of 38° for this domain. Variations in the distance between the N-terminal anchor domain and the HSD, ranging from 38 to 56 Å, were observed, indicating the protein's ability to transition between closed and open conformations, as depicted in figure 51a. Stability within the linker domain was observed, potentially attributed to a 3D motif that could serve as a structural stabilizer. The Root Mean Square Fluctuation (RMSF) values highlighted a dichotomy within the protein; a flexible N-terminal region contrasted with a rigid C-terminal transpeptidase area, as shown in figure 51b. Moreover, the B-factor values extrapolated from the MD simulations were in close agreement with those obtained from the X-ray data refinement, reinforcing the validity of the simulation results illustrated in figure 51c. The Root Mean Square Deviation (RMSD) values are in a range of 5 to 7 Å, underscoring the inherent flexibility of the *SePBP3* structure, as the HSD is also commuting. Importantly, the secondary structural elements were preserved throughout the simulation, as demonstrated in figure 52, ensuring that the higher RMSD values did not correspond to a loss of structural integrity. The ability of the interface between the N-terminal anchor domain and the

HSD to adopt both open and closed states could potentially modulate interactions with interaction partners, maintaining the transpeptidase body's rigidity. This dynamic behavior, captured through MD simulations, is crucial for understanding the functional adaptability of *Se*PBP3, facilitating diverse molecular interactions while preserving the essential rigidity for enzymatic activity.

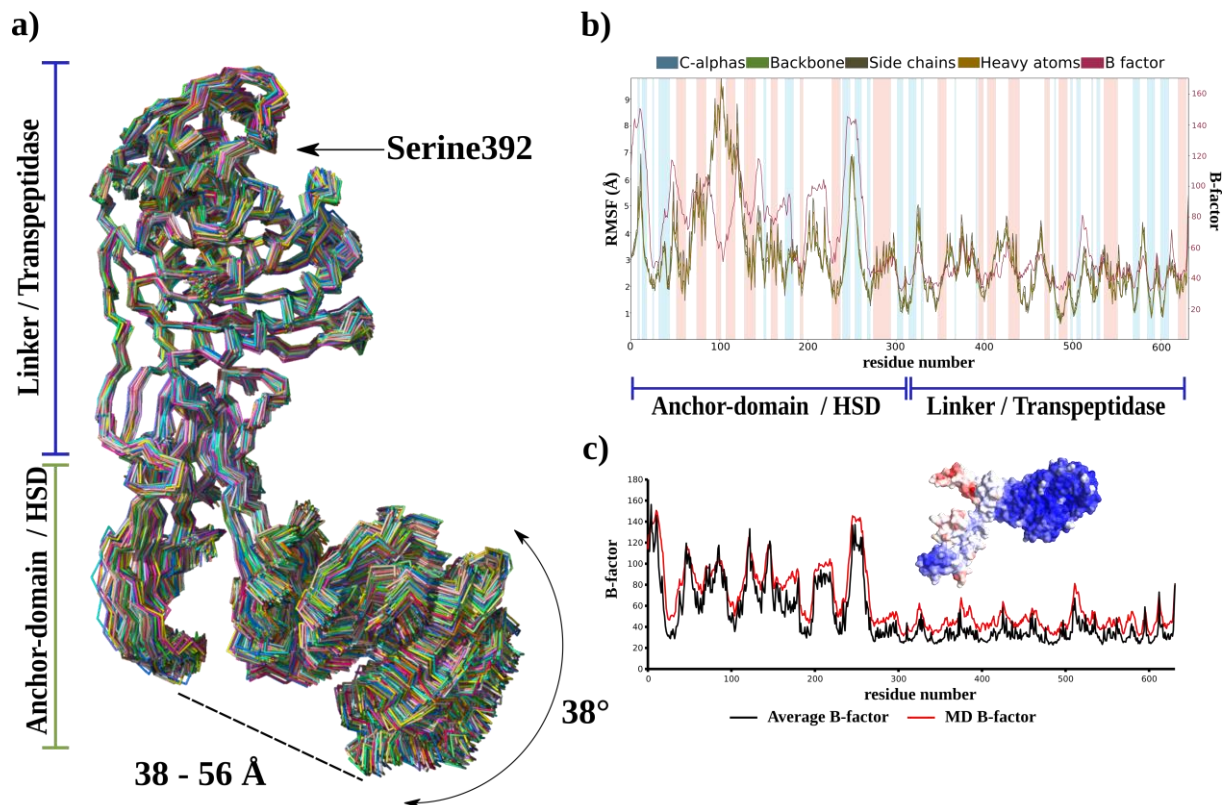


**Figure 51. Dynamic Flexibility Analysis of *Se*PBP3 Post 100 ns Molecular Dynamics Simulation.** a) Superimposition of 250 frames extracted over a 100 ns simulation duration. Delineations of flexible and rigid regions, span between the N-terminal anchor domain and HSD and angular mobility of the HSD are annotated. b) Root Mean Square Fluctuation (RMSF) and B-factor plots characterizing the fluctuations of C $\alpha$ , backbone, side chains, and heavy atoms for each residue. Secondary structure elements are highlighted with different colours:  $\alpha$ -helices are highlighted in blue and  $\beta$ -sheets in pink. Regions of flexibility and rigidity are annotated in accordance with their corresponding domains. c) Comparative B-factor plot derived from both diffraction data (average B-factor) and the MD simulation. The surface representation of *Se*PBP3 is color-coded to emphasize variations in B-factor values, providing a visual indication of structural dynamics.

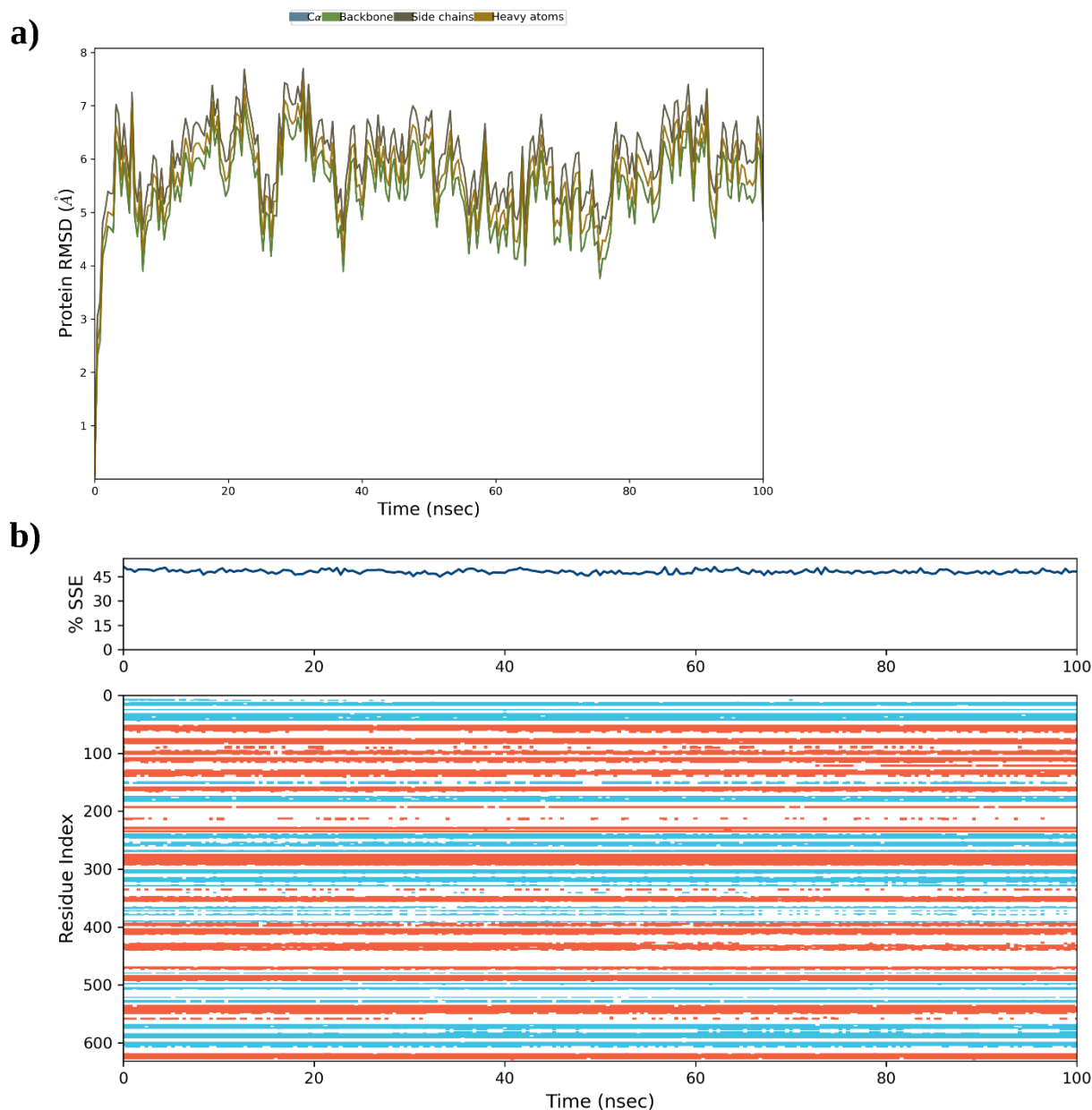


**Figure 52: Molecular Dynamics Stability Analysis of SePBP3 Over 100 ns.** a) Trajectories of RMSD values for C $\alpha$  atoms, the backbone, side chains, and heavy atoms across the 100 ns simulation period. b) Evolution of SePBP3's secondary structure content throughout the 100 ns simulation, depicted both in terms of overall percentage and per-residue distribution. Blue sections represent  $\alpha$ -helices, while red sections denote  $\beta$ -sheets.

The observations collectively indicate that SePBP3 displays inter-domain flexibility. The transpeptidase domain, characterized by its rigid body behavior aligns closely with other class B PBPs due to its structural conservation. In a similar way, the linker domain of SePBP3, featuring conserved motifs, such as R69, R230, and E277, mirrors these characteristics. However, a notable contrast is seen in the pedestal region of various class B PBPs, where the N-terminal anchor domain frequently shows weak electron density in

crystal structures. Additionally, the HDS exhibits varied spatial orientations in relation to the N-terminal anchor domain, facilitating an open and closed state at this interface.

## **Part One: Conclusion and Outlook**

This chapter presented a comprehensive investigation into *SePBP3*, as crucial targets in the development of new antibacterial drugs. The successful co-crystallization of *SePBP3* with antibiotics cefotaxime and vaborbactam is a significant contribution in understanding bacterial resistance mechanisms. Cefotaxime, a third-generation cephalosporin, exhibits broad-spectrum efficacy against both Gram-positive and Gram-negative bacteria and is particularly effective in severe infections. The combination with vaborbactam, a beta-lactamase inhibitor, enhances its antibacterial scope and strength.

The high-affinity interaction observed between *SePBP3* and these antibiotics sheds light on the potential of *SePBP3* to function as a decoy receptor. This insight could lead to novel strategies in overcoming bacterial resistance regarding multi-resistance in absence of the *MecA* gene. Furthermore, the in-depth analysis of *SePBP3*'s dynamic structural states, through SAXS and MD simulations, has been pivotal in deciphering its open and closed conformations. These conformations are crucial for interactions with yet-to-be-identified molecular entities. A further experimental validation of the flexibility of the pedestal region in class B PBPs could be achieved by leveraging advanced methodologies such as Cryo-Electron Microscopy. This approach would potentially unravel the complexities of this phenomenon.

The study of *SePBP3*'s interaction with cefotaxime and vaborbactam has laid a robust foundation for future research in antibacterial therapy. Moving forward, the exploration of *SePBP3* as a decoy receptor opens up new avenues in the fight against bacterial resistance. This approach could improve the way we prescribe antibiotics, while targeting PBPs.

In summary, the data presented not only advances the knowledge of *SePBP3* and bacterial resistance but also propels us towards innovative solutions in antibacterial drug development. The findings from this study hold significant potential for impacting future research and clinical applications in the realm of infectious diseases.

## **Part Two: Penicillin-binding Protein 2a from *Staphylococcus epidermidis* and *aureus* Recombinant Expression and Purification**

Producing and purifying SaPBP2a proved challenging, as it consistently partitioned into the insoluble fraction in *Escherichia coli*. The gene sequence, sourced directly from the *Staphylococcus aureus* genome, was modified to remove the lipid anchor and signal peptide before its incorporation into the pET11d vector, which confers ampicillin resistance. Cell lysis and protein extraction were achievable solely using a French press at 20,000 psi, as sonication did not yield successful results. Afterward, inclusion bodies were collected. The protein then required renaturation, initially in the presence of guanidine. This was followed by a meticulous refolding process, gradually eliminating guanidine through dialysis. The final yield of purified protein was about 2.27 mg per gram of bacterial pellet (Frank et al., 1995; Lim and Strynadka, 2002).

In this study, a new way of expression and purification was established to accelerate the process with a high concentration of soluble protein. The protein was engineered to omit the signal peptide and lipid anchor, substituting them with an His-tag and a TEV protease cleavage site. Adding tags can increase the solubility of recombinant proteins during the expression in *Escherichia coli* (Woestenenk et al., 2004; Paraskevopoulou and Falcone, 2018). Additionally, the entire nucleotide sequence was codon-optimized for *Escherichia coli*'s tRNA. The plasmid used for expression was switched to the pET-28a(+) vector due to its kanamycin resistance, rather than ampicillin resistance. This change was made because, despite not occurring in previous experiments, there is a possibility that ampicillin could bind to the active site of PBP2a. For protein extraction, standard sonication is sufficient, eliminating the need for a French press. In the subsequent section, the quality of the newly optimized expression and purification protocol for the protein will be detailed.

The production of *Se*PBP2a followed the procedure outlined in the 'Methods' section. Optimization of the expression protocol involved initial trials with different *Escherichia coli* strains, varying the temperature at 20 °C and 30 °C, and adjusting the length of expression time. The optimal results, depicted in figure 53, were achieved using the *Escherichia coli* BL21 DE3 Star strain. This protocol proved robust, yielding consistent

success in protein expression across a range of times and temperatures (Figure 53). However, the finalized expression protocol was determined to be a 4-hour cultivation at 30 °C post-induction when the optical density (OD<sub>600</sub>) reached 0.6, using 1 mM IPTG as the inducer.

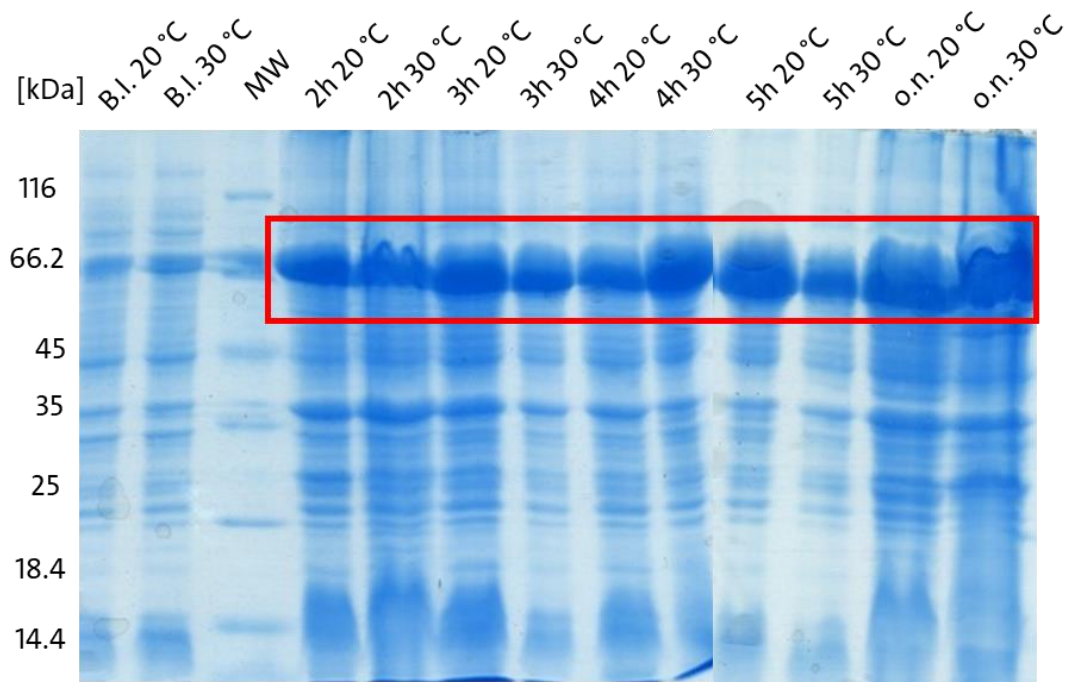


**Figure 53: SDS-PAGE Analysis of the Test Expression at 20 °C and 30 °C of SePBP2a in BL21 DE3 cells at a 12% Polyacrylamide Gel.** MW: Unstained Protein Molecular Weight; B.I.: before induction with 1mM IPTG; 2h: two hours of expression; 3h: three hours of expression; 4h: four hours of expression; 5h: five hours of expression; o.n.: overnight expression. Overexpressed SePBP2a is highlighted within red rectangle and fits approximately with the calculated size of 74.8 kDa.

Modifying the protein to eliminate the lipid anchor and add an His-tag sequence, along with a TEV protease cleavage site, does not hinder the expression of Class B PBPs. The protein is highly abundant in the Ni-NTA matrix and therefore are only little unspecific bindings of *Escherichia coli* proteins (Figure 54). The elution of the Ni-NTA affinity chromatography was loaded onto the SEC as a polishing step. The final concentration of SePBP2a after the SEC was 20 mg per liter of expression culture.

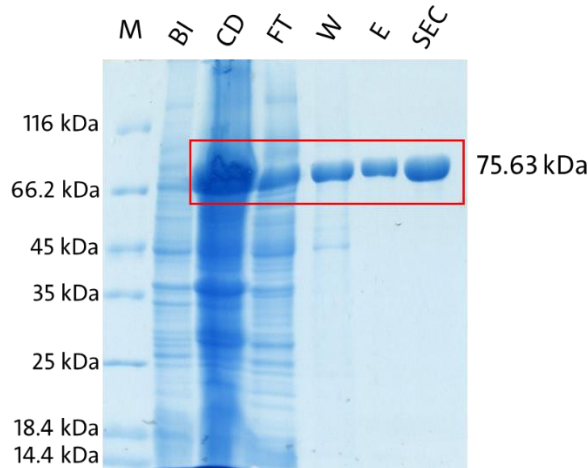


**Figure 54: SDS-PAGE Analysis of the Expression and Purification of SePBP2a at a 12% Polyacrylamid Gel.** M: unstained protein molecular weight; CD: cell debris after sonification and centrifugation; FT: flow-through of unbound protein; W: removal of unspecific bound protein with 20 mM imidazole; E: elution of SePBP2a with 250 mM imidazole; SEC: size-exclusion chromatography. FT, W and E refers to Ni-NTA affinity chromatography purification. Overexpressed SePBP2a is highlighted within red rectangle and fits approximately with the calculated size of 75.63 kDa.

Following the chromatography, only the fractions corresponding to the targeted protein peak, shown in figure 55, were collected.

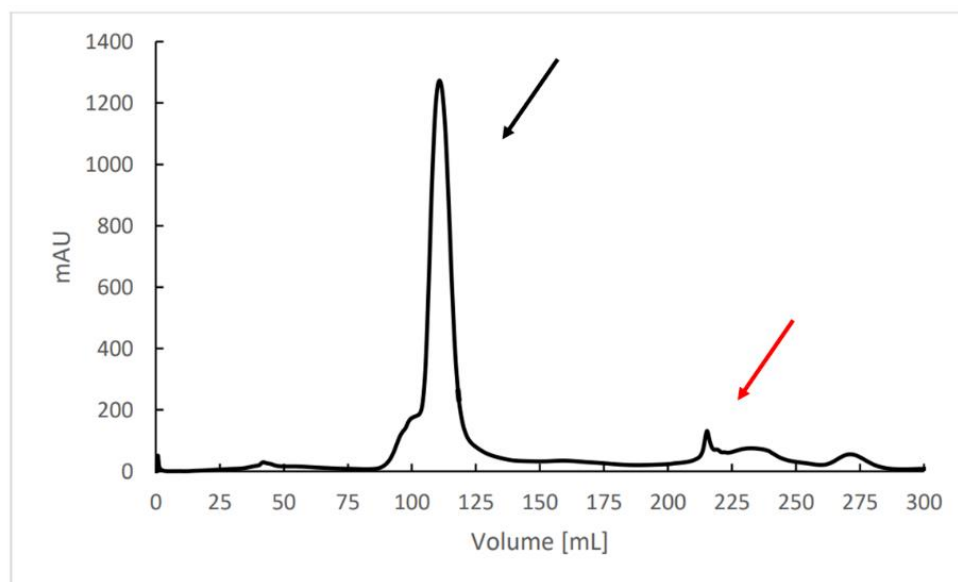


**Figure 55: Size Exclusion Chromatogram (SEC) of SePBP2a after Ni-NTA Affinity Chromatography Purification.** SEC was used after Ni-NTA affinity chromatography purification as a polishing step. SePBP2a SEC profile (black arrow) exhibits a distinct peak between 100 and 125 ml. Small impurities (red arrow) were not collected.



The His-tag was cleaved from the protein by treating the purified *Se*PBP2a with TEV protease, which, as a cysteine protease, requires DTT for activation (Raran-Kurussi et al., 2017). The enzymatic reaction used a ratio of 1 mg of TEV protease to 15 mg of *Se*PBP2a. Following a 5-hour incubation period at 7 °C, the reaction was concluded, and the protein underwent a subsequent round of purification through size-exclusion chromatography (SEC). To verify the efficacy of the cleavage, *Se*PBP2a was subjected to SDS-PAGE analysis. The resulting lower migration of the *Se*PBP2a band on the gel served as an indicator of successful cleavage (Figure 56).

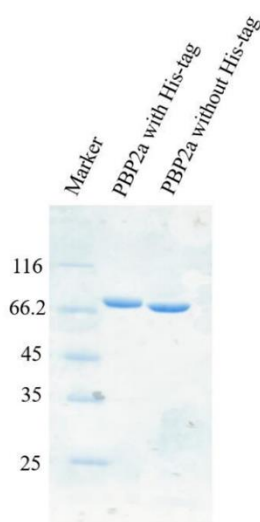


**Figure 56: SDS-PAGE Analysis of the of *Se*PBP2a with His-Tag and after Removal of the His-Tag at a 12% Polyacrylamid Gel.** The protein's molecular weight is reduced by 2.26 kDa due to the removal of the His-tag and TEV protease cleavage sequences.

Bocillin-FL, a fluorescent  $\beta$ -lactam antibiotic, serves as an effective agent for testing  $\beta$ -lactam binding at the active site of the transpeptidase domain. The assay followed the protocol established by Zhao G et al. (G. Zhao et al., 1999). *Se*PBP2a exhibited the ability to bind Bocillin-FL both with and without the His-tag, indicating that the tag's removal does not impair the transpeptidase activity. Moreover, cefotaxime was incorporated in a competitive binding assay to explore the binding potential of *Se*PBP2a with other antibiotics (Figure 57).

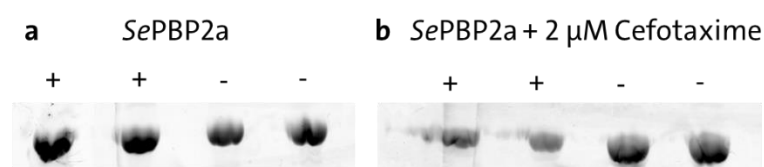


**Figure 57: Binding Assay of *SePBP2a* with and without His-tag and with Cefotaxime.** The protein demonstrated the ability to bind Bocillin-FL, a fluorescent  $\beta$ -lactam antibiotic used in binding assays, indicating its functional integrity in  $\beta$ -lactam binding. This binding capacity was maintained despite the presence of the His-tag (a; + means with His-tag and – without). Additionally, cefotaxime, representing other classes of antibiotics, is able to bind as well (b; + means with cefotaxime and – without).

The expression protocol proves to be effective, allowing for the production of the protein at a high concentration of 20 mg per liter of culture. Crucially, the protein is predominantly found in the soluble fraction, and its solubility remains unaffected by the removal of the His-tag. The functionality of the transpeptidase domain is retained, affirming that the protein is suitable for experimental applications.

### Protein Characterization

DLS was performed to assess the dispersity of the purified and concentrated *SePBP2a* protein solution. As depicted in figure 58, the hydrodynamic radius of the protein solution, which was monodisperse and had a concentration of 18 mg/ml, measured  $4.51 \pm 0.06$  nm. This corresponds to a calculated molecular weight of 104.3 kDa, which is larger than the theoretical molecular weight of the protein (without His-tag) sequence (73.37 kDa). It's important to note that the calculation for the hydrodynamic radius is optimized for spherical particles, and in this case, *SePBP2a* exists as a monomeric protein in the solution.

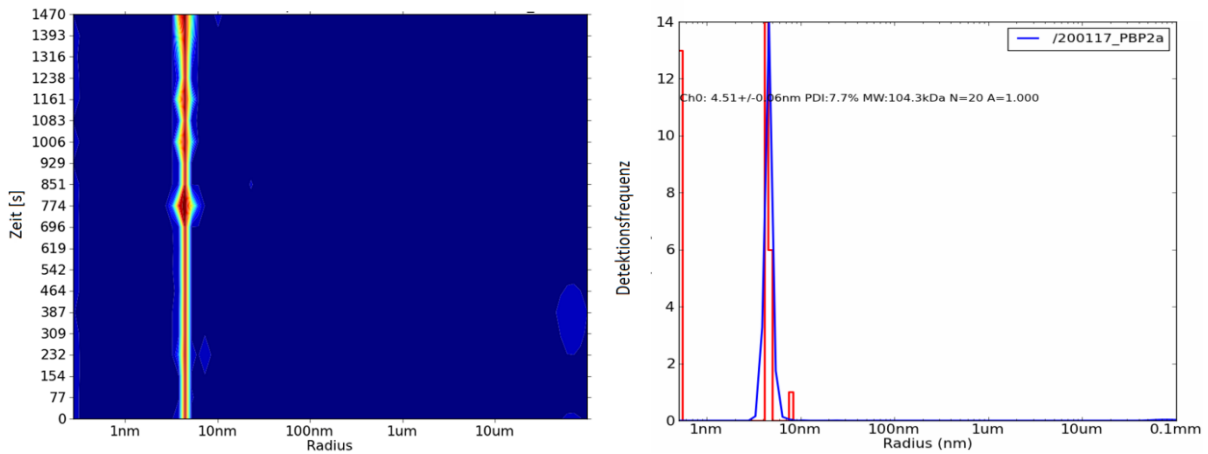


**Figure 58: Dynamic Light Scattering Dispersity Profile of SePBP2a after Removal of the His-tag.** Monodispersity of purified protein solution (18 mg/ml) was confirmed by DLS measurements. Left: heat map of radius distribution. Right: hydrodynamic radii against frequency of detection confirmed a monomer in solution. Calculation of the molecular weight (104.3 kDa) is optimized for spherical particles and therefore not correlating with the actual molecular weight of the L-shaped PBP2a (73.37 kDa).

The secondary structure of the SePBP2a protein in a monodisperse solution was analyzed using CD spectroscopy in the wavelength range of 190 to 260 nm. The CD spectrum of SePBP2a was recorded 15 times, with all individual spectra being subsequently merged to enhance accuracy. To establish a baseline, the buffer solution was measured five times; these measurements were also merged to form a consolidated background signal. The final spectrum of the protein was obtained by subtracting this aggregated buffer spectrum from the merged SePBP2a spectrum. Figure 59 illustrates the relationship between millidegree and wavelength in the protein's spectrum. The presence of a high percentage of folded protein is indicated by the spectral features, revealing a composite of  $\alpha$ -helices,  $\beta$ -sheets, and disordered regions. Additionally, identical measurements were performed on the monodisperse protein after removal of the His-tag. The results indicate that the protein's folding remains unaffected by this modification, as evidenced by the similarity of the spectra in both cases (Figure 59).

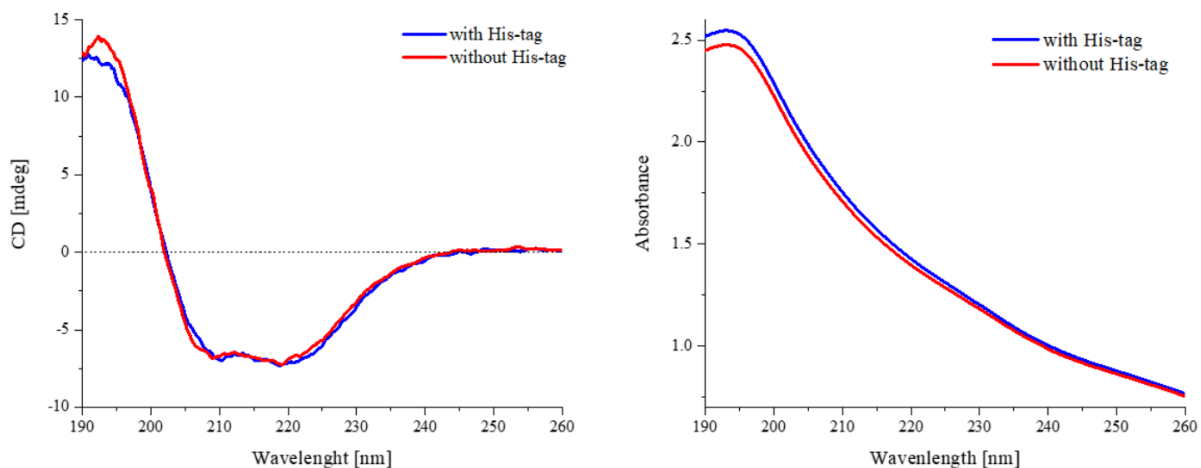


**Figure 59: Circular Dichroism Plot of *SePBP2a* before and after SEC Removal of the His-tag.** Secondary structure analysis of *SePBP2a* revealed a mixture of  $\alpha$ -helices and  $\beta$ -sheets and confirmed a folded protein, also after removing the His-tag. Measurement was conducted with a concentration of 0.1 mg/ml.

The characterization of *SePBP2a* underscores the success of the revised expression and purification protocol. This protocol results in a protein that is not only highly concentrated and soluble, but also correctly folded and exhibits a monodisperse profile. Thus, this study presents an effective alternative to the more time-consuming and complex established protocols (Frank et al., 1995), demonstrating a streamlined approach to protein production.

### Crystallization

The purified protein was subjected to crystallization using the established protocol of Lim et al. (Lim and Strynadka, 2002). This protocol involves a crystallization mixture containing 20% (v/v) PEG 550 MME, 0.95 M NaCl, 0.1 M HEPES at pH 7, and 16 mM CdCl<sub>2</sub>, maintained at 18 °C. Cadmium chloride is a critical component in this setup, known for its role in facilitating the bridging between two protein molecules within the crystal lattice.

PEG 550 MME (Polyethylene Glycol 550 MonoMethyl Ether) is a commonly used precipitating agent in protein crystallization. Its role is to induce protein crystallization by reducing the solubility of proteins in solution, a process known as "salting out." PEG 550 MME is particularly effective due to its relatively low molecular weight, which allows

for better control over the crystallization environment and can lead to the formation of more well-defined crystals (Hata et al., 2021).

The high salt concentration, in this case, provided by NaCl, plays a dual role in protein crystallization. First, it helps in maintaining the ionic strength of the solution, which is crucial for maintaining protein stability and solubility. Second, at higher concentrations, salt can promote protein crystallization by a mechanism like PEG, where it reduces the solubility of proteins in the solution. This is particularly useful in cases where proteins are less responsive to crystallization solely by PEG (Yamanaka et al., 2011).

Crystallization attempts were unsuccessful when the protein retained the His-tag and TEV cleavage site. This outcome aligns with established observations in protein biochemistry, which suggest that the presence of such tags often impedes crystallization due to the introduction of increased conformational flexibility (Kim et al., 2011). This enhanced flexibility, while advantageous for maintaining protein solubility in solution, paradoxically acts as a hindrance in the crystallization process by disrupting the protein's ability to form a regular, orderly lattice essential for crystal formation.

Crystallization efforts with the tag-free protein variant also did not yield successful results. Consequently, a comprehensive screening of the crystallization conditions was undertaken. This included maintaining a high salt concentration, utilizing PEG 550 MME, and incorporating cadmium chloride. The specific concentrations and conditions explored in this process are detailed in figures 60 and 61.

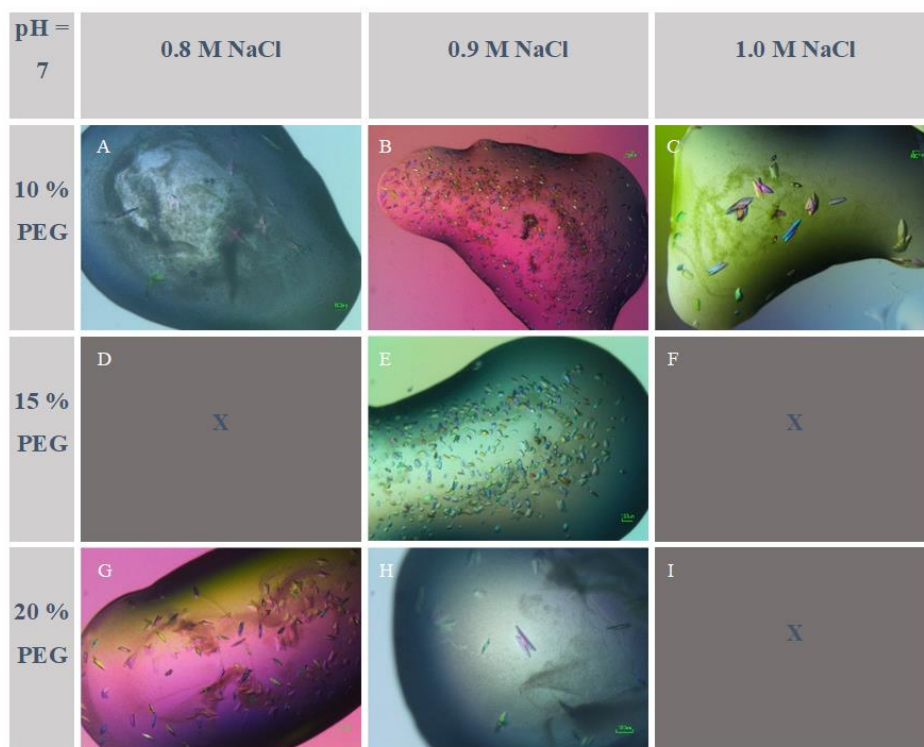


**Figure 60: Crystallization Approach of *SePBP2a* under the pH value of 7.** The crystallization approach was adopted from Lim et al (Lim and Strynadka, 2002). The differences are the concentration of NaCl and PEG at a pH value of 7.

The alteration of the pH value from 6 to 8 revealed that crystal formation did not occur at a pH of 6. Crystallization was only successful at pH values of 7 and 8, and even then, only under certain conditions. As depicted in figures 60 A, H, and 61 C, D, G, some of the resulting crystals displayed a "hairpin" morphology. Notably, these crystals did not produce diffraction patterns during X-ray crystallography measurements. Furthermore, in several conditions, as shown in figures 60 B, E, and 61 H, the formation of micro-sized crystals was observed.

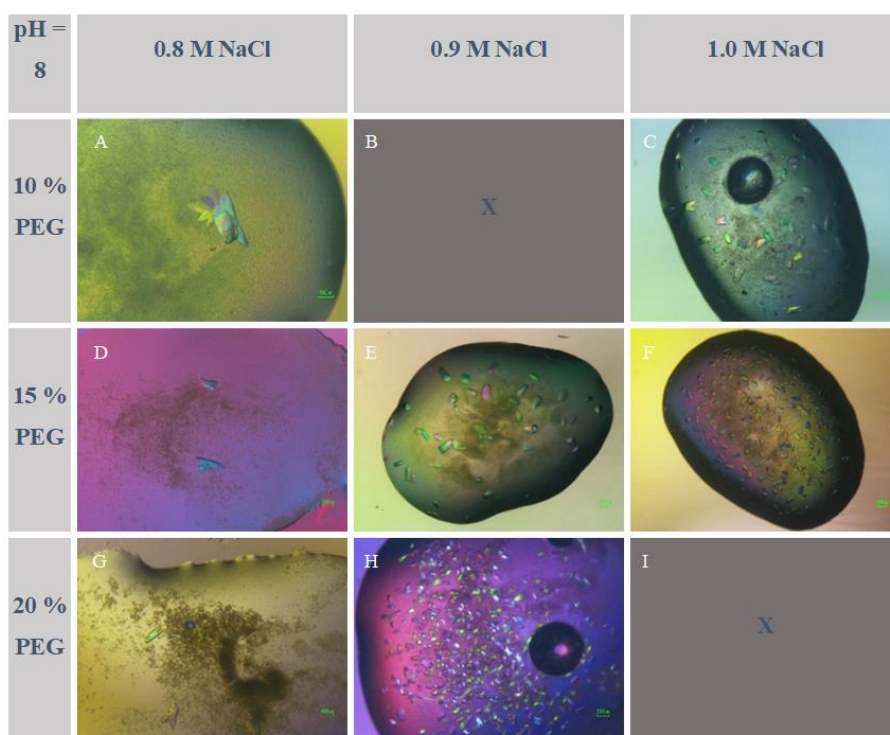


**Figure 61: Crystallization Approach of SePBP2a under the pH value of 8.** The crystallization approach was adopted from Lim et al (Lim and Strynadka, 2002). The differences are the concentration of NaCl and PEG at a pH value of 8.

In the crystallization setup, the observed crystal growth occurred within a distinctive phase exhibiting a membrane-like texture, a condition that supported to for the crystal growth. This specific growth environment posed significant challenges in the isolation of individual crystals. Utilizing capton or nylon loops for harvesting often resulted in the concurrent collection of multiple crystals, complicating the selection process for X-ray crystallography.

Additionally, the cryoprotection step, involving the immersion of crystals in a cryo buffer (compositionally akin to the mother liquor but supplemented with an additional 12% glycerol), encountered difficulties. The unique membrane-like phase of the crystal environment hindered effective diffusion of the cryo buffer into the crystal matrix. This impediment in buffer infiltration could potentially impact the cryoprotection efficacy and, by extension, the structural integrity of the crystals during cryogenic X-ray analysis.

#### **Data Collection of the Macromolecular Crystals**

The data collection was conducted at the beamline P11 of PETRA III, DESY (Meents et al., 2013). During this process, the crystal was systematically rotated to ensure a complete

capture of diffraction data from all angular orientations, while consistently maintaining a temperature of 100 K.

### **Direct Comparison of Crystallographic Data to *Sa*PBP2a (PDBID: 1VQQ)**

In the assessment of crystallographic data quality, specific parameters are critical to demonstrate the reliability of the dataset. This study aims to compare our collected data directly with that of the established *Sa*PBP2a (PDBID: 1VQQ), focusing on parameters such as the space group, unit cell dimensions, and quality indicators.

### **Space Group and Unit Cell Dimensions**

Both datasets share the space group  $P2_12_12_1$ , a testament to the similar three-dimensional arrangement of molecules within the crystal lattice. The unit cell dimensions are virtually identical, with both datasets presenting cell dimensions of  $a = 80.87 \text{ \AA}$ ,  $b = 100.6 \text{ \AA}$ , and  $c = 186.23 \text{ \AA}$ . This correspondence suggests that the crystalline environments are nearly equivalent, highlighting that the removal of the His- tag leads to the same crystallization.

### **Resolution**

While the overall parameters of the dataset closely resemble those of *Sa*PBP2a, a notable distinction lies in the resolution limits. *Sa*PBP2a boasts an impressive high-resolution limit of  $1.8 \text{ \AA}$ . The dataset of *Se*PBP2a, however, attains a resolution of  $2.51 \text{ \AA}$ . This disparity is likely attributable to the suboptimal diffusion of the cryoprotectant into the crystals. Inadequate penetration of the cryoprotectant can lead to crystal imperfections and the presence of ice rings in the diffraction pattern, phenomena that were indeed observed during our data collection. These ice rings are indicative of the formation of crystalline ice, which scatters X-rays in a manner that can obscure the finer details of the protein crystal diffraction, thus limiting the resolution (Garman and Schneider, 1997).

### **Quality Indicators**

The Wilson B-factor of  $23.9 \text{ \AA}^2$ , mirroring that of *Sa*PBP2a and reflecting a similar level of clarity in the electron density map. The total number of reflections and unique reflections in our dataset closely align with the 152,181 and 71,280 reported for *Sa*PBP2a, respectively, suggesting a comparable degree of data redundancy and coverage. Further, the CC1/2 value of 0.999 is consistent with the high correlation coefficient seen in



*SaPBP2a*, reinforcing the signal strength and reliability. The  $I/\sigma$  ratio, another indicator of data strength, stands at 23.4 for *SePBP2a*'s data, on par with the 23.4 reported for *SaPBP2a*, indicating a strong signal across the dataset. *SePBP2a* achieves a completeness of 99.6%, closely matching the 97.4% completeness of *SaPBP2a*.

**Table 24: Data Collection and Refinement of *SaPBP2a* and *SePBP2a* – a Comparison of the Data Quality**

Data Collection	<i>SaPBP2a</i> (PDBID 1VQQ)	<i>SePBP2a</i>
X-ray source	NSLS X8C1	P11, Petra III, DESY
Detector	ADSC Quantum 4	EIGER 2X 16M
Space group	P2 <sub>1</sub> 2 <sub>1</sub> 2 <sub>1</sub>	P2 <sub>1</sub> 2 <sub>1</sub> 2 <sub>1</sub>
Cell dimensions a, b, c (Å)	80.87, 100.6, 186.23	80.87, 100.6, 186.23
Wavelength (Å)	Not available	1.033
Resolution (Å)	24.92- 1.8 (1.9-1.8)	49.24 – 2.5 (2.6-2.5)
Total reflections	71280 (7833)	70884 (7997)
Total unique reflections	152181 (2318)	167722 (11304)
Wilson B-factor (Å <sup>2</sup> )	23.9	21.6
R <sub>meas</sub>	Not available	0.026 (0.227)
CC1/2	0.999 (0.996)	0.999 (0.956)
$I/\sigma$	23.4 (2.7)	29.67 (1.17)
Completeness	97.4 (97.3)	99.6 (98.4)
<b>Refinement</b>		
Reflection used	137299	137292
R <sub>work</sub>	0.23	0.22
R <sub>free</sub>	0.27	0.29
No. atoms		
Protein	10.125	10.125
Ligand/ion	11	11
Water	508	496

<b>Average B-factor (<math>\text{\AA}^2</math>)</b>		
<b>Protein</b>	33.2	30.8
<b>Ligand/ion</b>	Not available	42.6
<b>Water</b>	Not available	26.11
<b>R.m.s. deviations</b>		
<b>Bond lengths (<math>\text{\AA}</math>)</b>	0.0082	0.0084
<b>Bond angles (<math>^\circ</math>)</b>	1.04	1.035
<b>Ramachandran</b>		
<b>avored (%)</b>	93.02	98.2
<b>allowed (%)</b>	5.55	1.72
<b>outliers (%)</b>	1.43	0.08
<b>PDBID</b>	1VQQ	

The dataset (Table 24) obtained for *Se*PBP2a not only meets but closely aligns with the quality parameters of the *Sa*PBP2a dataset in all assessed metrics. Consequently, the newly developed expression and purification protocol, optimized for crystallization, holds significant promise for future research. This approach is particularly advantageous as it eliminates the need to address challenges associated with inclusion bodies and solubility issues.

### **Analysis of the Influence of the allosteric Domain on the active Site of PBP2a**

In this chapter, the influence of the allosteric center of PBP2a in relation to the active site is discussed. This allosteric center is unique among all PBPs and is located in the pedestal region with a distance of about 60  $\text{\AA}$  to the active center (Figure 62). The precise function of the allosteric site in PBP2a remains uncertain. However, the prevailing hypothesis within the scientific community suggests that a segment of the peptidoglycan, already integrated into the cell wall, binds to this allosteric site. This interaction is thought to induce a conformational change that opens the enzyme's active site. The opening of the active site facilitates the interaction of newly synthesized peptidoglycan with the active serine residue of PBP2a. Ultimately, this interaction is believed to be critical for the

cross-linking of peptidoglycan chains, a key step in bacterial cell wall synthesis (Otero et al., 2013). A targeted molecular dynamics (MD) simulation predicted signal transduction from the allosteric domain to the active site, mediated by a series of charge transfers between charged amino acid side chains. However, the precise mechanistic pathway remained elusive (Acebron et al., 2015). Additionally, another targeted MD simulation demonstrated conformational dynamics of the protein, characterized by bending, wiggling, and twisting motions, concurrent with the binding of muramic acid at the allosteric domain (Chiang et al., 2020).

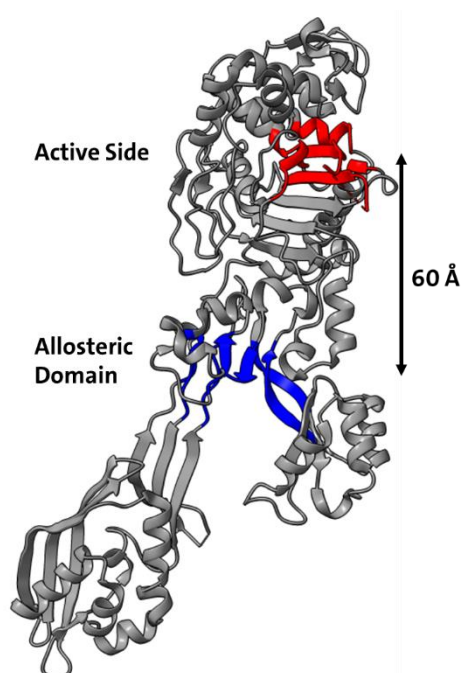


**Figure 62: PBP2a Structure with highlighted allosteric Domain and active Site.** The active site (red) is approximately 60 Å away from the allosteric domain (blue).

There are two crystal structures that can demonstrate a connection with a ligand in this context. Ceftaroline (PDBID: 3ZG0) binds both at the active and at the allosteric center, and muramic acid (PDBID: 3ZG5), as a peptidoglycan substitute, also binds in the allosteric center (Otero et al., 2013). In pursuit of novel therapeutic agents, this study adopted an alternative approach, utilizing a specialized collection of 2,000 natural compounds. This unique library, meticulously curated and characterized by the Molecular Bank at the International Center for Chemical and Biological Sciences (ICCBS), Karachi, Pakistan, serves as the foundation for our structure-based drug design endeavors (for more information, see (International Center for Chemical and Biological

Sciences - Welcome (iccs.edu)). The natural compounds, primarily derived from botanical sources within the ICCBS Molecular Bank, exhibit a broad spectrum of pharmacologically pertinent properties. These include anti-tumor, anti-oxidant, anti-inflammatory, and notably antiviral activities. An additional advantage of these compounds lies in their generally milder side effect profile and the potential for reduced production costs, compared to many conventional pharmaceuticals currently available in the market (Calland et al., 2012).

The assessment of binding affinity was conducted through molecular docking techniques. From an extensive library of 2,000 compounds, the most promising candidates emerged, categorizable into two distinct groups (Figure 63 and Table 25).

**Quercetin:** Among the compounds analyzed, a subset based on quercetin, notably rutin, has shown significant bactericidal effectiveness against MRSA cells (Rani et al., 2014). Additionally, Isorhamnetin-3-robinobioside and 5-O-Quercetibinoside, also quercetin derivatives, have demonstrated high docking scores, indicating potential efficacy. Clinical studies have shown that oral quercetin glycosides, at doses of 3-1,000 mg/day for up to three months, are generally safe with minimal adverse effects (Harwood et al., 2007). However, a study on chronic prostatitis patients noted mild, temporary side effects like headache and tingling at 1,000 mg/day (Shoskes et al., 1999). In a cancer trial, intravenous quercetin at doses  $\geq 10.5$  mg/kg caused nausea, vomiting, and other symptoms, and very high doses (up to 51.3 mg/kg) led to kidney toxicity but no severe renal issues (Ferry et al., 1996). Quercetin generally exhibits low bioavailability and results in minimal plasma levels. However, the type of glycosides in various food sources significantly influences its bioavailability. Onions, containing glucosides, provide a more bioavailable form of quercetin compared to apples and tea, which are rich in rutin and other glycosides (Manach et al., 2005). 5-O-Quercetibinoside, sourced from *Nerium oleander* leaves, and Isorhamnetin-3-robinobioside, extracted from *Opuntia ficus-indica*, *Hippophae rhamnoides*, and *Ginkgo biloba*, both exhibit improved bioavailability and reduced cytotoxicity. Consequently, they present as viable alternatives to rutin. (Siddiqui et al., 2012; Antunes-Ricardo et al., 2017).

**Pentacyclic triterpene-backbone:** These compounds are grouped together due to their shared pentacyclic triterpene backbone structure. While specific research on their effects against MRSA is lacking, they all display some degree of anti-tumor, anti-viral, and anti-bacterial activities. Their glycosylation is known to enhance solubility, thereby improving bioavailability (Manach et al., 2005). Cucurbitacins, notably, have a recognized human lethal dose of around 300 mg (Ponsankar et al., 2020). Cucurbitacin-I-glucoside, an extract from *Citrullus lanatus*, has the potential to be significantly reduced regarding the toxicity as it is glycosylated (Kaushik et al., 2015). Compounds with the origin of glycyrrhetic acid, also known as enoxolone, are known to serve anti-viral, anti-tumor and anti-bacterial activity. There is nothing known about the bioavailability and toxicity (Asl and Hosseinzadeh, 2008).

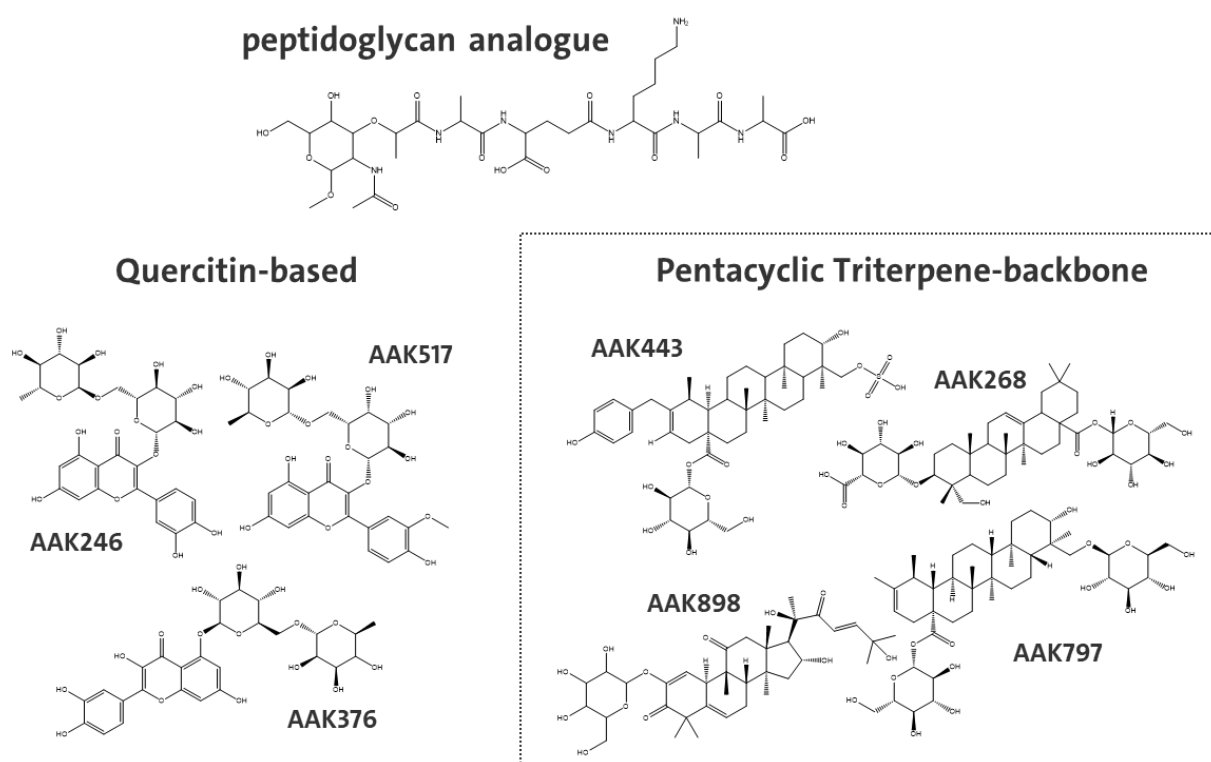


**Figure 63: Compounds with the highest Docking Score.** The best hits from the compounds can be separated into two groups: Quercetin-based and compounds with a pentacyclic triterpene-backbone. The peptidoglycan analogue is used for a comparison.

**Table 25: Compounds with the best Docking Score.**

ID-Number	[Da]	NAME	IUPAC NAME
AAK246	610.518	Rutin <i>Quercitin-based</i>	2-(3,4-dihydroxyphenyl)-5,7-dihydroxy-3-[[[(2S,3R,4S,5S,6R)-3,4,5-trihydroxy-6-({[(2R,3R,4R,5R,6S)-3,4,5-trihydroxy-6-methyloxan-2-yl]oxy}methyl)oxan-2-yl]oxy}-4H-chromen-4-one
AAK517	624.544	Isorhamnetin-3-robinobioside <i>Quercitin-based</i>	5,7-dihydroxy-2-(4-hydroxy-3-methoxyphenyl)-3-((2S,3R,4S,5R,6R)-3,4,5-trihydroxy-6-(((2R,3R,4R,5R,6S)-3,4,5-trihydroxy-6-methyltetrahydro-2H-pyran-2-yloxy)methyl)tetrahydro-2H-pyran-2-yloxy)-4H-chromen-4-one
AAK376	610.518	5-O-Quercetibinoside <i>Quercitin-based</i>	2-(3,4-dihydroxyphenyl)-3,7-dihydroxy-5-((2S,3R,4S,5S,6R)-3,4,5-trihydroxy-6-(((2R,3R,4R,6S)-3,4,5-trihydroxy-6-methyltetrahydro-2H-pyran-2-yloxy)methyl)tetrahydro-2H-pyran-2-yloxy)-4H-chromen-4-one
AAK443	807	<i>pentacyclic triterpene-backbone</i>	3b,23,dihydroxyurs-20-en-28-al-23-sulfate-30-hydroxyphenyl-28-O-a-D-glucopyranosyl ester
AAK268	810.964	<i>pentacyclic triterpene-backbone</i>	3-O-b-D-Glucuronopyranosyl-24-hydroxy-olean-12-en-28-oic acid 28-O-b-D-glucopyranoside
AAK898	676,791	Cucurbitacin-I-glucoside <i>pentacyclic triterpene-backbone</i>	(8S,9R,10R,13R,14S,16R,17R)-17-((E)-2,6-dihydroxy-6-methyl-3-oxohept-4-en-2-yl)-16-hydroxy-4,4,9,13,14-pentamethyl-2-(3,4,5-trihydroxy-6-(hydroxymethyl)tetrahydro-2H-pyran-2-yloxy)-7,8,9,10,12,13,14,15,16,17-decahydro-3H-cyclopenta[a]phenanthrene-3,11(4H
AAK797	796,981	<i>pentacyclic triterpene-backbone</i>	3beta-hydroxy-23,28-di-O-beta-D-glucopyranosyl-taraxer-20-en-28-oic acid

### **Molecular Docking and MD Simulation reveals Mechanism of Serine 403 Displacement**

In this comprehensive analysis of molecular docking results, we have assessed the interaction of various compounds with a target protein, using Docking Score and E Model values as primary indicators of binding affinity and stability. The Docking Score predicts

the strength of the interaction, with lower scores indicating higher affinity, while the E Model reflects the energy stability of the compound within the protein-ligand complex, where more negative values denote greater stability (Table 26).

Compound AAK246, Rutin, emerges as the front-runner, exhibiting the strongest binding affinity with a Docking Score of -8.6, and the most stable interaction, as suggested by the E Model value of -100.1. In contrast, compound AAK268 appears less promising, reflected by a Docking Score of -8.25 and an E Model of -79.0, which are the least favorable metrics among the group. Overall, the remaining compounds exhibit interactional similarities to rutin, which has previously demonstrated bactericidal activity against MRSA. Such a correlation suggests the potential of the remaining compounds in exerting comparable therapeutic effects against this resistant bacterial strain.

Across the dataset, the amino acid residues GLU170, GLU239 and ARG151 are the notable point of interaction for multiple compounds. These are the residues are the ones which are mutated in resistance strains (Otero et al., 2013).

**Table 26: Compounds with the AA Interactions, Dockings Scores and E Model.**

ID-Number	AA interaction	Docking Score [kcal/mol]	E Model [kcal/mol]
AAK246	GLU170, GLU239, THR165, THR216, LYS148, ARG151, PRO213, MET372, TYR373	-8.6	-100.1
AAK517	GLU170, GLU239, THR165, THR238, MET372, LYS148	-8.6	-99.1
AAK376	GLU170, SER149, THR165, ARG151, MET372	-8.8	-95.8
AAK443	GLU170, THR165, SER191, THR216, SER240, ARG151, LYS215, TYR373	-8.5	-90.3

<b>AAK268</b>	GLU239, ASP295, SER149, THR216, SER240, HIS293, LYS148, LYS273, TYR196	-8.25	-79.0
<b>AAK898</b>	ASP275, ARG151, ARG241	-8.4	-94.4
<b>AAK797</b>	THR165, ARG241, MET372	-8.3	-95.4

The engagement of the candidate compounds with the allosteric domain induces a conformational shift, characterized by the displacement of Tyrosine 445—a residue that ordinarily occludes access to the active site cavity. This structural alteration is depicted in figure 64, where it becomes evident that subsequent to allosteric activation, Serine 403—critical for substrate and inhibitor interaction—is rendered accessible for potential binding events.

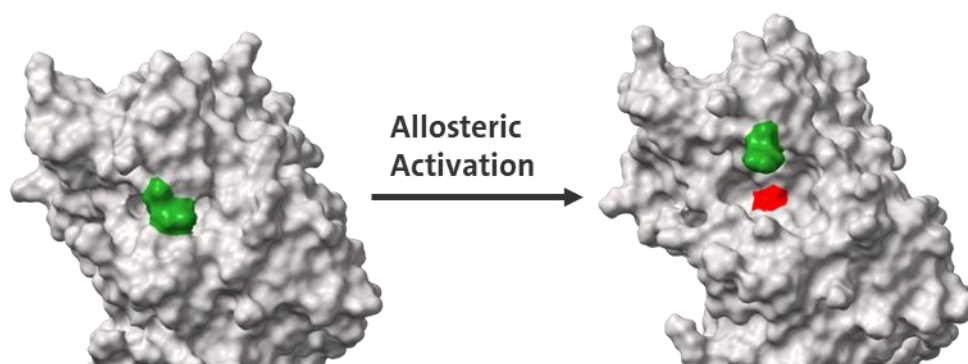


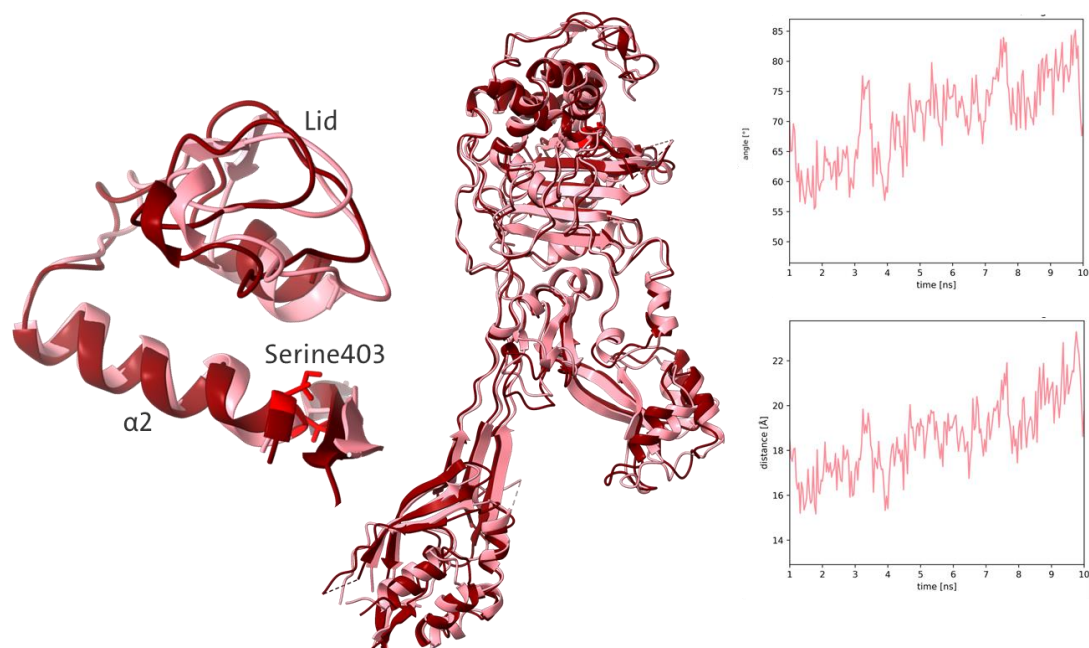
**Figure 64: PBP2a Transpeptidase Cavity with open and closed State.** After allosteric activation, tyrosine 445 (green) undergoes a displacement and opens the cavity to make the active serine 403 accessible.

In the subsequent section, a detailed analysis is conducted on three specific parameters crucial to the functionality of the active site. Initially, an investigation is conducted on the dynamics of the protein's lid, a structure situated atop the transpeptidase domain and intricately linked to the second  $\alpha$ -helix which contains the active serine. This helix harbors the active serine residue, a site of paramount importance for enzymatic activity. It is established that the effective binding of inhibitors necessitates a strategic displacement of this serine residue, enabling the inhibitors to occupy the active site (Lim and Strynadka, 2002). Subsequent to the investigation of lid movement, the analysis



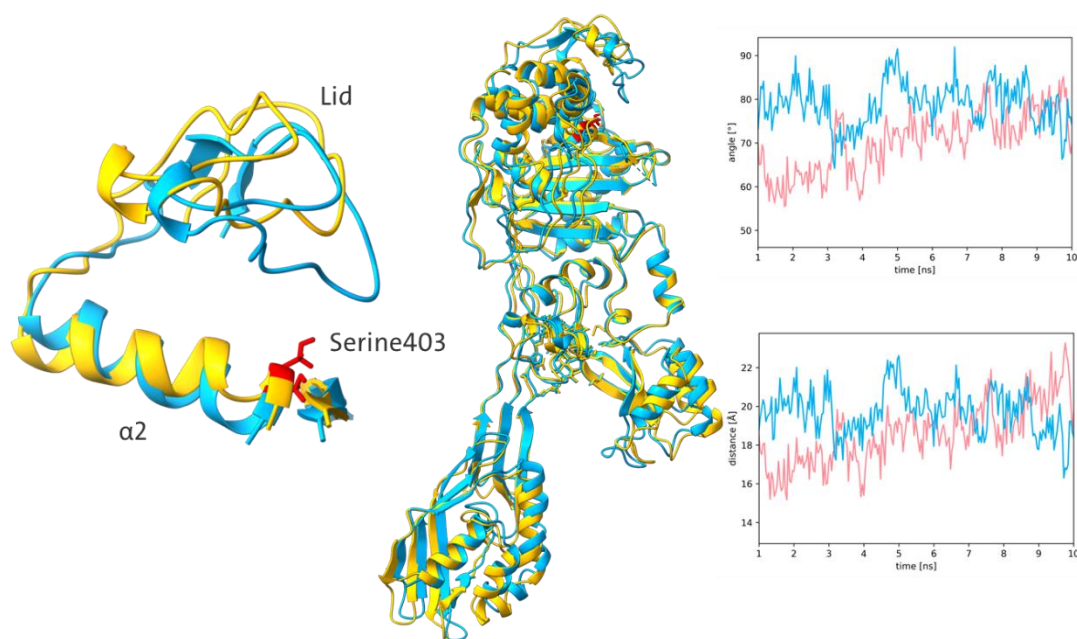
extends to quantifying the spatial configuration of the active site cavity. Two additional parameters are meticulously evaluated: the linear distance spanning the cavity's extremities and the angular degree of the cavity's aperture. The former is quantified by measuring the distance between amino acid residues TYR446 and ASP638. Concurrently, the angular parameter is determined by calculating the angle subtended by TYR446, SER402, and ASP638. These measurements are monitored over a simulation period of 10 nanoseconds to capture the dynamic nature of the active site conformation.

Figure 65 illustrates the inherent capacity of the protein to undergo conformational opening in the absence of any external activation. Following a 10 ns molecular dynamics simulation, a subtle repositioning of the lid towards the upper region is observed, which corresponds to an increase in the cavity's openness. Despite this shift, the helix retains its alignment comparative to the initial timepoint, and the active serine remains obscured by the  $\beta$ -sheet. This spontaneous structural transition might elucidate the occurrence of co-crystal X-ray structures of PBP2a with inhibitors, suggesting that elevated concentrations of an inhibitor could potentiate binding to the active site even when the serine residue is not readily exposed.



**Figure 65: PBP2a during a 10 ns MD Simulation.** The cavity of the active site is gradually opening during the simulation. The active serine is still partly hidden behind the  $\beta$ -sheet.

Figure 66 presents a comparative analysis of the dynamic behavior of PBP2a in isolation and in complex with a peptidoglycan analogue, monitored over a simulation timespan of 10 nanoseconds. In the presence of the peptidoglycan analogue, the active site cavity immediately adopts an open conformation, which is sustained throughout the duration of the simulation. This persistent openness is accompanied by an upward shift in the position of the lid, prompting a notable conformational adjustment in  $\alpha$ -helix 2. As a result, the active serine residue is no longer sequestered by the  $\beta$ -sheet, rendering it fully accessible. These observations support the hypothesis that the binding of a peptidoglycan fragment to the allosteric domain is a prerequisite for the PBP2a protein to facilitate the subsequent association of newly synthesized peptidoglycan with the active serine (Acebron et al., 2015).



**Figure 66: PBP2a with and without the Peptidoglycan Analogue during a 10 ns Simulation Time.** The PBP2a peptidoglycan analogue complex (yellow) exhibits an open active site cavity and an accessible serine 403 during the measurement.

Figure 67 delineates the outcomes from simulations comparing the PBP2a protein in isolation and in complex with compound AAK443 over a 10 ns period. The data indicates that AAK443's interaction with the allosteric domain does not significantly alter the

openness of the active site cavity. Similar to the protein in its unbound state, the lid undergoes a vertical shift after the simulation period, and the accessibility of active serine 403 is marginally enhanced. Therefore, it appears that AAK443 acts principally by occupying the allosteric domain, which could preclude the binding of a peptidoglycan molecule. This mechanism of action could be advantageous for the inhibition of PBP2a, as it suggests a novel inhibitory pathway by allosteric blockade rather than direct active site competition.

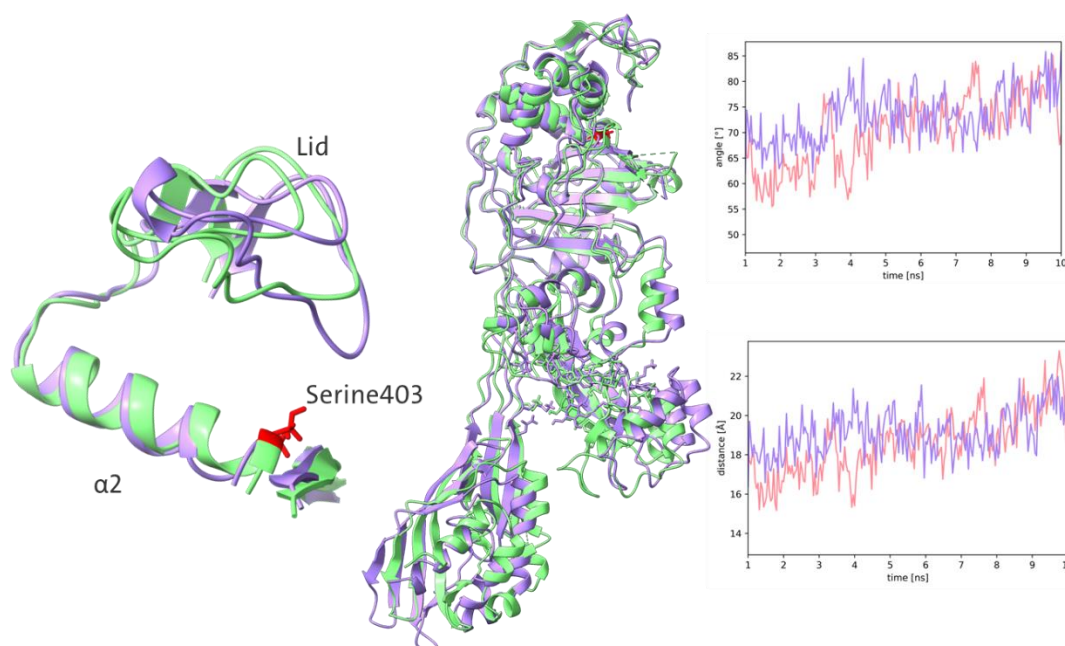


**Figure 67: PBP2a with and without the AAK443 Compound during a 10 ns Simulation Time.** The PBP2a AAK443 compound complex (magenta) exhibits no difference between the unbound simulation of PBP2a.

Figure 68 provides a comparative analysis of the structural dynamics of PBP2a when complexed with compound AAK489 across a simulation timeframe of 10 nanoseconds. Remarkably, AAK489 exhibits an effect on the protein similar to that of the peptidoglycan analogue depicted in figure 67. It induces a comparable degree of openness within the active site cavity and precipitates a similar displacement within  $\alpha$ -helix 2, which includes the repositioning of the active serine403. These results suggest that AAK489 is capable of activating the allosteric domain, which in turn leads to the activation of the active site, mirroring the mechanism observed with the peptidoglycan analogue. Thus, AAK489

emerges as a potential allosteric activator, signifying its promise as a lead compound in the modulation of PBP2a's activity.

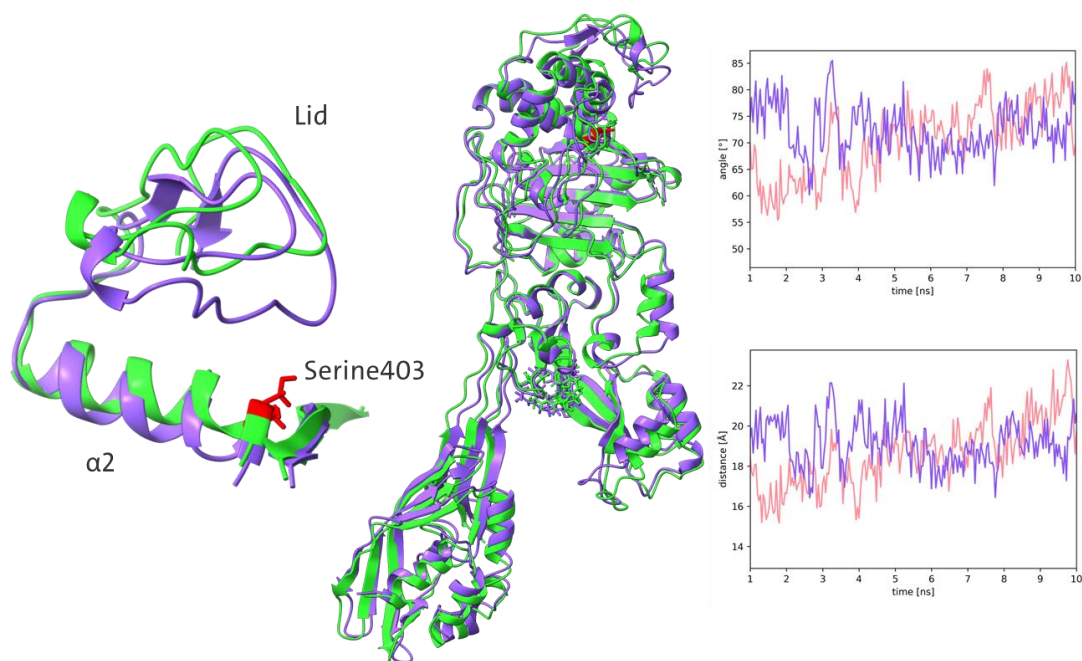


**Figure 68: PBP2a with and without the AAK489 Compound during a 10 ns Simulation Time.** The PBP2a AAK489 compound complex (purple) exhibits the same openness and serine displacement as the complex with the peptidoglycan analogue.

Figure 69 presents a comparative analysis of PBP2a's structural dynamics both native and in complex with compound AAK767 over a 10 ns simulation period. The data illustrates that the interaction with AAK767 prompts a displacement of the lid, which consequently induces a bending in  $\alpha$ -helix 2. This bending motion repositions the serine403 residue in an upward direction, enhancing its accessibility and thus potentially increasing the protein's susceptibility to inhibitor binding.

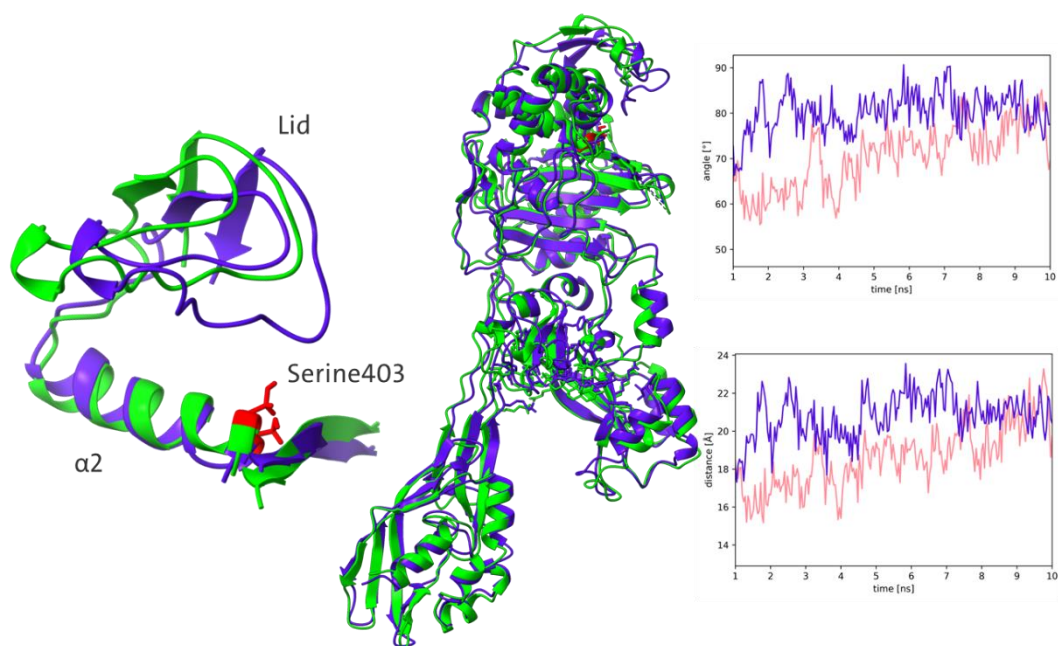


**Figure 69: PBP2a with and without the AAK797 Compound during a 10 ns Simulation Time.** The PBP2a AAK797 compound complex (blue) exhibits the same openness and serine displacement as the complex with the peptidoglycan analogue.

Figure 70 shows the differences in the structural conformation of PBP2a in its native state versus when complexed with compound AAK268. While the compound induces a significant displacement of the lid, akin to the effects observed with the peptidoglycan analogue and compounds AAK489 and AAK479, the subsequent conformational state of the cavity remains relatively closed. This is evidenced by measurements of distances and angles within the active site that are comparable to those in the uncomplexed, native protein.

Although AAK268 shows a degree of activation at the active site concurrent with its binding at the allosteric domain, the actual openness of the cavity does not significantly change. This emphasizes the necessity of not solely focusing on the displacement of structural components such as the lid,  $\alpha$ -helix 2, and serine403, but also on the overall accessibility of the active site cavity, which is critical for the potential binding and efficacy of inhibitors.

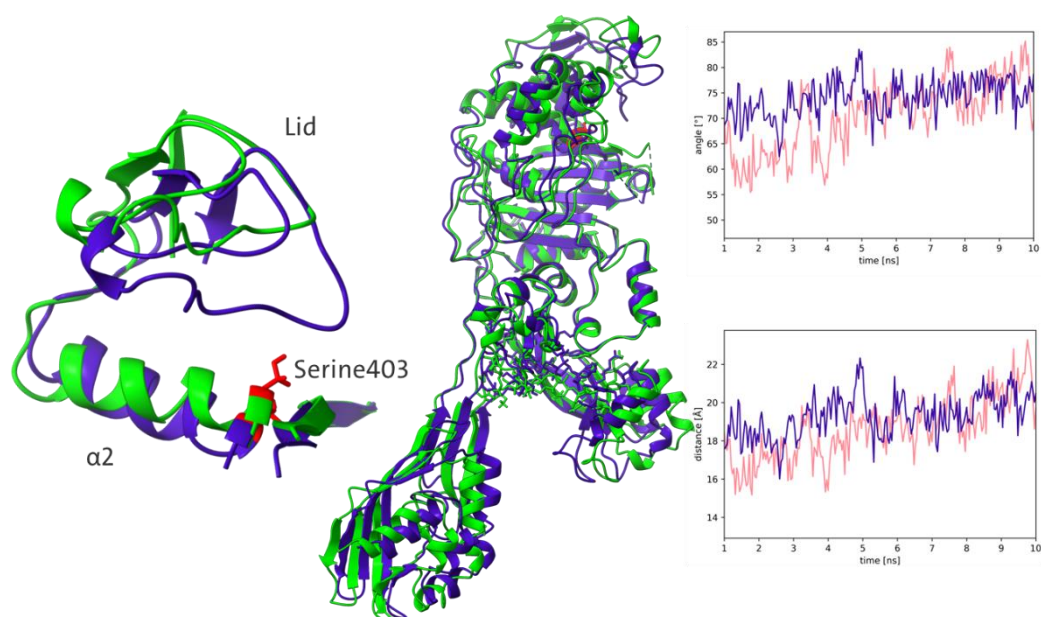


**Figure 70: PBP2a with and without the AAK268 Compound during a 10 ns Simulation Time.** The PBP2a AAK268 compound complex (dark blue) exhibits the same openness and serine displacement as the complex with the peptidoglycan analogue.

This section of the analysis has revealed the potential for significant conformational changes within the active site of PBP2a, highlighting a dynamic behavior that may be distinctive to class B PBPs. The observed alterations could be a consequence of the activation of the allosteric domain, a feature uniquely characteristic of class B PBPs. Moreover, the influence of glycosylated compounds that possess a pentacyclic triterpene backbone structure on both the activation and inhibition of the PBP2a active site underscores their potential as highlighted in this study. These data also suggest that such compounds could represent a novel avenue for the modulation of PBP2a activity, offering a promising strategy for the design of new antibacterial agents.

## **Part Two: Conclusion and Outlook**

The data presented extends our understanding of PBP2a from *Staphylococcus aureus* and *Staphylococcus epidermidis*. The research incorporates a comprehensive in silico analysis of PBP2a, integrating molecular docking and MD simulations with natural compounds from the Karachi library. This detailed study highlights the binding effectiveness of specific quercetin derivatives and introduces pentacyclic triterpene as a novel class of binding agents for PBP2a. Remarkably, the interaction of pentacyclic triterpene with the allosteric site of PBP2a triggers notable conformational changes, notably the opening of the active site cavity. This is characterized by the displacement of the protein's lid, altering the  $\alpha$ -helix 2 structure and thereby rendering the active serine site accessible for the compound binding. This deep dive into the molecular dynamics of PBP2a, facilitated by docking and MD simulations, not only enhances our understanding of its functionality but also paves the way for developing new therapeutic agents against antibiotic-resistant strains of *Staphylococcus aureus*. Looking ahead, the data obtained from this study offer exciting prospects for future antibacterial therapies, especially in the context of antibiotic resistance. The identification and characterization of novel binding agents such as pentacyclic triterpene open up potential pathways for the development of innovative treatments. The elucidation of these new interactions and their impact on PBP2a's structure and function could lead to the creation of more effective drugs against resistant bacterial strains.

Additionally, the development and validation of a new expression and purification protocol for PBP2a is simplifying future biochemical and structural investigations. Its ability to reduce the time required for PBP2a production, while eliminating the formation of inclusion bodies, simplifies the process and could have far-reaching implications for future protein research and drug development. This novel protocol could streamline the study of other class B PBPs as well, accelerating advancements in both structural biology and pharmacology.

## References

- Abascal, J.L., and Vega, C. (2005). A general purpose model for the condensed phases of water: TIP4P/2005. *J Chem Phys* 123, 234505.
- Abraham, E.P., and Chain, E. (1940). An Enzyme from Bacteria able to Destroy Penicillin. *Nature* 146, 837-837.
- Acebron, I., Chang, M., Mobashery, S., and Hermoso, J.A. (2015). The Allosteric Site for the Nascent Cell Wall in Penicillin-Binding Protein 2a: An Achilles' Heel of Methicillin-Resistant *Staphylococcus aureus*. *Curr Med Chem* 22, 1678-1686.
- Adams, Paul D., Aertgeerts, K., Bauer, C., et al. (2016). Outcome of the First wwPDB/CCDC/D3R Ligand Validation Workshop. *Structure* 24, 502-508.
- Adams, P.D., Afonine, P.V., Bunkoczi, G., et al. (2010). PHENIX: a comprehensive Python-based system for macromolecular structure solution. *Acta Crystallogr D Biol Crystallogr* 66, 213-221.
- Afonine, P.V., Grosse-Kunstleve, R.W., Echols, N., et al. (2012). Towards automated crystallographic structure refinement with phenix.refine. *Acta Crystallogr D Biol Crystallogr* 68, 352-367.
- Ahmad-Mansour, N., Loubet, P., Pouget, C., et al. (2021). *Staphylococcus aureus* Toxins: An Update on Their Pathogenic Properties and Potential Treatments. *Toxins* 13, 677.
- Alanis, A.J. (2005). Resistance to Antibiotics: Are We in the Post-Antibiotic Era? *Archives of Medical Research* 36, 697-705.
- Andrade, F.F., Silva, D., Rodrigues, A., and Pina-Vaz, C. (2020). Colistin Update on Its Mechanism of Action and Resistance, Present and Future Challenges. *Microorganisms*. Vol. 8.
- Antunes-Ricardo, M., Rodriguez-Rodriguez, C., Gutierrez-Urbe, J.A., et al. (2017). Bioaccessibility, Intestinal Permeability and Plasma Stability of Isorhamnetin Glycosides from *Opuntia ficus-indica* (L.). *Int J Mol Sci* 18.
- Argudín, M.Á., Mendoza, M.C., and Rodicio, M.R. (2010). Food Poisoning and *Staphylococcus aureus* Enterotoxins. *Toxins* 2, 1751-1773.
- Aronson, J.K., and Green, A.R. (2020). Me-too pharmaceutical products: History, definitions, examples, and relevance to drug shortages and essential medicines lists. *British Journal of Clinical Pharmacology* 86, 2114-2122.
- Asherie, N. (2004). Protein crystallization and phase diagrams. *Methods* 34, 266-272.
- Asl, M.N., and Hosseinzadeh, H. (2008). Review of pharmacological effects of *Glycyrrhiza* sp. and its bioactive compounds. *Phytother Res* 22, 709-724.
- Aubert, E., and Lecomte, C. (2007). Illustrated Fourier transforms for crystallography. *Journal of Applied Crystallography* 40, 1153-1165.
- Bastos, M., Abian, O., Johnson, C.M., et al. (2023). Isothermal titration calorimetry. *Nature Reviews Methods Primers* 3, 17.
- Becker, K., Schaumburg, F., Fegeler, C., et al. (2017). *Staphylococcus aureus* from the German general population is highly diverse. *International Journal of Medical Microbiology* 307, 21-27.
- Beer. (1852). Bestimmung der Absorption des rothen Lichts in farbigen Flüssigkeiten. *Annalen der Physik* 162, 78-88.



- Benvenuti, M., and Mangani, S. (2007). Crystallization of soluble proteins in vapor diffusion for x-ray crystallography. *Nat Protoc* 2, 1633-1651.
- Bergfors, T. (2003). Seeds to crystals. *J Struct Biol* 142, 66-76.
- Beychok, S. (1966). Circular Dichroism of Biological Macromolecules. *Science* 154, 1288-1299.
- Beyer, D., and Pepper, K. (1998). The streptogramin antibiotics: update on their mechanism of action. *Expert Opin Investig Drugs* 7, 591-599.
- Bigger, J.W., Boland, C.R., and O'Meara, R.A.Q. (1927). Variant colonies of *Staphylococcus aureus*. *The Journal of Pathology and Bacteriology* 30, 261-269.
- Blanchet, C.E., Spilotros, A., Schwemmer, F., et al. (2015). Versatile sample environments and automation for biological solution X-ray scattering experiments at the P12 beamline (PETRA III, DESY). *J Appl Crystallogr* 48, 431-443.
- Bochevarov, A.D., Watson, M.A., Greenwood, J.R., and Philipp, D.M. (2016). Multiconformation, Density Functional Theory-Based pKa Prediction in Application to Large, Flexible Organic Molecules with Diverse Functional Groups. *Journal of Chemical Theory and Computation* 12, 6001-6019.
- Bowers, K.J., Chow, D.E., Xu, H., et al. (2006). Scalable Algorithms for Molecular Dynamics Simulations on Commodity Clusters. SC '06: Proceedings of the 2006 ACM/IEEE Conference on Supercomputing. 43-43.
- Bragg, L. (1968). X-ray crystallography. *Sci Am* 219, 58-70.
- Bragg, W.H., and Bragg, W.L. (1913). The reflection of X-rays by crystals. *Proceedings of the Royal Society of London. Series A, Containing Papers of a Mathematical and Physical Character* 88, 428-438.
- Brautigam, C.A. (2015). Calculations and Publication-Quality Illustrations for Analytical Ultracentrifugation Data. *Methods Enzymol* 562, 109-133.
- Brunelle, J.L., and Green, R. (2014). One-dimensional SDS-polyacrylamide gel electrophoresis (1D SDS-PAGE). *Methods Enzymol* 541, 151-159.
- Bush, K., and Bradford, P.A. (2020). Epidemiology of  $\beta$ -Lactamase-Producing Pathogens. *Clinical Microbiology Reviews* 33, 10.1128/cmr.00047-00019.
- Calland, N., Dubuisson, J., Rouille, Y., and Seron, K. (2012). Hepatitis C virus and natural compounds: a new antiviral approach? *Viruses* 4, 2197-2217.
- Casey, J.A., Curriero, F.C., Cosgrove, S.E., et al. (2013). High-Density Livestock Operations, Crop Field Application of Manure, and Risk of Community-Associated Methicillin-Resistant *Staphylococcus aureus* Infection in Pennsylvania. *JAMA Internal Medicine* 173, 1980-1990.
- Chang, S., Sievert, D.M., Hageman, J.C., et al. (2003). Infection with Vancomycin-Resistant *Staphylococcus aureus* Containing the vanA Resistance Gene. *New England Journal of Medicine* 348, 1342-1347.
- Chen, V.B., Arendall, W.B., III, Headd, J.J., et al. (2010). MolProbity: all-atom structure validation for macromolecular crystallography. *Acta Crystallographica Section D* 66, 12-21.
- Chi, F., Nolte, O., Bergmann, C., et al. (2007). Crossing the barrier: Evolution and spread of a major class of mosaic pbp2x in *Streptococcus pneumoniae*, *S. mitis* and *S. oralis*. *International Journal of Medical Microbiology* 297, 503-512.

- Chiang, Y.-C., Wong, M.T.Y., and Essex, J.W. (2020). Molecular Dynamics Simulations of Antibiotic Ceftaroline at the Allosteric Site of Penicillin-Binding Protein 2a (PBP2a). *Israel Journal of Chemistry* 60, 754-763.
- Cianci, M., Bourenkov, G., Pompidor, G., et al. (2017). P13, the EMBL macromolecular crystallography beamline at the low-emittance PETRA III ring for high- and low-energy phasing with variable beam focusing. *J Synchrotron Radiat* 24, 323-332.
- Claus, F., Sachse, A., and Ried, W. (2014). [On the economic burden of MRSA in Germany]. *Gesundheitswesen* 76, 800-806.
- Coico, R. (2006). Gram Staining. *Current Protocols in Microbiology* 00, A.3C.1-A.3C.2.
- Colclough, A.L., Alav, I., Whittle, E.E., et al. (2020). RND efflux pumps in Gram-negative bacteria; regulation, structure and role in antibiotic resistance. *Future Microbiology* 15, 143-157.
- Conlan, S., Mijares, L.A., Becker, J., et al. (2012). Staphylococcus epidermidis pan-genome sequence analysis reveals diversity of skin commensal and hospital infection-associated isolates. *Genome Biology* 13, R64.
- Contreras-Martel, C., Dahout-Gonzalez, C., Martins Ados, S., et al. (2009). PBP active site flexibility as the key mechanism for beta-lactam resistance in pneumococci. *J Mol Biol* 387, 899-909.
- Correia, S., Poeta, P., Hébraud, M., et al. (2017). Mechanisms of quinolone action and resistance: where do we stand? *J Med Microbiol* 66, 551-559.
- Costa, S.S., Viveiros, M., Amaral, L., and Couto, I. (2013). Multidrug Efflux Pumps in Staphylococcus aureus: an Update. *Open Microbiol J* 7, 59-71.
- Costerton, J.W., Lewandowski, Z., Caldwell, D.E., et al. (1995). MICROBIAL BIOFILMS. *Annual Review of Microbiology* 49, 711-745.
- Costerton, J.W., Stewart, P.S., and Greenberg, E.P. (1999). Bacterial Biofilms: A Common Cause of Persistent Infections. *Science* 284, 1318-1322.
- Crouzet, M., Le Senechal, C., Brözel, V.S., et al. (2014). Exploring early steps in biofilm formation: set-up of an experimental system for molecular studies. *BMC Microbiology* 14, 253.
- D'Costa, V.M., King, C.E., Kalan, L., et al. (2011). Antibiotic resistance is ancient. *Nature* 477, 457-461.
- Davis BD, C.L., Tai PC. (1986 ). Misread protein creates membrane channels: an essential step in the bactericidal action of aminoglycosides. *Proc Natl Acad Sci U S A* 83.
- Do, N.T.T., Vu, H.T.L., Nguyen, C.T.K., et al. (2021). Community-based antibiotic access and use in six low-income and middle-income countries: a mixed-method approach. *Lancet Glob Health* 9, e610-e619.
- Dong, Y., Speer, C.P., and Glaser, K. (2018). Beyond sepsis: Staphylococcus epidermidis is an underestimated but significant contributor to neonatal morbidity. *Virulence* 9, 621-633.
- Dowson, C.G., Hutchison, A., Brannigan, J.A., et al. (1989). Horizontal transfer of penicillin-binding protein genes in penicillin-resistant clinical isolates of Streptococcus pneumoniae. *Proceedings of the National Academy of Sciences* 86, 8842-8846.
- Draper, P. (1998). The outer parts of the mycobacterial envelope as permeability barriers. *FBL* 3, 1253-1261.

- Emsley, P., Lohkamp, B., Scott, W.G., and Cowtan, K. (2010). Features and development of Coot. *Acta Crystallogr D Biol Crystallogr* 66, 486-501.
- Enright, M.C., Robinson, D.A., Randle, G., et al. (2002). The evolutionary history of methicillin-resistant *Staphylococcus aureus* (MRSA). *Proc Natl Acad Sci U S A* 99, 7687-7692.
- Fenton, B.A., Tomberg, J., Sciandra, C.A., et al. (2021). Mutations in PBP2 from ceftriaxone-resistant *Neisseria gonorrhoeae* alter the dynamics of the beta3-beta4 loop to favor a low-affinity drug-binding state. *J Biol Chem* 297, 101188.
- Ferry, D.R., Smith, A., Malkhandi, J., et al. (1996). Phase I clinical trial of the flavonoid quercetin: pharmacokinetics and evidence for in vivo tyrosine kinase inhibition. *Clin Cancer Res* 2, 659-668.
- Finlay Ac Fau - Hobby, G.L. (1950). Terramycin, a new antibiotic. *Science*.
- Finn, R.D., Coghill, P., Eberhardt, R.Y., et al. (2016). The Pfam protein families database: towards a more sustainable future. *Nucleic Acids Res* 44, D279-285.
- Fišarová, L., Botka, T., Du, X., et al. (2021). *Staphylococcus epidermidis* Phages Transduce Antimicrobial Resistance Plasmids and Mobilize Chromosomal Islands. *mSphere* 6, 10.1128/msphere.00223-00221.
- Fleming, A. (1929). On the Antibacterial Action of Cultures of a *Penicillium*, with Special Reference to their Use in the Isolation of *B. influenzae*. *The British Journal of Experimental Pathology* 10.
- Flemming, H.-C., and Wingender, J. (2010). The biofilm matrix. *Nature Reviews Microbiology* 8, 623-633.
- Floss, H.G., and Yu, T.-W. (2005). Rifamycin Mode of Action, Resistance, and Biosynthesis. *Chemical Reviews* 105, 621-632.
- Fontana, R., Aldegheri, M., Ligozzi, M., et al. (1994). Overproduction of a low-affinity penicillin-binding protein and high-level ampicillin resistance in *Enterococcus faecium*. *Antimicrob Agents Chemother* 38, 1980-1983.
- Fontana, R., Grossato, A., Rossi, L., et al. (1985). Transition from resistance to hypersusceptibility to beta-lactam antibiotics associated with loss of a low-affinity penicillin-binding protein in a *Streptococcus faecium* mutant highly resistant to penicillin. *Antimicrobial Agents and Chemotherapy* 28, 678-683.
- Frank, L.J., Wisniewski, D., Hammond, G.G., et al. (1995). High-Yield Expression, Refolding, and Purification of Penicillin-Binding Protein 2a from Methicillin-Resistant *Staphylococcus aureus* Strain 27R. *Protein Expression and Purification* 6, 671-678.
- Friesner, R.A., Murphy, R.B., Repasky, M.P., et al. (2006). Extra Precision Glide: Docking and Scoring Incorporating a Model of Hydrophobic Enclosure for Protein-Ligand Complexes. *Journal of Medicinal Chemistry* 49, 6177-6196.
- Garman, E.F., and Schneider, T.R. (1997). Macromolecular Cryocrystallography. *Journal of Applied Crystallography* 30, 211-237.
- Gelmo, P. (1908). Über Sulfamide der p-Amidobenzolsulfonsäure. *Journal für Praktische Chemie* 77, 369-382.
- Gill, S.C., and von Hippel, P.H. (1989). Calculation of protein extinction coefficients from amino acid sequence data. *Anal Biochem* 182, 319-326.
- Goffin, C., and Ghuysen, J.M. (2002). Biochemistry and comparative genomics of SxxK superfamily acyltransferases offer a clue to the mycobacterial paradox: presence

- of penicillin-susceptible target proteins versus lack of efficiency of penicillin as therapeutic agent. *Microbiol Mol Biol Rev* 66, 702-738, table of contents.
- Goldmann, D.A., and Pier, G.B. (1993). Pathogenesis of infections related to intravascular catheterization. *Clinical Microbiology Reviews* 6, 176-192.
- Gore, S., Velankar, S., and Kleywegt, G.J. (2012). Implementing an X-ray validation pipeline for the Protein Data Bank. *Acta Crystallographica Section D* 68, 478-483.
- Graef, J., Ehrt, C., and Rarey, M. (2023). Binding Site Detection Remastered: Enabling Fast, Robust, and Reliable Binding Site Detection and Descriptor Calculation with DoGSite3. *Journal of Chemical Information and Modeling* 63, 3128-3137.
- Greenfield, N.J. (2004). Circular dichroism analysis for protein-protein interactions. *Methods Mol Biol* 267, 55-78.
- Greither, A. Syphilis as a diagnostic and therapeutic problem.
- Grossman, C.M. (2008). The First Use of Penicillin in the United States. *Annals of Internal Medicine* 149, 135-136.
- Haag, A.F., Fitzgerald, J.R., and Penades, J.R. (2019). Staphylococcus aureus in Animals. *Microbiol Spectr* 7.
- Harkins, C.P., Pichon, B., Doumith, M., et al. (2017). Methicillin-resistant Staphylococcus aureus emerged long before the introduction of methicillin into clinical practice. *Genome Biol* 18, 130.
- Harwood, M., Danielewska-Nikiel, B., Borzelleca, J.F., et al. (2007). A critical review of the data related to the safety of quercetin and lack of evidence of in vivo toxicity, including lack of genotoxic/carcinogenic properties. *Food Chem Toxicol* 45, 2179-2205.
- Hata, Y., Li, X., Chung, U.-i., and Sakai, T. (2021). Molecular crystallization directed by polymer size and overlap under dilute and crowded macromolecular conditions. *Polymer Journal* 53, 633-642.
- Henze, U.U., and Berger-Bächi, B. (1996). Penicillin-binding protein 4 overproduction increases beta-lactam resistance in Staphylococcus aureus. *Antimicrobial Agents and Chemotherapy* 40, 2121-2125.
- Høiby, N., Bjarnsholt, T., Givskov, M., et al. (2010). Antibiotic resistance of bacterial biofilms. *International Journal of Antimicrobial Agents* 35, 322-332.
- Hopkins, J.B., Gillilan, R.E., and Skou, S. (2017). BioXTAS RAW: improvements to a free open-source program for small-angle X-ray scattering data reduction and analysis. *J Appl Crystallogr* 50, 1545-1553.
- Hutchings, M.I., Truman, A.W., and Wilkinson, B. (2019). Antibiotics: past, present and future. *Current Opinion in Microbiology* 51, 72-80.
- Jain, S., Self, W.H., Wunderink, R.G., et al. (2015). Community-Acquired Pneumonia Requiring Hospitalization among U.S. Adults. *New England Journal of Medicine* 373, 415-427.
- Jerala, R. (2007). Synthetic lipopeptides: a novel class of anti-infectives. *Expert Opin Investig Drugs* 16, 1159-1169.
- Jones, H.W. (1911). Report of a Series of Cases of Syphilis Treated by Ehrlich's Arsenobenzol at the Walter Reed General Hospital, District of Columbia. *The Boston Medical and Surgical Journal* 164, 381-383.
- Kabsch, W. (2010). Xds. *Acta Crystallogr D Biol Crystallogr* 66, 125-132.

- Kantardjieff, K.A., and Rupp, B. (2003). Matthews coefficient probabilities: Improved estimates for unit cell contents of proteins, DNA, and protein-nucleic acid complex crystals. *Protein Sci* 12, 1865-1871.
- Kaushik, U., Aeri, V., and Mir, S.R. (2015). Cucurbitacins - An insight into medicinal leads from nature. *Pharmacogn Rev* 9, 12-18.
- Keller, S., Vargas, C., Zhao, H., et al. (2012). High-precision isothermal titration calorimetry with automated peak-shape analysis. *Anal Chem* 84, 5066-5073.
- Kim, Y., Babnigg, G., Jedrzejczak, R., et al. (2011). High-throughput protein purification and quality assessment for crystallization. *Methods* 55, 12-28.
- Kishida, H., Unzai, S., Roper, D.I., et al. (2006). Crystal Structure of Penicillin Binding Protein 4 (dacB) from *Escherichia coli*, both in the Native Form and Covalently Linked to Various Antibiotics. *Biochemistry* 45, 783-792.
- Kleywegt, G.J. (2000). Validation of protein crystal structures. *Acta Crystallogr D Biol Crystallogr* 56, 249-265.
- Kloos, W.E. (1980). Natural Populations of the Genus *Staphylococcus*. *Annual Review of Microbiology* 34, 559-592.
- Kohanski, M.A., Dwyer, D.J., and Collins, J.J. (2010). How antibiotics kill bacteria: from targets to networks. *Nat Rev Microbiol* 8, 423-435.
- Krediet, T.G., Mascini, E.M., Rooij, E.v., et al. (2004). Molecular Epidemiology of Coagulase-Negative *Staphylococci* Causing Sepsis in a Neonatal Intensive Care Unit over an 11-Year Period. *Journal of Clinical Microbiology* 42, 992-995.
- Laible, G., Spratt, B.G., and Hakenbeck, R. (1991). Interspecies recombinational events during the evolution of altered PBP 2x genes in penicillin-resistant clinical isolates of *Streptococcus pneumoniae*. *Molecular Microbiology* 5, 1993-2002.
- Landini, P., Antoniani, D., Burgess, J.G., and Nijland, R. (2010). Molecular mechanisms of compounds affecting bacterial biofilm formation and dispersal. *Applied Microbiology and Biotechnology* 86, 813-823.
- Laskowski, R.A. (2022). PDBsum1: A standalone program for generating PDBsum analyses. *Protein Sci* 31, e4473.
- Lee, J.Y.H., Monk, I.R., Gonçalves da Silva, A., et al. (2018). Global spread of three multidrug-resistant lineages of *Staphylococcus epidermidis*. *Nature Microbiology* 3, 1175-1185.
- Lewis, K. (2001). Riddle of Biofilm Resistance. *Antimicrobial Agents and Chemotherapy* 45, 999-1007.
- Liebschner, D., Afonine, P.V., Baker, M.L., et al. (2019). Macromolecular structure determination using X-rays, neutrons and electrons: recent developments in Phenix. *Acta Crystallogr D Struct Biol* 75, 861-877.
- Lim, D., and Strynadka, N.C.J. (2002). Structural basis for the  $\beta$  lactam resistance of PBP2a from methicillin-resistant *Staphylococcus aureus*. *Nature Structural Biology* 9, 870-876.
- Lima, L.M., Silva, B.N.M.d., Barbosa, G., and Barreiro, E.J. (2020).  $\beta$ -lactam antibiotics: An overview from a medicinal chemistry perspective. *European Journal of Medicinal Chemistry* 208, 112829.

- Liu, Q., Liu, Q., Meng, H., et al. (2020). Staphylococcus epidermidis Contributes to Healthy Maturation of the Nasal Microbiome by Stimulating Antimicrobial Peptide Production. *Cell Host & Microbe* 27, 68-78.e65.
- Liu, Y.-Y., Wang, Y., Walsh, T.R., et al. (2016). Emergence of plasmid-mediated colistin resistance mechanism MCR-1 in animals and human beings in China: a microbiological and molecular biological study. *The Lancet Infectious Diseases* 16, 161-168.
- Long, K.S., Poehlsaard, J., Kehrenberg, C., et al. (2006). The Cfr rRNA Methyltransferase Confers Resistance to Phenicols, Lincosamides, Oxazolidinones, Pleuromutilins, and Streptogramin A Antibiotics. *Antimicrobial Agents and Chemotherapy* 50, 2500-2505.
- Lou, H., Chen, M., Black, S.S., et al. (2011). Altered Antibiotic Transport in OmpC Mutants Isolated from a Series of Clinical Strains of Multi-Drug Resistant E. coli. *PLOS ONE* 6, e25825.
- Lowy, F.D. (1998). Staphylococcus aureus Infections. *New England Journal of Medicine* 339, 520-532.
- Lu, C., Wu, C., Ghoreishi, D., et al. (2021). OPLS4: Improving Force Field Accuracy on Challenging Regimes of Chemical Space. *J Chem Theory Comput* 17, 4291-4300.
- Lu, S., Wang, J., Chitsaz, F., et al. (2020). CDD/SPARCLE: the conserved domain database in 2020. *Nucleic Acids Res* 48, D265-D268.
- Lu, W.P., Sun, Y., Bauer, M.D., et al. (1999). Penicillin-binding protein 2a from methicillin-resistant Staphylococcus aureus: kinetic characterization of its interactions with beta-lactams using electrospray mass spectrometry. *Biochemistry* 38, 6537-6546.
- Macheboeuf, P., Contreras-Martel, C., Job, V., et al. (2006). Penicillin binding proteins: key players in bacterial cell cycle and drug resistance processes. *FEMS Microbiol Rev* 30, 673-691.
- Madhavi Sastry, G., Adzhigirey, M., Day, T., et al. (2013). Protein and ligand preparation: parameters, protocols, and influence on virtual screening enrichments. *Journal of Computer-Aided Molecular Design* 27, 221-234.
- Manach, C., Williamson, G., Morand, C., et al. (2005). Bioavailability and bioefficacy of polyphenols in humans. I. Review of 97 bioavailability studies. *The American Journal of Clinical Nutrition* 81, 230S-242S.
- Markley, J.L., and Wencewicz, T.A. (2018). Tetracycline-Inactivating Enzymes. *Front Microbiol* 9, 1058.
- Martin, C., Sibold, C., and Hakenbeck, R. (1992). Relatedness of penicillin-binding protein 1a genes from different clones of penicillin-resistant Streptococcus pneumoniae isolated in South Africa and Spain. *The EMBO Journal* 11, 3831-3836.
- Matthews, B.W. (1968). Solvent content of protein crystals. *J Mol Biol* 33, 491-497.
- Matuszewska, M., Murray, G.G.R., Harrison, E.M., et al. (2020). The Evolutionary Genomics of Host Specificity in Staphylococcus aureus. *Trends Microbiol* 28, 465-477.
- McCormick, M.H., McGuire, J.M., Pittenger, G.E., et al. (1955). Vancomycin, a new antibiotic. I. Chemical and biologic properties. *Antibiot Annu* 3, 606-611.
- McCoy, A.J., Grosse-Kunstleve, R.W., Adams, P.D., et al. (2007). Phaser crystallographic software. *J Appl Crystallogr* 40, 658-674.

- McGuinness, W.A., Malachowa, N., and DeLeo, F.R. (2017). Vancomycin Resistance in *Staphylococcus aureus*. *Yale J Biol Med* *90*, 269-281.
- McPherson, A., and Gavira, J.A. (2014). Introduction to protein crystallization. *Acta Crystallogr F Struct Biol Commun* *70*, 2-20.
- Meents, A., Reime, B., Stuebe, N., et al. (2013). Development of an in-vacuum x-ray microscope with cryogenic sample cooling for beamline P11 at PETRA III: SPIE.
- Miner, K.R., D'Andrilli, J., Mackelprang, R., et al. (2021). Emergent biogeochemical risks from Arctic permafrost degradation. *Nature Climate Change* *11*, 809-819.
- Mishra, N.N., Bayer, A.S., Tran, T.T., et al. (2012). Daptomycin Resistance in Enterococci Is Associated with Distinct Alterations of Cell Membrane Phospholipid Content. *PLOS ONE* *7*, e43958.
- Moon, T.M., D'Andréa, É.D., Lee, C.W., et al. (2018). The structures of penicillin-binding protein 4 (PBP4) and PBP5 from Enterococci provide structural insights into  $\beta$ -lactam resistance. *Journal of Biological Chemistry* *293*, 18574-18584.
- Moreno, A. (2017). Advanced Methods of Protein Crystallization. *Methods Mol Biol* *1607*, 51-76.
- Mühlberg, E., Umstätter, F., Kleist, C., et al. (2020). Renaissance of vancomycin: approaches for breaking antibiotic resistance in multidrug-resistant bacteria. *Canadian Journal of Microbiology* *66*, 11-16.
- O'Neill, J. (2016). TACKLING DRUG-RESISTANT INFECTIONS GLOBALLY: FINAL REPORT AND RECOMMENDATIONS, THE REVIEW ON ANTIMICROBIAL RESISTANCE. Wellcome Trust 1.
- Ogston, A. (1882). Micrococcus Poisoning. *J Anat Physiol* *16*, 526-567.
- Olsen, J.E., Christensen, H., and Aarestrup, F.M. (2006). Diversity and evolution of blaZ from *Staphylococcus aureus* and coagulase-negative staphylococci. *Journal of Antimicrobial Chemotherapy* *57*, 450-460.
- Otero, L.H., Rojas-Altuve, A., Llarrull, L.I., et al. (2013). How allosteric control of *Staphylococcus aureus* penicillin binding protein 2a enables methicillin resistance and physiological function. *Proc Natl Acad Sci U S A* *110*, 16808-16813.
- Otto, M. (2009). *Staphylococcus epidermidis* — the 'accidental' pathogen. *Nature Reviews Microbiology* *7*, 555-567.
- Paraskevopoulou, V., and Falcone, F.H. (2018). Polyionic Tags as Enhancers of Protein Solubility in Recombinant Protein Expression. *Microorganisms* *6*.
- Parastan, R., Kargar, M., Solhjoo, K., and Kafilzadeh, F. (2020). *Staphylococcus aureus* biofilms: Structures, antibiotic resistance, inhibition, and vaccines. *Gene Reports* *20*, 100739.
- Park, S., and Ronholm, J. (2021). *Staphylococcus aureus* in Agriculture: Lessons in Evolution from a Multispecies Pathogen. *Clinical Microbiology Reviews* *34*, 10.1128/cmr.00182-00120.
- Pasquina-Lemonche, L., Burns, J., Turner, R.D., et al. (2020). The architecture of the Gram-positive bacterial cell wall. *Nature* *582*, 294-297.
- Perron, G.G., Whyte, L., Turnbaugh, P.J., et al. (2015). Functional characterization of bacteria isolated from ancient arctic soil exposes diverse resistance mechanisms to modern antibiotics. *PLoS One* *10*, e0069533.

- Peters, G., Locci, R., and Pulverer, G. (1981). Microbial colonization of prosthetic devices. II. Scanning electron microscopy of naturally infected intravenous catheters. *Zentralbl Bakteriol Mikrobiol Hyg B* 173, 293-299.
- Peters, G., Locci, R., and Pulverer, G. (1982). Adherence and Growth of Coagulase-Negative Staphylococci on Surfaces of Intravenous Catheters. *The Journal of Infectious Diseases* 146, 479-482.
- Petinaki, E., Dimitracopoulos, G., and Spiliopoulou, I. (2001). Decreased affinity of PBP3 to methicillin in a clinical isolate of *Staphylococcus epidermidis* with borderline resistance to methicillin and free of the *mecA* gene. *Microb Drug Resist* 7, 297-300.
- Petrelli, D., Zampaloni, C., D'Ercole, S., et al. (2006). Analysis of different genetic traits and their association with biofilm formation in *Staphylococcus epidermidis* isolates from central venous catheter infections. *European Journal of Clinical Microbiology and Infectious Diseases* 25, 773-781.
- Phillips, J.E., Crane, T.P., Noy, M., et al. (2006). The incidence of deep prosthetic infections in a specialist orthopaedic hospital. *The Journal of Bone & Joint Surgery British Volume* 88-B, 943-948.
- Piessens, V., De Vlieghe, S., Verbist, B., et al. (2012). Characterization of coagulase-negative staphylococcus species from cows' milk and environment based on *bap*, *icaA*, and *mecA* genes and phenotypic susceptibility to antimicrobials and teat dips. *Journal of Dairy Science* 95, 7027-7038.
- Pinho, M.G., de Lencastre, H., and Tomasz, A. (2000). Cloning, characterization, and inactivation of the gene *pbpC*, encoding penicillin-binding protein 3 of *Staphylococcus aureus*. *J Bacteriol* 182, 1074-1079.
- Pizauro, L.J.L., de Almeida, C.C., Silva, S.R., et al. (2021). Genomic comparisons and phylogenetic analysis of mastitis-related staphylococci with a focus on adhesion, biofilm, and related regulatory genes. *Scientific Reports* 11, 17392.
- Pletzer-Zelgert, J., Ehrt, C., Fender, I., et al. (2023). LifeSoaks: a tool for analyzing solvent channels in protein crystals and obstacles for soaking experiments. *Acta Crystallographica Section D* 79, 837-856.
- Poehlsgaard, J., and Douthwaite, S. (2005). The bacterial ribosome as a target for antibiotics. *Nature Reviews Microbiology* 3, 870-881.
- Ponsankar, A., Sahayaraj, K., Senthil-Nathan, S., et al. (2020). Toxicity and developmental effect of cucurbitacin E from *Citrullus colocynthis* L. (Cucurbitales: Cucurbitaceae) against *Spodoptera litura* Fab. and a non-target earthworm *Eisenia fetida* Savigny. *Environmental Science and Pollution Research* 27, 23390-23401.
- Potluri, L., Karczmarek, A., Verheul, J., et al. (2010). Septal and lateral wall localization of PBP5, the major D,D-carboxypeptidase of *Escherichia coli*, requires substrate recognition and membrane attachment. *Mol Microbiol* 77, 300-323.
- Pratt, L.A., Hsing, W., Gibson, K.E., and Silhavy, T.J. (1996). From acids to *osmZ*: multiple factors influence synthesis of the OmpF and OmpC porins in *Escherichia coli*. *Molecular Microbiology* 20, 911-917.
- Raju, T.N. (1999). The Nobel chronicles. 1939: Gerhard Domagk (1895-1964). *Lancet* 353, 681.



- Rambo, R.P., and Tainer, J.A. (2011). Characterizing flexible and intrinsically unstructured biological macromolecules by SAS using the Porod-Debye law. *Biopolymers* 95, 559-571.
- Rani, N., Vijayakumar, S., Thanga Velan, L.P., and Arunachalam, A. (2014). Quercetin 3-O-rutinoside mediated inhibition of PBP2a: computational and experimental evidence to its anti-MRSA activity. *Molecular BioSystems* 10, 3229-3237.
- Raran-Kurussi, S., Cherry, S., Zhang, D., and Waugh, D.S. (2017). Removal of Affinity Tags with TEV Protease. In: Burgess-Brown, N.A. (ed). *Heterologous Gene Expression in E.coli: Methods and Protocols*. New York, NY: Springer New York, 221-230.
- Rebstock, M.C., Crooks, H.M., Controulis, J., and Bartz, Q.R. (1949). Chloramphenicol (Chloromycetin).1 IV.1a Chemical Studies. *Journal of the American Chemical Society* 71, 2458-2462.
- Reed, J., and Reed, T.A. (1997). A Set of Constructed Type Spectra for the Practical Estimation of Peptide Secondary Structure from Circular Dichroism. *Analytical Biochemistry* 254, 36-40.
- Ridley, M., and Phillips, I.A.N. (1965). Relative Instability of Cephaloridine to Staphylococcal Penicillinase. *Nature* 208, 1076-1078.
- Riethmiller, S. (2005). From Atoxyl to Salvarsan: searching for the magic bullet. *Chemotherapy* 51, 234-242.
- Robert, X., and Gouet, P. (2014). Deciphering key features in protein structures with the new ENDscript server. *Nucleic Acids Res* 42, W320-324.
- Roberts, M.C. (2008). Update on macrolide–lincosamide–streptogramin, ketolide, and oxazolidinone resistance genes. *FEMS Microbiology Letters* 282, 147-159.
- Rodriguez-Tebar, A., and Vazquez, D. (1984). Penicillin-binding proteins and peptidoglycan peptide-interacting proteins. *Microbiol Sci* 1, 211-214.
- Rosenbach, F.J. (1884). *Mikro-organismen bei den Wund-Infektions-Krankheiten des Menschen*. Wiesbaden: J.F. Bergmann.
- Ross-Murphy, S.B. (1977). Dynamic Light Scattering. *British Polymer Journal* 9, 177-177.
- Rupp, M.E., and Archer, G.L. (1994). Coagulase-Negative Staphylococci: Pathogens Associated with Medical Progress. *Clinical Infectious Diseases* 19, 231-245.
- Rutenburg, A.M., Greenberg, H.L., and Schweinburg, F.B. (1960). Clinical Experiences with 2, 6-Dimethoxyphenyl Penicillin Monohydrate in Staphylococcal Infections. *New England Journal of Medicine* 263, 1174-1178.
- Sastry, G.M., Adzhigirey, M., Day, T., et al. (2013). Protein and ligand preparation: parameters, protocols, and influence on virtual screening enrichments. *J Comput Aided Mol Des* 27, 221-234.
- Sauvage, E., Kerff, F., Terrak, M., et al. (2008). The penicillin-binding proteins: structure and role in peptidoglycan biosynthesis. *FEMS Microbiol Rev* 32, 234-258.
- Schatz A Fau - Bugie, E., Bugie E Fau - Waksman, S.A., and Waksman, S.A. (1944). Streptomycin, a substance exhibiting antibiotic activity against gram-positive and gram-negative bacteria. . *Clinical Orthopaedics and Related Research*.
- Schleifer, K.H., and Kloos, W.E. (1975). Isolation and Characterization of Staphylococci from Human Skin I. Amended Descriptions of *Staphylococcus epidermidis* and *Staphylococcus saprophyticus* and Descriptions of Three New Species: *Staphylococcus cohnii*, *Staphylococcus haemolyticus*, and *Staphylococcus*

- xylosus. *International Journal of Systematic and Evolutionary Microbiology* 25, 50-61.
- Schneidman-Duhovny, D., Hammel, M., Tainer, J.A., and Sali, A. (2013). Accurate SAXS profile computation and its assessment by contrast variation experiments. *Biophys J* 105, 962-974.
- Schwarz, S., Shen, J., Kadlec, K., et al. (2016). Lincosamides, Streptogramins, Phenicol, and Pleuromutilins: Mode of Action and Mechanisms of Resistance. *Cold Spring Harb Perspect Med* 6.
- Schwarz, S., Zhang, W., Du, X.-D., et al. (2021). Mobile Oxazolidinone Resistance Genes in Gram-Positive and Gram-Negative Bacteria. *Clinical Microbiology Reviews* 34, 10.1128/cmr.00188-00120.
- Shapiro, D.J., Hicks, L.A., Pavia, A.T., and Hersh, A.L. (2014). Antibiotic prescribing for adults in ambulatory care in the USA, 2007-09. *J Antimicrob Chemother* 69, 234-240.
- Shoskes, D.A., Zeitlin, S.I., Shahed, A., and Rajfer, J. (1999). Quercetin in men with category III chronic prostatitis: a preliminary prospective, double-blind, placebo-controlled trial. *Urology* 54, 960-963.
- Sibold, C., Henrichsen, J., König, A., et al. (1994). Mosaic pbpX genes of major clones of penicillin-resistant *Streptococcus pneumoniae* have evolved from pbpX genes of a penicillin-sensitive *Streptococcus oralis*. *Molecular Microbiology* 12, 1013-1023.
- Siddiqui, B.S., Khatoon, N., Begum, S., et al. (2012). Flavonoid and cardenolide glycosides and a pentacyclic triterpene from the leaves of *Nerium oleander* and evaluation of cytotoxicity. *Phytochemistry* 77, 238-244.
- Sifaoui, F., Arthur, M., Rice, L., and Gutmann, L. (2001). Role of penicillin-binding protein 5 in expression of ampicillin resistance and peptidoglycan structure in *Enterococcus faecium*. *Antimicrob Agents Chemother* 45, 2594-2597.
- Sjodt, M., Rohs, P.D.A., Gilman, M.S.A., et al. (2020). Structural coordination of polymerization and crosslinking by a SEDS–bPBP peptidoglycan synthase complex. *Nature Microbiology* 5, 813-820.
- Sköld, O. (2000). Sulfonamide resistance: mechanisms and trends. *Drug Resistance Updates* 3, 155-160.
- Spížek, J., and Řezanka, T. (2017). Lincosamides: Chemical structure, biosynthesis, mechanism of action, resistance, and applications. *Biochemical Pharmacology* 133, 20-28.
- Stetefeld, J., McKenna, S.A., and Patel, T.R. (2016). Dynamic light scattering: a practical guide and applications in biomedical sciences. *Biophys Rev* 8, 409-427.
- Stogios, P.J., and Savchenko, A. (2020). Molecular mechanisms of vancomycin resistance. *Protein Science* 29, 654-669.
- Stohrer, C., Horrell, S., Meier, S., et al. (2021). Homogeneous batch micro-crystallization of proteins from ammonium sulfate. *Acta Crystallogr D Struct Biol* 77, 194-204.
- Svergun, D. (1992). Determination of the regularization parameter in indirect-transform methods using perceptual criteria. *Journal of Applied Crystallography* 25, 495-503.
- Svergun, D.I., and Koch, M.H.J. (2003). Small-angle scattering studies of biological macromolecules in solution. *Reports on Progress in Physics* 66, 1735-1782.

- Swaney Steve, M., Aoki, H., Ganoza, M.C., and Shinabarger Dean, L. (1998). The Oxazolidinone Linezolid Inhibits Initiation of Protein Synthesis in Bacteria. *Antimicrobial Agents and Chemotherapy* 42, 3251-3255.
- System, A.r.f.t.N. (2004). National Nosocomial Infections Surveillance (NNIS) System Report, data summary from January 1992 through June 2004, issued October 2004. *American Journal of Infection Control* 32, 470-485.
- Tang, S.S., Apisarnthanarak, A., and Hsu, L.Y. (2014). Mechanisms of  $\beta$ -lactam antimicrobial resistance and epidemiology of major community- and healthcare-associated multidrug-resistant bacteria. *Advanced Drug Delivery Reviews* 78, 3-13.
- Teng, T.Y., and Moffat, K. (2000). Primary radiation damage of protein crystals by an intense synchrotron X-ray beam. *J Synchrotron Radiat* 7, 313-317.
- Thom, G., and Prescott, C.D. (1997). The selection in vivo and characterization of an RNA recognition motif for spectinomycin. *Bioorganic & Medicinal Chemistry* 5, 1081-1086.
- Thomas, J.C., Vargas, M.R., Miragaia, M., et al. (2007). Improved Multilocus Sequence Typing Scheme for *Staphylococcus epidermidis*. *Journal of Clinical Microbiology* 45, 616-619.
- Tipper, D.J., and Strominger, J.L. (1965). Mechanism of action of penicillins: a proposal based on their structural similarity to acyl-D-alanyl-D-alanine. *Proceedings of the National Academy of Sciences* 54, 1133-1141.
- Tiseo, K., Huber, L., Gilbert, M., et al. (2020). Global Trends in Antimicrobial Use in Food Animals from 2017 to 2030. *Antibiotics (Basel)* 9.
- Tomasz, A., Drugeon, H.B., de Lencastre, H.M., et al. (1989). New mechanism for methicillin resistance in *Staphylococcus aureus*: clinical isolates that lack the PBP 2a gene and contain normal penicillin-binding proteins with modified penicillin-binding capacity. *Antimicrob Agents Chemother* 33, 1869-1874.
- Tong, S.Y.C., Davis, J.S., Eichenberger, E., et al. (2015). *Staphylococcus aureus* Infections: Epidemiology, Pathophysiology, Clinical Manifestations, and Management. *Clinical Microbiology Reviews* 28, 603-661.
- ur Rahman, S., Ali, T., Ali, I., et al. (2018). The Growing Genetic and Functional Diversity of Extended Spectrum Beta-Lactamases. *BioMed Research International* 2018, 9519718.
- Van Boeckel, T.P., Glennon, E.E., Chen, D., et al. (2017). Reducing antimicrobial use in food animals. *Science* 357, 1350-1352.
- Vázquez-Laslop, N., and Mankin, A.S. (2018). How Macrolide Antibiotics Work. *Trends in Biochemical Sciences* 43, 668-684.
- Volkamer, A., Griewel, A., Grombacher, T., and Rarey, M. (2010). Analyzing the Topology of Active Sites: On the Prediction of Pockets and Subpockets. *Journal of Chemical Information and Modeling* 50, 2041-2052.
- Volkamer, A., Kuhn, D., Grombacher, T., et al. (2012). Combining Global and Local Measures for Structure-Based Druggability Predictions. *Journal of Chemical Information and Modeling* 52, 360-372.
- Wachino, J.-I., Doi, Y., and Arakawa, Y. (2020). Aminoglycoside Resistance: Updates with a Focus on Acquired 16S Ribosomal RNA Methyltransferases. *Infectious Disease Clinics of North America* 34, 887-902.

- Washington, J.A., and Wilson, W.R. (1985). Erythromycin: A Microbial and Clinical Perspective After 30 Years of Clinical Use (Second of Two Parts)\* \*The first part of this two-part article was published in the March issue of the Proceedings. *Mayo Clinic Proceedings* 60, 271-278.
- Wertheim, H.F.L., Melles, D.C., Vos, M.C., et al. (2005). The role of nasal carriage in *Staphylococcus aureus* infections. *The Lancet Infectious Diseases* 5, 751-762.
- Wey, J.S., and Karpinski, P.H. (2002). 10 - Batch crystallization. In: Myerson, A.S. (ed). *Handbook of Industrial Crystallization (Second Edition)*. Woburn: Butterworth-Heinemann, 231-248.
- Wilson, D.N. (2014). Ribosome-targeting antibiotics and mechanisms of bacterial resistance. *Nature Reviews Microbiology* 12, 35-48.
- Wlodawer, A. (2017). Stereochemistry and Validation of Macromolecular Structures. In: Wlodawer, A., Dauter, Z. and Jaskolski, M. (eds). *Protein Crystallography: Methods and Protocols*. New York, NY: Springer New York, 595-610.
- Wlodawer, A., Minor, W., Dauter, Z., and Jaskolski, M. (2008). Protein crystallography for non-crystallographers, or how to get the best (but not more) from published macromolecular structures. *The FEBS Journal* 275, 1-21.
- Woestenenk, E.A., Hammarstrom, M., van den Berg, S., et al. (2004). His tag effect on solubility of human proteins produced in *Escherichia coli*: a comparison between four expression vectors. *J Struct Funct Genomics* 5, 217-229.
- Wong, J.L.C., Romano, M., Kerry, L.E., et al. (2019). OmpK36-mediated Carbapenem resistance attenuates ST258 *Klebsiella pneumoniae* in vivo. *Nature Communications* 10, 3957.
- WorldHealthOrganization. (2023). Global action plan on antimicrobial resistance. WHO Library Cataloguing-in-Publication Data.
- Wróbel, A., Arciszewska, K., Maliszewski, D., and Drozdowska, D. (2020). Trimethoprim and other nonclassical antifolates an excellent template for searching modifications of dihydrofolate reductase enzyme inhibitors. *The Journal of Antibiotics* 73, 5-27.
- Yamanaka, M., Inaka, K., Furubayashi, N., et al. (2011). Optimization of salt concentration in PEG-based crystallization solutions. *J Synchrotron Radiat* 18, 84-87.
- Yang, J.T., Wu, C.S., and Martinez, H.M. (1986). Calculation of protein conformation from circular dichroism. *Methods Enzymol* 130, 208-269.
- Yang, Z., Ye, Z., Qiu, J., et al. (2023). A mutation-induced drug resistance database (MdrDB). *Communications Chemistry* 6, 123.
- Yocum, R.R., Rasmussen, J.R., and Strominger, J.L. (1980). The mechanism of action of penicillin. Penicillin acylates the active site of *Bacillus stearothermophilus* D-alanine carboxypeptidase. *J Biol Chem* 255, 3977-3986.
- Yoshida, H., Kawai, F., Obayashi, E., et al. (2012). Crystal Structures of Penicillin-Binding Protein 3 (PBP3) from Methicillin-Resistant *Staphylococcus aureus* in the Apo and Cefotaxime-Bound Forms. *Journal of Molecular Biology* 423, 351-364.
- Zapun, A., Contreras-Martel, C., and Vernet, T. (2008). Penicillin-binding proteins and  $\beta$ -lactam resistance. *FEMS Microbiology Reviews* 32, 361-385.

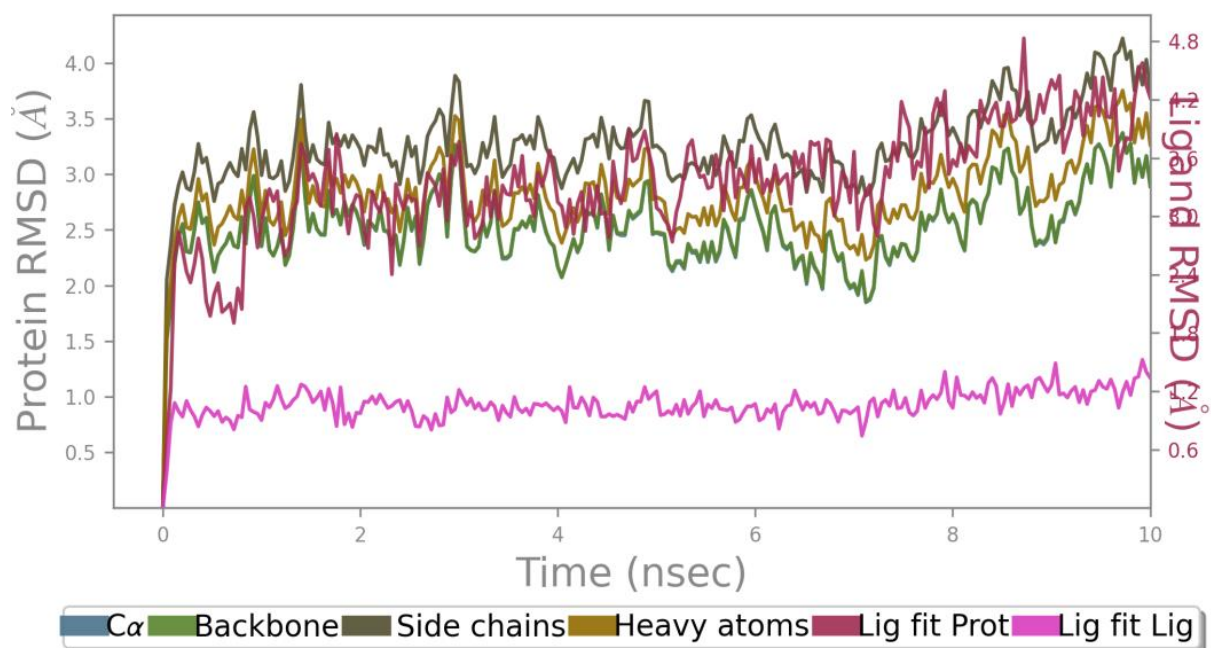
- Zeng, D., Debabov, D., Hartsell, T.L., et al. Approved Glycopeptide Antibacterial Drugs: Mechanism of Action and Resistance. LID - 10.1101/cshperspect.a026989 [doi] LID - a026989.
- Zhao, G., Meier, T.I., Kahl, S.D., et al. (1999). BOCILLIN FL, a sensitive and commercially available reagent for detection of penicillin-binding proteins. *Antimicrob Agents Chemother* 43, 1124-1128.
- Zhao, H., Piszczek, G., and Schuck, P. (2015). SEDPHAT--a platform for global ITC analysis and global multi-method analysis of molecular interactions. *Methods* 76, 137-148.
- Zhou, W., Li, X., Osmundson, T., et al. (2018). WGS analysis of ST9-MRSA-XII isolates from live pigs in China provides insights into transmission among porcine, human and bovine hosts. *J Antimicrob Chemother* 73, 2652-2661.

## **SUPPLEMENTARY INFORMATION**

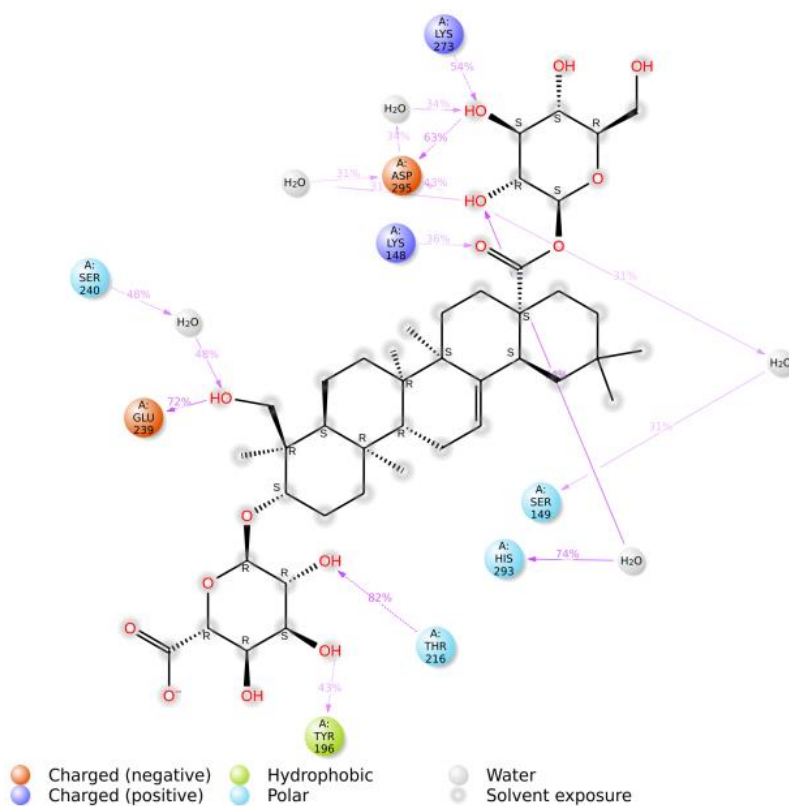
This section encompasses additional data and resources, including supplementary figures, providing details on chemicals and hazardous substances, as well as comprehensive lists of figures and tables. This auxiliary content supports and extends the methodologies presented in the main part of the thesis.

## SUPPLEMENTARY FIGURES

### Protein-Ligand RMSD

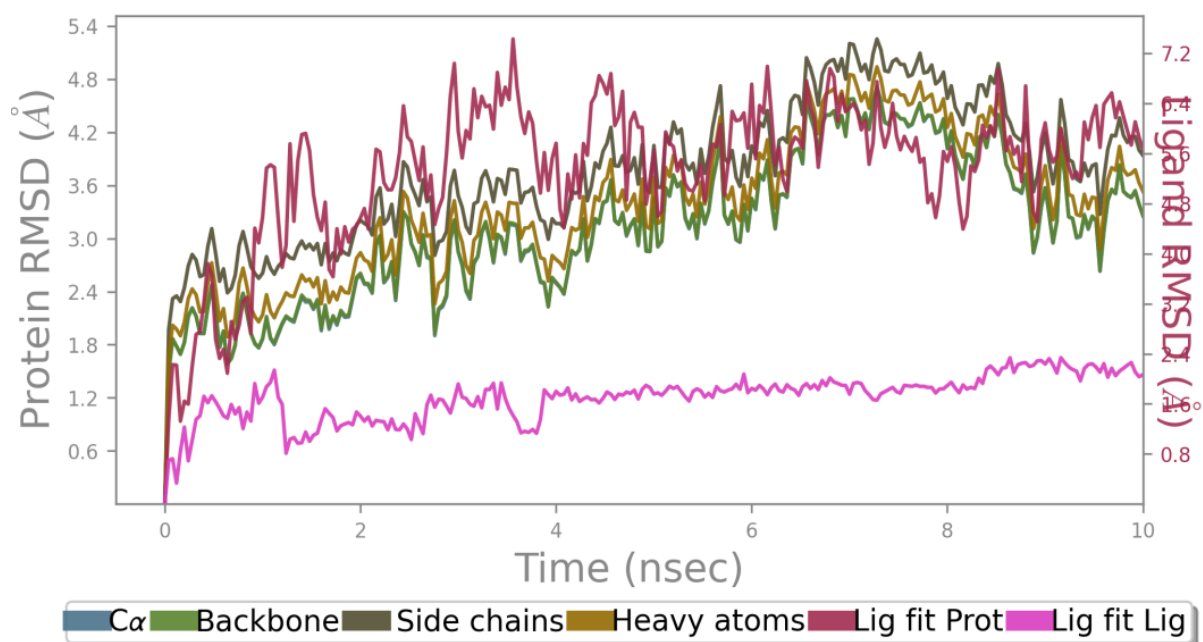


Supplementary Figure 1: RMSD Values of PBP2a and the Compound AAK268.

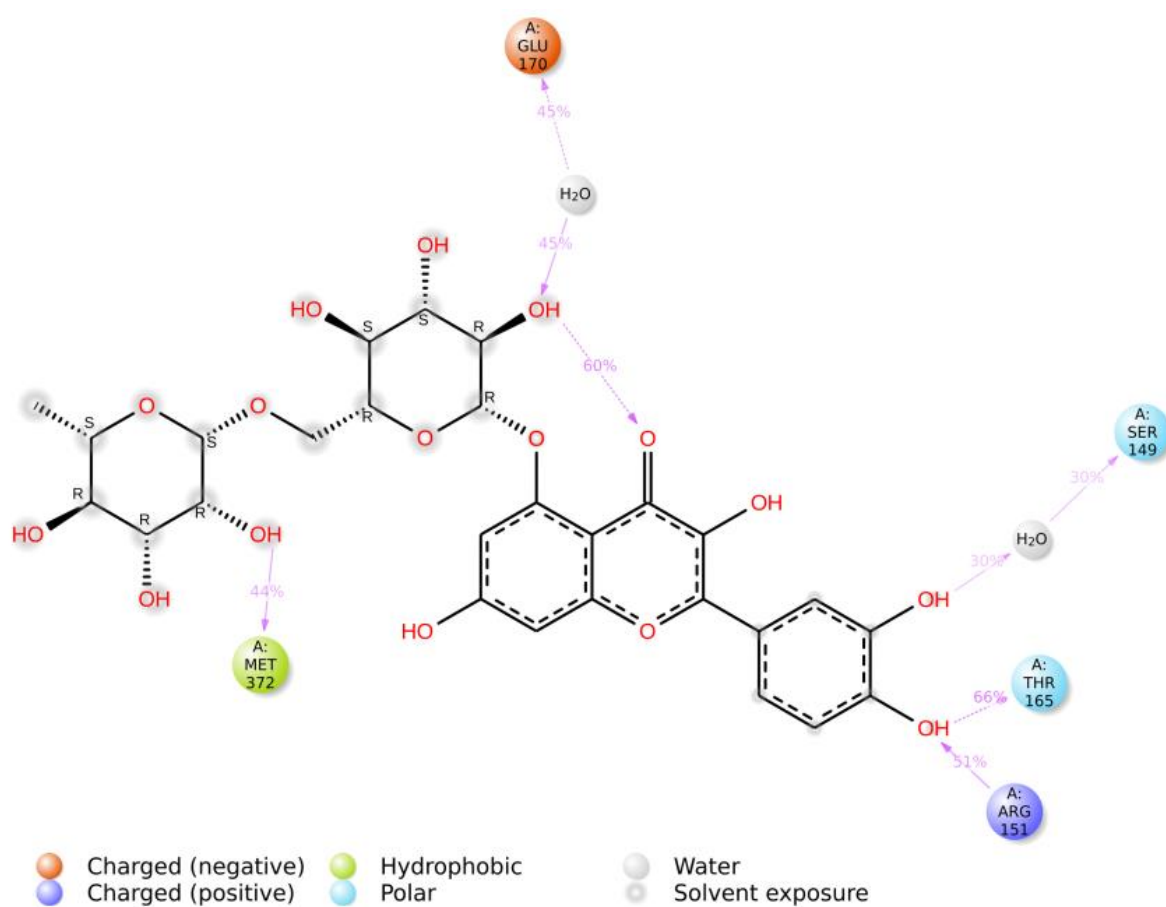


Supplementary Figure 2: A schematic Figure of detailed Ligand (AAK268) Atom Interactions with the Protein Residues.

## Protein-Ligand RMSD



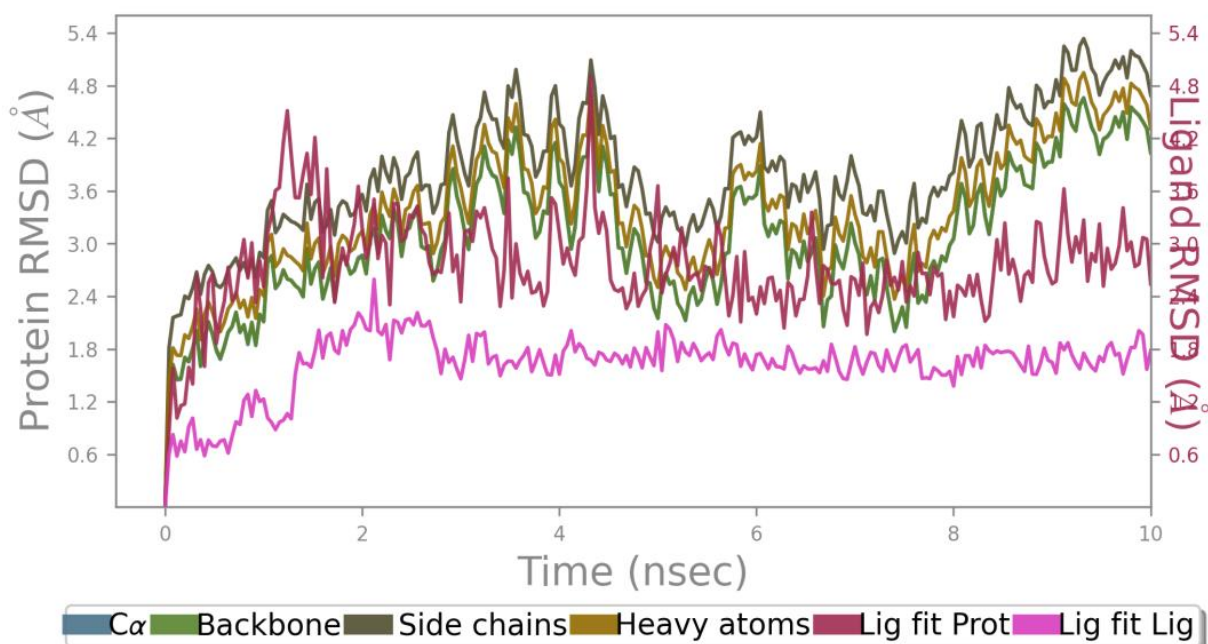
Supplementary Figure 3: RMSD Values of PBP2a and the Compound AAK376.



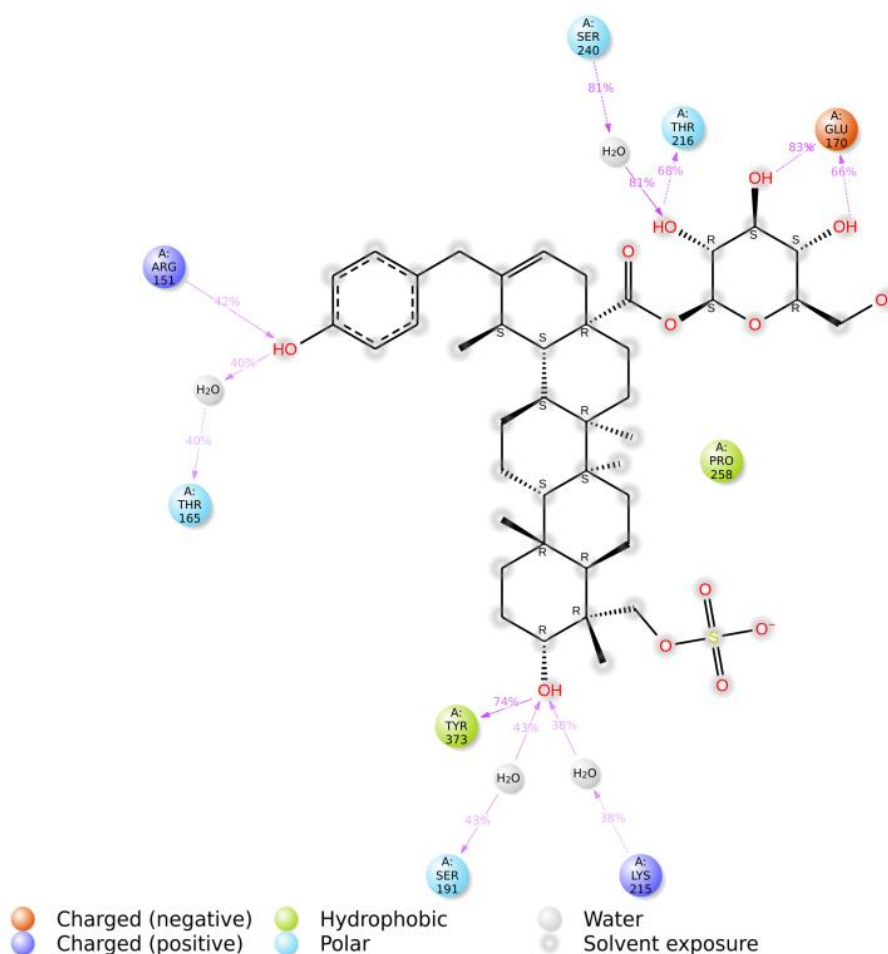
Supplementary Figure 4: A schematic Figure of detailed Ligand (AAK376) Atom Interactions with the Protein Residues.



## Protein-Ligand RMSD

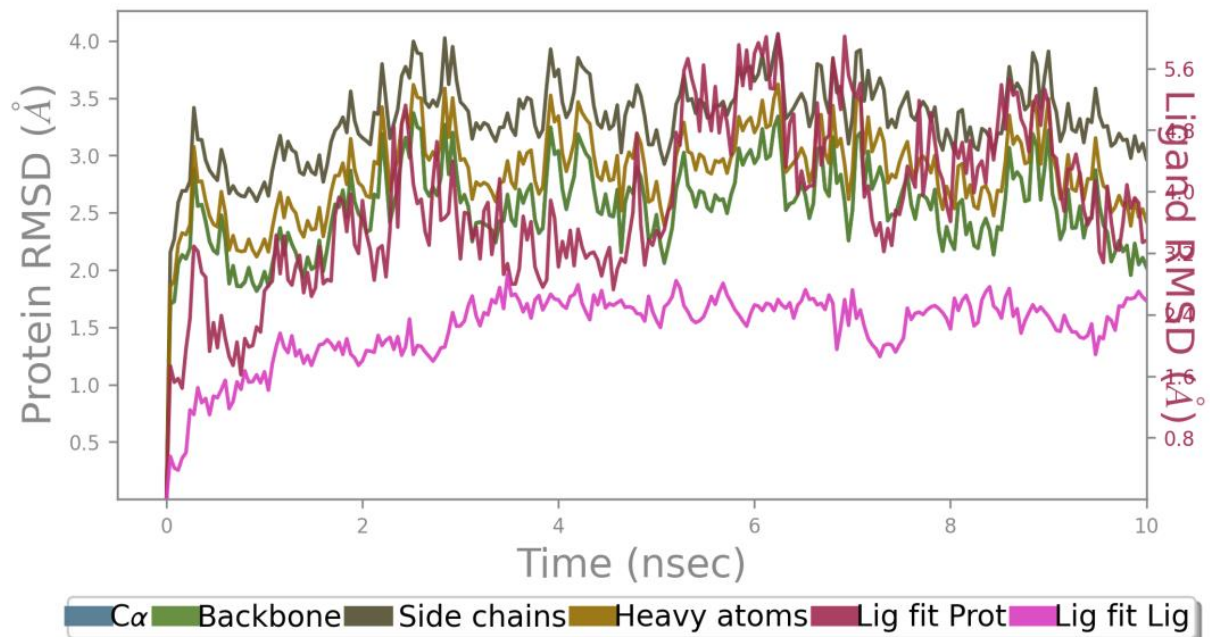


Supplementary Figure 5: RMSD Values of PBP2a and the Compound AAK433.

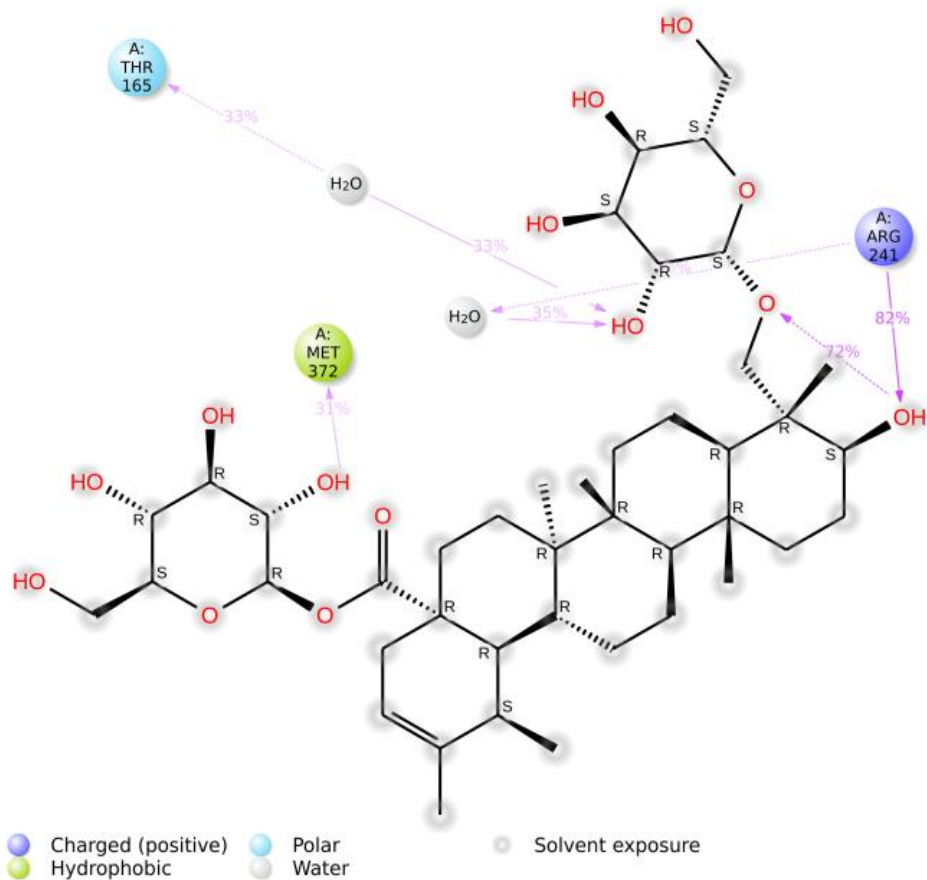


Supplementary Figure 6: A schematic Figure of detailed Ligand (AAK433) Atom Interactions with the Protein Residues.

## Protein-Ligand RMSD













Supplementary Figure 7: RMSD Values of PBP2a and the Compound AAK797.













Supplementary Figure 8: A schematic Figure of detailed Ligand (AAK797) Atom Interactions with the Protein Residues.

## CHEMICALS AND HAZARDOUS SUBSTANCES

Chemical	GHS-Pictogram	H-Code	P-Code
Acetic Acid	 	H226, H314	P210, P280, P305+P351+P338, P310
Acrylamide	 	H301, H312, H315, H317, H318, H332, H341, H350, H361	P201, P202, P261, P264, P270, P272, P280, P301+P312, P302+P352, P305+P351+P338, P308+P313, P312, P321, P332+P313, P333+P313, P337+P313, P362, P363, P405, P501
Ammonium Sulfate	 	-	-
Bromophenol Blue	-	-	-
Cadmium Chloride		H350, H410	P201, P273, P308+P313, P501

			
Glucose	-	-	-
Glycerol	-	-	-
4-(2-hydroxyethyl)-1-piperazineethanesulfonic acid		-	-
Hydrochloric Acid		H314	P260, P264, P280, P301+P330+P331, P303+P361+P353, P363, P304+P340, P310, P321, P305+P351+P338, P337+P313
Imidazole		H225, H319, H336	P210, P233, P240, P241, P242, P243, P261, P264, P271, P280, P303+P361+P353, P304+P340, P305+P351+P338, P370+P378,

			P403+P233, P403+P235, P405, P501
Liquid Nitrogen		H281	P202, P210, P377, P381, P403, P404
Magnesium Chloride		-	-
Magnesium Sulfate	-	-	-
Disodium Phosphate	-	-	-
Sodium Dihydrogen Phosphate	-	-	-
Sodium Hydroxide	 	H314	P260, P264, P280, P301+P330+P331, P303+P361+P353, P363, P304+P340, P310, P321, P305+P351+P338, P337+P313
Polyethylene Glycol 550	-	-	-

Sodium Dodecyl Sulfate	  	H315, H335	H318, P261, P305+P351+P338
N,N,N',N'- Tetramethylethylenediamine	  	H314, H317, H341	H315, H335, P261, P280, P303+P361+P353, P305+P351



Supplementary Figure 9: Globally Harmonized System of Classification (GHS) Pictograms.

## H-Code

H225	Highly flammable liquid and vapor.
H226	Flammable liquid and vapor.
H228	Flammable solid.
H271	May cause fire or explosion; strong oxidizer.
H272	May intensify fire; oxidizer.
H290	May be corrosive to metals.
H301	Toxic if swallowed.
H302	Harmful if swallowed.
H302+332	Harmful if swallowed or inhaled.
H310	Fatal in contact with skin.
H311	Toxic in contact with skin.
H312	Harmful in contact with skin.
H314	Causes severe skin burns and eye damage.
H315	Causes skin irritation.
H317	May cause an allergic skin reaction.
H318	Causes serious eye damage.
H319	Causes serious eye irritation.
H330	Fatal if inhaled.
H332	Harmful if inhaled.
H334	May cause allergy or asthma symptoms or breathing difficulties if inhaled.
H335	May cause respiratory irritation.
H336	May cause drowsiness or dizziness.
H340	May cause genetic defects.
H341	Suspected of causing genetic defects.
H350	May cause cancer.
H350i	May cause cancer if inhaled.
H351	Suspected of causing cancer.
H360	May damage fertility or the unborn child.
H361d	Suspected of damaging the unborn child.
H361f	Suspected of damaging fertility.
H372	Causes damage to organs through prolonged or repeated exposure.
H400	Very toxic to aquatic life.
H410	Very toxic to aquatic life with long lasting effects.

## P-Code

P201	Obtain special instructions before use.
P210	Keep away from heat, hot surfaces, sparks, open flames, and other ignition sources. No smoking.
P220	Keep/Store away from clothing/combustible materials.
P233	Keep container tightly closed.
P260	Do not breathe dust/fume/gas/mist/vapors/spray.
P261	Avoid breathing dust/fume/gas/mist/vapors/spray.

**P264** Wash thoroughly after handling.  
**P273** Avoid release to the environment.  
**P280** Wear protective gloves/protective clothing/eye protection/face protection.  
**P301+310** IF SWALLOWED: Immediately call a POISON CENTER/doctor.  
**P301+330+331** IF SWALLOWED: Rinse mouth. Do NOT induce vomiting.  
**P302+352** IF ON SKIN: Wash with plenty of water/soap.  
**P303+361+353** IF ON SKIN (or hair): Take off immediately all contaminated clothing. Rinse skin with water/shower.  
**P304+340** IF INHALED: Remove person to fresh air and keep comfortable for breathing.  
**P305+351+338** IF IN EYES: Rinse cautiously with water for several minutes. Remove contact lenses, if present and easy to do. Continue rinsing.  
**P308+313** IF exposed or concerned: Get medical advice/attention.  
**P310** Immediately call a POISON CENTER/doctor.  
**P320** Specific treatment is urgent (see ... on this label).  
**P321** Specific treatment (see ... on this label).  
**P337+313** If eye irritation persists: Get medical advice/attention.  
**P342+311** If experiencing respiratory symptoms: Call a POISON CENTER/doctor.  
**P361** Take off immediately all contaminated clothing.  
**P403+233** Store in a well-ventilated place. Keep container tightly closed.  
**P405** Store locked up.  
**P501** Dispose of contents/container to ...



## LIST OF FIGURES

Figure 1: Chronological Presentation of selected Antibiotics and their corresponding Emergence of Antibiotic-resistant Bacterial Strains

Figure 2: A schematic Elucidation of Antibiotic Targets within Bacteria

Figure 3: A schematic Representation of Antibiotic Resistance Mechanisms

Figure 4: Schematic Representation of the gram-positive Bacterial Cell Wall

Figure 5: Biofilm Formation Cycle

Figure 6: A simplified schematic Figure of Class A and B PBPs

Figure 7: Biochemical Reaction Mechanism of Transpeptidases

Figure 8: Vector map of pEt-28b(+) created with SnapGene®

Figure 9: Output of SignalP - 5.0 signal peptide prediction for *SePBP3*

Figure 10: Output of SignalP - 5.0 signal peptide prediction for *SaPBP2a*

Figure 11: A schematic Figure of a Transformation

Figure 12: A schematic Figure of the final Gene Expression Protocol

Figure 13: A schematic Figure of the Principle of a Ni-NTA Affinity Chromatography

Figure 14: A schematic Figure of the 6 x His-tagged Protein binding to a Ni-NTA Matrix

Figure 15: A schematic Figure of the Principle of Dialysis

Figure 16: A schematic Figure of the Principle of a Size Exclusion Chromatography used as a polishing Step

Figure 17: A schematic Figure of the Principle of an Isothermal Titration Calorimetry Setup

Figure 18: A schematic Figure of the Principle of a CD Spectroscopic Analysis of the Secondary Structure

Figure 19: A schematic Figure of the Principle of a Bragg Diffraction. Figure by Hadmack/CC BY

Figure 20: A schematic Figure of the Principle of a Hanging Drop and Sitting Drop as Examples of Vapour Diffusion Crystallization Approach and of the Phase Diagram

Figure 21: SDS-PAGE Analysis of the Test Expression at 20 °C and 30 °C of *SePBP3* in BL21 DE3 cells at a 12% Polyacrylamide Gel

Figure 22: SDS-PAGE Analysis of the Expression and Purification of *SePBP3* at a 12% Polyacrylamid Gel

Figure 23: Size Exclusion Chromatogram (SEC) of *SePBP3* after Ni-NTA Affinity Chromatography Purification

**Figure 24: Dynamic Light Scattering Dispersity Profile of SePBP3 after SEC Purification**

**Figure 25: Circular Dichroism Plot of SePBP3 after SEC Purification**

**Figure 26: Secondary Structure Estimation and Reference Plot according to Yang et al. (J. T. Yang et al., 1986)**

**Figure 27: Secondary Structure Estimation and Reference Plot according to Reed et al. (Reed and Reed, 1997)**

**Figure 28: Melting Curves of SePBP3 as measured via Circular Dichroism (CD) Spectroscopy**

**Figure 29: Apo-Crystals in two different Morphologies**

**Figure 30: Co-Crystals of Vaborbactam and Cefotaxime**

**Figure 31: One SePBP3 Crystal inside a Micro-loop**

**Figure 32: Resolution, Number of Spots and Intensity of the Crystal during the Measurement**

**Figure 33: One Protein is in one Asymmetric Unit**

**Figure 34: The Symmetry  $P4_12_12$  has a fourfold Symmetry Axis**

**Figure 35: Approximate eight Proteins are fitting inside one Unit Cell**

**Figure 36: A Super Cell of the Protein Crystal with the extended Solvent Channels**

**Figure 37: The Solvent Content within a Unit Cell of the SePBP3 Crystal (Pletzer-Zelgert et al., 2023)**

**Figure 38: Volume (green) of the active Site of SePBP3 (red)**

**Figure 39: Diffraction Pattern of SePBP3 with a magnified Area to highlight the Closeness of Spots**

**Figure 40: Secondary Structure Elements according to the X-ray Structure of SePBP3 (Laskowski, 2022)**

**Figure 41: Secondary Structure Elements together with the Sequence of SePBP3**

**Figure 42: Cartoon and Topology Plot of SePBP3**

**Figure 43: Conservation of Structure in the Transpeptidase Domain**

**Figure 44: Comparative C-alpha Backbone Analysis of Penicillin-binding Protein Structures: Conserved Transpeptidase and Linker Domains with varied N-terminal Anchor and Head Sub-domains**

**Figure 45: Sequence Alignment of SePBP3 from *Staphylococcus epidermidis*, SaPBP2a and SaPBP3 from *Staphylococcus aureus*, SpPBP2B from *Streptococcus pneumoniae* and PaPBP3 from *Pseudomonas aeruginosa* including Secondary Structure of SePBP3**

**Figure 46. Comparative Structural Analysis of SePBP3 and SaPBP2a**

**Figure 47: Binding Characterization of Cefotaxime and Vaborbactam with *SePBP3***

**Figure 48. Superimposed Structures of Penicillin-binding Protein 3 (PBP3) from *Staphylococcus epidermidis* (*SePBP3*; blue) and *Staphylococcus aureus* (*SaPBP3*, green)**

**Figure 49: SAXS Data Summary for *SePBP3***

**Figure 50: Exploiting of the Porod Power-Law Relation to Analyse the *SePBP3* Conformation**

**Figure 51. Dynamic Flexibility Analysis of *SePBP3* Post 100 ns Molecular Dynamics Simulation**

**Figure 52: Molecular Dynamics Stability Analysis of *SePBP3* Over 100 ns**

**Figure 53: SDS-PAGE Analysis of the Test Expression at 20 °C and 30 °C of *SePBP2a* in BL21 DE3 cells at a 12% Polyacrylamide Gel**

**Figure 54: SDS-PAGE Analysis of the Expression and Purification of *SePBP2a* at a 12% Polyacrylamid Gel**

**Figure 55: Size Exclusion Chromatogram (SEC) of *SePBP2a* after Ni-NTA Affinity Chromatography Purification**

**Figure 56: SDS-PAGE Analysis of the of *SePBP2a* with His-Tag and after Removal of the His-Tag at a 12% Polyacrylamid Gel**

**Figure 57: Binding Assay of *SePBP2a* with and without His-tag and with Cefotaxime**

**Figure 58: Dynamic Light Scattering Dispersity Profile of *SePBP2a* after Removal of the His-tag**

**Figure 59: Circular Dichroism Plot of *SePBP2a* before and after SEC Removal of the His-tag**

**Figure 60: Crystallization Approach of *SePBP2a* under the pH value of 7**

**Figure 61: Crystallization Approach of *SePBP2a* under the pH value of 8**

**Figure 62: PBP2a Structure with highlighted allosteric Domain and active Site**

**Figure 63: Compounds with the highest Docking Score**

**Figure 64: PBP2a Transpeptidase Cavity with open and closed State**

**Figure 65: PBP2a during a 10 ns MD Simulation**

**Figure 66: PBP2a with and without the Peptidoglycan Analogue during a 10 ns Simulation Time.**

**Figure 67: PBP2a with and without the AAK443 Compound during a 10 ns Simulation Time**

**Figure 68: PBP2a with and without the AAK489 Compound during a 10 ns Simulation Time.**

**Figure 69: PBP2a with and without the AAK797 Compound during a 10 ns Simulation Time**

**Figure 70: PBP2a with and without the AAK268 Compound during a 10 ns Simulation Time**

**Supplementary Figure 1: RMSD Values of PBP2a and the Compound AAK268**

**Supplementary Figure 2: A schematic Figure of detailed Ligand (AAK268) Atom Interactions with the Protein Residues**

**Supplementary Figure 3: RMSD Values of PBP2a and the Compound AAK376**

**Supplementary Figure 4: A schematic of Figure detailed Ligand (AAK376) Atom Interactions with the Protein Residues**

**Supplementary Figure 5: RMSD Values of PBP2a and the Compound AAK433**

**Supplementary Figure 6: A schematic Figure of detailed Ligand (AAK433) Atom Interactions with the Protein Residues**

**Supplementary Figure 7: RMSD Values of PBP2a and the Compound AAK797.**

**Supplementary Figure 8: A schematic Figure of detailed Ligand (AAK797) Atom Interactions with the Protein Residues**

**Supplementary Figure 9: Globally Harmonized System of Classification (GHS) Pictograms**

## LIST OF TABLES

Table 1: Historical Introduction of selected antibiotics: A Chronological Overview

Table 2: A detailed overview of selected antibiotic classes, emphasizing their mode of action and associated resistance mechanisms

Table 3: Comprehensive Catalog of selected PBP Classes (Sauvage et al., 2008)

Table 4: Media and Composition

Table 5: Buffers and Composition

Table 6: Overview of Equipment

Table 7: Overview of Consumables

Table 8: Overview of Software

Table 9: Confidently predicted Domains, Repeats, Motifs and Features made by SMART

Table 10: Original Nucleotide Sequences of *SePBP3* from RP62A (PMID: 15774886)

Table 11: Modified and *Escherichia coli* -Codon optimized Nucleotide Sequence of *SePBP3*

Table 12. Original Protein Sequence of *SePBP3* from RP62A

Table 13. Protein Sequences of *SePBP3* from RP62A

Table 14: Confidently predicted Domains, Repeats, Motifs and Features made by SMART

Table 15. Original Nucleotide Sequences of *MecA* from RP62A (PMID: 15774886)

Table 16: Modified and *Escherichia coli* -Codon optimized Nucleotide Sequence of *MecA*

Table 17: Original Protein Sequence of *SePBP2a* from RP62A

Table 18: Protein Sequences of *SePBP2a* from RP62A

Table 19: Gene Expression Tests

Table 20: Composition of the Stacking Gel, the Separation Gel and the running Buffer

Table 21: Composition of the Sample Buffer, Coomassie staining Solution and the destaining Solution

Table 22: Data Collection and Refinement of *SePBP3*, *SePBP3*– Cefotaxime and *SePBP3*-Vaborbactam

Table 23. Guinier Analysis and P(r) Function Analysis of SAXS Measurement

Table 24: Data Collection and Refinement of *SaPBP2a* and *SePBP2a* – a Comparison of the Data Quality

Table 25: Compounds with the best Docking Score against PBP2a

Table 26: Compounds with the AA Interactions, Dockings Scores and E Model

## **ACKNOWLEDGMENTS**

First and foremost, I would like to express my sincere gratitude to my doctoral advisor, Prof. Dr. Christian Betzel, for providing me with the opportunity to pursue my research topics, for his guidance throughout my doctoral studies, and for his review of my work.

I am also deeply thankful to Prof. Holger Rohde for his role as my co-supervisor, whose insights and support have significantly advanced my research.

Additionally, I extend my appreciation to Prof. Rohde for accepting the role of secondary reviewer of my dissertation and to my disputation examiners, Prof. Hartmut Schlüter and Dr. Thomas Hackl, for their assessments.

A heartfelt thank you goes out to the staff of the Beamlines P11 at DESY, P12, and P13 at EMBL, and the European XFEL in Hamburg for their patient support during numerous experimental sessions.

I am grateful to all the members of our research group for their collaboration and for the shared experiences and insights that have enriched this journey.

Lastly, I want to thank my family and friends for their support during my studies.

## EIDESSTÄTTLICHE ERKLÄRUNG

„Hiermit versichere ich an Eides statt, die vorliegende Dissertation selbst verfasst und keine anderen als die angegebenen Hilfsmittel benutzt zu haben.“

M Schwinzer Hamburg, 29.01.2023

Martin Schwinzer